

# **Low-cost and Transferable Precision Agriculture Technique to Monitor Crop Anomalies in Rice Fields**

**Liliana Carolina Castillo Villamor**

*A thesis submitted in fulfilment of the requirements for the degree of*

**Doctor of Philosophy**

January 2022

Aberystwyth University

Supervisors: Dr. Andrew Hardy and Dr. Peter Bunting



*A Lilia y Ulfran, mis padres,  
este logro es tan suyo como mío.*

*To Lilia and Ulfran, my parents,  
this achievement is as much theirs as mine.*



## ABSTRACT

Global agricultural land is expected to keep expanding in the coming years, especially in Sub-Saharan Africa and Latin American countries. However, many existing Precision agriculture (PA) techniques are challenging to transfer to agricultural systems in these regions as they rely on prohibitively expensive crop monitoring systems. Satellite remote sensing has the potential to support the delimitation of Site-specific Management Zones as it offers an inexpensive and non-destructive way of providing frequent information systematically at different spatial scales.

This research presents the Earth Observation-based Anomaly Detection (EOAD) approach: a system that detects underperforming areas in croplands using medium and high-resolution satellite EO imagery. The EOAD is a simple anomaly detection technique, based on the deviation of image statistics from a normal distribution using dynamic thresholding, without the need for manual calibration or prior expertise in spectral analysis of crops.

The EOAD approach demonstrated a strong agreement, 80% overall accuracy, with field observations of crop anomalies within rice plots in the Ibagué Plateau, Colombia, using vegetation indices derived from optical Sentinel-2 and PlanetScope imagery. Areas identified as anomalous during the booting stage were significantly ( $p < 0.005$ ) associated with a decrease in final yield. Additionally, the percentage of anomalies detected with the EOAD using Sentinel-2 Vegetation indices improved the detection of underperforming plots in early growth stages. The method was unreliable when applied to Sentinel-1 radar data but may be improved by isolating backscatter mechanisms prior to analysis.

The results demonstrate that the EOAD approach is transferable across different optical EO systems and data types. Most of the Sentinel-2 indices that produced the highest accuracies and best predicted underperforming plots are transferable to other systems such as Landsat and PlanetScope. This consistency is especially important in regions with a constant presence of clouds, as the availability of two data sources improves the data acquisition frequency by increasing the chances of retrieving cloud-free imagery.

Currently, there is a limited offer of methods that detect in-field anomalies in croplands under low agronomic data availability scenarios and even fewer reports of the actual impacts of these anomalies on yield. As such, the EOAD approach presented in this research represents an efficient and low-cost means of supporting informed agricultural practices, especially in relatively resource-poor regions of the world where food security is paramount.

## ACKNOWLEDGEMENT

First and foremost, I would like to acknowledge my supervisors: I would like to thank Dr Andy Hardy for his encouragement, guidance, and having the best disposition to give me academic advice and support. Thanks to Dr Pete Bunting for his academic advice and for never getting tired of helping me solve coding issues.

I am grateful to the staff of Environment Systems involved in the EO4cultivar project for trusting me and making me feel more welcome in the UK. Thank you to Steve, Pascale, and Jackeline for giving me the chance to learn more about the space sector in the UK. I would also like to thank Johanna Breyer for her wise advice on doing a PhD without dying in the attempt. Iain Cameron for his constant support and for sharing with me some of his knowledge on radar imagery. Thanks to my PhD project mates Angela and Cristian for walking together with me along this journey. I also want to express my sincere thanks to the International Partners of the EO4cultivar project, especially Raul and Luis Jose in Danper and Harry in Barfoots, who kindly taught us about their agricultural production systems.

This work would not have been possible without the support of Hacienda El Escobal, that welcomed me to carry out the fieldwork. Thanks to Jose Maria Madrid, Miguel Zamora and Yeison Rodriguez for the long knowledge exchange sessions that were definitive for the development of this research.

I would also like to thank the UK space agency for funding this research through the EO4cultivar project. A special thank you to Liz Cox from the International Partnership Programme for allowing me to learn more about the space industry in the UK. I express my sincere thanks to the Douglas Bomford Trust for the financial support to carry out fieldwork and multiple knowledge exchange sessions in Colombia and Peru.

I would also like to thank my colleagues from the Earth Observation and Ecosystem Dynamics Research Group for the many laughs we shared and the exciting discussions that made me grow professionally and personally. Thanks to Osian for his patience in teaching me all the coding tricks in Python and Elikana John for the lovely chats while we both were missing our warm countries.

Special thanks to Amaya, Azam and Suvarna for their warm and sincere friendship in the cold days of Aberystwyth. They are my friends and a role model for women in science. A very special word of thanks goes to Douglas Gomez for his lessons on climatology but, most importantly, for his support and writings that transported me to invisible cities. Thanks to Willian Llanos for his patience in teaching me some statistics; your lessons were fundamental in this research. Thank you to my friends from Colombia and around the world that stayed in contact with me and gave me support as if the distance did not exist. The day will come when I thank you with a big hug and a cold beer. Finishing this document would not have been possible without the support and patience of Mauro, who patiently accompanied me during the final long days of writing.

Finally, I wish to thank my parents, who always believe in me and support me in everything. Your love, continued encouragement, and guidance made me the person I am today.

## TABLE OF CONTENTS

<b>ABSTRACT</b> . . . . .	ii
<b>ACKNOWLEDGEMENT</b> . . . . .	iv
<b>LIST OF FIGURES</b> . . . . .	x
<b>LIST OF TABLES</b> . . . . .	xiv
<b>LIST OF TERMS AND ABBREVIATIONS</b> . . . . .	xvi
<b>1 Introduction</b>	<b>1</b>
1.1 Agriculture in a changing world . . . . .	1
1.2 Challenges . . . . .	4
1.3 Precision agriculture . . . . .	5
1.4 Satellite Earth Observation for Precision Agriculture applications . . . . .	6
1.5 Research Questions and Objectives . . . . .	8
1.6 Thesis structure . . . . .	9
<b>2 Literature Review</b>	<b>11</b>
2.1 Introduction . . . . .	11
2.2 Rice production . . . . .	11
2.2.1 Rice Cultivation in Colombia . . . . .	12
2.2.2 Rice agronomic features . . . . .	15
2.3 Optical Remote Sensing in agriculture monitoring . . . . .	16
2.3.1 Optical satellite sensors . . . . .	18
2.3.2 Optical Vegetation indices as indicators of crop condition . . . . .	26
2.4 Synthetic Aperture Radar (SAR) products as indicators of crop condition . . . . .	31
2.4.1 SAR Systems Configurations . . . . .	33
2.4.2 Scattering from croplands . . . . .	35
2.4.3 Applications of SAR on crop monitoring . . . . .	37

2.5	Machine learning approaches for retrieving agricultural variables using satellite RS . . . . .	38
2.5.1	ML approaches for crop yield prediction . . . . .	39
2.5.2	Measuring Models performance . . . . .	44
2.5.3	Multicollinearity . . . . .	48
2.6	Remote Sensing for crop anomaly detection . . . . .	52
<b>3</b>	<b>Study locations</b>	<b>57</b>
3.1	Introduction . . . . .	57
3.2	Location . . . . .	57
3.3	Rice production system in the Ibague Plateau . . . . .	60
<b>4</b>	<b>Datasets and pre-processing</b>	<b>66</b>
4.1	Satellite datasets description . . . . .	66
4.1.1	Sentinel-2 . . . . .	68
4.1.2	PlanetScope . . . . .	71
4.1.3	Sentinel-1 . . . . .	73
4.2	Image pre-processing . . . . .	76
4.2.1	Optical Imagery . . . . .	76
4.2.2	Sentinel-1 . . . . .	83
4.2.3	Vegetation Indices . . . . .	86
4.3	Ground data . . . . .	91
4.3.1	Weather data . . . . .	91
4.3.2	Agronomic data . . . . .	92
<b>5</b>	<b>In-field Anomaly detection</b>	<b>97</b>
5.1	Introduction . . . . .	97
5.2	Methods . . . . .	102
5.2.1	Datasets Description . . . . .	103
5.2.2	The Earth Observation-based Anomaly Detection (EOAD) Technique	105
5.2.3	Accuracy Assessment . . . . .	108
5.2.4	Typical Rainfall Period . . . . .	110

5.2.5	Discrimination of Anomalous from Non-anomalous Areas at Different Growth Stages . . . . .	111
5.3	Results . . . . .	112
5.3.1	Accuracy assessment . . . . .	113
5.3.2	Typical Rainfall Period . . . . .	118
5.3.3	Discrimination of Anomalous from Non-anomalous Areas at Different Growth Stages . . . . .	119
5.4	Discussion . . . . .	125
5.4.1	Accuracy assessment . . . . .	126
5.4.2	Typical Rainfall Period . . . . .	129
5.4.3	Discrimination of anomalous from non-anomalous areas for different growth stages . . . . .	130
5.5	Conclusions . . . . .	133
<b>6</b>	<b>Effects of in-field anomalies on crop yield</b>	<b>135</b>
6.1	Introduction . . . . .	135
6.2	Methods . . . . .	137
6.2.1	Datasets Description . . . . .	138
6.2.2	Impact of Frequency of Anomalies on Yield . . . . .	140
6.2.3	Impact of anomalies at different crop stages over yield . . . . .	144
6.2.4	Early detection of underperforming plots . . . . .	147
6.3	Results . . . . .	153
6.3.1	Impact of frequency of anomalies on yield . . . . .	153
6.3.2	Impact of anomalies at different crop stages over yield . . . . .	159
6.3.3	Early detection of underperforming plots . . . . .	164
6.4	Discussion . . . . .	176
6.4.1	Impact of frequency of anomalies on yield . . . . .	178
6.4.2	Impact of anomalies at different crop stages over yield . . . . .	179
6.4.3	Early detection of underperforming plots . . . . .	181
6.5	Conclusions . . . . .	184
<b>7</b>	<b>Conclusions</b>	<b>188</b>

7.1	Future Work . . . . .	191
7.1.1	In-field Anomaly detection . . . . .	192
7.1.2	Effects of in-field anomalies on crop yield . . . . .	193
7.1.3	Transferability . . . . .	194
7.2	Wider importance . . . . .	194
<b>REFERENCES</b>		<b>195</b>
<b>LIST OF PUBLICATIONS . . . . .</b>		<b>242</b>
<b>Appendices</b>		
<b>Appendix A</b>	<b>One-way Data Transfer Agreement</b>	<b>244</b>
<b>Appendix B</b>	<b>Pictures Taken During the Field Visit</b>	<b>252</b>
<b>Appendix C</b>	<b>Validation Points Records</b>	<b>254</b>



## LIST OF FIGURES

1.1	Historical trends of global food and non-food agricultural demand . . . .	2
1.2	Historical per capita calorie intake by source . . . . .	2
1.3	Change in cropland, 2018 to 2030 . . . . .	3
1.4	Association between endemism richness and potential for cropland expansion . . . . .	3
2.1	Average grain yield and total production per year (2016) for the five rice-growing regions in Colombia . . . . .	13
2.2	Total of irrigated and rainfed areas harvested during Semester 1 and Semester 2 2016 . . . . .	14
2.3	Rice growth stages as defined in the BBCH scale and the farm scale . . .	16
2.4	Spectral reflectance characteristics of healthy green vegetation in the region from 0.35 - 2.6 $\mu m$ . . . . .	17
2.5	Spectral range of bands for different sensors (0.4 - 1.8 $\mu m$ ) . . . . .	23
2.6	Observation geometry of a SAR imager . . . . .	32
2.7	Normalisation areas for SAR backscatter . . . . .	33
2.8	Scattering mechanisms in rice crops . . . . .	36
2.9	Example of a dataset and its associated decision tree . . . . .	41
2.10	Random forest structure . . . . .	42
2.11	Example of the structure of Gradient Boosted Decision Trees . . . . .	45
2.12	Examples of ROC curves. . . . .	47
2.13	Example of 5-fold cross-Validation . . . . .	48
3.1	Map showing the Ibagu� plateau study site, Colombia . . . . .	58
3.2	Digital Elevation Model of the Ibagu� plateau, Colombia . . . . .	58
3.3	Soil taxonomy map of the Ibagu� plateau, Colombia. . . . .	60

3.4	Box plots of the total monthly harvested area in Hacienda El Escobal (i.e., 605 plots harvested between 2014 and 2018) and monthly rainfall values between January 2014 and December 2018. . . . .	62
3.5	Rice field with contour-levee irrigation system . . . . .	64
3.6	Rice field that received two different Nitrogen dosages . . . . .	65
3.7	Two combines and a truck in a rice field in the Hacienda El Escobal farm	65
4.1	Acquisition dates of the PlanetScope, Sentinel-2 and Sentinel-1 scenes .	67
4.2	Example of the types of satellite images used. . . . .	68
4.3	Sentinel-2 and Planet Scope spectral bands . . . . .	69
4.4	Spectral response functions for the visible and infrared bands of the Sentinel-2 A MultiSpectral MSI (19 December 2017) . . . . .	71
4.5	Spectral response functions for the short wave infrared bands of the S2-A MultiSpectral Instrument (19 December 2017) . . . . .	72
4.6	Sentinel-1 Acquisition Modes (from Bourbigot et al., 2016) . . . . .	74
4.7	Spatial distribution of look angles in Sentinel-1 images over the study area	75
4.8	Scheme of the reflection angles of a vegetation canopy on a horizontal surface and an inclined surface (from Shepherd and Dymond, 2003). . .	79
4.9	Flowchart of pre-processing operations performed over Sentinel-2 L 1C products . . . . .	82
4.10	Homogenised rainfall data from the "Aeropuerto Perales" weather station	92
5.1	Flowchart describing the processes involved in the Earth EOAD method and assessment. . . . .	103
5.2	Distribution of sample points used for validation . . . . .	105
5.3	Extraction of thresholds using the histogram analysis approach . . . . .	106
5.4	Example of the histogram analysis performed over one rice field . . . . .	107
5.5	Location of the Perales Airport weather station in relation to the study area	111
5.6	Examples of anomaly surfaces built after applying the EOAD technique over Sentinel-2/PlanetScope NDVI and Sentinel-1 VH products for a rice plot at the tillering stage (BBCH 21 - BBCH 30). . . . .	114
5.7	Types of anomalies identified in the rice fields . . . . .	115

5.8	Anomaly detection accuracy metrics obtained with the optical vegetation indices . . . . .	116
5.9	Anomaly detection accuracy metrics obtained with the Sentinel-1 products	116
5.10	SPI values from January 2016 until March 2020 . . . . .	119
5.11	Optical and SAR imagery available for the typical-rainfall period . . . .	119
5.12	Box plots of the average plot values of VI/SAR-products for non-anomalous and anomalous areas at different growth stages and t-statistic obtained for each independent two-sample t-test. . . . .	122
5.13	Sentinel-2 and Planet Scope spectral response functions . . . . .	128
5.14	Relationship between C-band $\sigma^0$ and total dry biomass . . . . .	131
5.15	Temporal variation of VV and VH $\sigma^0$ for two types of rice productive systems using s1) imagery. . . . .	133
6.1	Flowchart describing the analysis perform on each plot to assess the effects of in-field anomalies on crop yield . . . . .	138
6.2	Example of the frequency surface built for a rice field using the NDVI_b8 anomaly surface for one crop cycle. . . . .	140
6.3	Flowchart describing the processes involved in the analysis of frequency	141
6.4	Example of the Dunn's multiple comparison output for the NDVI_b8A_6 frequency pixels. . . . .	145
6.5	Example of the compact letter display format to present the result of the Dunn's test for the NDVI_b8A_6 frequency pixels. . . . .	145
6.6	Box plots of yield per number of scenes in which the pixels are predicted anomalous within one crop cycle . . . . .	155
6.7	Box plots of yield obtained for anomalous and non-anomalous pixels values at different growth stages. . . . .	161
6.8	Heat maps presenting Pearson's correlation analysis of proposed variables to predict underperforming plots using different VIs during the seedling stage. . . . .	166
6.9	Heat maps presenting Pearson's correlation analysis of proposed variables to predict underperforming plots using different VIs during the tillering stage. . . . .	167

6.10	Heat maps presenting Pearson's correlation analysis of proposed variables to predict underperforming plots using different VIs during the panicle formation stage. . . . .	168
6.11	Heat maps presenting Pearson's correlation analysis of proposed variables to predict underperforming plots using different VIs during the booting stage. . . . .	169
6.12	Heat maps presenting Pearson's correlation analysis of proposed variables to predict underperforming plots using different VIs during the ripening stage. . . . .	170
6.13	Histogram of farm average yield values per plot and thresholds used to classify the fields into high and low performing. . . . .	171
6.14	Cross validated mean AUC values of the GB classifier for all the VIs at different growths stages using the set of predictors A and B . . . . .	176
6.15	Standard deviation of cross-validated AUC values of the GB classifier fit to the set of variables B at different crop growth stages for the VIs presented in Table 4.5 . . . . .	177
6.16	Heat maps presenting the cross-validated AUC-ROC values computed for the classifier trained and validated on the set of predictors B at different rice stages and the 4 thresholds. . . . .	177

## LIST OF TABLES

2.1	Overview of some satellite optical sensors most used in crop monitoring	19
2.2	Common vegetation indices used in agricultural applications . . . . .	29
2.3	SAR microwave bands in which most of civilian spaceborne sensors operate . . . . .	34
2.4	Relative scattering strength by polarisation (adapted from Flores et al., 2019) . . . . .	36
2.5	Confusion matrix. . . . .	46
4.1	Spectral bands for the Sentinel-2 sensors (ESA 2013) . . . . .	70
4.2	Ortho Scene PlanetScope imagery bands and pixel size (ESA 2013) . . .	73
4.3	SAR acquisition geometries . . . . .	75
4.4	Sentinel-1 products . . . . .	85
4.5	Multi-spectral vegetation indices evaluated. . . . .	88
4.6	Agronomic data available for the rice productive system . . . . .	93
5.1	Confusion matrix used to evaluate the anomaly detection method accu- racy. . . . .	109
5.2	Performance metrics derived from the confusion matrix . . . . .	110
5.3	Thresholds used to interpret the strength of agreement of TSS statistics .	110
5.4	Correctly predicted anomalies per type of problem identified in the field using PS, S1 and S2 imagery . . . . .	117
5.5	t-scores for comparing the average plot values of VI/SAR-products for non-anomalous and anomalous areas at different growth stages. . . . .	120
6.1	Datasets registered per plot. . . . .	139
6.2	Two sets of predictors per plot proposed to predict underperforming plots	148
6.3	Yield thresholds. . . . .	149

6.4	Parameters entered in TPOT to find the best pipeline to predict the high/low yield classes using the NDVI_b8 data at the seedling and booting stages . . . . .	151
6.5	Kruskal-Wallis metrics derived from the comparison of yield for pixels with different frequencies of anomalies using S2 and S1 products. . . .	153
6.6	Two sets of definitive predictors to be used in the yield classification model	165
6.7	Number of high and low performing plots per threshold . . . . .	171
6.8	AUC-ROC values obtained from TPOT for the yield threshold at the booting stage using the NDVI_b8 . . . . .	172
6.9	Hyperparameters of the Gradient Boosting Classifier selected by TPOT as the best pipeline to predict underperforming plots using the NDVI_b8 during the booting stage . . . . .	173

## LIST OF TERMS AND ABBREVIATIONS

<b>AGB</b> Above-Ground Biomass . . . . .	24
<b>ANN</b> Artificial Neural Network . . . . .	39, 184
<b>API</b> Application Programming Interface . . . . .	151
<b>ARD</b> Analysis Ready Data . . . . .	66
<b>ASTER</b> Advanced Spaceborne Thermal Emission and Reflection Radiometer . . . .	27
<b>AUC-ROC</b> Area under the ROC Curve xiii, xv, 46, 148, 152, 172, 175, 177, 183, 184	
<b>AutoML</b> Automated Machine Learning . . . . .	147, 151
<b>AVHRR</b> Advanced Very High Resolution Radiometer . . . . .	19, 22, 23, 27, 43, 55
<b>BBCH</b> Biologische Bundesanstalt, Bundessortenamt und Chemische Industrie . .	15
<b>BRT</b> Boosted Regression Trees . . . . .	49
<b>BW</b> Histogram Bin Width . . . . .	106
<b>CART</b> Classification and Regression Trees . . . . .	41
<b>CI<sub>green</sub></b> Green Chlorophyll Index . . . . .	29, 88, 115, 160, 164, 180, 181
<b>CI<sub>Red-edge</sub></b> Red-edge Chlorophyll Index . . . . .	28, 29, 88, 115, 160, 164, 180, 181, 183
<b>CPCA</b> Constrained principal component analysis . . . . .	49
<b>CV</b> Cross-validation . . . . .	47, 175
<b>DAE</b> Day After Emergence . . . . .	15, 16, 64, 65, 94, 105, 112, 113
<b>DEM</b> Digital Elevation Model . . . . .	63
<b>df</b> Degrees of Freedom . . . . .	153, 154
<b>ENL</b> Equivalent Number of Looks . . . . .	128, 193
<b>EO</b> Earth Observation . . . . .	7, 31, 54, 99, 127, 138
<b>EOAD</b> Earth Observation-based Anomaly Detection ii, vii, 10, 104, 105, 108, 125–129, 137, 139, 140, 146–148, 159, 164, 189, 192–194	

<b>ET</b> Evapotranspiration . . . . .	129, 130
<b>ETM</b> Enhanced Thematic Mapper . . . . .	19
<b>ETM+</b> Enhanced Thematic Mapper Plus . . . . .	19
<b>ETo</b> Reference Evapotranspiration . . . . .	130
<b>EVI</b> Enhanced Vegetation Index . . . . .	27–29, 88
<b>EVI2</b> 2-Band Enhanced Vegetation Index . . . . .	27, 29, 40
<b>EW</b> Extra Wide Swath Mode . . . . .	73
<b>FAO</b> Food and Agriculture Organisation . . . . .	2
<b>fAPAR</b> Fraction of Absorbed Photosynthetically Active Radiation . . . .	27, 39, 55
<b>FEDEARROZ</b> Colombian National Federation of Rice Growers . . . . .	12, 60
<b>FN</b> False Negative . . . . .	46, 108
<b>FP</b> False Positive . . . . .	46, 108
<b>FPR</b> False Positive-rate . . . . .	46
<b>GAI</b> Green Area Index . . . . .	39
<b>GBC</b> Gradient Boosting Classifier . . . . .	172, 175, 181, 184, 185, 193
<b>GBR</b> Gradient Boosted Regression Model . . . . .	44, 184
<b>GBT</b> Gradient Boosted Trees . . . . .	39, 44
<b>GEE</b> Google Earth Engine . . . . .	84, 129
<b>GHG</b> Greenhouse gas . . . . .	4
<b>gNDVI</b> Green Normalised Difference Vegetation Index 28, 89, 113, 127, 133, 134, 190, 191	
<b>GNSS</b> Global Navigation Satellite System . . . . .	63
<b>GPP</b> Gross Primary Production . . . . .	28
<b>GPS</b> Global Positioning System . . . . .	94
<b>GRD</b> Ground Range Detected . . . . .	73, 74, 129
<b>Green LAI</b> Green Leaf Area Index . . . . .	27



<b>GVIF</b> Generalised Variance Inflation Factor . . . . .	181
<b>HRG</b> High-Resolution Geometric . . . . .	20, 22
<b>HRV</b> High Resolution Visible . . . . .	20, 22
<b>HRVIR</b> High-Resolution Visible and InfraRed . . . . .	20, 22
<b>IDEAM</b> Instituto de Hidrologia, Meteorologia y Estudios Ambientales . . . . .	91
<b>IW</b> Interferometric Wide Swath Mode . . . . .	73, 129
<b>LAC</b> Latin America and the Caribbean . . . . .	11
<b>MAE</b> Mean Absolute Error . . . . .	45
<b>MARS</b> Multivariate Adaptive Regression Splines . . . . .	49
<b>MASL</b> Meters Above Sea Level . . . . .	57, 59
<b>MERIS</b> Edium Resolution Imaging Spectrometer . . . . .	55
<b>ML</b> Machine Learning . . . . .	38, 39, 43, 44
<b>MLR</b> Multiple Linear Regression . . . . .	40
<b>MODIS</b> Moderate Resolution Imaging Spectroradiometer 8, 20, 22, 23, 40, 43, 44, 54, 135	
<b>MSE</b> Mean Squared Error . . . . .	44
<b>MSI</b> Multispectral Instrument . . . . .	xi, 69, 71
<b>MSS</b> Multi Spectral Scanner . . . . .	19
<b>N</b> Nitrogen . . . . .	179, 180, 182, 183, 185, 186, 191, 192
<b>NDII</b> Normalised Different Water Index . . . . .	28, 30, 90, 180
<b>NDMI</b> Normalised Difference Moisture Index . . . . .	30
<b>NDVI</b> Normalised Difference Vegetation Index 26–29, 43, 55, 88, 112–114, 180, 191	
<b>NDVI<sub>Red-edge</sub></b> Red-edge Normalised Difference Vegetation Index . . . . .	28, 30, 89, 180
<b>NDWI</b> Normalised Difference Water Index . . . . .	28, 30, 40
<b>NIR</b> Near-Infrared . . . . .	17, 27, 64, 113
<b>OBIA</b> Object-based image analysis . . . . .	54

<b>OLI</b> Operational Land Imager . . . . .	19
<b>ORS</b> Optical Remote Sensing . . . . .	16
<b>PA</b> Precision agriculture . . . . .	ii, 5, 6, 54
<b>PCR</b> Principal Component Regression . . . . .	49
<b>PDSI</b> Palmer Drought Severity Index . . . . .	130
<b>PIF</b> Pseudo-Invariant Feature . . . . .	76
<b>PLS</b> Partial Least Squares . . . . .	49
<b>PS</b> PlanetScope . . . . .	xiv, 10, 117, 118
<b>RF</b> Random Forests . . . . .	39, 42–44, 184
<b>RMSE</b> Root Mean Square Error . . . . .	43–45
<b>ROC</b> Receiver Operating Characteristic . . . . .	45, 46
<b>RS</b> Remote Sensing . . . . .	6, 7, 39, 48, 53, 55
<b>RTK</b> Real-time kinematic positioning . . . . .	63
<b>S1</b> Sentinel-1 . . . . .	xiv, xv, 10, 38, 74, 111, 113, 117, 118, 129, 136, 138, 153, 178, 179
<b>S2</b> Sentinel-2 . . . . .	xiv, xv, 6, 10, 24, 25, 43, 55, 111, 117, 127, 136, 138, 153, 179, 187
<b>SACZ</b> South Atlantic Convergence Zone . . . . .	31
<b>SALLJ</b> South American low-level jet east of the Andes . . . . .	31
<b>SAR</b> Synthetic Aperture Radar vi, x, xiv, 31–35, 37, 38, 55, 73, 83, 110, 179, 185, 189	
<b>SAVI</b> Soil-adjusted Vegetation Index . . . . .	27, 29, 88, 113, 127
<b>SLC</b> Single Look Complex . . . . .	73, 74
<b>SM</b> Stripmap Mode . . . . .	73
<b>SNHT</b> Standard Normal Homogeneity Test . . . . .	92
<b>SPI</b> Standardised Precipitation Index . . . . .	110, 111, 118
<b>SPOT</b> Systeme Pour l’Observation de la Terre . . . . .	22
<b>SPOT-VGT</b> Other way to call the Vegetation Monitoring Instrument on board the SPOT- 4 and SPOT- satellites . . . . .	8, 22, 23, 43, 54, 55

<b>SR</b> Simple Ratio . . . . .	29
<b>SSMZ</b> Site-specific Management Zones . . . . .	6, 7, 52, 53, 98, 188
<b>Suomi NPP</b> . . . . .	21
<b>SVM</b> Support Vector Machine . . . . .	39, 49, 184
<b>SWIR</b> Short-Wave Infrared . . . . .	17, 28
<b>TIRS</b> Thermal Infrared Sensor . . . . .	19
<b>TN</b> True Negative . . . . .	45, 108
<b>TOA</b> Top Of Atmosphere Reflectance . . . . .	76, 77
<b>TP</b> True Positive . . . . .	45, 108
<b>TPOT</b> Tree-based Pipeline Optimisation Tool . . . . .	xv, 147, 150, 151, 172, 173, 184, 193
<b>TPR</b> True Positive-rate . . . . .	46
<b>TSS</b> True Skill statistic . . . . .	109
<b>VI</b> Vegetation Index . . . . .	17, 26, 27, 102, 103, 110, 113, 114, 121, 132, 134, 137, 138, 154, 178, 179, 182, 185, 189, 192
<b>VIF</b> Variance Inflation Factor . . . . .	51
<b>VIIRS</b> Visible Infrared Imaging Radiometer Suite . . . . .	23, 135
<b>VMI</b> Vegetation Monitoring Instrument . . . . .	20
<b>VWC</b> Vegetation and soil Water Content . . . . .	28, 90
<b>WS</b> Water Shortage . . . . .	117
<b>WV</b> Wave Mode . . . . .	73

## **CHAPTER 1**

### **Introduction**

#### **1.1 Agriculture in a changing world**

For centuries, agriculture has provided people with food, clothing, medicine, and heating; however, agricultural production and food demands have changed over the last decades (Federico 2008). Economic and population dynamics are driving these changes in global economies, which will influence poverty, hunger, food security and the sustainability of food and farming systems in the coming years (Food and Agriculture Organization (FAO) 2017). Figure 1.1 presents the historical changes of global food and non-food agricultural demand. Historically, most agricultural production has been dedicated to satisfying the growing human food demand (Food and Agriculture Organization (FAO) 2018). This includes the direct consumption of agricultural products and the production of feed for animals that humans will later consume.

The world's population is projected to reach more than 9 billion by 2050 and may peak at more than 11 billion by the end of the century (Chaherli and Nash 2013; United Nations 2019). In the last decades, per capita caloric availability and the diversity of foods consumed have increased globally (See Figure 1.2). Particularly, the income growth in low- and middle-income countries would lead to higher consumption of meat, fruits and vegetables, demanding changes in the production and increasing the pressure over natural resources (Food and Agriculture Organization (FAO) 2017). Satisfying the increasing demands of agricultural goods is leading to a global cropland expansion and intensification (Food and Agriculture Organization (FAO) 2017; Zabel et al. 2019).

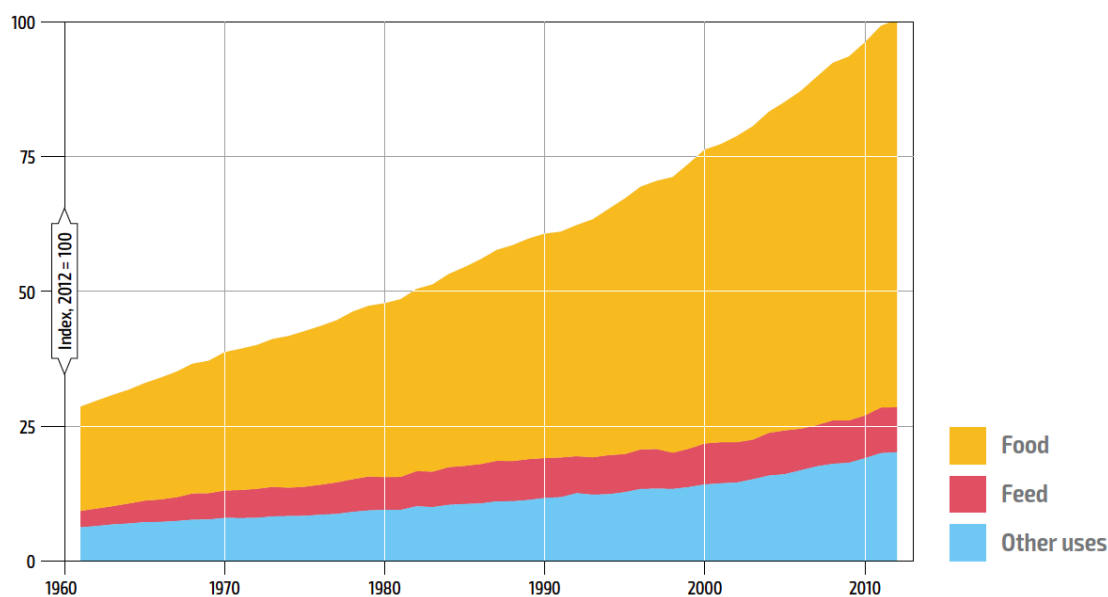


**Fig. 1.1** Historical trends of global food and non-food agricultural demand (from Food and Agriculture Organization (FAO), 2018). The index 2012=100 is based on the volume of food demand expressed in monetary terms at 2012 prices.

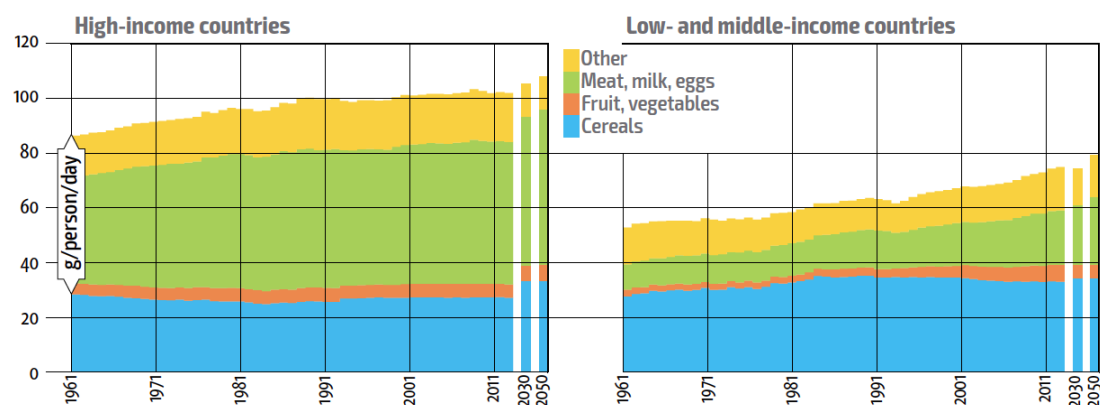


**Fig. 1.2** Historical per capita calorie intake by source (from Food and Agriculture Organization (FAO), 2017)

Agricultural production increased significantly from the 1960s as a result of the Green Revolution, the expansion in the use of natural resources for farming purposes and the industrialisation and globalisation of food and agriculture (Food and Agriculture Organization (FAO) 2017; Knudsen et al. 2006; Mazoyer and Roudart 2006). FAO projects that, by 2050, the area of arable land will expand around 5%, compared to 2009. This estimate comprises a 12% increase in low-income regions offset by an 8% decline in the high-income areas (Bruinsma 2003; Kirova et al. 2019). Almost all of the expansion in low-medium income countries is forecast to take place in Sub-Saharan Africa, and Latin America and the Caribbean (Alexandratos and Bruinsma 2012; Kirova et al. 2019). Figure 1.3 shows the changes in cropland estimated by Organisation for Economic

Co-operation and Development (OECD) and Food and Agriculture Organization (FAO) (2021) for different regions. The modelling approach developed by Zabel et al. (2019) aligns with FAO projections. It suggests that agricultural production gains will occur at the costs of increased deforestation, greenhouse gas emissions and land degradation, predominantly in developing tropical regions with significantly high endemism richness that are important for conservation. Figure 1.4 presents the global map of the relationship between endemism richness and potential for cropland expansion.

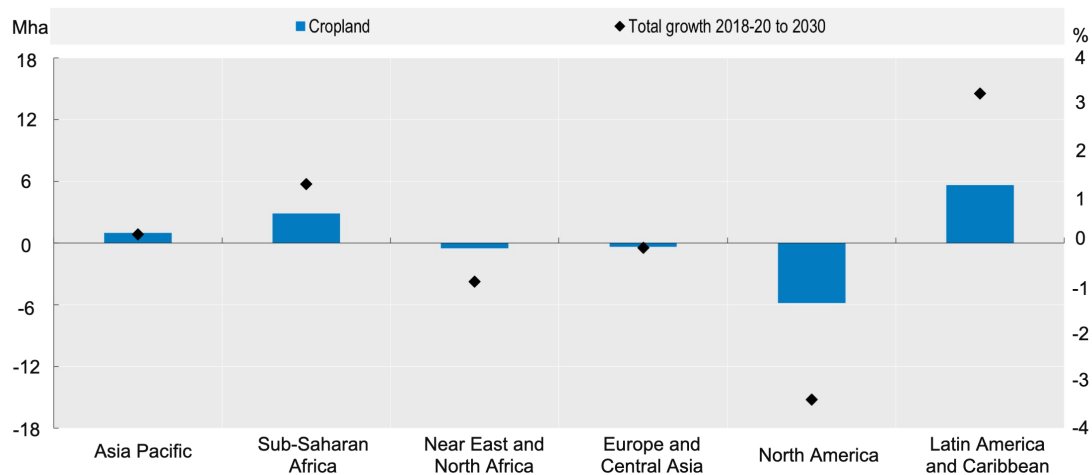


**Fig. 1.3** Change in cropland, 2018 to 2030 (from Organisation for Economic Co-operation and Development (OECD) and Food and Agriculture Organization (FAO), 2019)

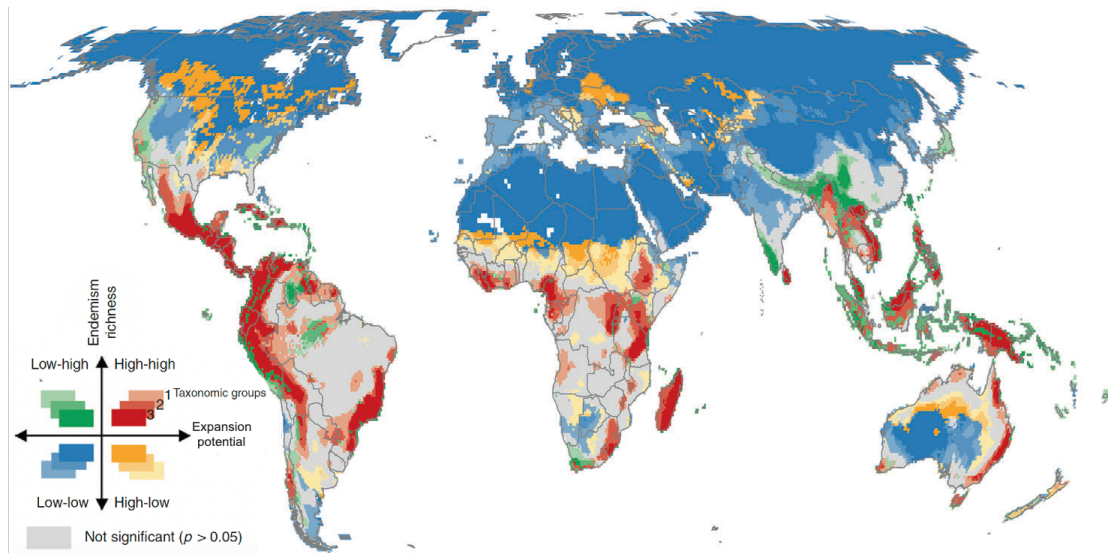


**Fig. 1.4** Association between endemism richness and potential for cropland expansion (adapted from Zabel et al., 2019). The blue clusters show areas with low potential for expansion, associated with low values of endemism richness. The three shades of colours indicate significant results for one, two or all three taxonomic groups (i.e. birds, mammals, amphibians).

Agricultural expansion is the primary driver of deforestation and forest fragmentation

(Food and Agriculture Organization (FAO) 2017; Franco-Solís and Montanía 2021; Knudsen et al. 2006). Between 2000 and 2010, large-scale agriculture accounted for 40% of tropical deforestation and small-scale subsistence farming for another 33%. These alarming rates of deforestation and forest degradation not only contribute significantly to the ongoing loss of biodiversity but also greenhouse gas (GHG) emissions, responsible for global warming (Food and Agriculture Organization (FAO) and UN Environment Programme (UNEP) 2020). Around 21-37% of total GHG emissions are attributable to the food system. They include emissions from agricultural practices and land use, transport, storage, packaging, processing, retail, consumption and land degradation (Mbow et al. 2019). Land degradation is also responsible for reduced rates of carbon uptake and a further expansion of cropland areas to compensate for the land taken out of production due to severe soil degradation (Alexandratos and Bruinsma 2012; Olsson et al. 2019). Likewise, degradation of natural resources threatens the sustainability of food systems and limits the world's capacity to meet the global population food needs, hampering the acceleration in agricultural productivity growth (Food and Agriculture Organization (FAO) 2017).

## 1.2 Challenges

Global trends pose a series of challenges to food production and agriculture to eradicate hunger and malnutrition, achieve food security for all, improve rural livelihoods, and make agriculture more resilient, productive and sustainable. Current high-input agricultural systems, which have caused massive deforestation, natural resources degradation and high levels of GHG emissions, cannot deliver a sustainable agricultural production (Food and Agriculture Organization (FAO) 2017).

Substantial improvements in resource-use efficiency and resource conservation must be achieved globally to meet the growing and changing food demand and stop and reverse environmental degradation (Food and Agriculture Organization (FAO) 2017; Wohlmeyer and Quendler 2002). It requires innovative systems that use fewer inputs, protect and improve the natural resource base, produce enough quality food and make it accessible and affordable for consumers around the world (Organisation for Economic Co-operation and Development (OECD) and Food and Agriculture Organization (FAO) 2019). Adopting environmentally sustainable cropping systems, particularly in those regions where most agricultural expansion is forecast to take place, will increase resistance to environmental

stress, enhance nutritional content, and ultimately safeguard the global food supplies.

### 1.3 Precision agriculture

Precision agriculture (PA), also known as "precision farming", is a management strategy that takes account of temporal and spatial variability within fields to improve the productivity and sustainability of agricultural production (Delgado et al. 2018; Groher et al. 2020; Hunt and Daughtry 2018; International Society of Precision Agriculture 2019; Mulla 2013; Zhang 2016). Precision farming involves data collection and analysis, information management, and technological developments in areas such as computer processing, field positioning, yield monitoring, remote sensing, and sensors design (Joint Research Centre of the European Commission 2014; Mulla 2013; Shafi et al. 2019). These technologies and procedures allow providing differentiated agronomic management for every specific site during the crop cycle (Cisternas et al. 2020; Salcedo and Carvajal 2021).

PA has been used for the last few decades to enhance crops' yield with reduced costs and human effort (Shafi et al. 2019). However, the adoption of PA technologies has been slow in developing countries due to different reasons that include culture in the producer community, skills, current information management processes, and particularly the high costs associated with the hardware development, deployment and maintenance (Cisternas et al. 2020; Delgado 2009; Shafi et al. 2019). Rapid changes in the socio-economic of the developing world, coupled with demands from specialised markets, call for the development of affordable PA approaches that are both scalable and transferable (Mondal and Basu 2009). Even in developing countries, there is an evident imbalance between less-modern regions and more developed ones. However, the latter are prone to accept more advanced technologies and can act as incubators for agricultural innovations based on their domestic conditions (Maohua 2001).

In recent years there has been a significant growth in agricultural innovation conceived in resource-constrained contexts (Molina-Maturano et al. 2020) for different purposes that include irrigation management (Food and Agriculture Organization (FAO) 2020), soil fertility (Benhamou et al. 2020), plant diseases (Carolan 2020), precision conservation (Delgado et al. 2019) and image acquisition for farm management (Oberthür et al. 2007). In particular, remote sensing, including satellite imagery and low-cost proximal sensors,



has proved to be cost-effective to develop PA decision support systems (Sishodia et al. 2020).

#### 1.4 Satellite Earth Observation for Precision Agriculture applications

Remote sensing appears as a fundamental tool to respond to many food production and agriculture challenges in developing countries, especially because the technical advances in this field are making PA more affordable and cost-effective (Weiss et al. 2020). RS offers a non-destructive way of providing frequent information systematically at different spatial scales, facilitating the characterisation of the spatiotemporal variability within a given area (Weiss et al. 2020). It makes Remote Sensing (RS) one of the principal means to provide spatial and temporal information on the crop status (Hunt and Daughtry 2018; Mulla 2013) for a wide range of PA applications that cover weed and diseases detection (López-Granados 2011; Mahlein 2016; Pérez et al. 2000), water and nutrients stress (Baret et al. 2007; Calera et al. 2017), yield optimisation (Haghverdi et al. 2018; Rembold et al. 2013) and soil characterisation (Ge et al. 2011; Mulla and Khosla 2015).

The application of Satellite EO in conventional agriculture started in the 1970s with the launch of Landsat 1 and soon led to the first applications in PA (Mulla 2013). Subsequent developments to increase the availability and spatial, spectral and temporal resolutions of satellite imaging systems, coupled with softer PA approaches, have made precision farming affordable, cost-effective and easier to transfer among productive systems (Weiss et al. 2020). For instance, systems like Sentinel-2 (S2) offer improved spatial and temporal resolutions appropriate for affordable crop growth monitoring at the farm level (Segarra et al. 2020; Weiss et al. 2020).

Softer approaches that rely on EO are supporting the development of affordable applications for Precision farming (Delgado 2009). This is the case of Site-specific Management Zones (SSMZ), defined as within-field homogeneous regions that evidence particular combinations of crop biophysical attributes (Gavioli et al. 2019; Koch et al. 2004; Méndez-Vázquez et al. 2019). SSMZ can enable precision agriculture for a larger number of producers than hard PA techniques because it makes possible to standardise the management for each management zone, varying agricultural practices and formulations only when transitioning from one subarea to another (Gavioli et al. 2016). Identifying such homogeneous management zones at distinct points during the growing season facil-

itates the implementation of site-specific practices and therefore, maximises agricultural productivity and profitability (Chlingaryan et al. 2018; Pérez et al. 2000; Shaw and Kelley 2005).

Field-based observations can be used to delineate SSMZ, however, it is unlikely to be a feasible operational monitoring approach due to the changing nature in space and time of agricultural features that makes it complex and labour-intensive to frequently map agronomic variables during the crop cycle (Leones Bazzi et al. 2019; Méndez-Vázquez et al. 2019). The recent advances in information technologies, remote and proximal sensing and geospatial analyses offer more tools that facilitate identifying and analysing the spatial and temporal variability within fields (Nawar et al. 2017). Particularly, the measurement of crop growth variability with remote and proximal sensing to delineate management zones has meant that a wide range of yield-limiting factors in the soil and crop properties can be measured rapidly at finer resolutions (Mulla 2013; Nawar et al. 2017; Yao et al. 2014).

Delineation of site-specific management zones using RS have applications that include identification of areas with equal productivity potential (Yao et al. 2014), variable rate fertilisation (Fleming et al. 2000; Khosla and Alley 1999; Koch et al. 2004; Tripathi et al. 2015), characterisation of the spatial variability of soil properties (Mzuku et al. 2005), soil classification (Chen et al. 2005; Fraisse et al. 2001; Frogbrook and Oliver 2007; Mzuku et al. 2005), and linkage of yield, soil and topographic parameters for crop-modeling evaluation (Fraisse et al. 2001). The definition of anomalous areas is closely related to the concept of Site-specific Management Zones (SSMZ), which are areas with homogeneous properties known to impact crop yield (Ohana-Levi et al. 2019; Zhang et al. 2010). The delimitation of SSMZ allows for defining anomalous areas within crop fields.

In particular, Satellite Earth Observation (EO) has the potential to support affordable delimitation of homogeneous areas, reducing the frequent detailed scouting required to detect anomalous zones. It can be achieved because agronomic features are highly variable over space and time and can be related to time series of remotely sensed data to support crop monitoring in large extensions (Eerens et al. 2014). However, satellite imagery has been mainly used for regional surveys due to its relatively coarse spatial resolution. In contrast, most anomaly detection approaches have relied mainly on aerial imagery and near-ground sensors at a cost-prohibitive to many farmers, particularly in resource-poor regions of the World (Pérez et al. 2000; Shaw and Kelley 2005).

Medium spatial resolution satellite imagery, such as Landsat (30 m), have been used primarily to map croplands and land cover change within agricultural areas rather than monitoring anomalies within crops (e.g. Defourny et al. 2019; Dutrieux et al. 2016; Gao et al. 2017; King et al. 2017). Studies that analyse temporal patterns of crop growth are usually performed with higher frequency imagery, such as MODIS and SPOT-VGT (e.g., Bolton and Friedl 2013; Eerens et al. 2014; Funk and Budde 2009; Lasaponara 2006; Rembold et al. 2019) at a sacrifice of spatial resolution (i.e., MODIS:250 m and daily frequency, SPOT-VGT: 1000 m and daily frequency).

The increased temporal and spatial resolution of Sentinel-2 imagery provides a promising and affordable direction for monitoring crop changes from an object-based perspective, considering the crop plot as the spatial unit of analysis. The object-based approach is fundamental in crop monitoring and for decision-makers, given the fact that management decisions are generally made at the level of agricultural parcels (Belgiu and Csillik 2018; Long et al. 2013). Despite this, there are limited studies that address the use of satellite imagery to detect in-field anomalous regions. Moreover, existing approaches rely, to some degree, on agronomic or weather data and therefore still require a certain level of capacity and resources to implement (e.g., Franke and Menz 2007).

## 1.5 Research Questions and Objectives

Despite increasing interest in the use of satellite remote sensing to support Precision Agriculture practices, there are still gaps in literature for relatively resource-poor regions where the availability of agronomic data is limited. These gaps consist of: (1) Lack of automated anomaly-detection techniques for precision agriculture systems that can be easily transferred to other production systems. (2) Lack of evidence as to how remote sensing-detected anomalies manifest themselves in subsequent crop yield.

The aim of this study is to address these shortcomings by developing an automated approach to detecting in-field anomalies using medium and high-resolution EO data. The following research objectives were considered. The analysis and results associated to the objectives 1, 2, 5, 6 and 7 were already published in Castillo-Villamor et al. (2021b).

**Objective 1:** Develop an automatic thresholding technique to delimit in-field anomalies using optical/radar EO imagery.

**Objective 2:** Identify the EO metrics that provide the best discrimination of in-field anomalies.

**Objective 3:** Identify the growth stage that provides the best discrimination of in-field anomalies.

**Objective 4:** Assess the extent to which the number of anomaly occurrences registered within a cycle manifests itself in subsequent crop yield reduction.

**Objective 5:** Assess the extent to which remote sensing-detected anomalies at different growth stages manifest themselves in subsequent crop yield reduction.

**Objective 6:** Assess the performance of a Machine Learning model to forecast underperforming plots using as predictors basic agronomic data, statistics of vegetation indices and the percentage of anomalies per plot.

**Objective 7:** Assess the extent to which the anomalies detected provide farm managers with sufficient opportunity to implement corrective agricultural practices.

## 1.6 Thesis structure

The overall aim of this thesis was to develop automated methodology to detect anomalous areas that affect crop yield using medium and high-resolution EO data. The purpose was to create a simple anomaly detection technique without manual calibration or, prior expertise in spectral analysis of crops that identify problematic in-field areas and crop plots when limited agronomic data is available.

The study is divided into 7 chapters, being Chapters 5 and 6 the sections that describe the analyses associated to the research objectives.

- *Chapter 2* provides a literature review on the use of commonplace optical and radar RS techniques for crop monitoring, particularly those focused on anomaly detection.

- *Chapter 3* provides a full description of the study site used in this work.
- *Chapter 4* describes the datasets and the preprocessing operations performed on them.
- *Chapter 5* presents the EOAD, a novel technique to identify anomalous areas within crop fields using optical and SAR imagery. The aim of the study was to assess the method's feasibility to detect in-field anomalies using vegetation indices retrieved from S2, PS, and S1.
- *Chapter 6* explores the ability of the EOAD to support the identification of low-performance areas across the crop cycle stages using optical satellite products. The analysis first evaluates the impact of the frequency of anomalies on grain yield. Secondly, it assesses the impact that the in-field anomalies detected at different moments along the crop cycle have on crop yield. Finally, the percentage of anomalous areas per plot at different growth stages is used to predict low-yield fields using vegetation indices derived from Sentinel-2.
- *Chapter 7* outlines conclusions regarding the potential of the EOAD system to detect in-field crop anomalies and the method capability to support the early detection underperforming plots.

## **CHAPTER 2**

### **Literature Review**

#### **2.1 Introduction**

The following literature review focuses on the use of satellite remotely sensed resources in agricultural field monitoring. Emphasis is placed on precision agriculture applications and in-field anomaly detection. However, the applicability of other remotely sensed techniques to detect anomalies and Machine learning approaches used by RS applications on agriculture are also considered.

The review is separated into four broad topics: 1) Section 2.2 presents the characteristics of rice production in Colombia, focusing on the agronomic features and management conditions in the demonstration area. 2) Sections 2.3 - 2.4 address the capabilities of optical and radar Remote Sensing for agricultural applications; 3) Section 2.5 outlines the use of machine learning techniques over remotely sensed data for Precision agriculture applications; 4) Section 2.6 discusses recent advances in space-borne, aerial and satellite sensors to monitor crop anomalies;

#### **2.2 Rice production**

Rice is one of the three major cereals cultivated and harvested around the world and one of the most important sources of food for humans (Yang et al. 2021). It is a major food staple in Asia, Latin America and the Caribbean (LAC), and the most rapidly

growing source of food in Africa (Kuenzer and Knauer 2013; Yang et al. 2021). Rice is particularly important in most tropical Latin American countries as it is the cheapest source of carbohydrates and protein for the poorest population (Global Rice Science Partnership 2013; Maclean et al. 2002). It provides a daily calorie intake that ranges from 8% in Central America to 47% in the Caribbean (Zorrilla et al. 2012).

### 2.2.1 Rice Cultivation in Colombia

In Colombia, rice represents 10% of the value of agricultural activity (Global Rice Science Partnership 2013). It is the crop with the third-largest area planted after coffee and corn, representing approximately 5% of the agricultural GDP and 0.4% of the National GDP. According to FEDEARROZ, rice production generates more than 500 thousand direct and indirect jobs in 23 departments and 210 municipalities, where the contribution of rice can exceed 80% of the territorial income (Becerra et al. 2020; Chica et al. 2016).

Despite the relative importance of rice in Colombia, the production does not cover the local demand, leading the country to import around 150,000 t per year. This is due to the higher production costs in Colombia in comparison to other countries and the relatively lower yields (Okada and Lopez-Galvis 2018). Some authors attribute these low yields to the country's equatorial location. Two hours less of light means less productivity compared to temperate countries such as Australia, Egypt, USA, Uruguay, Turkey or Spain, which register the highest yields (Becerra et al. 2020). The relatively low productivity of rice crops in Colombia is also associated with the country's large rainfed areas. Although rainfed crops produce lower yields, the low costs of production make them competitive compared with irrigated systems (Becerra et al. 2020; Ministerio de Agricultura y Desarrollo Rural 2019)

Rice crops are cultivated in large part of the warm areas and are distributed in five zones: Central, Low Cauca, Northern Coast, Eastern Plains and Santanderes (Departamento Administrativo Nacional de Estadísticas (DANE) and Federacion Nacional de Arroceros (FEDEARROZ) 2017). Given the Colombian territory's diverse agrological and geographic conditions, crop attributes such as productivity and growing season duration vary significantly among different regions. They have particular climatic and environmental conditions, which, added to the specific management practices of each area, are reflected

in the different productivity patterns along the Country. Fig. 2.1 shows the average rice yields and total production in the five rice-growing regions in Colombia . The study area is located in the Central region, which reports the highest yields.

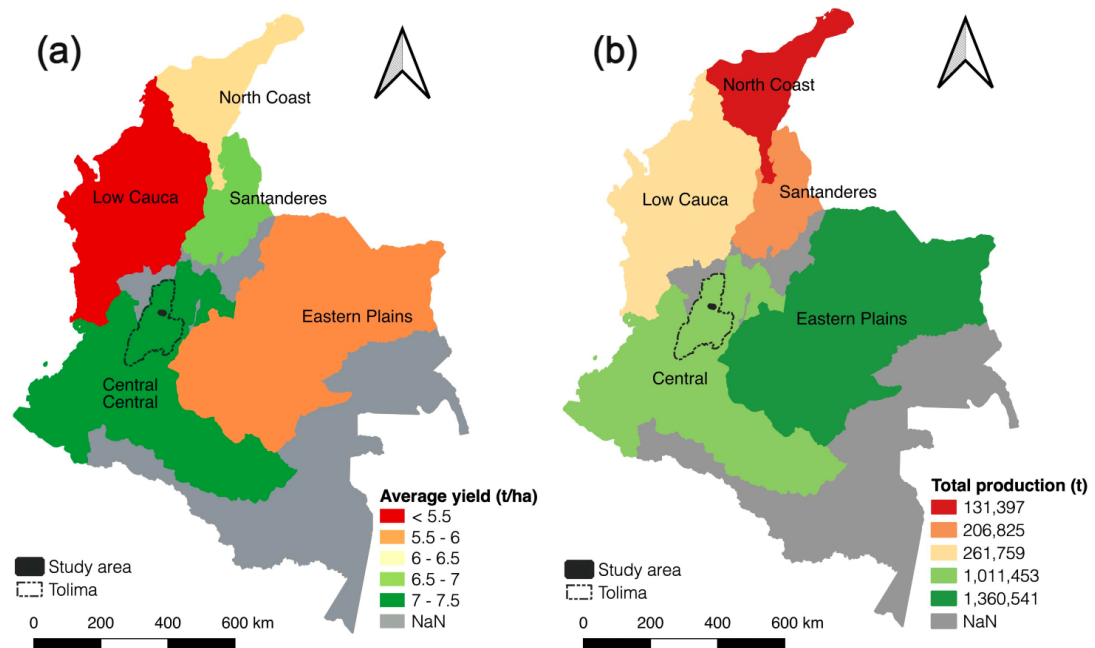


**Fig. 2.1** Average yield and total production per year (2016) in the five rice-growing regions in Colombia (Source: Departamento Administrativo Nacional de Estadísticas (DANE) and Federacion Nacional de Arroceros (FEDEARROZ) 2017)

Due to the equatorial climatic conditions, rice tends to be produced throughout the year, making it possible to have two cycles per year. For statistical analysis purposes and policymaking, rice production is summarised by semester. Semester 1 corresponds to those areas sown between January 1<sup>st</sup> and June 30<sup>th</sup>, and semester 2 refers to those areas sown between July 1<sup>st</sup> and December 31<sup>st</sup>.

Irrigation infrastructure is an essential driver of rice productivity. Currently, around 52% of the rice-growing areas in Colombia are irrigated (Becerra et al. 2020). Fig. 2.2 shows the extent of each region's rainfed and irrigated areas. The highest yields are registered in the Central region, where the most popular productive system is irrigated rice. Irrigated area in the Central region represented 60.3% of the total national production under this system in 2016-2 (Departamento Administrativo Nacional de Estadísticas (DANE) and Federacion Nacional de Arroceros (FEDEARROZ) 2017). In the North Coast and Santanderes regions also predominates the irrigated production, however, their productivity tends to be lower compared with the Central region. Rice production in the Eastern Plains is mostly rainfed mechanised. This is the region with the largest planted area under this system, representing 84% of the national rainfed production



(Becerra et al. 2020). The Low Cauca region encompasses 13.6% of the national area planted and aggregates 35% of the rice growers in the Country. Although the rainfed production is the most extensive in this region, there are also irrigated crops located within the boundaries of irrigation districts such as Mocari, La Doctrina and Maria La Baja (Departamento Administrativo Nacional de Estadísticas (DANE) and Federacion Nacional de Arroceros (FEDEARROZ) 2017).

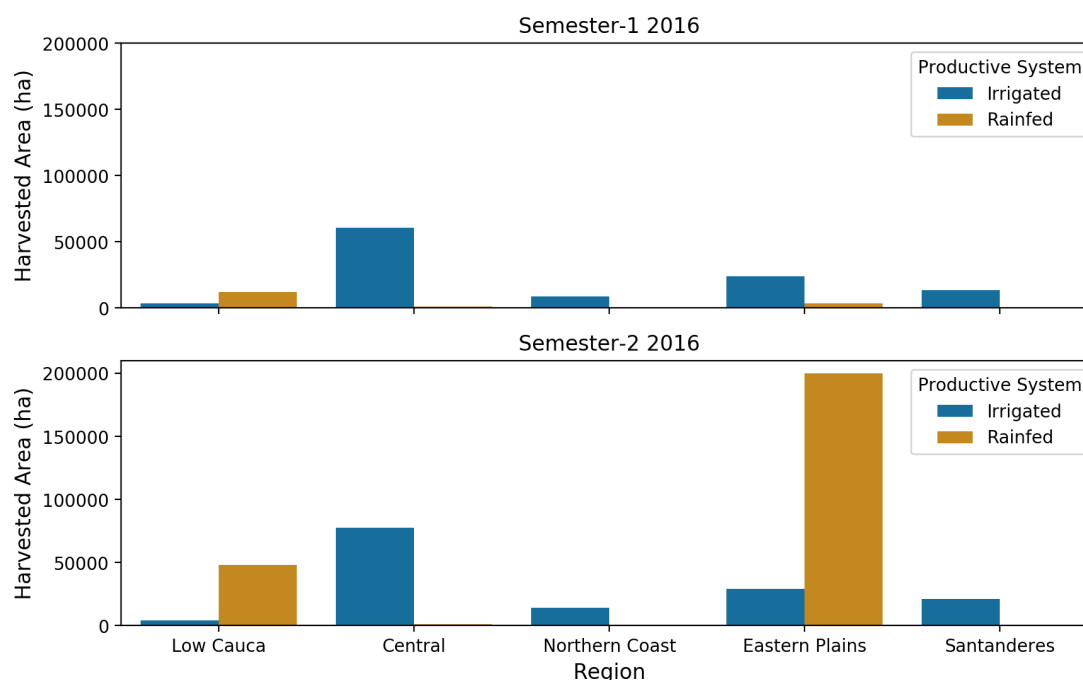


**Fig. 2.2** Total of irrigated and rainfed areas harvested during Semester 1 and Semester 2 2016 (Source: Departamento Administrativo Nacional de Estadísticas (DANE) and Federacion Nacional de Arroceros (FEDEARROZ) (2017))

Irrigated rice is the primary agricultural production system in the Tolima department, located in the Central region. With approximately 107500 ha of rice planted annually, Tolima is the second-largest rice producer in the Country and contributes 18% of the National production (Departamento Administrativo Nacional de Estadísticas (DANE) and Federacion Nacional de Arroceros (FEDEARROZ) 2017). The approximately 7235 production units in the department produce average yields of 7.17 t/ha, the highest compared to the Country average of 4.07 t/ha (Ministerio de Agricultura y Desarrollo Rural 2019). The superior performance of rice crops in this region is due to its favourable soil and climate conditions and the generalised availability of irrigation infrastructure (Departamento Administrativo Nacional de Estadísticas (DANE) and Federacion Nacional de Arroceros (FEDEARROZ) 2017).

### 2.2.2 Rice agronomic features

Rice (*Oryza sativa*) is an annual grass with round, hollow, jointed culms (stems), flat leaves, and a terminal panicle (Peace Corps 1982). The duration of the growing cycle depends on the variety of rice and the climate conditions (Kuenzer and Knauer 2013). In the region of Ibagué, the whole cycle duration ranges between 120 to 130 days. Due to the equatorial climatic conditions, rice tends to be produced throughout the year and, therefore, the crop calendar among neighbouring fields can be different.

The period of rice growth can be divided into three main agronomic phases: vegetative, reproductive and ripening (Kuenzer and Knauer 2013; Moldenhauer et al. 2013). The classification of the sub-phases within these three (3) main stages vary among farming systems. Growers in the Ibagué Plateau sub-divide the vegetative phase of rice into two sub-stages: i) germination, ii) seedling emergence and iii) tillering. Fig. 2.3 shows a diagram of the main phenological stages registered in the Ibagué Plateau as described by the Yamid Luna, the agricultural manager of the rice production. Fig. 2.3 also shows the corresponding stages in the Biologische Bundesanstalt, Bundessortenamt und Chemische Industrie (BBCH) scale for rice (Meier 2001). The BBCH scale is a uniform system to code phenologically-similar growth stages of mono- and dicotyledonous plant species (Meier et al. 2009).

Seed germination occurs when there is water available in the soil. It is followed by the seedling emergence (BBCH 09), which occurs when the coleoptile breaks through soil surface (Duquette and Kimball 2020; Yzarra Tito and Lopez Rios 2011). The crop age is counted from the field date of emergence, which is defined as the date when 80% of the plants have emerged. Rice tillering (BBCH 21) begins around 12-15 days after emergence (DAE) (Li et al. 2003). Soil water conditions during the period between sowing and emergence particularly affect crop establishment (Takeda et al. 2019) and therefore is important to guarantee proper and homogeneous water supply to the whole field.

The reproductive phase starts with the panicle initiation (BBCH 32) between the 45-55 DAE. Then, as a result of the increase in panicle size, the flag leaf sheath swells in a stage known as booting (Moldenhauer et al. 2013). The heading (BBCH 51) is a milestone that occurs when the panicle has at least partially exerted (headed) from the boot (Moldenhauer et al. 2013). From the RS perspective, the reflectance at near-infrared

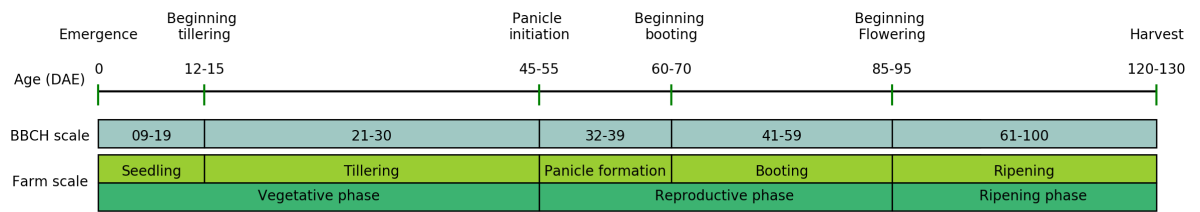


**Fig. 2.3** Rice growth stages as defined in the BBCH scale (Meier 2001) and the farm scale (Source: Luna Y. personal communication, August 15, 2019)

wavelengths is expected to reach a maximum at the heading when both the () and the vegetation coverage on the rice field are at their maximum (Maki and Homma 2014). In the Ibagu  plateau plain, the heading date typically occurs a couple of days before flowering. The reproductive phase (BBCH 32-59) is considered to be finished around 85 and 95 DAE, when the booting period ends.

The ripening phase starts with flowering (BBCH 61) and continues with the development of fruit (BBCH 71) and grain ripening (BBCH 83). During the maturation, the starch and sugars are translocated from the stems and leave sheaths, where they have been accumulated. During this stage, leaves continue to senescence (BBCH 92) and gradually turn yellowish due to a decrease of chlorophyll pigments (Wang et al. 2014). The cycle finishes when the rice is harvested, around 125-130 DAE (BBCH 99).

## 2.3 Optical Remote Sensing in agriculture monitoring

After the launch of the first Earth-observation satellite, Landsat in 1972, advances in optical remote sensing (ORS) have contributed to the development and improvement of cropland monitoring (Prudente et al. 2020). Spectral reflectance provided by multi-temporal optical remote sensed data have been used to monitor phenology, stage type and crop health over time to understand better natural and human-induced changes (Chen et al. 2008; Rodrigues et al. 2016).

The processes involved in photosynthesis determine how the leaves and canopy appear radiometrically in satellite imagery (Jensen 2014). The pigments are molecules in a typical green plant that have evolved to absorb very well wavelengths of light in the visible region of the spectrum (0.35 - 0.7  $\mu m$ ). Chlorophyll a and b are the most important plant pigments that absorb blue and red light required for photosynthesis. The

reflectance and transmittance of plants increase dramatically in the Near-Infrared (NIR) region of the spectrum. It occurs because plants have adapted to reflect this massive amount of near-infrared energy and avoid becoming too warm, which could denature the proteins irreversibly (Jensen et al. 2011). Fig. 2.4 presents an overview of the spectral reflectance characteristics of healthy green vegetation, the dominant factors that control leaf reflectance, and the leaves' transmittance properties in the wavelength interval from 0.35 - 2.6  $\mu\text{m}$ .

Optical sensors allow monitoring crop canopy reflectance in the visible, near-infrared (NIR) and short-wave infrared (SWIR) regions of the electromagnetic spectrum over time. The amount of solar energy absorbed, reflected and transmitted by vegetation

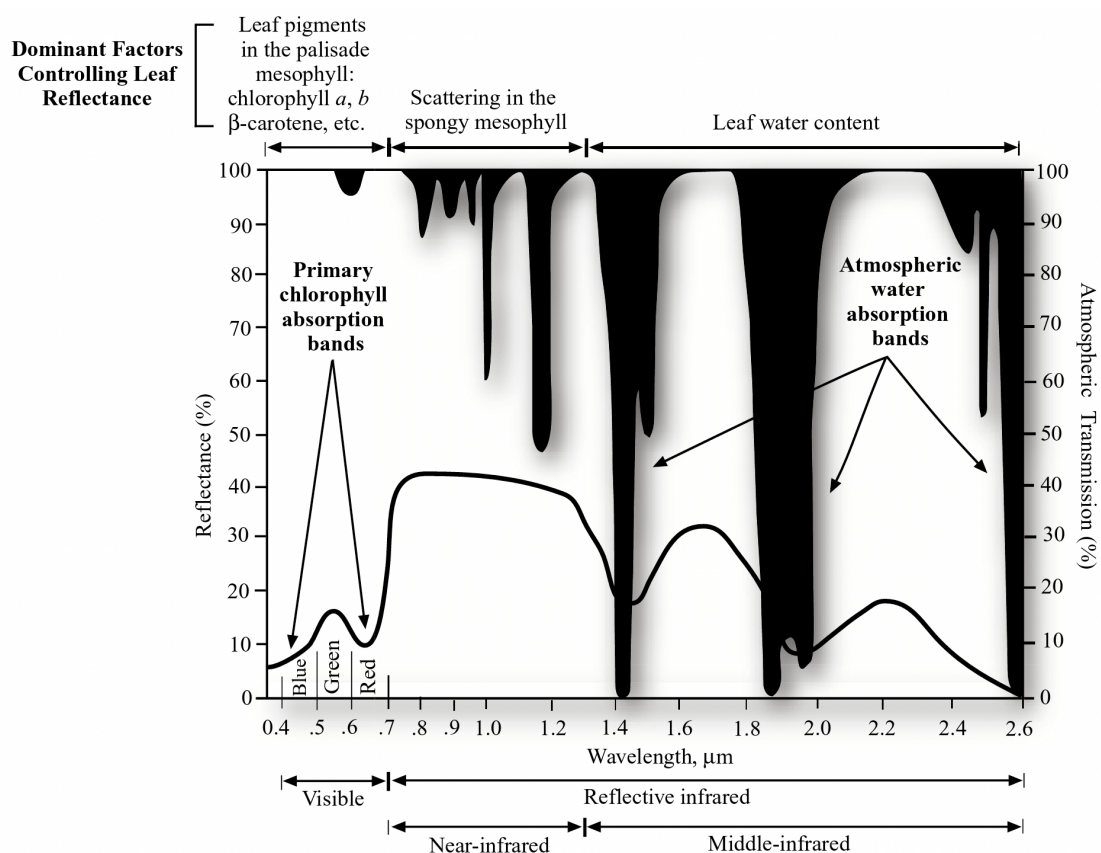


**Fig. 2.4** Spectral reflectance characteristics of healthy green vegetation in the region from 0.35 -2.6  $\mu\text{m}$  (from Jensen, 2014)

in these regions is mainly determined by plant pigmentation, internal leaf structure and moisture content, respectively (Davidson et al. 2014; Jensen 2007). The abrupt change in plants reflectance between the visible and NIR wavelengths, caused by the combined effects of strong chlorophyll absorption (visible) and internal leaf scattering (NIR), has been exploited to derive vegetation indices (VIs) that are indicators of plant traits (Jones and Vaughan 2010) such as crop type, nitrogen content, crop phenology or

crop productivity.

### 2.3.1 Optical satellite sensors

Different authors have used RS data acquired from optical sensors onboard satellites to study the multitemporal behaviour of vegetation and crops. Optical satellite products are commonly available as multispectral images consisting of several bands of data. The selection of adequate imagery and methods for a specific agricultural purpose results from contrasting the nature of the target phenomenon with the spectral, temporal and spatial resolutions of available sensors. Table 2.1 summarises the features of some of the optical satellite sensors most used in agricultural studies, and Fig. 2.5 shows the spectral range of bands for these sensors in the range between  $0.4\ \mu m$  to  $1.8\ \mu m$ .

**Table 2.1** Overview of some satellite optical sensors most used in crop monitoring

Platform	Launch date	Sensor	Temporal resolution (days)	Number of bands	Spectral range ( $\mu m$ )	Spatial resolution (m)	Studies on agriculture
NOAA satellite platforms	1978 (First) 2018 (Last)	AVHRR	1	6	0.58-12.5	1090	Gim et al. (2020) You et al. (2013)
Landsat-1	1972						
Landsat-2	1975	MSS	18	4	0.5-1.1	60	
Landsat-3	1978						Badhwar (1984)
Landsat-4	1982	MSS	16	4	0.5-1.1	60	Dong et al. (2015)
Landsat-4	1982	TM	16	7	0.5-12.5	30, 120 <sup>b</sup>	Gao et al. (2017)
Landsat-5	1984	MSS	16	4	0.5-1.1	60	Li et al. (2015)
Landsat-5	1984	TM	16	7	0.5-12.5	30, 120 <sup>b</sup>	Tatsumi et al. (2015)
Landsat-6 <sup>a</sup>	1993	ETM	16	8	0.5-12.5	30, 120 <sup>b</sup>	Vieira et al. (2012)
Landsat-7	1999	ETM+	16	8	0.5-12.5	30, 60, 15 <sup>c</sup>	Xu et al. (2020)
Landsat-8	2013	OLI	16	9	0.4-2.3	30, 15 <sup>c</sup>	
Landsat-8	2013	TIRS	16	2	10.6-12.5	100	

*Continue on next page*

(continued)

Platform	Launch date	Sensor	Temporal resolution (days)	Number of bands	Spectral range ( $\mu m$ )	Spatial resolution (m)	Studies on agriculture
TERRA AQUA	1999 2002	MODIS	1,8,16, monthly quarterly, yearly	36	0.5-14.4	250, 500, 1000	Funk and Budde (2009) Gómez et al. (2021) Mkhabela et al. (2011) Pan et al. (2012) Xiong et al. (2017)
SPOT-1	1986						
SPOT-2	1990	HRV	26	4	0.5-0.9	20, 10 <sup>c</sup>	Nguyen et al. (2012)
SPOT-3	1993						Chen et al. (2002)
SPOT-4	1998	HRVIR	26	5	0.5-1.8	20, 10 <sup>c</sup>	Khan et al. (2010)
SPOT-4	1998	VMI	1	4	0.5-1.8	1000	Liu et al. (2017)
SPOT-5	2002	VMI	1	4	0.5-1.8	1000	Meroni et al. (2014)
SPOT-5	2002	HRG	26	5	0.5-1.8	10, 20, 5 <sup>c</sup>	

Continue on next page

(continued)

Platform	Launch date	Sensor	Temporal resolution (days)	Number of bands	Spectral range ( $\mu m$ )	Spatial resolution (m)	Studies on agriculture
Sentinel-2 A	2015	MSI	5 <sup>c</sup>	110	0.4-2.2	10, 20, 60	Belgiu and Csillik (2018)
Sentinel-2 B	2017				0.4-2.3		Clevers and Gitelson (2013) Defourny et al. (2019) Guzinski and Nieto (2019) Lambert et al. (2018)
Suomi NPP	2011	VIIRS	1,8,16, monthly, yearly	22	0.4 - 12.0	375, 750	Becker-Reshef et al. (2010b)
NOAA-20 <sup>d</sup>	2017						Liu et al. (2018) Skakun et al. (2017)
RapidEye Constellation	2008	RapidEye	1	5	0.4-0.9	5	Dong et al. (2019) Kross et al. (2015) Shang et al. (2015)
PlanetScope constellation	2016 2018	DOVE-C DOVE-R	1	4	0.5-0.9	3	Breunig et al. (2020) Mudereri et al. (2019) Sagan et al. (2021)

<sup>a</sup> Launch failure.

<sup>b</sup> Thermal

<sup>c</sup> Panchromatic

<sup>d</sup> Prior to launch, NOAA-20 was known as the Joint Polar Satellite System, or JPSS-1, satellite.

<sup>e</sup> At the equator



Satellite agricultural monitoring began almost immediately after the launch of Landsat-1 in 1972 and is one of the longest-standing operational applications for the Landsat program. (Leslie et al. 2017). Since then, the 30 m spatial resolution Landsat imagery have been widely used for crop classification (Li et al. 2015), crop mapping (Graesser and Ramankutty 2017), disease detection (Chen et al. 2007), crop evapotranspiration estimation (Wang et al. 2021), crop modelling (Huang et al. 2019), yield prediction (Haghverdi et al. 2018), crop water content (Xu et al. 2020) and biomass estimation (Khan et al. 2019). The Systeme Pour l’Observation de la Terre (SPOT) missions have also provided long-term historical imagery for agricultural applications since 1986. SPOT high resolution imagery (i.e. HRV, HRVIR and HRG sensors) have been used for applications that include crop yield estimation (Aboelghar et al. 2012; Wiegand et al. 1991), crop modelling (Moulin et al. 1995), agricultural practices monitoring (El Hajj et al. 2009), soil salinity (Wiegand et al. 1996) and crop disease detection (Yuan et al. 2014). The spatial resolution from Landsat and SPOT have provided long-term data to perform local and regional agricultural analysis, however, due to their relatively low temporal resolution, compiling a temporally consistent cloud-free datasets over large areas is not always possible (Avitabile et al. 2012).

Due to the highly dynamic nature of crops in a year, the availability of more frequent imagery is one of the most critical requirements for agricultural system analysis throughout the growing season (Kuenzer and Knauer 2013). Sensors with higher frequency of observations and comparative lower spatial resolutions such as MODIS, SPOT-VGT, and AVHRR have been widely used for characterisation, mapping and monitoring of croplands at regional and global scales (Vrieling et al. 2008) using approaches that include temporal profiles of crop phenology, classification of multitemporal data and time-series analysis techniques (Jakubauskas et al. 2003). However, despite the high revisit frequency of MODIS, SPOT-VGT and AVHRR sensors, their coarse spatial resolution is inconvenient for phenology studies in areas with fragmented landscapes because mixed pixels may affect the image spectral characteristics (Sakamoto et al. 2005). Mixed pixels occur when the observed reflectance in a pixel reflects properties of multiple surface materials that constitute the pixel area (Arai 2008).

Satellite products derived from MODIS have been integrated into operational agricultural monitoring systems at regional, national and global scales (Becker-Reshef et al. 2010a; Skakun et al. 2017). Applications of MODIS in agriculture include crop phenological studies (Funk and Budde 2009; Pan et al. 2015), soil salinity detection (Zhang et al. 2015b), yield prediction (Mkhabela et al. 2011; Mokhtari et al. 2018), crop water

content monitoring (Xu et al. 2020), crop anomaly detection (Meroni et al. 2019), crop monitoring systems (Ji-Hua et al. 2006), and crop classification (Li et al. 2015). The Visible Infrared Imaging Radiometer Suite (VIIRS) was planned to provide continuity with MODIS (Skakun et al. 2017). Since its launch, VIIRS imagery has been used in various agricultural applications, including crop monitoring systems (Becker-Reshef et al. 2010a) and phenology monitoring (Liu et al. 2018).

Similarly to MODIS and AVHRR, SPOT-VGT <sup>1</sup> data have been widely used for investigating crop patterns and phenology at global and regional scales since its launch in 1998 (Liu et al. 2017). SPOT-VGT applications include seasonal crop phenological detection (Liu et al. 2017), crop mapping (Nguyen et al. 2012; Verbeiren et al. 2008), yield estimation (Kowalik et al. 2014), and drought monitoring (Meroni et al. 2014). SPOT-VGT and MODIS supply higher quality data, however, its relatively short service record compared to AVHRR has been a limiting factor to carry out long-term analyses (Yin et al. 2012).

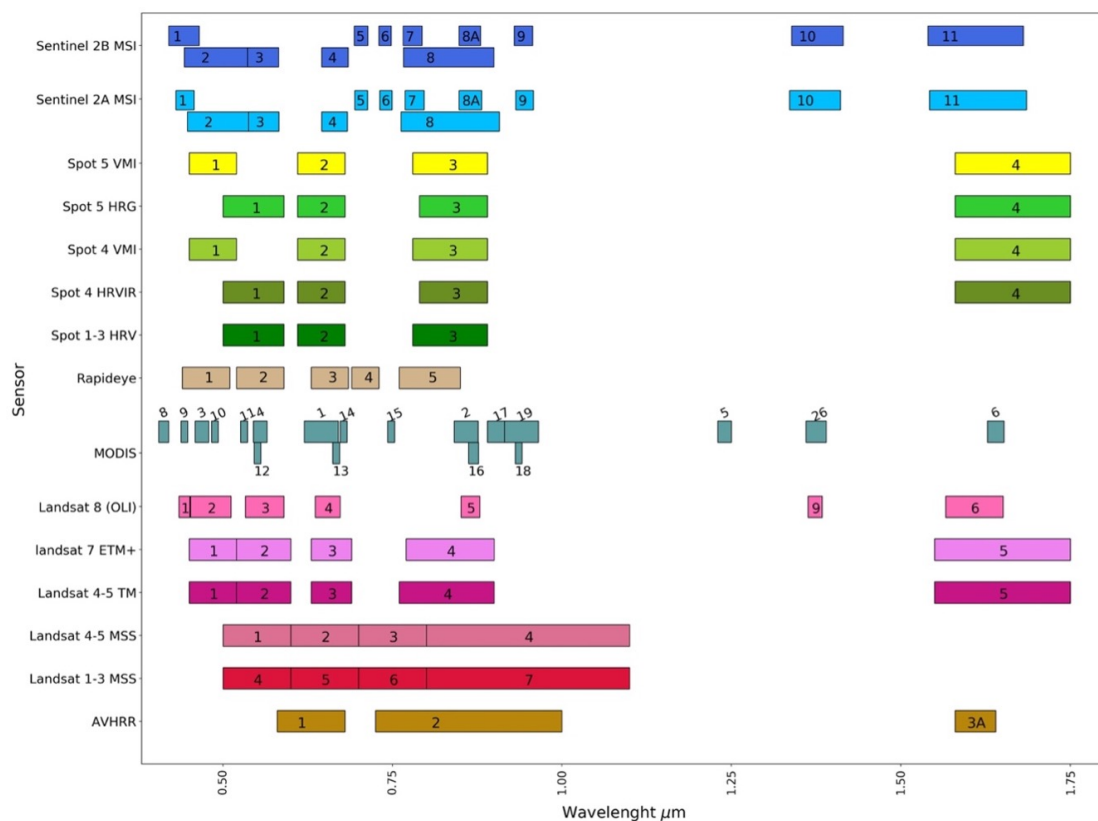


**Fig. 2.5** Spectral range of bands for different sensors (0.4 - 1.8  $\mu m$ )

The sensors mentioned above (i.e. Landsat, SPOT, MODIS, AVHRR and VIIRS) have their pros and cons for crop monitoring, which mainly arise from their spatial, temporal

<sup>1</sup> Also called Vegetation

and spectral resolutions (Sadeh et al. 2021). Technical efforts have been focused on the design of satellite imaging systems with higher spatial resolution and quicker revisit cycles (Mulla 2013). The emergence of constellations of CubeSats and availability of free Sentinel-2 (S2) images allow fulfilling both the spatial and temporal requirements for crop growth monitoring at the farm level (Aragon et al. 2018; Weiss et al. 2020).

Over the last decade, CubeSats have aimed to overcome the limitations of temporal and spatial resolution by establishing constellations with large numbers of satellites (Li et al. 2021). Initially envisioned as educational tools or demonstration platforms nowadays, the CubeSats offer opportunities for low-cost earth observation applications (Poghosyan and Golkar 2017). CubeSats are low-cost and miniaturised satellites, relatively inexpensive to build and launch to a low earth orbit, allowing acquisition of large image collections at high spatial and temporal resolutions, enhancing the ability to identify within-field variability in crop growing conditions (Houborg et al. 2015; Sadeh et al. 2021). An example of this new generation of satellites is the PlanetScope constellation (PS). Since its launch, different researchers have used PlanetScope imagery to monitor within-field variability in croplands. For example, Aragon et al. (2018) detected heterogeneous plant growth and captured the day-to-day variability in evapotranspiration to estimate crop water use. Also, Breunig et al. (2020) showed that the estimates of AGB using PlanetScope imagery for four different crops at the beginning of the flowering stage were a cost-effective method to delineate management zones.

Images obtained from CubeSat constellations, such as PlanetScope, have been used for other precision farming applications such as yield prediction (Sagan et al. 2021), phenology detection (Sadeh et al. 2019), and soil mapping (Silvero et al. 2021); however, their use is still limited. First, the costs of CubeSat imagery, such as Planet's PlanetScope, represent a limiting factor for a wide use on PA applications. Secondly, there are concerns about their quality for scientific investigations and monitoring applications (Dash and Ogutu 2016; Houborg and McCabe 2016; Li et al. 2021). The lack of limited operational onboard radiometric calibration makes it difficult to ensure radiometric consistency through time, both within and among sensors onboard many CubeSats. (Houborg and McCabe 2016; Houborg and McCabe 2018; Li et al. 2021; Sadeh et al. 2021). In addition, it is difficult to ensure the same atmospheric and illumination conditions in the images from different CubeSats in a constellation, affecting the spatial mosaics and temporal stacks of images for time series analysis in large areas (Li et al. 2021). Some authors, such as Moon et al. (2021) have assessed the quality of Planetscope imagery by comparing them with metrics derived from other satellite sensors. These inconsistencies

in the data calibration have motivated a few approaches to fuse CubeSat imagery with other types of imagery, such as Landsat (Houborg and McCabe 2018) and S2 (Li et al. 2019).

The recent availability of Sentinel-2 (S2), which provides higher temporal and spatial resolution data than previous open data satellite missions, has enabled improving the analysis of multi-temporal data for crop monitoring purposes, considering the in-field variability (e.g. Battude et al., 2016). Building on the Landsat and SPOT missions' legacy, freely available S2 imagery make precision farming affordable and cost-effective and, thus, almost operational (Defourny et al. 2019; Weiss et al. 2020). Belgiu and Csillik (2018), for example, highlighted how S2 data create new possibilities for generating accurate datasets on available crop types considering an object-based perspective, which is helpful for agricultural applications since crop management decisions are generally made at per-field basis (Belgiu and Csillik 2018).

The applications of Sentinel-2 (S2) range from crop monitoring at national scale, crop classification (Vuolo et al. 2018), crop water requirements estimation (Vanino et al. 2018) and crop yield estimation for smallholder agricultural systems (Karlson et al. 2020; Lambert et al. 2018). A very well-known application of S2 features at field monitoring is the Sen2-Agri system which generates cloud-free composites, dynamic cropland masks, crop type maps and vegetation indicators along the growing season (Segarra et al. 2020). Sen2-Agri has successfully differentiated crop types (80% of overall accuracy) even in regions with no clearly delineated fields (Defourny et al. 2019). In Europe, the experience gathered in Sen2-Agri is being used to develop the project Sen4-CAP, a system that aims to facilitate an integrated administration and control system of the Common Agriculture Policy (CAP; Bontemps et al. 2019).

In some regions with a high presence of clouds, the temporal resolution of Sentinel-2 is not good enough for continuous monitoring, and waiting for a S2 cloud-free image can result in a very late image to act in the field (Khan et al. 2018). To overcome these limitations, spatio-temporal integration methods with other imagery such as Landsat or higher spatial resolution data such as PlanetScope have been proposed. For example, the Sen2Agri System merges Sentinel-2 and Landsat-8 products to produce monthly cloud-free imagery for crop monitoring (Defourny et al. 2019), and Sadeh et al. (2021) proposed a linear interpolation to fill data gaps between the cloud-free images for PlanetScope and S2 images to create evenly spaced time series.

In summary, the availability of Sentinel-2 offers significant advantages for monitoring agriculture globally compared to the existing satellite sensors. Compared with traditional sensors, the combined higher temporal and spatial resolutions of Sentinel-2 facilitate monitoring the in-field variability of croplands. Despite the more detailed spatial resolution and shorter revisit times that CubeSats offer, their potential use for operational crop monitoring is limited in agricultural contexts such as smallholder farming systems in developing countries. This, because CubeSats do not provide free and open-access world coverage and, in some cases, only capture data at controlled moments when contracted (Segarra et al. 2020).

### 2.3.2 Optical Vegetation indices as indicators of crop condition

Vegetation indices (VIs) have been developed to relate reflectance from leaves or canopies with canopy characteristics (Hatfield and Prueger 2010). The purpose of VIs is to synthesise and enhance the information contained in multispectral imagery in a single parameter related to vegetation traits (Coppin et al. 2004; Palacios-Orueta et al. 2012; Hatfield and Prueger 2010; Semeraro et al. 2019). They are obtained as a simple algebraic combination of the spectral band values at two or more specific wavelengths (Semeraro et al. 2019). Table 2.2 presents the formulae of some of the most commonly used VI in agriculture applications.

VIs have been widely used for different agricultural applications (Ihuoma and Madramootoo 2019; Weiss et al. 2020), including estimation of crop yield (Johnson et al. 2016), Gross Primary Production (GPP), canopy radiation use efficiency (Garbalsky et al. 2011), crop coefficient (Glenn et al. 2011), crop nitrogen content (Clevers and Gitelson 2013; Delloye et al. 2018), and crop water stress (Bellvert et al. 2014).

The usefulness of a VI for a specific application, including crop anomaly detection, relies upon its correlation with the biophysical parameters of plants and low sensitivity to factors that restrict remote sensing data interpretation, such as soil background, relief, non-photosynthetic plant organs, atmosphere, viewing and illumination geometry (Wójtowicz et al. 2016).

The Normalised Difference Vegetation Index (NDVI), developed by Rouse et al. 1973, is the most widely used VI. It is especially useful because it reduces many forms of

multiplicative noise present in multiple bands such as illumination differences, cloud shadows or some topographic variations (Jensen 2007). The NDVI is recognised as a good indicator of changes in vegetation growth and activity as is representative of a wide number of variables sensitive to chlorophyll and photosynthetic vegetation (Jensen 2007; Lasaponara 2006; Tucker and Sellers 1986). It has been related with several biophysical variables such as , Fraction of Absorbed Photosynthetically Active Radiation (fAPAR), and primary production, among others (Campos and Di Bella 2012). In more recent studies, it has also been shown to be a good indicator of light interception by canopies as NDVI values saturate during the crop cycle (Hatfield et al. 2008; Serrano et al. 2000). However, this asymptotic behaviour over high biomass conditions is a drawback of NDVI to perform other types of analysis. In addition, the sensitivity to canopy background brightness, and the fact that the non-linearity of the index can be influenced by additive noise effects such as atmospheric path radiance, has led researchers to develop different indices (Huete et al. 2002). Indices such as the Soil-adjusted Vegetation Index (SAVI) and the Enhanced Vegetation Index (EVI) have been proposed to reduce the influence of soil and the low sensitivity in high biomass areas, respectively. The SAVI was proposed by Huete 1988 to minimise soil brightness influences from spectral vegetation indices involving red and near-infrared NIR wavelengths.

The SAVI is an important VI for crop monitoring because it is directly linked with ( ; McNairn and Shang 2016). It includes a parameter (L) which is a canopy background adjustment constant that accounts for differential red and near-infrared extinction through the canopy (Huete 1988).

The EVI is a modified NDVI with a soil adjustment factor (L), a Gain factor (G) set to 2.5, and two coefficients that describe the use of the blue band to correct the red band for aerosol scattering (Jensen 2007; Jones and Vaughan 2010). EVI has shown to be more sensitive than NDVI in high biomass areas (Sakamoto et al. 2005), as presented by Viña et al. (2011), who found that despite the asymptotic relationship with Green LAI, EVI showed more sensitivity than the NDVI at large Green values in maize and soybean crops. Despite EVI providing improved sensitivity in high biomass regions while minimising soil and atmosphere influences, it is largely affected by varying sun-sensor geometry characteristics, leading to potential artefacts in the data when used in time-series (Dutrieux et al. 2016). In addition, it is limited to sensor systems designed with a blue band, making it difficult to estimate it with instruments without a blue band, such as AVHRR and ASTER. In 2008, Jiang et al. proposed the 2-Band Enhanced Vegetation Index (EVI2), which has shown minimum differences in comparison with

EVI when atmospheric influences are insignificant, allowing to generate long-term EVI time series, especially at coarse resolution studies.

The Green Normalised Difference Vegetation Index (gNDVI) proposed by Gitelson et al. 1996 substitutes the green band for the red band in the NDVI equation. It has shown significant and consistent correlations to leaf chlorophyll and biomass yield in a variety of crop cultures (e.g. Shanahan et al. 2001; Taddeo et al. 2019)

Red-edge (RE) reflectance has shown to be sensitive to leaf chlorophyll content, which is directly correlated with photosynthesis and highly variable between different crops and different phenological states (Lin et al. 2019; Xie et al. 2018). It has led to the development of RE-based VIs such as the Red-edge Normalised Difference Vegetation Index ( $NDVI_{Red-edge}$ ; Gitelson and Merzlyak 1994) and the Red-edge Chlorophyll Index ( $CI_{Red-edge}$ ; Gitelson et al. 2003). These indices were found to be very effective in estimating (Delegido et al. 2013; Shang et al. 2015) and Gross Primary Production (GPP) for different crop systems (Lin et al. 2019) .

Vegetation and soil Water Content (VWC) is of vital significance in agriculture. The absorption features of liquid water in plant canopies at near-infrared and Short-Wave Infrared (SWIR) have led to derive vegetation indices such as the Normalised Difference Water Index (NDWI) and Normalised Different Water Index (NDII). Both, NDWI and NDII target on the strong water absorption features of the SWIR bands (Hunt et al. 2011; Xu et al. 2020), however, they use different SWIR wavelengths, being around  $1.2\ \mu\text{m}$  for NDWI and around  $1.6\ \mu\text{m}$  for NDII (Henrich et al. 2009).

**Table 2.2** Common vegetation indices used in agricultural applications

Vegetation Index	Formula	Studies on agriculture
Simple Ratio (SR)	$\frac{\rho_{red}}{\rho_{nir}}$	(Viña et al. 2011; Mokhtari et al. 2018)
Normalised Difference Vegetation Index (NDVI)	$\frac{\rho_{nir} - \rho_{red}}{\rho_{nir} + \rho_{red}}$	(Khan et al. 2010; Nguyen et al. 2012; Mokhtari et al. 2018; Pan et al. 2015; Gao et al. 2017; Lambert et al. 2018)
Soil-adjusted Vegetation Index (SAVI)	$\frac{(1 + L)(\rho_{nir} - \rho_{red})}{\rho_{nir} + \rho_{red} + L}$	(Campos et al. 2018; Mokhtari et al. 2018; Hatfield and Prueger 2010)
Enhanced Vegetation Index (EVI)	$G \frac{\rho_{nir} - \rho_{red}}{\rho_{nir} + C_1 \rho_{red} - C_2 \rho_{blue} + L}$	(Arvor et al. 2011; Viña et al. 2011)
2-Band Enhanced Vegetation Index (EVI2)	$2.5 \frac{\rho_{nir} - \rho_{red}}{\rho_{nir} + 2.4 \rho_{red} + 1}$	(Qiu et al. 2015; Graesser and Ramankutty 2017)
Green Chlorophyll Index ( $CI_{green}$ )	$\frac{\rho_{nir}}{\rho_{green}} - 1$	(Viña et al. 2011; Clevers and Gitelson 2013; Lambert et al. 2018)
Red-edge Chlorophyll Index ( $CI_{Red-edge}$ )	$\frac{\rho_{nir}}{\rho_{red-edge}} - 1$	(Viña et al. 2011; Clevers and Gitelson 2013; Lambert et al. 2018)



Vegetation Index	Formula	Studies on agriculture
Red-edge Normalised Difference Vegetation Index ( $NDVI_{Red-edge}$ )	$\frac{\rho_{nir} - \rho_{red-edge}}{\rho_{nir} + \rho_{red-edge}}$	(Lambert et al. 2018; Defourny et al. 2019)
Green NDVI (gNDVI)	$\frac{\rho_{nir} - \rho_{green}}{\rho_{nir} + \rho_{green}}$	(Haghverdi et al. 2018; Lambert et al. 2018)
Plant Senescence Reflectance Index	$\frac{\rho_{red} - \rho_{green}}{\rho_{nir}}$	(Defourny et al. 2019; Hatfield and Prueger 2010)
Normalised Different Water Index (NDII) / ( ) / Normalised Difference Moisture Index (NDMI) / Normalised Difference Water Index (NDWI) <sup>a</sup>	$\frac{\rho_{nir} - \rho_{swir}}{\rho_{nir} + \rho_{swir}}$	(Dong et al. 2015; Qiu et al. 2015; Dutrieux et al. 2016)

<sup>a</sup> Variations among indices depend on the NIR wavelength

## 2.4 Synthetic Aperture Radar (SAR) products as indicators of crop condition

Agricultural systems involve highly dynamic processes in space and time, therefore many monitoring applications require EO data with a relative high temporal resolution. Despite the contributions of satellite optical remote sensing for crop monitoring, acquiring useful scenes from satellite optical sensors is restricted to cloud-free areas. This is especially challenging during the rainy season in tropical regions (Mandal et al. 2020; Prudente et al. 2020). For example, the frequent cloud cover in many South American regions is consequence of several climate features and atmospheric currents that include the South Atlantic Convergence Zone (SACZ; Carvalho et al. 2004), the seasonal migration of intertropical convergence zone (Cook, 2009), and the South American low-level jet east of the Andes (SALLJ; Vera et al. 2006). The persistently cloudy nature of satellite optical imagery in Latin America is a main challenge to monitor croplands, as providing an 8-day revisit with more than 70% of cloud-free observation requires around a 2-day temporal resolution (Whitcraft et al. 2015).

The use of Synthetic Aperture Radar (SAR) sensors becomes a suitable alternative to meet the revisit frequency requirements of reasonably clear data during the agricultural growing season in persistently cloudy areas. The radar ability to monitor the earth surface under almost all weather conditions and the sensitivity of the microwave signal to the dielectric and geometrical properties of the surfaces makes SAR especially useful to monitor agricultural lands (McNairn and Shang 2016). SAR refers to a particular imaging radar system that uses the movement of the radar platform to simulate a larger antenna and generate high-resolution images (Zyl 2011).

SAR systems transmit microwave signals at an oblique angle and measure the backscattered portion of this signal (Flores et al. 2019). Fig. 2.6 shows the observation geometry of a SAR imager. The radar backscatter of targets in calibrated SAR images is expressed in terms of the backscatter coefficient, which is defined as the proportion of energy backscattered to the sensor compared to the return of an idealistic isotropic scatter per given reference area. The variable used to express the backscatter coefficient depends on the reference area chosen (Small 2011). These reference areas are illustrated in Fig. 2.7. If the reference area is in the slant range plane ( $A_\beta$ ), the backscatter coefficient is known as beta nought ( $\beta^\circ$ ). Slant range refers to the distance from the radar towards each target measured perpendicular to the line of flight (Woodhouse 2006). When the reference

area is defined to be tangent to an ellipsoidal model of the ground surface ( $A_\sigma$ ), the backscatter variable is known as sigma nought ( $\sigma^\circ$ ). Finally, if the reference area is defined to be perpendicular to the line of sight from sensor to an ellipsoidal model of the ground surface ( $A_\gamma$ ), the variable used to characterise backscatter is gamma nought ( $\gamma^\circ$ ).

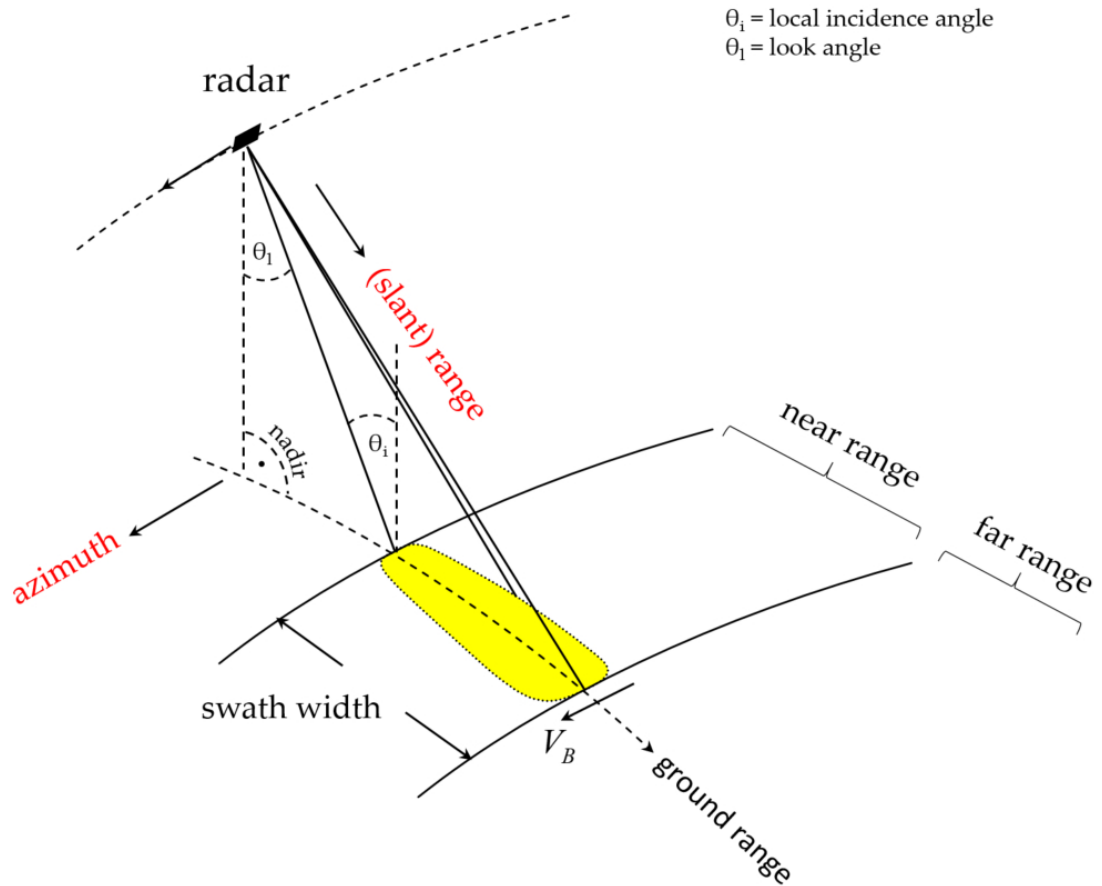


**Fig. 2.6** Observation geometry of a SAR imager (from Woodhouse, 2021).

As the backscatter intensity and scattering characteristics registered by the sensor depend on the interaction between the microwaves and the target surface, the capability of a SAR system to monitor crop condition is dependent on sensor-specific characteristics and ground parameters.

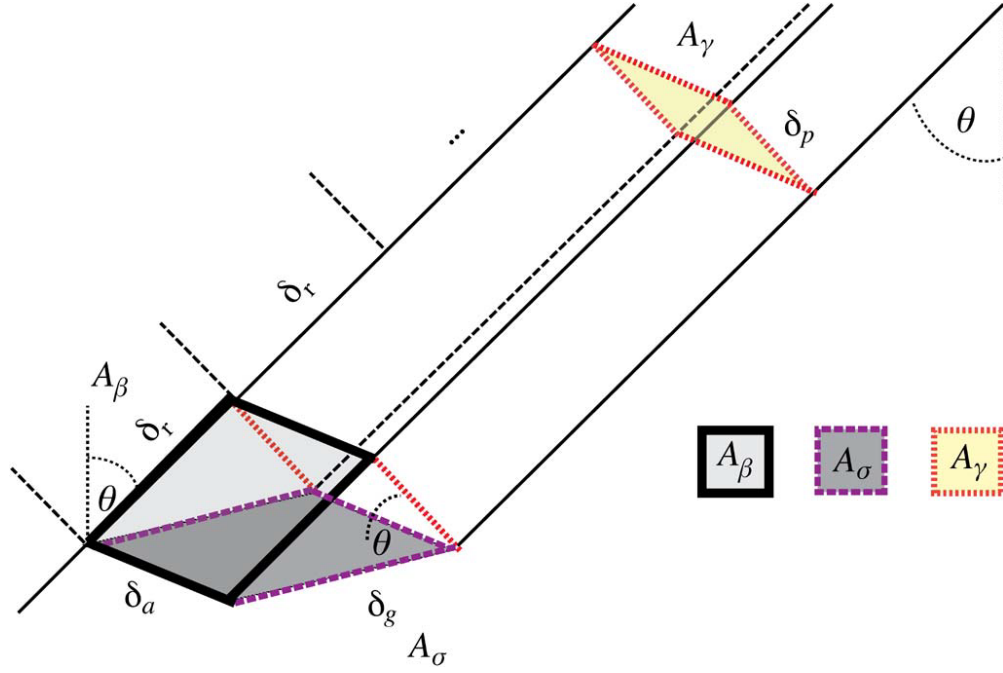


**Fig. 2.7** Normalisation areas for SAR backscatter (from Small, 2011).

#### 2.4.1 SAR Systems Configurations

The radar system configuration is defined by the radar operating wavelength, incidence angle and polarisation (McNairn and Shang 2016). SAR sensors transmit microwave signals at frequencies bands that range between 1 and 90 GHz. Table 2.3 shows the SAR microwave bands in which most of civilian spaceborne sensors operate. The wavelength of a SAR sensor is linked to the penetration capabilities of the signal (Flores et al. 2019). In general, shorter wavelengths (i.e. X-band) capture better upper canopy structures while larger wavelengths (i.e. L-Band and P-band) penetrate further and interact more with structures lower in the canopy (McNairn and Shang 2016). These interactions are also related with the architecture of the canopy. For example, McNairn et al. (2009b) suggested that the C-Band microwaves penetrate low biomass crops such as wheat without significant interference from soil, while L-Band waves penetrated further into larger biomass crops such as corn. Other studies have demonstrated that L-band backscattering exhibits a high sensitivity to biomass in crops with large leaves (e.g., corn and sunflowers). In contrast, higher frequency bands (i.e. C and X) described better the development of crops with narrower leaves such as wheat and rice (Liu et al. 2019; Marchesi et al. 2010).

**Table 2.3** SAR microwave bands in which most of civilian spaceborne sensors operate

Band designation	Wavelength (cm)	Frequency (GHz)
X	2.4 - 3.8	8 - 12
C	3.8 - 7.5	4 - 8
S	7.5 - 15	2 - 4
L	15 - 30	1 - 2
P	30 - 100	0.3 - 1

The local incidence angle is defined as the angle between the normal to the intercepting surface and the radar wave propagation vector (Flores et al. 2019). The look angle is defined as the angle between the vertical direction and the radar beam at the radar platform. Despite some authors use the terms look angle and incidence angle interchangeably, that is only correct for low-flying aircraft, when there is no topography present in the scene (Van Zyl and Kim 2010). The incidence angle is equal to the incidence angle at the surface when the surface curvature effects are neglected and the surface is flat (Van Zyl and Kim 2010). As the looking angle increases across the swath from the near to the far range, the signal intensity and the pixel size change, producing variations in brightness (Flores et al. 2019). These variations tend to be stronger in  $\beta^\circ$ , corrected but still present in  $\sigma^\circ$  and further reduced in  $\gamma^\circ$  (Small 2011).

Polarisation refers to the orientation of the electric field vector of the transmitted and received electromagnetic wave (McNairn and Shang 2016; Raney 1998). Most SAR sensors transmit and receive microwaves in the horizontal (H) and/or vertical (V) linear polarisations (McNairn and Shang 2016). The radar signal sent out by the antenna is polarised when it interacts with the surface. Part of the transmitted pulse of electromagnetic energy is backscattered towards the sensor and it is received vertically or horizontally polarised (Jensen 2007). HH and VV configurations produce like-polarised imagery and HV and VH produce cross-polarised imagery (Jensen 2007).

#### 2.4.2 Scattering from croplands

The backscatter response from croplands depends on the relationship between the SAR sensor configuration and ground parameters. Ground parameters are defined by the geometric and dielectric properties of the surface that interacts with the wavelength. The geometry determines the direction in which the energy is redirected by the target and the dielectric properties are mostly driven by variations in liquid water content (Woodhouse 2006).

Crop properties affect the scattering behaviour and intensity in different ways, however, these relationships are not straightforward. For example, the positive correlation between backscatter and the dielectric constant of a target has shown to be useful to monitor soil moisture. However, the sensitivity of SAR response to canopy structure makes it more complex to establish relationships between canopy water content and SAR backscatter, which varies depending on the crop type, growth stage and SAR configuration (McNairn and Shang 2016).

The echo returning from a target back to the sensor can be considered as a combination of three basic scattering mechanisms: single bounce or surface scattering, double bounce, and volume scattering (Maitra et al. 2013). Fig. 2.8 shows these scattering mechanisms. Surface scatterers are related to low-vegetation fields, bare soils, and water surfaces. Double-bounce scatterers include vertical structures that deflect an initial first forward reflection back to the sensor such as buildings, tree trunks or vertical stems. Volume scatterers are associated to vegetation canopies as the radar signal bounce multiple times as it propagates through the vegetation structure (McNairn and Shang 2016).

The complex interaction of the electromagnetic waves with water, soil and the rice plant in its various growing stages produces a backscatter signal consisting of multiple scattering mechanisms that contribute differently to each polarimetric channel (Clauss et al. 2018; Kuenzer and Knauer 2013; Le Toan et al. 1997). Table 2.4 shows the relative scattering power ( $|S|$ ) of the three main scattering mechanisms by polarisation. For example, the plant elements such as leaves stems, and fruits lead to multiple scattering events that depolarise the incident wave (McNairn et al. 2009a).

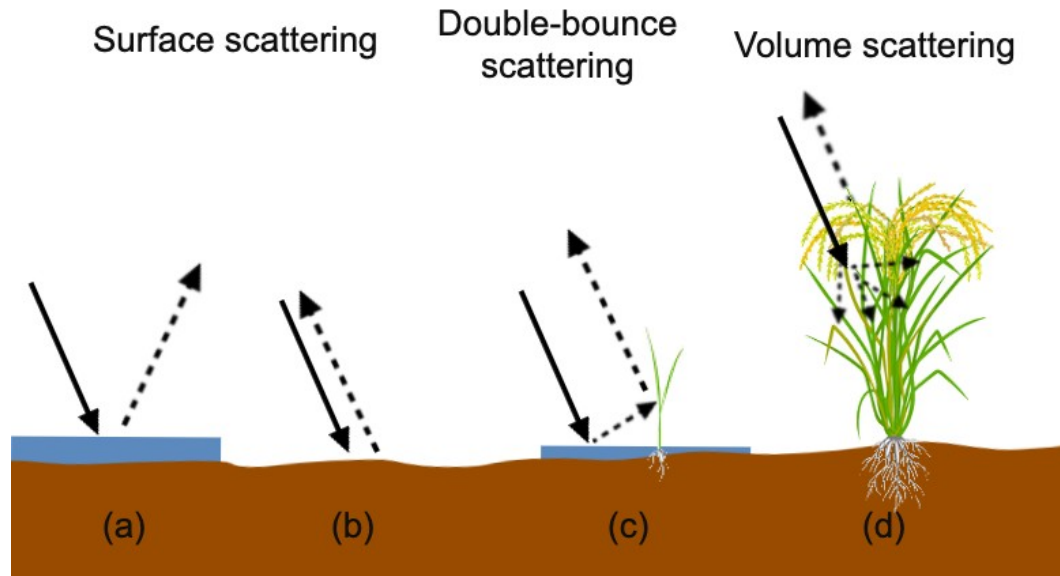


**Fig. 2.8** Scattering mechanisms in rice crops (a) Specular reflection; (b) Rough surface scattering; (c) Double-bounce; (d) Volume scattering.

**Table 2.4** Relative scattering strength by polarisation (adapted from Flores et al., 2019)

Scattering mechanism	Relative Scattering strength by polarisation
Rough Surface Scattering	$ S_{VV}  >  S_{HH}  >  S_{HV} $ or $ S_{VH} $
Double Bounce Scattering	$ S_{HH}  >  S_{VV}  >  S_{HV} $ or $ S_{VH} $
Volume Scattering	Main source of $ S_{HV} $ and $ S_{VH} $

At the early stages of rice plant development, surface or single bounce scattering is the dominant scattering mechanism (Mandal et al. 2020). First, when the ground is sowed but the field has not been irrigated yet, the soil acts as a rough surface scattering part of the energy back to the sensor. The low backscatter of areas where the rice fields are completely flooded and little crop biomass is exposed is consequence of the of the water layer, which acts a as a specular reflector and scatters the energy directly in the opposite direction to the sensor (Choudhury et al. 2007).

The predominantly vertical architecture of the rice plant during the early growth stages makes the VV backscatter tend to be higher than HH (Kim et al. 2008). In contrast, HH-polarised backscattering is higher than VV during most of the rice-growing season due to the attenuation of the wave by the vertical structure of the plants (Lam-Dao et al. 2007; Bouvet et al. 2009). As the plant grows and starts developing tillers, the VV and VH backscatter increase mostly due to the double bounce and volume scattering mechanisms (Chen and McNairn 2007; Choudhury and Chakraborty 2006). The contribution from the ground, mainly through the double-bounce scattering tends to be less important in non-flooded than flooded rice fields (Phan et al. 2021).

The majority of analyses that used band C have reported that the VV backscatter increases between the sowing and heading and then remains stable or experiences a slight decrease during maturation (Le Toan et al. 1997; Koay et al. 2007; Nguyen et al. 2016). This backscatter reduction is associated to the water content decrease inside the plants (Chen and McNairn 2007; Kuenzer and Knauer 2013) and the disappearance of standing water in flooding irrigating systems (Nguyen et al. 2016). However, there are discrepancies about the backscatter response after the heading. Phan et al. (2021), for example, observed a small increase for VV and VH after the heading till the harvest using Sentinel-1 imagery. These disagreements can be explained by differences in agricultural practices, such as plant density, irrigation system and differences across regions and epochs (Phan et al. 2021). For instance, the volume backscatter attenuation is stronger for higher plant density systems and the contribution of the ground scattering and the double bounce plant-ground scattering is reduced when the ground is not flooded (Kuenzer and Knauer 2013; Oliver and Quegan 2004).

#### 2.4.3 Applications of SAR on crop monitoring

SAR products have been used for different agricultural applications, such as crop classification (e.g. Inglada et al. 2016; Denize et al. 2019; McNairn et al. 2009a) or phenology characterisation (e.g. Canisius et al. 2018; Mandal et al. 2020; McNairn et al. 2018; Silva-perez et al. 2020). While optical energy reflected by the vegetation relies upon leaf structure, pigmentation and moisture content, the microwave energy scattered by vegetation is affected by surface features such as size, density, orientation and dielectric properties of the surface (Joshi et al. 2016).

The optimal frequency and SAR configuration to study crop properties vary among crops and throughout each crop's growth (Davidson et al. 2014; McNairn et al. 2009a). Multiple researchers have shown higher performance of the linear cross polarisation in comparison to like-polarised configurations in crop classification (McNairn and Shang 2016). For example, Silva-perez et al. (2020) found that the Sentinel-1 VH polarisation showed to be better to monitor phenology in asparagus when integrated with temperature and cycle starting dates.

The backscatter sensitivity to the structure of crop canopies and the underlying soil surface is especially strong for crops with vertical, elongated canopy elements, such as



those present in cereals (e.g, stems and leaves). In particular, the variations in backscatter across the growing season for rice are much larger than in any other crop. This condition has enabled the development of a wide number of studies that characterise the interaction of microwaves with rice plants. The backscatter measured in rice crops is shown to be sensitive to above-ground plant biomass at the C- and L-band wavelengths (Aschbacher et al. 1995; Inoue et al. 2002; Le Toan et al. 1997), which has been exploited to monitor rice growth and estimate yield. Clauss et al. (2018), for instance, estimated rice production in the Mekong using random forest regression models over Sentinel-1 (S1) time-series. Lopez-Sanchez et al. (2012) used simple decision tree algorithms applied to dual-polarised TerraSAR-X data to retrieve rice phenology. Later on, Lopez-Sanchez et al. (2014) analysed fully polarimetric mode RADARSAT-2 images to extract the main features of the C-band radar backscatter as a function of rice phenology. A key limitation of SAR open products is that the main SAR sensors do not meet the spatial and temporal resolution requirements of precision agriculture (Liu et al. 2019).

## 2.5 Machine learning approaches for retrieving agricultural variables using satellite RS

The operational use of satellite remote-sensed data has increased in a variety of agricultural applications (Defourny et al. 2019). In recent years, there has been a sharp increase of technological developments in the acquisition systems, computing facilities, data storage, and algorithms for data processing (Weiss et al. 2020). As these technological improvements are becoming affordable and available for many users, the exploitation of remote Sensing is also more reliable and profitable (Wolfert et al. 2017).

Regarding methods and algorithms, the complexity and big size of available RS data has increased the application and development of machine and deep learning algorithms. This is due to the capacity of Machine Learning (ML) algorithms to process a large number of data and handle non-linear tasks and characterise complex relationships between variables while they do not have to be explicitly formalised (Chlingaryan et al. 2018; Weiss et al. 2020). ML is defined as a set of methods that can automatically uncover patterns in data, and then use these patterns to predict future data (Heung et al. 2016; Murphy 2012). Deep learning, an important subfield of machine learning aims to learn feature levels of increasing abstraction with minimum human interference (Alpaydin and Bach 2014; Bengio Yoshua 2009).

ML techniques provide a powerful set of tools useful to analyse satellite remote sensed data for different applications in agriculture and enable making better decisions on management across space and time (Whelan and Taylor 2013). The retrieval of agricultural variables from remote sensing data is main application of ML. These variables can or cannot be directly related to the radiative transfer mechanisms involved in remotely sensed observations (Weiss et al. 2020). For example, Camacho et al. (2021) compared the performances of several machine learning techniques to retrieve Green Area Index (GAI) and the Fraction of Absorbed Photosynthetically Active Radiation (fAPAR), two variables that are involved in the process of radiative transfer. Other authors have used ML techniques to estimate variables such as evapotranspiration (Bai et al. 2021), in-field anomalies (Mouret et al. 2021), crop yield and nitrogen content (Chlingaryan et al. 2018), variables that result from the interaction between soil-plant-atmosphere and indirectly drive the radiative transfer mechanisms (Weiss et al. 2020). ML techniques have also been widely used for delineation of in-field homogeneous zones to improve agricultural management (Boydell and McBratney 2002; Gili et al. 2017; Haghverdi et al. 2015)

### 2.5.1 ML approaches for crop yield prediction

Crop yield is one of the most vital pieces of information for agricultural decision making in precision agriculture. Crop yield prediction is a essential piece of information for decision making in precision agriculture (Ali et al. 2015). However, it has been a challenging problem because it is affected by multiple factors such as climate, weather, soil, or management practices, and seed variety (Chlingaryan et al. 2018; Xu et al. 2019). ML can determine patterns and correlations between several features and discover knowledge from datasets to provide better yield prediction (Klompenburg et al. 2020).

In the past few years multiple ML techniques have been implemented to predict yield for different crops using RS (Mishra et al. 2016). Regression modelling is one of the most widely-used approaches to estimate crop yield in RS studies, particularly, Random Forests (RF), neural networks, (), and Gradient Boosted Trees (GBT; Klompenburg et al. 2020). Also, classification methods such as, RF, Support Vector Machine (SVM), Artificial Neural Network (ANN) and k-means have been used to predict crop yield classes, rather than yield values (Pantazi et al. 2016; Yoosefzadeh-Najafabadi et al. 2021).

### 2.5.1.1 Linear regression

Multiple Linear Regression (MLR) is not considered properly a ML technique, however, it is one of the most widely used models for crop yield prediction (Gonzalez-Sanchez et al. 2014). It states that the response is a linear function of the inputs (Montgomery et al. 2012; Murphy 2012). A multiple linear regression model with  $k$  regressors takes the form presented in Eq 2.1.

$$y = \beta_0 + \beta_1 X_1 + \beta_2 X_2 + \dots + \beta_k X_k + \epsilon \quad (2.1)$$

Where:

The parameters  $\beta_j$ ,  $j = 0, 1, \dots, k$  are the regression coefficients.

$\epsilon$  is the residual error between the linear predictions and the true response.

Despite its simplicity, interpretability and wide usage, the MLR applications for crop yield prediction have showed rather weak results (Drummond et al. 2003; Gonzalez-Sanchez et al. 2014). Bolton and Friedl (2013) used linear regression models to predict maize and soybean yield combining spectral indices with phenology metrics derived from MODIS. They found that NDWI and EVI2 were the most suitable indices for predicting maize yield in semi-arid ( $R^2=0.63$ ) and non-semi-arid counties ( $R^2=0.59$ ), respectively. Kern et al. (2018) built multiple linear regression models to predict the yield for four crops in Hungary using meteorological variables, soil water content and NDVI as monthly predictors, achieving cross validated  $R^2$  values that ranged from 0.6-0.8. The multiple linear regression models proposed by Fall et al. (2021) to predict millet yields in Senegal, reached a maximum  $R^2$  of 0.6 when using the NDVI values in August and dry and wet periods indices as predictors. In addition, since MLR only looks at linear relationships, the chaotic and dynamic data from agricultural systems do not match the strong assumptions of linear models, which are also very sensitive to collinearity (Ali et al. 2015; Dormann et al. 2013).

### 2.5.1.2 Tree-based algorithms

Decision tree algorithms are predictive models that aim to mimic human-like decision-making systems and can be used to represent both classifiers and regression models (Murphy 2012; Rokach and Maimon 2008; Yang 2010). This type of models are often

referred to as CART, however, most of the time, CART refers to the algorithm initially proposed by Breiman et al. (1984). After CART, new algorithms such as ID3, C4.5, C5.0 and random forests were developed (Tufféry and Tufféry 2011). Decision trees algorithms are popular for crop yield estimation due to their simplicity, intuitiveness and because they are capable of handling numerical and categorical data with large dimensionality (Ali et al. 2015; Yang 2010).

Decision trees partition the input data by creating splits on nominal or interval inputs and divide the data into smaller, more homogeneous groups (Berry and Browne 2006). It is composed of decision nodes and terminal leaves (See Fig. 2.9). The process starts at the root node, and from there, the decision tree splits to different branches and generates more nodes (Yang 2010). CART targets binary classification at each node, and the later algorithms can handle multi-category classification (Lin and Li 2021). Each decision

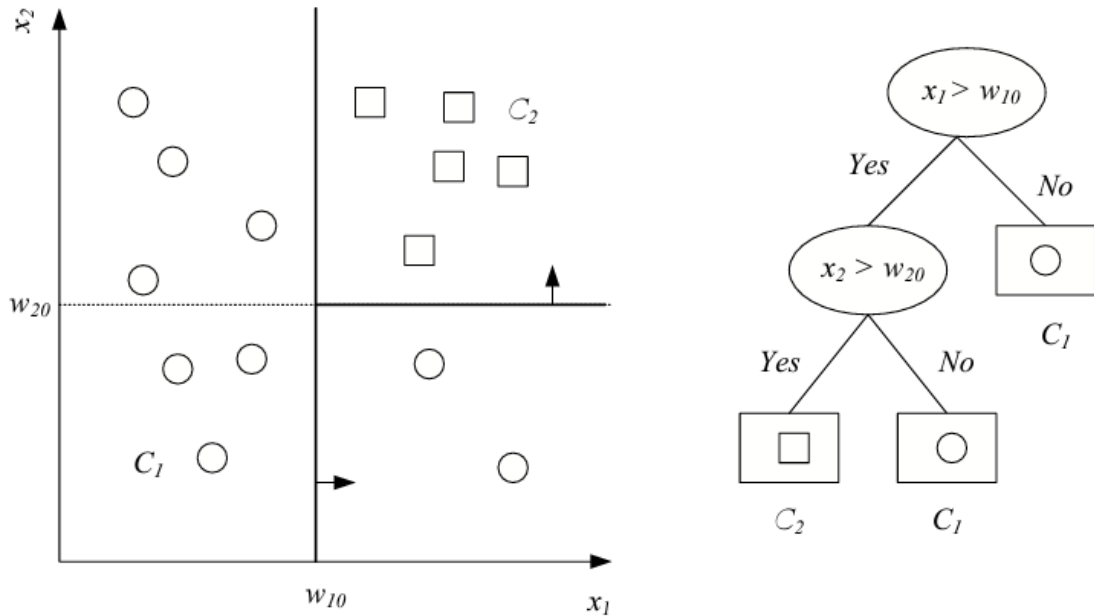


**Fig. 2.9** Example of a dataset and its associated decision tree (from Alpaydin and Bach, 2014). The oval nodes are the decision nodes and rectangles are leaf nodes

node implements a test function to select the optimal split or stop dividing (Larose 2004). If it stops, the node is called a leaf node and the value written in the leaf constitutes the output (Alpaydin and Bach 2014). The precise criterion to split each node depends on the type of tree (Tufféry and Tufféry 2011). The most common criteria include

- The Gini index (Breiman et al. 1984) is a measure of non-homogeneity, used for all types of independent variables (used in the CART)

- Information gain (Quinlan 1987) is an impurity-based criteria that uses the entropy measure. It is used when the target variable is categorical.
- Twoing criterion is used for any type of independent variable in the CART. It is preferred over the Gini index when the domain of the target attribute is relatively wide (Breiman et al. 1984). The Gini and Twoing criteria are equivalent when the target attribute is binary (Rokach and Maimon 2008).

A tree is pruned if it does not offer a better prediction performance compared to a tree with a simpler structure (Yang 2010). It prevents overfitting and avoids having very small nodes with no real statistical significance (Tufféry and Tufféry 2011).

The Random Forests (RF) algorithm proposed by Breiman (2001) is an extension to CART and can be used for classification and regression purpose (Jeong et al. 2016). A random forest ensemble (Breiman 2001) uses multiple, individual, unpruned decision trees that are created by randomising the split at each node. By combining these individual trees in an ensemble, overall, the accuracy is better than a single tree with exact splits (Rokach and Maimon 2008). Fig. 2.10 illustrates the general structure of a random forest.

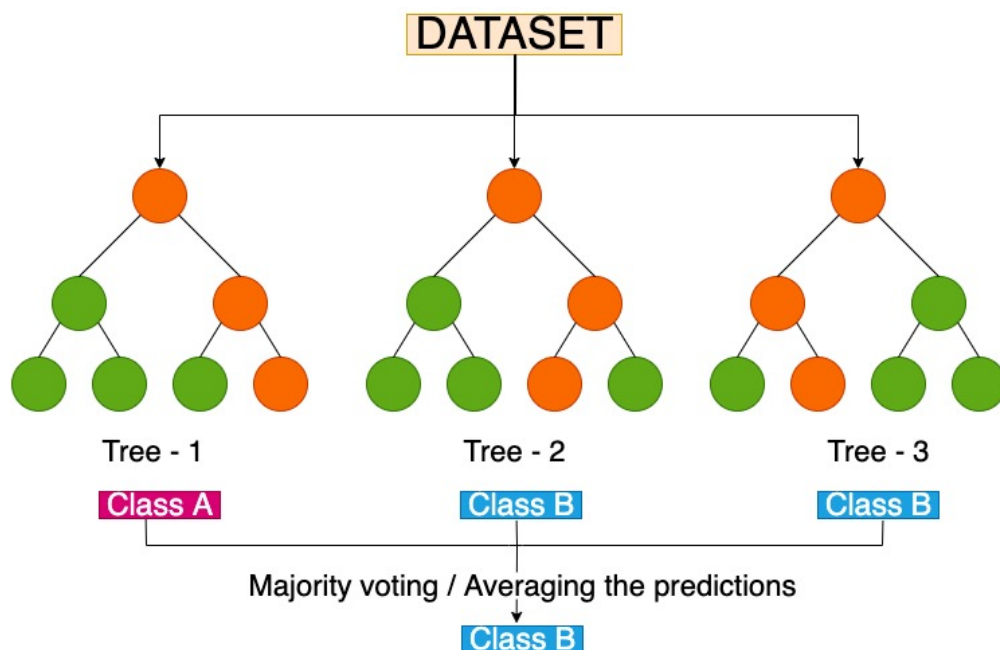


**Fig. 2.10** Random forest structure

Traditionally, RF has been used for classification, however, in recent years its use for regression has increased, as well as its applications for crop yield prediction. Previous

studies have highlighted the potential of random forest and low-resolution satellite imagery to predict crop yield. Heremans et al. (2015) used cumulated NDVI values, derived from SPOT-VGT, climatic variables and fertiliser input to estimate winter wheat yield at early crop stages achieving  $R^2 > 0.8$ . Zhu et al. (2021) reached  $R^2$  values above 0.7, and mean absolute relative errors below 0.14 when using NDVI AVH13C1 products<sup>2</sup> and meteorological data to develop a yield estimation model adopting RF.

The availability of Sentinel-2 data and very high-resolution satellite imagery have opened the door for mapping within-field variability. For example, Hunt et al. (2019) trained and validated Random Forest (RF) models using S2 imagery and data from yield monitors on-board combine harvesters for different periods throughout the growing season to estimate within-field wheat yield variability. They obtained maps of within-field yield variation with RMSE 0.66 t/ha and found further improvements in accuracy (RMSE = 0.61t/ha and  $R^2=0.91$ ) when environmental data was integrated.

Other authors have used RF to predict yield classes instead of following regression approaches. For example, Yoosefzadeh-Najafabadi et al. (2021) trained a RF model to identify the best soybean growth stage to predict the soybean yield using hyperspectral reflectance. Among all the models trained, RF produced the higher overall accuracy (84%) using as as predictors the 250 reflectance bands measured with a UniSpec-DC Spectral Analysis System.

RF has shown key advantages over traditional regression models for yield estimation, where the complex interactions between multiple predictors in crop systems (i.e. ecological, biophysical, ecological, physiological, and management) can complicate crop yield modelling. RF tolerates colinearity better than traditional regression models derived from linear regression because it uses the single best variable when it splits responses at each tree node and averages the predictions of the trees in the forest. It means that if multiple variables are correlated, only one of them can affect the RF regression model at a time (Jeong et al. 2016). In addition, authors such as Hunt et al. (2019) suggest that RF may increase the amount of data available for training as it intrinsically separates a random subset of data for testing from the calibration data and only the remaining set of data is used for model training. In contrast, RF may be less intuitive to interpret than MLR because it comprises an ensemble of a large number of decision trees that may not be fully described mechanistically (Jeong et al. 2016). In addition, similarly to other ML

---

<sup>2</sup>AVHRR and MODIS long-term dataset developed by the NASA-funded land long term data record (Pedelty et al. 2007)

algorithms, the predictions cannot be extrapolated beyond the training data range, where no training has been done, for example for the same crop type on a different growth cycle.

Gradient boosted decision trees (GBT; Friedman 2001) is an algorithm that uses boosting to combine individual decision trees. Fig. 2.11 presents an overview of the functioning of GBT. Boosting is a method for improving the performance of a weak learner, such as decision trees. It runs repeatedly a weak learner on various distributed training data. The classifiers produced by the weak learners are then connected sequentially into a single strong classifier to achieve a higher accuracy than the weak learners classifiers could reach (Rokach and Maimon 2008). In gradient boosted trees GBT, the weak learners are decision trees. Every time a new tree is added, it is fitted on a modified version of the initial dataset attempting to minimise the error of the previous tree. The residuals are detected using a loss function (e.g. MSE for regression and deviance for classification purposes; Pedregosa et al. 2011).

Similarly to RF, GBT has reported higher predictive capabilities for crop studies using Remote Sensing compared to traditional regression methods (Khanal et al. 2018; Zhang et al. 2019b). For example, Arumugam et al. (2021) achieved  $R^2$  values in average 220% higher than the linear models by training a Gradient Boosted Regression Model (GBR) to estimate rice yields for India using MODIS products. Such performance is because GBR adds, at each step, a new tree that best reduces the loss function (Elith et al. 2008). In addition, boosted trees can handle missing values and outliers by using surrogates (Breiman et al. 1984). However, boosted models, in general, are sensitive to the number of observations, requiring more training data than other linear and ML models (Shahhosseini et al. 2019). Unlike RF, GBT is prone to overfitting when adding too many trees because in later iterations it focuses on smaller subsets of the data (Rashmi and Gilad-Bachrach 2015). Often, regularisation techniques are used to reduce overfitting by ensuring the fitting procedure is constrained (Elith et al. 2008).

### 2.5.2 Measuring Models performance

There are standard metrics to assess how efficient a ML model is and choose the one that makes the best prediction for a specific application. For regression problems, for example, the most used metrics are Mean Squared Error (MSE), Root Mean Square

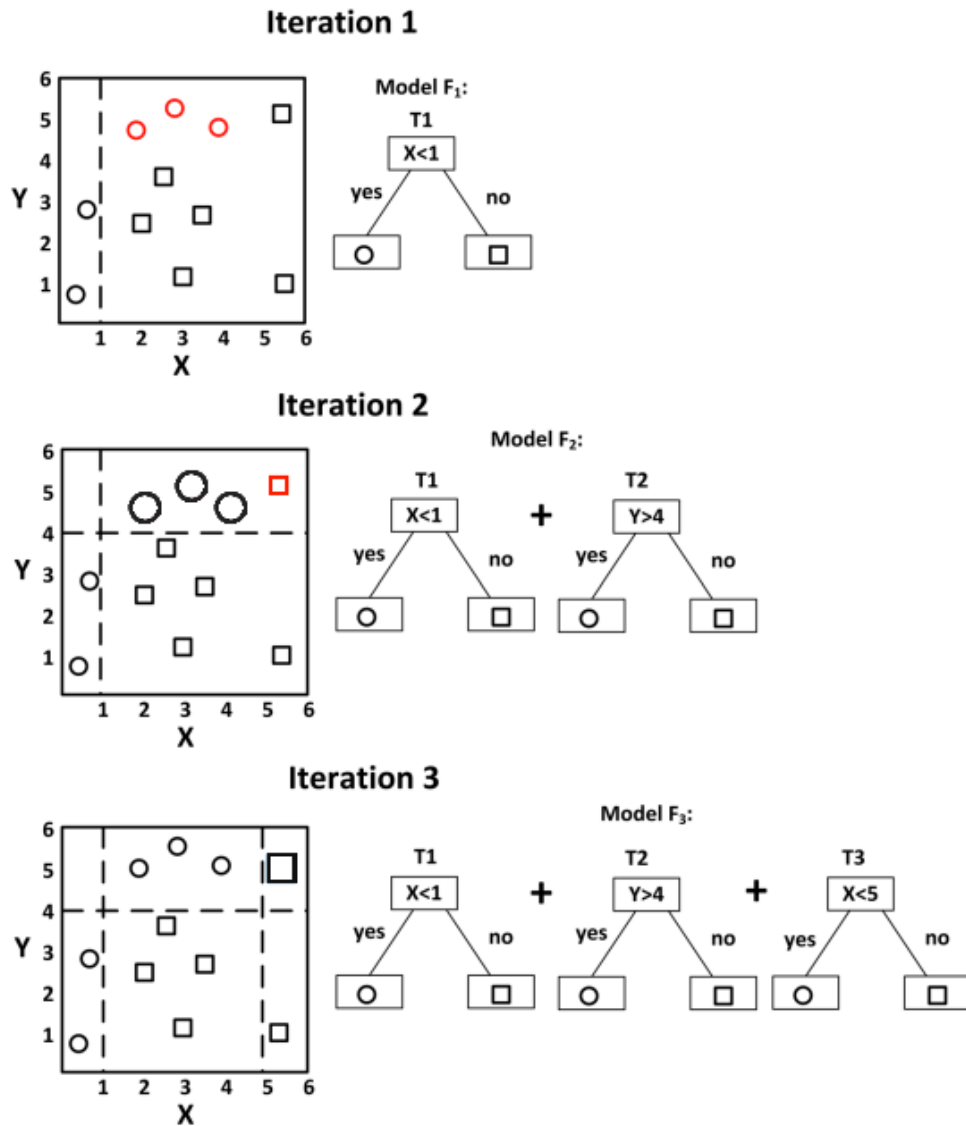


**Fig. 2.11** Example of the structure of Gradient Boosted Decision Trees (adapted from Zhang et al., 2018)

Error (RMSE) and Mean Absolute Error (MAE). For classification problems, frequently used metrics include accuracy, ROC curves and the F-measure (Rokach and Maimon 2008). Most of these metrics are derived from the confusion matrix.

The confusion matrix is a tool to assess how well a classifier can recognise elements of different classes. It presents the number of elements that have been correctly or incorrectly classified for each class. For each element in the test dataset, the actual class is compared with the class that was assigned by the trained classifier and results are summarised as presented in Table 2.5. True positives (TP) refer to the number of positive elements that were correctly labeled by the classifier. True negatives (TN) refer to the number of negative instances that were correctly labeled as negative. False positives



(FP) correspond to the number of negative elements that were incorrectly labeled as positive. False negatives (FN) are the number of positive elements that were mislabeled as negative (Han et al. 2011)

		Actual value	
		Positives	Negatives
Predicted value	Positives	TP	FP
	Negatives	FN	TN

**Table 2.5** Confusion matrix.

Classification accuracy is one single measure used to summarise the model performance (Sokolova et al. 2006; Tharwat 2021). It is defined as the ratio between the correctly classified points to the total number of points (See Eq. 2.2).

$$Accuracy = \frac{TP + TN}{TP + TN + FP + FN} \quad (2.2)$$

Accuracy has been criticised as it can be very misleading, especially with an imbalanced distribution of the class (Allouche et al. 2006; Gonzalez-Abril et al. 2014). In such cases, an Receiver Operating Characteristic (ROC) helps understand the trade-off in the true-positive rate (TPR) and false-positive rate (FPR) for different thresholds of the probability of class membership (Han et al. 2011). The TPR represents the rate at which the model can accurately recognise positive cases (See Eq. 2.3). The FPR corresponds to the rate at which the model wrongly identifies negative cases as positive (See Eq. 2.4). Fig. 2.12 illustrates different types of ROC curves. The ideal point on the ROC curve would be (0,100), that is, all positive examples are classified correctly and no negative examples are misclassified as positive. The Area Under the ROC curve (AUC-ROC) is used as a summary of the ROC curve. It is interpreted as the probability that the classifier ranks a randomly chosen positive instance above a randomly chosen negative one. The larger the AUC-ROC, the better the model at distinguishing between the positive and negative classes (Witten et al. 2011). This, as the classifier is able to detect more TP and TN than FN and FP.

$$TPR = \frac{TP}{TP + FN} \quad (2.3)$$

$$FPR = \frac{FP}{TN + FP} \quad (2.4)$$

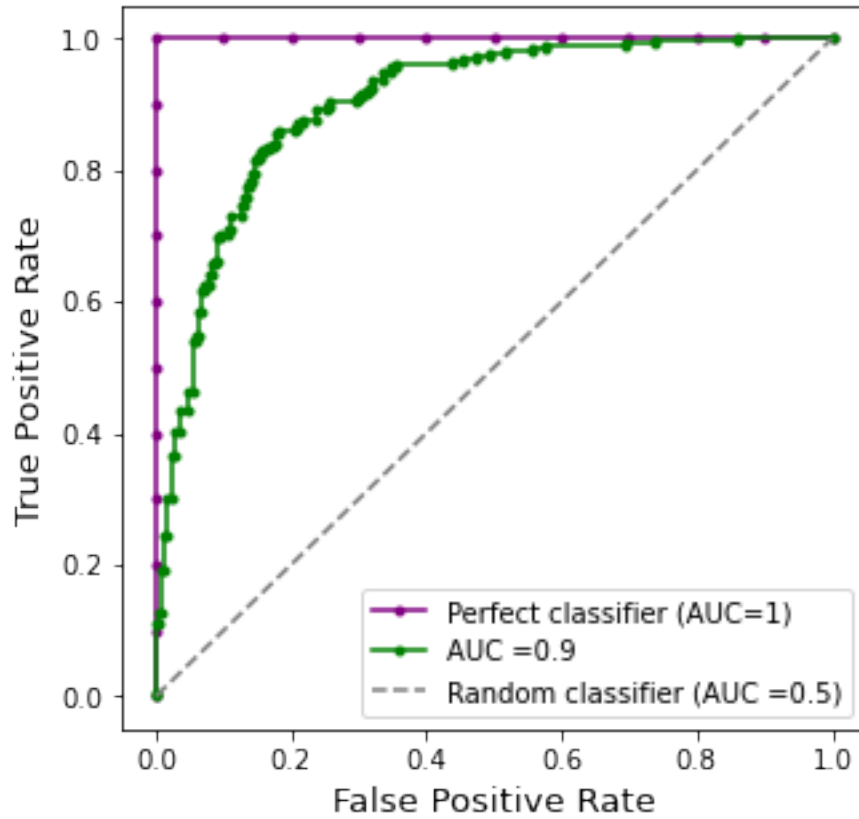


**Fig. 2.12** Examples of ROC curves.

The metrics used to test the performance of classification and regression models have shown useful to evaluate each model once, obtaining only a single sample point of evaluation with one test set. Cross-validation (CV) comprises a set of techniques to assess how well the results of a model will generalise given different batches of data from the same process (Rokach and Maimon 2008). CV is known for giving a more reliable perspective on how the model is expected to perform on out of sample data (Azzalini and Scarpa 2012), and for being particularly useful in situations where only a limited number of examples are available (Isaksson et al. 2008).

The main idea of CV is to randomly split a dataset  $X$  into a  $k$  number of training and validation set pairs. Since many datasets are never large enough to obtain between 10 and 30 parts, it has to be done with repeated use of the same data split differently and using smaller datasets (Alpaydin and Bach 2014). K-Fold Cross-Validation is a common type of CV that divides the training data into  $k$  parts or folds.  $k-1$  of these folds are used to train the model and the held-out fold is used for testing (Rokach and Maimon 2008).

The procedure is repeated several times, such that each fold serves as the test set (See Fig. 2.13). For each repetition, the performance metric is calculated on the test set and the average of the metric values obtained at each repetition and their standard deviation are then reported (Yang 2010).

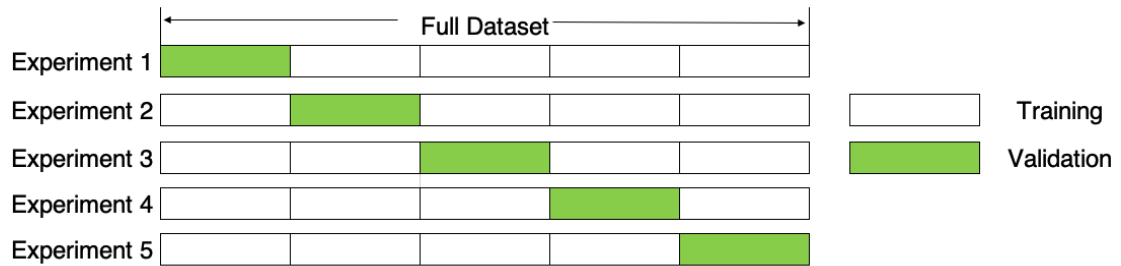


**Fig. 2.13** Example of 5-fold cross-Validation

Despite the significant developments and successful implementation of ML for different RS applications, these techniques have some limitations when implemented naively without deeper interpretation of the datasets. The accuracy of the predictions, as well as their uncertainties depend on the data quality, model scope and the correlation between predictors and target variables (Chlingaryan et al. 2018).

### 2.5.3 Multicollinearity

Multicollinearity relates to the existence of near-linear correlations among two or more predictors in regression and classification models (Chlingaryan et al. 2018; Freund et al. 2006). When the degree of correlation between variables is strong, it can impact the stability of classification and regression models as it affects the ability to estimate regression coefficients and classification criteria (Montgomery et al. 2012; Naes and Mevik 2001). This is particularly important when modelling variables in agricultural systems as many variables, such as climate, management, and soil, are often highly correlated with and within each other (Jeong et al. 2016).

Literature shows that multicollinearity can affect regression and classification differently. In regression models, the presence of severe multicollinearity reduces the power to identify independent variables because the regression coefficients are not unique and have influences from other features. It affects the model interpretability (Montgomery et al. 2012). Particularly, multicollinearity leads to unreliable estimates of the regression coefficients, which then have large variances and covariances, increasing the probability

that one or more regression coefficients have the wrong sign (Draper and Smith 1998; Naes and Mevik 2001). Multicollinearity may also seriously limit the usefulness of the regression model for prediction because highly correlated predictors can lead the model to overfit (Montgomery et al. 2012; Rosipal et al. 2001). It means the regression model fits the training data reasonably well but do a poor job on the test dataset.

As long as the correlation structure between variables does not change, the effects of collinearity are considered to have limited impact when the primary use of the model is to predict new cases within the range of the sampled data (i.e. to interpolate) (Harrell 2001). This, as the covariance structure is similar in both training and test datasets and does not influence the predictions and the goodness-of-fit (i.e., David Dalpiaz 2021; Freund et al. 2006; Kutner et al. 2005). Since a test dataset is usually a random subset of the entire dataset, it makes sense to assume that the covariance structure is also similar. However, extrapolation beyond the geographic or environmental extent of the data can lead to errors because the structure of collinearity might change (Dormann et al. 2013).

Methods such as Principal Component Regression (PCR; Jolliffe 1982), Partial Least Squares (PLS; Abdi 2003) or Constrained principal component analysis (CPCA; Vigneau et al. 2002) are designed to integrate collinear variables by constructing 'latent' variables: hidden variables that are inferred from the observed ones (Cichocki 2014). Other approaches, such as Ridge Regression (Hoerl and Kennard 1970), LASSO regression (Tibshirani 1996) and Octagonal shrinkage for clustering and regression (OSCAR; Bondell and Reich 2008) are not designed to be tolerant of collinearity, but are less sensitive (Dormann et al. 2013). This is also the case of Support Vector Machine (SVM; Boser et al. 1992), Multivariate Adaptive Regression Splines (MARS; Friedman 1991) and those methods built around Classification and Regression trees such as Boosted Regression Trees (BRT; Friedman et al. 2000) and Random Forest (Breiman 2001).

Collinearity impacts more negatively other methods such as Fisher Discriminant Analysis (Tufféry and Tufféry 2011) and clustering techniques. The presence of linear links between independent variables might affect clustering methods as the redundant parameters are weighted more heavily than others and might cause unnecessary fluctuation in the clustering results due to a few outliers (Ntoumanis 2002; Rafiei Sardooi et al. 2019).

### 2.5.3.1 Diagnose

Multicollinearity can be detected using different methods, with the most common being the correlation matrix and the variance inflation factor (Vu et al. 2015).

#### *Correlation matrix*

A correlation matrix (Cooley and Lohnes 1971) is a table showing correlation coefficients between each pair of variables. Most correlation matrixes use Pearson's correlation coefficient, also called Pearson's  $r$ . It is also common to use a non-parametric measure of correlation, such as Spearman's  $\rho$  or Kendall's Tau. (Dormann et al. 2013).

The Pearson's coefficient of correlation, also called Pearson's  $r$ , quantifies the strength and the direction of the linear relationship between two variables (Tufféry and Tufféry 2011). It is calculated as the covariance of the two variables divided by the product of their standard deviations. It ranges between -1 and 1, where the sign of  $r$  indicates the direction of the association. The closer  $r$  is to one in absolute value, the stronger the relationship (Hayes 2005). The formula for the Pearson's correlation coefficient is presented in Eq. 2.5.

$$\rho = \frac{cov(X, Y)}{\sigma_X \sigma_Y} \quad (2.5)$$

Where:

$cov$  is the covariance

$\sigma_X$  is the standard deviation of  $X$

$\sigma_Y$  is the standard deviation of  $Y$

The spearman's rank correlation coefficient can be used to measure the relationship between two variables which may be continuous, discrete or ordinal and it is good at detecting monotonic relationships, even if they are non-linear (Tufféry and Tufféry 2011). It computes the correlation between two variables using their ordinal positions in the distribution (Hayes 2005) and is calculated in the same way as Pearson's coefficient, but instead of the actual measurements, it replaces the values of the variables with their ranks (Eq.2.6):

$$\rho = \frac{cov(r_x, r_y)}{\sigma_{r_x} \sigma_{r_y}} \quad (2.6)$$

x Where:

$cov$  is the covariance of the rank variables

$\sigma_{r_x}$  and  $\sigma_{r_y}$  are the standard deviation of the rank variables.

The Kendall's Tau coefficient is also a rank order correlation coefficient, useful to determine if a monotonic relationship exists. If  $(x_1, y_1), \dots, (x_n, y_n)$  are a set of observations of the variables X and Y, then, any pair of observations  $(x_i, y_i)$  and  $(x_j, y_j)$  are said to be concordant if the ranks for both elements agree: i.e. if both  $(x_i > x_j \text{ and } y_i > y_j)$  or if both  $(x_i < x_j \text{ and } y_i < y_j)$ . If  $(x_i > x_j \text{ and } y_i < y_j)$  or if  $(x_i < x_j \text{ and } y_i > y_j)$ , they are said to be discordant. If  $x_i = x_j$  and/or  $y_i = y_j$ , the pair is neither concordant nor discordant (Puth et al. 2015). For a sample of size n there are no unique unordered pairs nor tied ranks, the Kendall's tau ( $\tau$ ) is given by Eq.2.8:

$$\tau = \frac{n_c - n_d}{n_0} \quad (2.7)$$

Where:

$n_c$  is the number of pairs that are concordant

$n_d$  is the number of discordant pairs

$$n_0 = 0.5n(n - 1)$$

### *Variance Inflation Factor*

If a method is sensitive to collinearity, it might not be sufficient to assess the collinearity of the variables in pairs. This, as there may be a linear relationship between three variables even when there is no linear relationship between any two of the three (Tufféry and Tufféry 2011). Better diagnostics are produced with an index called 'tolerance', and its reciprocal, called variance inflation factor (Midi et al. 2013). The tolerance is the proportion of the variance of a variable that is not explained by the other variables (Tufféry and Tufféry 2011). The Variance Inflation Factor (VIF) is defined as:

$$VIF = \frac{1}{1 - R^2} \quad (2.8)$$

Where:

$R^2$  is the coefficient of determination for the regression of that explanatory variable on all remaining variables

The higher the value of VIF, the higher the collinearity between the related variables. If there is no multicollinearity, the  $R^2$  equals to zero, and VIF equals to 1. There is

no formal cutoff tolerance/VIF values for determining presence of multicollinearity, however, as a rule of thumb, a tolerance below 0.1 ( $VIF = 10$ ) is a cause for concern (Midi et al. 2013; Tufféry and Tufféry 2011)

## 2.6 Remote Sensing for crop anomaly detection

Agricultural fields are highly variable over space and time. This variability is a consequence of the interactions between different factors such as the biological life cycle of crops, management practices, and fluctuations in climate and soil properties (Basso et al. 2001; Shaw and Kelley 2005). Anomalies occur when the characteristics of a region deviate in excess of the normal field variation (Carter et al. 2008). Understanding the variability of agronomic factors in the field is key to identifying agricultural anomalies at distinct points during the growing season (Chen et al. 2008) in order to implement corrective actions and maximise the production.

Carter et al. (2008) defines agricultural cropland anomalies as observed areas within fields that show abnormal characteristics. Following this definition, in this document, crop anomalies refer to observed areas within fields that show atypical characteristics compared to the behaviour of the majority of plants in a field. Such anomalies can be caused by the presence of different levels of plant stress or species within the same area, variable soil properties or management practices (Carter et al. 2008; McCann et al. 2017). Identifying crop anomalies at distinct points during the growing season facilitates their management with site-specific practices and thus, maximise agricultural productivity and profitability (Shaw and Kelley 2005). However, early detection of crop anomalies is difficult due to their sporadic nature and lack of clearly visible symptoms without close observation (Shaw and Kelley 2005), demanding frequent and detailed ground inspection.

The definition of anomalous areas is closely related to the concept of Site-specific Management Zones (SSMZ), which are areas with homogeneous properties known to impact crop yield (Ohana-Levi et al. 2019; Zhang et al. 2010). Implicitly, the delimitation of SSMZ allows for defining anomalous areas within crop fields. The delineation of management zones has been traditionally performed using cluster analysis techniques on agronomic variables that vary along the field, such as crop yield or soil chemical and physical properties (Gavioli et al. 2019). For example, Assis Silva et al. (2021)

presented satisfactory results in outlining management zones for cocoa plantations based on the crop productivity and the apparent soil electrical conductivity using the fuzzy k-means algorithm. Also, Moral et al. (2010) measured soil physical variables from soil samples to generate potential management zones using principal component analysis and the Fuzzy C-means algorithm. Most techniques used to delimit SSMZ require the collection of soil cores for further laboratory analysis or the use of handheld or machine-mounted sensors, such as electronic soil compaction meters, harvest monitors, conductivity meters, or chlorophyll meters to collect samples of agronomic variables (e.g., soil apparent electrical conductivity, nitrogen content, soil moisture/temperature). In addition, a large number of samples is required to determine management zones with statistical significance among samples, which reflects in considerable expenses in cost and time (Franzen et al. 2002).

Researchers have used remote sensing techniques to detect different types of spatial and seasonal anomalies reducing the need of frequent and detailed ground inspection. RS methods for in-field anomaly detection have been focused mostly on the use of aerial imagery, near-ground sensors and high-resolution satellite imagery (Pérez et al. 2000). For example, Shaw and Kelley (2005), detected soybean anomalies due to stress on plants using aerial multispectral imagery, with accuracies ranging from 83-90%. Pérez et al. (2000) determined the relative number of weeds in a field using near-ground images with accuracies that ranged between 75% and 80%. Franke and Menz (2007) found in-field heterogeneities of crop vigour with overall accuracies that ranged between 56.8% and 88.6% when using a decision tree and the NDVI over Quickbird images for winter wheat.

In spite that the identification of anomalous areas within crop fields has been successfully used to improve agricultural practices (Pérez et al. 2000; Shaw and Kelley 2005) current approaches have largely relied on the use of aerial imagery and near-ground sensors at a cost that is prohibitive to many farmers, particularly in resource-poor regions of the world. Additionally, these approaches rely on continuous sampling of crop properties throughout the growing cycle (Pérez et al. 2000; Shaw and Kelley 2005) because the biophysical characteristics of the crop, and associated anomalies, are highly variable over time. In addition, the pixel-based nature of these approaches is sensitive to noise (producing a salt and pepper effect) as well as being difficult to account for contextual information (Chen et al. 2012).

The use of kernel filters, or moving windows, enables pixels contextual information to be



considered (Tewkesbury et al. 2015). Under this approach, hard thresholds are applied to spectral data in a plot based on statistical metrics retrieved from the distribution of the data within a moving window. For example, McCann et al. (2017) mapped local anomalies based on the number of Median Absolute Deviations (MADS) for a given pixel area surrounding a centre pixel. The accuracy obtained varied highly depending on the window size, growth stage and number of MADS chosen (McCann et al. 2017). Although demonstrating promising results, there is no standard way in which thresholds are chosen, often being tailored to a particular crop location or the agricultural system.

Rather than using variable kernels to define anomalous pixels, Object-based image analysis (OBIA) offers an opportunity to use the agricultural plot as a fixed spatial unit of analysis. It eliminates the window size variable and is especially relevant for in-field anomaly detection, given the fact that agricultural management decisions are usually made at field basis (Belgiu and Csillik 2018; Long et al. 2013). However, OBIA is preferred only if the objects of interest (i.e. agricultural fields) are significantly larger than the pixels of the image (Blaschke 2010; Gilbertson and Niekerk 2017). In this regard, JRC et al. (2017) recommend that, in order to derive meaningful information from crop plots, the parcel should contain at least 20 to 30 pixels. This, therefore, excludes the use of broad spatial resolution sensors such as MODIS and SPOT-VGT, for in-field anomaly detection and restricts the use of Landsat when monitoring plots smaller than 4 ha, as there would not be a sufficient number of pixels to carry out the analysis. However, Sentinel-2 imagery, with a 10-20m spatial resolution and revisit time of 5 days, provides an opportunity to explore the use of freely available Earth Observation (EO) data for conducting OBIA-based crop monitoring in small to medium size crop plots ( $\geq 1$ ha).

An additional challenge concerns the thresholds chosen to determine whether areas are anomalous or not. Firstly, the spectral behaviour of an area, flagged as anomalous within one field, might not be considered atypical in other crop plots, where most of the plants share this "atypical behaviour". This is because each crop plot has its own particular characteristics (e.g. soil properties, plant species, phenological stage, weather conditions, or management practices) that need to be accounted for independently. An optimal threshold should be different for each crop plot and scene, as its distribution depends on biophysical variables that fluctuate over space and time. Detecting such dynamic thresholds using freely available EO offers the potential to develop transferable, scalable and low-cost Precision agriculture (PA) solutions to detect in-field crop anomalies and implement corrective actions that maximise the production along the crop cycle.

In contrast to spatial anomalies detection, satellite remote sensing has been more widely used for the detection of seasonal anomalies using optical imagery, especially at regional and global scales (Rembold et al. 2015). In general, optical RS methods for seasonal anomalies detection compare the actual crop status to what is assumed to be an average condition based on the seasonal patterns of Vegetation indices associated with the crops life cycles (Kanjir et al. 2018; Rembold et al. 2015). Traditionally, these methods have been applied over vegetation indices derived from broad resolution satellite images such as AVHRR, MODIS and MERIS imagery allowed highlighting the unusual behaviour of rice plots that occurred during a climatologically anomalous year (Boschetti et al. 2009). In Food Security and Nutrition Analysis Unit and FSNAU (2013), the computation of z-scores of NDVI showed to be an effective way of analysing the possible yield reductions by allowing rapid identification of positive or negative outliers as compared to the historical crop seasons in Somalia. Meroni et al. 2014 computed the anomalies of cumulative fraction of absorbed photosynthetically active radiation CfAPAR from SPOT-VGT data over the horn of Africa to detect drought and the cause of such drought considering associated phenology parameters and Lobell et al. 2013 detected yield declines in wheat using crop phenology derived from MODIS data in north-west India. More recently, the improved spatial and temporal resolutions of Sentinel-2 have been exploited for anomaly detection based on time series analysis. Kanjir et al. (2018) found that applying a time series analysis over NDVI derived from S2 imagery provided an efficient tool to detect anomalies of inconsistent land use in crop fields and meadows to support the European Common Agricultural Policy. However, this approach had limitations for analysing anomalies in areas under heterogeneous patterns of crop rotation (Kanjir et al. 2018). This is also a common practice in many agricultural systems in Colombia and Peru, as the climatic conditions favour the presence of different crops at different growth stages all year around (Perfetti et al. 2013).

Despite radar data being independent of clouds and solar illumination (Kuenzer and Knauer 2013; Yousif and Ban 2016; Silva-perez et al. 2020) and the backscatter of crops being very sensitive to the structure of the canopy and that of the underlying soil surface (Kuenzer and Knauer 2013), specific SAR applications on crop anomaly detection are almost non-existent, neither to detect spatial or seasonal anomalies. For example, (Oza et al. 2008), used the QuikSCAT Ku-band scatterometer (Wavelength  $\sim 1$  cm) to derive the temporal behaviour of  $\sigma^\circ$  and analysed the first-order derivatives to detect the maximum anomalies that were related to the puddling/transplanting of rice. However, this approach considered the use of coarse spatial resolution data of the order of 1-25 km. (Zhu et al. 2019) presented an unsupervised method to detect anomaly surface changes, to be used as a pre-procedure of soil moisture retrieval from time-series SAR images. The method

was evaluated on airborne L-band radar, RADARSAT-2 at C-band and COSMO SkyMed at X-band and accurately identified errors in multi-temporal soil moisture retrieval ( $>0.9$ ), caused by abrupt roughness and vegetation changes.

Optical and microwave satellite remote Sensing has demonstrated a high potential to describe the spatiotemporal variability of crop biophysical variables (Battude et al. 2016; Chen et al. 2008). It has enabled the development of satellite-derived products for different proposes such as crop mapping (Dheeravath et al. 2010; Nguyen et al. 2012), phenology extraction (Palacios-Orueta et al. 2012), growth monitoring (Gao et al. 2017), or climate change impacts on crops (Vrieling et al. 2008).

However, the potential of optical and radar satellite remote sensing to monitor crop variability over space and time, applications for crop anomaly detection remain limited. Current approaches are even fewer in tropical and equatorial countries, especially in tropical countries that are characterised for having heterogeneous crop rotation schemes and the presence of different crops at different growth stages all year around (Perfetti et al. 2013).

## **CHAPTER 3**

### **Study locations**

#### **3.1 Introduction**

This chapter introduces the study site used in this work. It provides the location of the study area and presents an overview of the biophysical, social and economic features of rice production in this region.

#### **3.2 Location**

The rice production system studied belongs to the Hacienda El Escobal farm. It is located within the Ibagué plateau plain in the department of Tolima, Colombia. Figure 3.1 shows the location of the study area. The latitude of the study site ranges from 4.3 °N to 4.4° N, and the longitude from 75.2° W to 75.0° W. The altitude varies between 704 and 934 meters above sea level MASL (See Figure 3.2). The climate is semi-humid, with an average temperature of 23.2° C and an annual average precipitation of 1690 mm (Instituto de Hidrología Meteorología y Estudios Ambientales de Colombia 2020). The area has a bi-modal rainfall pattern with two wet seasons, the first one typically between late March and early June; and the second one between late September and early December.

From the geomorphological point of view, the Ibagué Plateau is defined as a piedmont plain constituted by an alluvial cone originated by the Coello River (Bonilla Alvis et al.

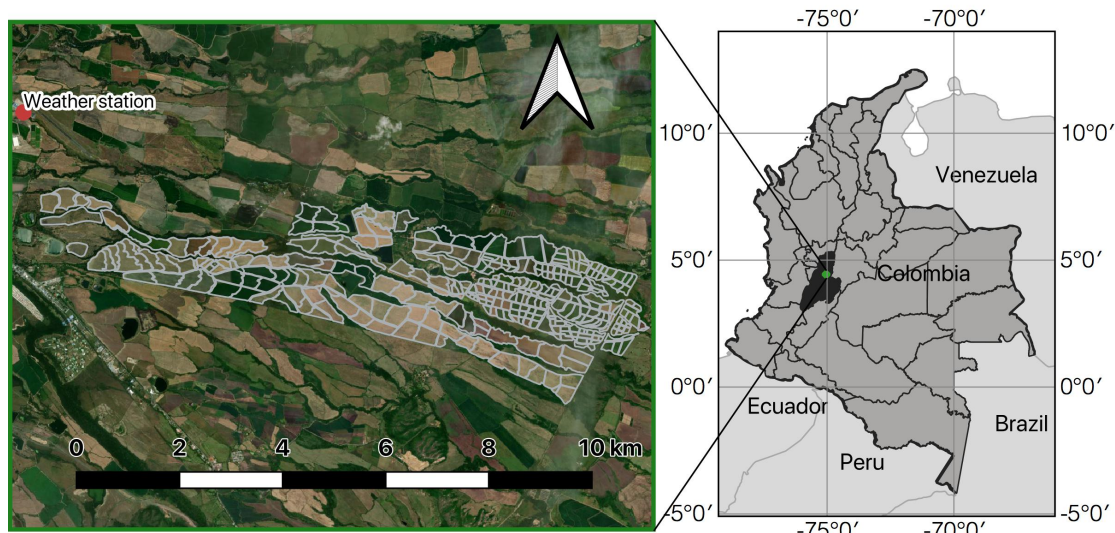


**Fig. 3.1** Map showing the Ibagué plateau study site, Colombia

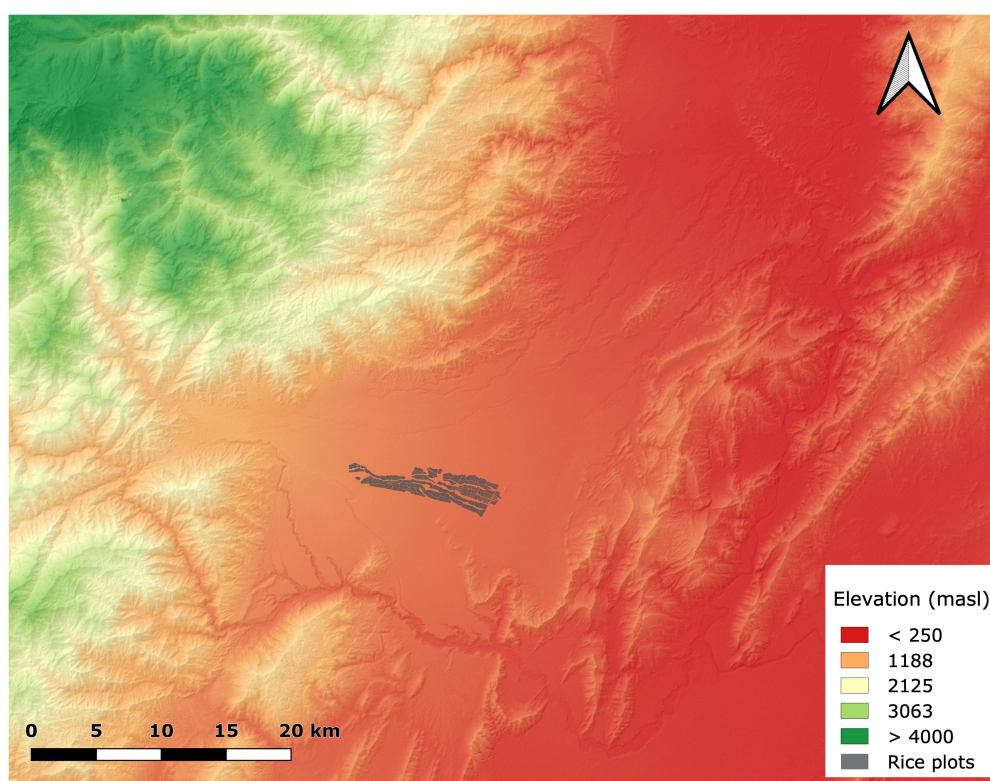


**Fig. 3.2** Digital Elevation Model of the Ibagué plateau, Colombia

2012). In general, most of the material that forms the plateau has been brought by the Coello River, which flowed through this plain in the recent geological past, bringing volcanic materials from the eruptions of the Machin volcano (Nuñez Tello and Lozano Quiroga 2017). Soils of volcanic origin are highly fertile due to the variety of minerals and chemical elements (Minasny et al. 2021). These materials have high porosity and permeability that allow the development of plant roots and the infiltration of rainwater

(Shoji and Takahashi 2002). Fig. 3.3 presents the total soil map units in the Ibagué Plateau, mainly occupied (  $\approx 88\%$  ) by two soil units: PWD and PWF.

- ***PWD Soil Map Unit -Typic Haplustalf:*** The soils in this unit have evolved from mud and agglomerates of volcanic origin and alluvium. They are characterised by moderate fertility, being well-drained, moderately deep, and the presence of varying textures. The soils of this unit have evolved from mud and agglomerates of volcanic origin and alluvium (Bonilla Alvis et al. 2012). They are characterised by having moderate fertility, being well-drained, moderately deep and presenting variable textures (Subdirección de Agrología 2004). Around 90% of the extent of the Hacienda El Escobal is located within this unit.
- ***PWF Soil Map Unit - association of Typic Ustorthents, Lithic Ustorthents, and Fluventic Ustropepts soils:*** This soil unit is located at an altitude of 300 to 600 MASL. The parent material formed of sludge flows from the Tolima and Santa Isabel volcanoes and heteromeric alluvium. The relief is slightly inclined and undulating with slopes of 1% to 12% (Subdirección de Agrología 2004). The low availability of water, the shallow soil depth, and the presence of rocks and gravel limit agricultural activity in this unit (Bonilla Alvis et al. 2012).

With approximately 107,500 ha of rice planted annually, Tolima is the second-largest rice producer in the Country and contributes 18% of the National production (Departamento Administrativo Nacional de Estadísticas (DANE) and Federación Nacional de Arroceros (FEDEARROZ) 2017). The rice production system in the Hacienda El Escobal was chosen due to two main reasons: First, it is located in the Tolima department, which contributes 18% of the National production (Departamento Administrativo Nacional de Estadísticas (DANE) and Federación Nacional de Arroceros (FEDEARROZ) 2017)). By validating the EOAD performance in this region, a large proportion of the Country rice areas are represented, generating more confidence about the transferability of the results to other rice-farming areas. Secondly, as the Ibagué Plateau has been a traditional rice-growing region, it guarantees that a large amount of historical agronomic data is available to carry out the analyses.

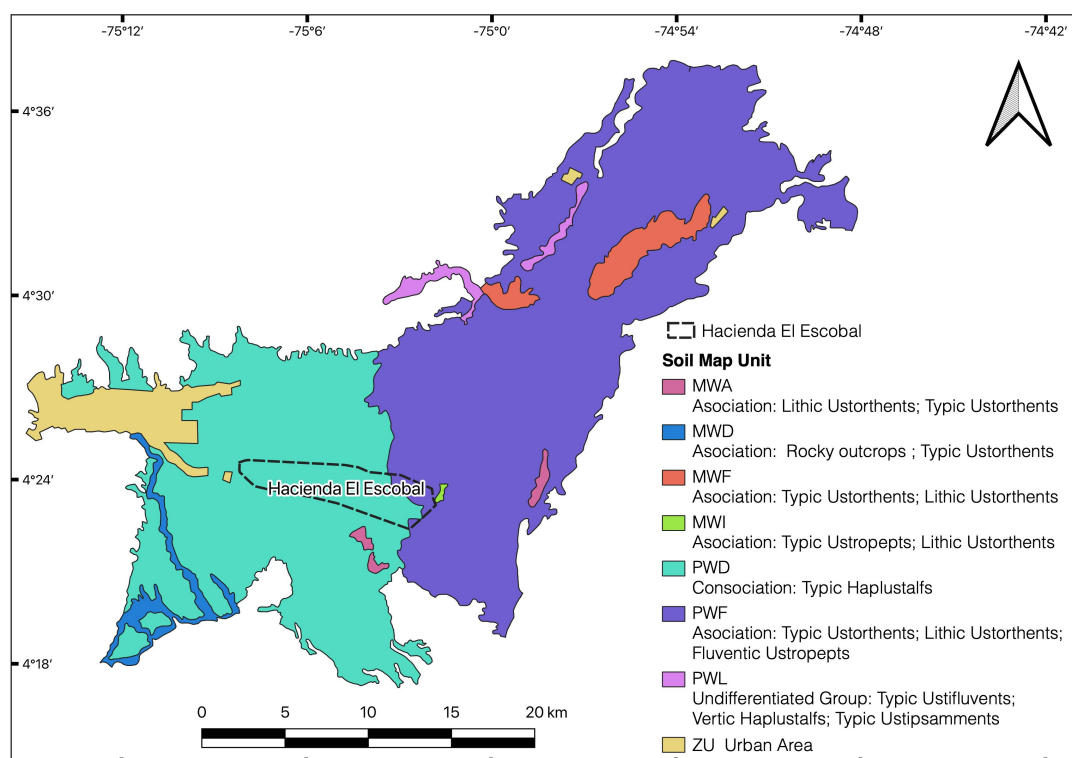


**Fig. 3.3** Soil taxonomy map of the Ibagué plateau, Colombia. Fuller explanation of the main soil types is given in the nearby text. Source: Subdirección de Agrología (2004)

### 3.3 Rice production system in the Ibagué Plateau

In Colombia, rice is the crop with the third-largest area planted after coffee and corn, representing approximately 5% of the agricultural GDP and 0.4% of the National GDP. According to FEDEARROZ, rice production generates more than 500 thousand direct and indirect jobs in 23 departments and 210 municipalities, where the contribution of rice can exceed 80% of the territorial income (Becerra et al. 2020; Chica et al. 2016).

In the Tolima department, agriculture is the activity that most contribute to the regional GDP (15% in 2013; Delgado et al. 2015), being irrigated rice (*Oryza sativa*) the primary agricultural production system. With approximately 107500 ha of rice planted annually, Tolima is the second-largest rice producer in the Country and contributes 18% of the National production (Departamento Administrativo Nacional de Estadísticas (DANE) and Federación Nacional de Arroceros (FEDEARROZ) 2017). The production in the department is distributed in 7235 production units, the most significant number among all departments. They produce average yields of 7.17 t/ha, the highest compared to the Country average of 4.07 t/ha (Ministerio de Agricultura y Desarrollo Rural 2019).

The superior performance of rice crops in this region is due to its favourable soil and climate conditions and the wide availability of irrigation infrastructure in most of the farming systems (Departamento Administrativo Nacional de Estadísticas (DANE) and Federacion Nacional de Arroceros (FEDEARROZ) 2017). Owing to these favourable conditions, the Ibagué plateau plain has the first designation of origin of rice in the country (Londoño 2016). Although this designation means that growers can demand higher prices, there is pressure on farms to maximise quality and production, as any loss in yield or quality results in a significant loss of money. It demands close monitoring of the crop throughout the growing cycle.

The duration of the rice cycle in the Ibagué Plateau ranges between 120 to 130 days. In order to guarantee a minimum of values that allow performing an analysis with statistical validity, only those plots containing at least 30 pixels from each type of satellite image were considered. The number of pixels contained within a crop plot varies depending on the image, plot size and shape. Based on the average number of pixels per plot obtained using the three types of images considered in this study (i.e., Sentinel-2, PlanetScope, Sentinel-1), the following minimum field sizes were established for the anomaly detection analysis:

- Sentinel-2: 1 ha
- PlanetScope: 0.5 ha
- Sentinel-1: 2 ha

Due to the equatorial climatic conditions, rice tends to be produced throughout the year, being possible to have two crop cycles in the same plot during one year. However, when a high presence of weeds is detected (e.g., red rice), the field is rotated with corn. As presented in Figure 3.4, the harvesting dates are spread along the year and rely highly on rainfall patterns. The rice is harvested mainly during the dry periods to facilitate manoeuvring machinery and minimise soil compaction (McPhee et al. 2020). Around 80% of the production is harvested during the two dry seasons: May - August and November - February. The average grain yield in the rice production system studied was 8.4 t/ha between 2015 and 2020, which is higher than the country average (i.e., 5.5 t/ha).

The rice production area in the Hacienda El Escobal farm can be divided into around 120 plots, with areas between 2 and 15 ha that coincide with the typical plot extension



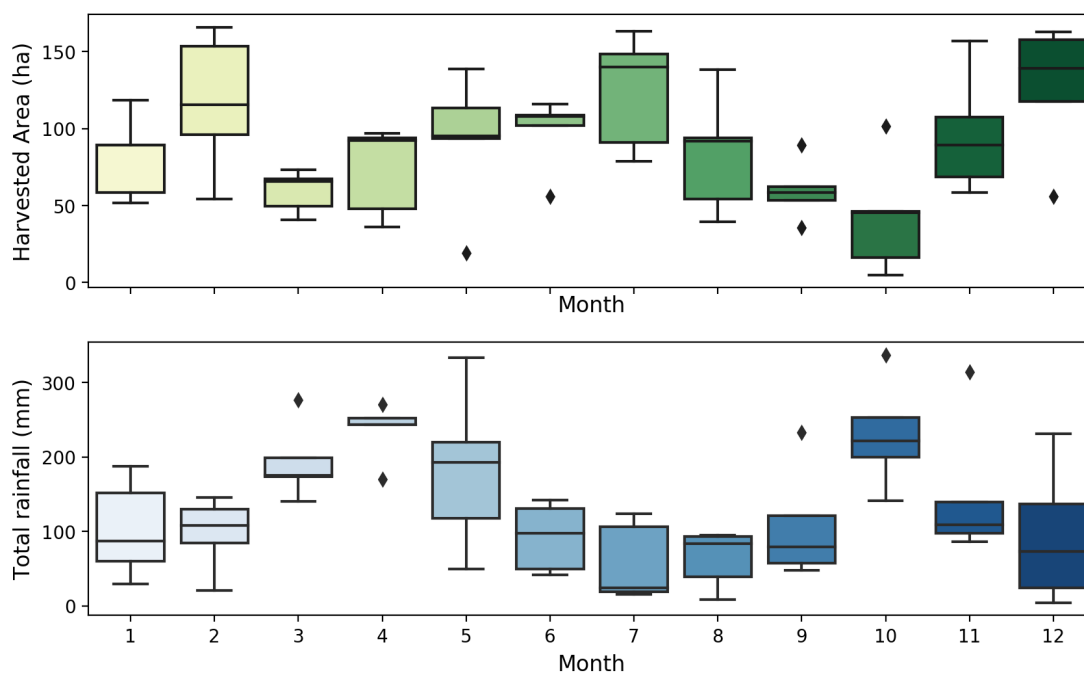


**Fig. 3.4** Box plots of the total monthly harvested area in Hacienda El Escobal (i.e., 605 plots harvested between 2014 and 2018) and monthly rainfall values between January 2014 and December 2018.

in the region. Due to the equatorial climatic conditions of the study site, crops benefit from permanent luminosity throughout the year. This condition added to the need to optimise the water management means that new rice fields are planted throughout the year, and their cultivation calendars tend to differ one from another. It makes an essential difference with the studies carried out in temperate countries, where all the plots share similar crop calendars due to the abrupt changes in temperature and luminosity experienced through the seasons. Some farm areas can hold up to two crop cycles within one year, increasing the number of plots harvested yearly. However, the land is not always sewed immediately after the harvest and can be rotated with corn or cattle raising.

In the Hacienda El Escobal, the field preparation takes around 60 days and includes six types of activities:

1. Harvest residue incorporation by tillage
2. Primary tillage using a chisel-plough
3. Soil clods breaking using a disk harrow
4. Ground levelling using a landplane attached to the back of the tractor.

5. Build levees of 15-30 cm that follow contours of the same elevation using a ridge plough. The levees are built in two ways:

- Demarcation of levees with the GNSS and Real-time kinematic positioning (RTK) correction: A tractor equipped with a Global Navigation Satellite System (GNSS)-Real-time kinematic positioning (RTK) system goes through the plot to create a DEM, which is used to design the levees (Bueno et al. 2019). Then, the levees are built in the field with the ridge plough attached to the tractor back.
- Levees demarcation using a laser technology system: A base station emits a laser signal towards the receptor of a tractor with a special elevating detector. The farmer drives the tractor along the contour by observing the signals in the detector (Bueno et al. 2019), and the levees are built by the ridge plough attached to the tractor's back.
- Sowing begins at least one month after the levees are built, allowing the weeds to grow and making it easier to control them with a herbicide before the crop is established.

The seeds are sown directly in the field using a Semeato brand seeder, model TDNG 320. Usually, seeds are planted with a grain density of 100-150 kg/ha; however, for hybrid varieties, the seed density is lower (30-35 kg/ha), as they can produce between 12-15 tillers.

The rice production system in Hacienda El Escobal, as in most of the farms in the Ibagu  plateau, combines rainfed with a gravity irrigation system. The rice plots are irrigated using a contour-levee technique (Fig. 3.5). In this irrigation system, the entire parcel is at a particular slope, and 15-30 cm levees are built using a special roller along the contour before the sowing. The water is conveyed to the highest point of the plot, and then it is guided towards the lowest part through the breaks of the levees that are manually made at specific intervals (Okada and Lopez-Galvis 2018). The water depth dynamically changes over space and time, which might produce a heterogeneous development of rice plants and weeds when the levees' architecture does not guarantee a homogeneous distribution of water along the field. When these patches are identified on time, the proper irrigation system levees are broken to allow the water flow, so the plants grow at the expected rate.

Once water is available in the soil, either due to the rain or because the irrigation is started, the seed imbibition begins (BBCH 01), allowing the radicle to emerge from caryopsis (BBCH 05). The growth of weeds due to the increase in soil moisture is controlled by



**Fig. 3.5** Rice field with contour-levee irrigation system

applying a pre-emergent herbicide just after the irrigation begins and before seedling emergence (BBCH 09). The crop age is counted from the field date of emergence, i.e., the date when 80% of the plants have emerged. By this time, the seedlings' emergence homogeneity is visually checked in the field, identifying the patches that need to be resown or those with low water availability to fix the water supply.

The crop is fertilised between 5 and 6 times within the first 60 DAE, with urea and potassium chloride being the most abundant fertilisers. Nitrogen is usually applied to the fields using drones or an aeroplane, which are rented. The farm agronomists indicate the application date and the fertiliser dosage per field to the company that flights the drones or the aeroplanes. This company's staff is in charge of mixing and applying the fertiliser. In some occasions, due to human errors, the doses might vary significantly even within the same field, which is later reflected in yellow strips along the field. Fig ?? shows a field which received different Nitrogen doses due to an error during the mixture preparation and the associated NDVI surface derived from a PlanetScope image. It shows a significant difference in NDVI between the under fertilised area and the region that received the adequate Nitrogen dosage. Previous studies have demonstrated that optical images, in particular, the NIR and red-edge bands are sensitive to chlorophyll and Nitrogen content of plants (e.g., Clevers and Gitelson 2013). Although these evident differences should be easily detected by an anomaly detection method, such extreme behaviour might hide other types of anomalies.

Other fertilisers applied include monoammonium phosphate, diammonium phosphate, monopotassium phosphate, Calcium and ammonium sulphate. The control of narrow-

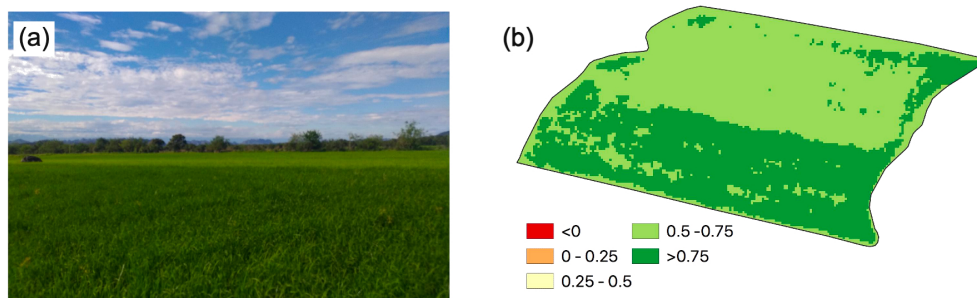


**Fig. 3.6** Rice field that received two different Nitrogen dosages. (a) Photography of the plot, (b) NDVI surface derived from a PlanetScope image.

leaf weeds after the emergence is done manually, and the broad-leaf weeds are controlled with chemicals until the 77 DAE. The harvest is mechanised using a Massey Fergusson model 5650 combines (See Figure 3.7).



**Fig. 3.7** Two combines and a truck in a rice field in the Hacienda El Escobal farm. The truck transports the paddy rice to the mill. The John Deere brand harvester shown to the right is used occasionally.

## CHAPTER 4

### Datasets and pre-processing

The EOAD method was tested using optical and radar satellite products. The analyses with optical products were carried out using Sentinel-2 and PlanetScope imagery, while the radar-based analyses were performed using Sentinel-1 scenes. Agronomic data came from the historical management records registered by the field staff, the anomalies collected during fieldwork campaigns and the data recorded by a weather station. The following section first presents the characteristics of the satellite datasets used, followed by the description of the pre-processing techniques applied on the imagery to produce Analysis Ready Data (ARD). It finishes by describing the agronomic datasets and associated preparation activities to get the data ready for further analyses.

#### 4.1 Satellite datasets description

Crop biophysical features are highly variable over space and time. These temporal and spatial properties offer good potential for multi-temporal remote sensed data to support crop monitoring (Eerens et al. 2014). This research used 47 Sentinel-2, 15 PlanetScope, 39 Sentinel-1 ascending and 56 Sentinel-1 descending images acquired over 2018-2020 to detect in-field and inter-field anomalies in croplands (See Fig. 4.1). The aim was to assess the applicability of the anomaly detection method over products derived from non-commercial and commercial satellites with different temporal, spatial and radiometric resolutions. Fig. 4.2 presents examples of how some rice plots and forest areas in the Hacienda el Escobal farm are observed by the different types of satellite imagery used in this study.

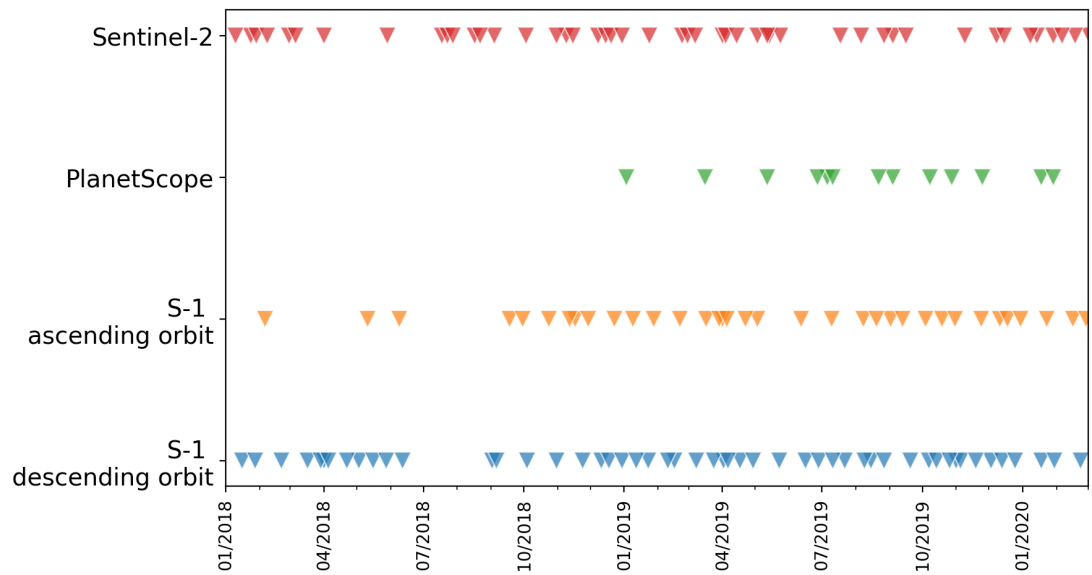


**Fig. 4.1** Acquisition dates of the PlanetScope, Sentinel-2 and Sentinel-1 scenes. The optical imagery considered included only those images with cloud cover below 40%.

Sentinel-2 and PlanetScope imagery have different capabilities in terms of spatial, temporal and spectral resolution. The commercial PlanetScope imagery offers increased temporal and spatial resolution in comparison to the freely available Sentinel-2 imagery, however, its spectral coverage is inferior (Mudereri et al. 2019). In addition, the two sensors bands in the blue, green, red, and NIR regions cover a different range of wavelengths (See Fig. 4.3). These differences affect the vegetation indices and their sensitivity to discriminate anomalies as they depend highly upon the spectral differences between different crops. On the other hand, the C-band products acquired by the Sentinel-1 constellation are not impeded by cloud cover and allow retrieving information about crops more often. However, Sentinel-1 products have a lower spatial resolution in comparison to Sentinel-2 and PlanetScope as the standard GRD products have an approximate spatial resolution of 20 x 22m and square pixel spacing of 10 x 10 m (European Space Agency 2020).

Image preparation processes were different for the different types of imagery. Sentinel-2 L1C products pre-processing operations included radiometric, geometric corrections, as well as cloud masking, while only cloud masking operations were applied over the PlanetScope 3B processing level products. On the other hand, for the SAR products, a morphological reducer filter was applied to the already calibrated, ortho-corrected products.



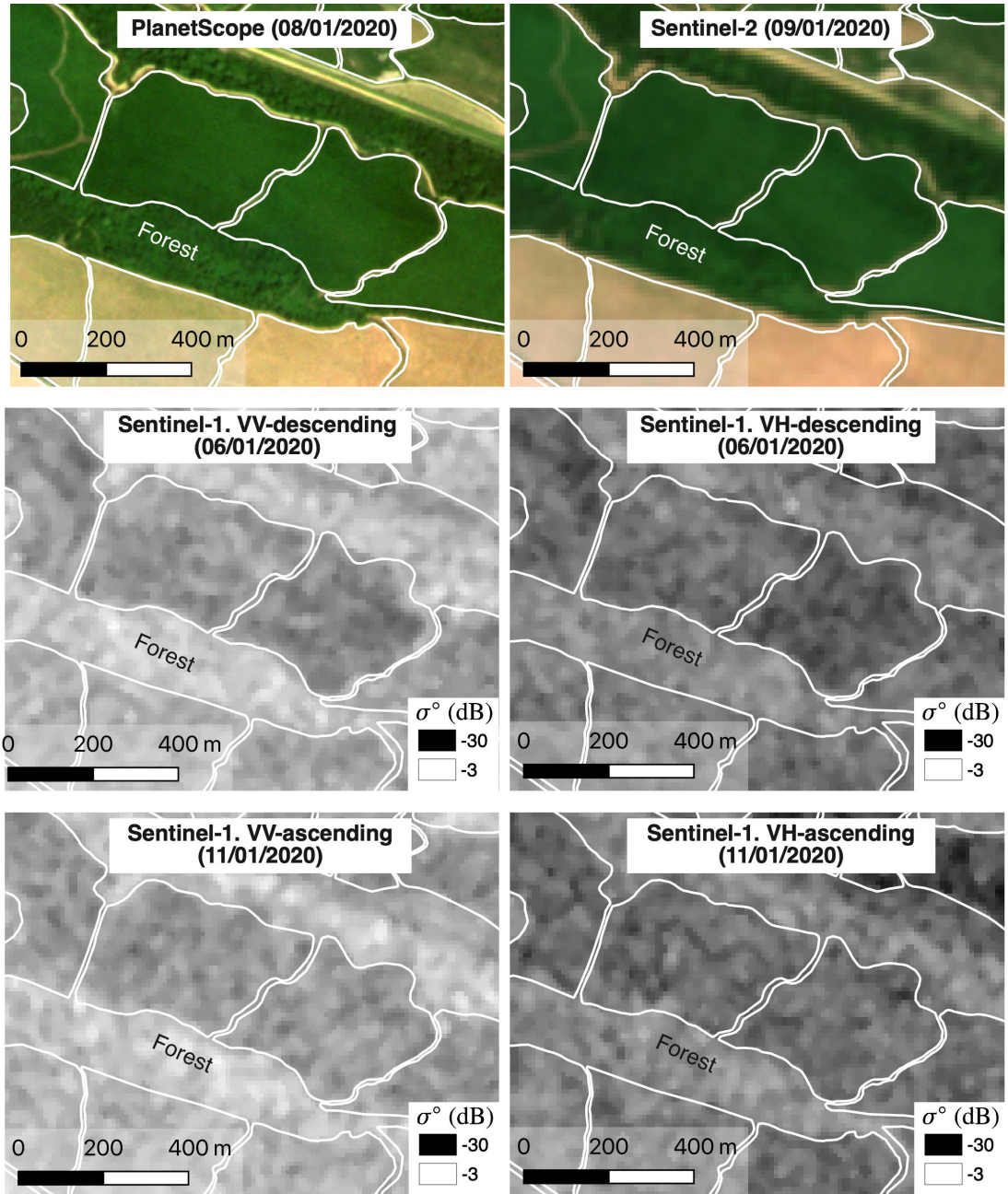


**Fig. 4.2** Example of the types of satellite images used. The optical images (i.e., Sentinel-2 and PlanetScope) are displayed using an RGB composition and the SAR images are displayed in grayscale.

#### 4.1.1 Sentinel-2

The improved spatial and temporal resolutions of Sentinel-2 have enabled improving the analysis of multi-temporal data for crop monitoring purposes. The higher spatial resolution of S2 (10 m pixel size), in comparison to satellite sensors such as Landsat (30m pixel size) or MODIS (250 m pixel size), has enabled more precision in the analyses

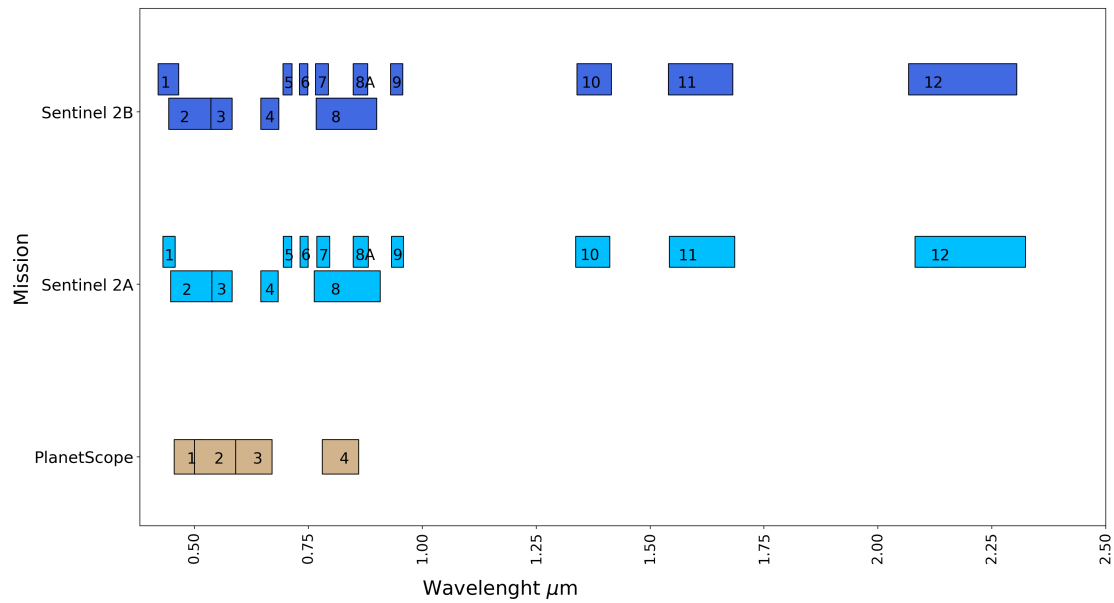


**Fig. 4.3** Sentinel-2 and Planet Scope spectral bands

performed at field and agro-ecosystem scales. This is relevant in agricultural contexts, especially smallholder farming systems in developing countries (Segarra et al. 2020). On the other hand, the improved temporal resolution of S2 (5 days) in comparison to Landsat (16 days), has allowed performing high-frequency time-series analyses and has expanded the opportunities to carry out multi-temporal studies on locations facing frequent cloud cover problems (Mandanici and Bitelli 2016).

The Copernicus Sentinel-2 mission was launched to monitor variability in land surface conditions. It comprises a constellation of two polar-orbiting satellites (Sentinel-2A, Sentinel-2B), placed in the same sun-synchronous orbit, phased at 180° to each other, with coverage between latitudes 56° south and 84° north. It provides a wide swath width (290 km) and ten days revisit time at the equator with one satellite, and five days with two satellites under cloud-free conditions, which results in 2-3 days at mid-latitudes (ESA 2013). Each of the Sentinel-2 mission satellites carries a single payload: the Multispectral Instrument (MSI). The MSI measures the Earth's reflected radiance in 13 spectral bands, including Visible to Near Infra-Red (VNIR) and Short Wave Infrared (SWIR) bands. Table 4.1 presents the spectral band's central wavelength values and spatial resolutions for the Sentinel-2 sensors. Fig. 4.4 and Fig. 4.5 show the spectral reflectance functions for the VNIR and SWIR Sentinel-2A MSI bands, respectively. These functions are applicable from 15 January 2018.



**Table 4.1** Spectral bands for the Sentinel-2 sensors (ESA 2013)

Sentinel-2 bands	Sentinel-2A Central wavelength (nm)	Sentinel-2B Central wavelength (nm)	Spatial resolution (m)
B1- Coastal aerosol	442.7	442.2	60
B2- Blue	492.4	492.1	10
B3- Green	559.8	559.0	10
B4- Red	664.6	664.9	10
B5- Vegetation red-edge	704.1	703.8	20
B6- Vegetation red-edge	740.5	739.1	20
B7- Vegetation red-edge	782.8	779.7	20
B8- NIR	832.8	832.9	10
B8A- Narrow NIR	864.7	864	20
B9- Water vapour	945.1	943.2	60
B10- SWIR - Cirrus	1373.5	1376.9	20
B11- SWIR	1613.7	1610.4	20
B12- SWIR	2202.4	2185.7	20

This research accessed 47 Level 1C Sentinel-2 products between January 2018 and March 2020 via Google Cloud. The Sentinel-2 Level-1C products are 100 x 100 km<sup>2</sup> top-of-atmosphere reflectance ortho-images in UTM/WGS84 projection. They are resampled with a constant Ground Sampling Distance (GSD) of 10, 20, and 60 m depending on the native resolution of each spectral band (ESA 2013).

Despite the improvements in temporal resolution, the single-use of Sentinel-2 imagery can lead to an insufficient number of observations in areas characterised by persistent cloud cover (Mandanici and Bitelli 2016). A sufficient number of cloud-free observations is critical to represent the within-season dynamics in agricultural systems accurately. For this reason, different spatio-temporal fusion methods have been developed to complement

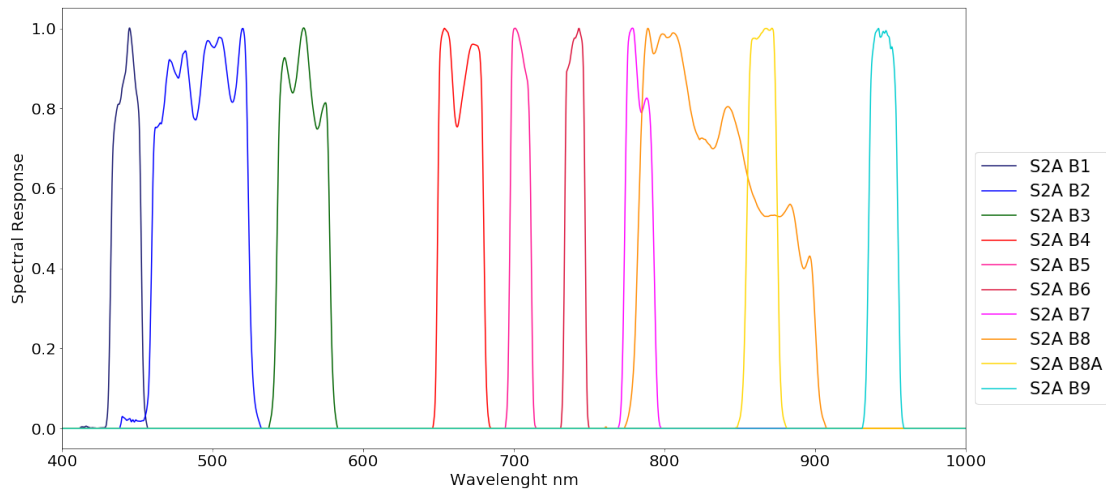


**Fig. 4.4** Spectral response functions for the visible and infrared bands of the Sentinel-2 A MultiSpectral MSI (19 December 2017)

Sentinel-2 with other sensors' data to obtain more frequent imagery for timely monitoring. For example, Sadeh et al. (2021) proposed an interpolation to fill data gaps between the cloud-free PlanetScope and S2 acquisitions to create evenly spaced time series.

#### 4.1.2 PlanetScope

Over the last decade, the CubeSats have aimed to overcome the limitations of temporal and spatial resolution by establishing constellations with large numbers of satellites (Li et al. 2021). The PlanetScope constellation (PS) is an example of this new generation of satellites. Since its launch, different researchers have used PlanetScope imagery to monitor within-field variability in croplands.

The commercial PlanetScope constellation consists of multiple launches of groups of individual satellites (Doves) that follow a Sun-Synchronous orbit and an International Space Station (ISS) orbit (Lemajic Blanka et al. 2018; Wicaksono and Lazuardi 2018). The complete PlanetScope constellation comprises approximately 130 satellites and is able to acquire images from the entire Earth's surface every day in four spectral bands. Since the first launch in 2016, Planet has released three PlanetScope instrument types on board of Dove CubeSats (Planet Labs 2019):

- Dove Classic (PS2): Four-band frame imager with a split-frame Visible + Near-Infrared filter

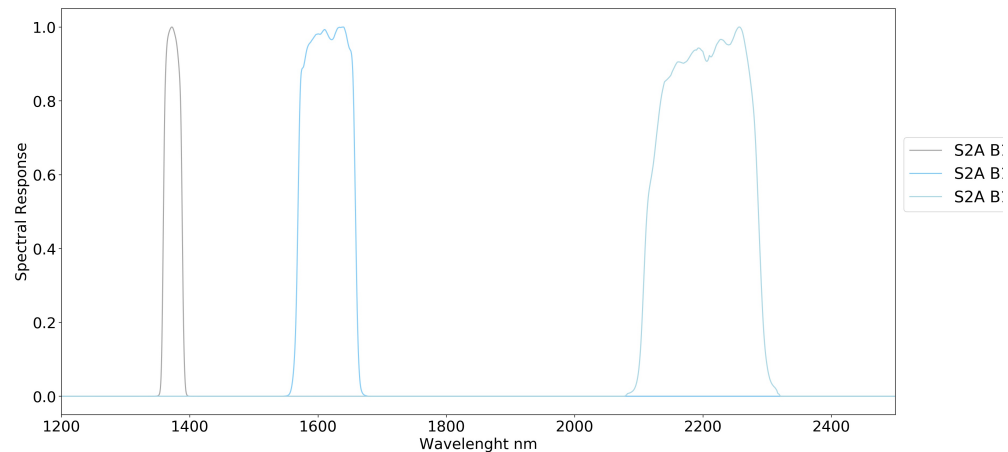


**Fig. 4.5** Spectral response functions for the short wave infrared bands of the S2-A MultiSpectral Instrument (19 December 2017)

- Dove-R (PS2.SD): Four-band frame imager with a butcher-block filter made up of 4 individual pass-band filters, that separate the light into the blue, green, red and NIR channels. PS2.SD bands are interoperable with those of Sentinel-2 (Planet Labs Inc 2021).
- SuperDove (PSB.SD): Eight-band frame imager that provides red, green, blue, near infrared, and red edge channels.

The PlanetScope constellation products have a Ground Sampling Distance (GSD) of 3.7 at nadir and delivered at three processing levels:

- Basic Scene Product (Level 1B): Scaled Top of Atmosphere Radiance corrected products that are not projected to any cartographic projection.
- Ortho Scene Product (Level 3B): Orthorectified products, scaled to Top of Atmosphere Radiance or Surface Reflectance and projected to a UTM projection.
- Ortho Tile Product (Level 3A): 25 km x 25 km orthorectified and tiled products generated from a set of consecutive scenes within a strip (usually 4 or 5) and projected to a UTM projection.

In this research, 15 PS2 surface reflectance images 3B level, acquired between January 2019 and February 2020, were used. The images were accessed through the Planet

Explorer browser (Planet Labs Inc. 2021). They are provided as GeoTIFF images resampled at 3 m and projected in the UTM projection using the WGS84 datum. Table 4.2 presents the PlanetScope spectral bands' specifications.

**Table 4.2** Ortho Scene PlanetScope imagery bands and pixel size (ESA 2013)

PlanetScope bands	Central wavelength ( $\mu\text{m}$ )
B1- Blue	0.49
B2- Green	0.55
B3- Red	0.63
B4- Near Infrared	820

#### 4.1.3 Sentinel-1

While optical wavelengths are more intuitively linked with crop features, atmospheric conditions cause absorption and scattering that affects the spectral responses (McNairn and Shang 2016). SAR is an effective technique for monitoring croplands as its quality does not depend on weather conditions (Liu et al. 2019). In particular, the high revisit frequency of Sentinel-1 (12-day repeat cycle) over other missions such as ERS-1/2 and ENVISAT ASAR provides unique opportunities for crop monitoring (Mandal et al. 2020).

Sentinel-1 is composed of a constellation of two satellites: Sentinel-1A and Sentinel-1B, sharing the same orbit planes with a 180° orbital phasing difference. Each Sentinel-1 satellite operates a C-band Synthetic Aperture Radar (SAR) in a near-polar, sun-synchronous orbit, with a 12-day repeat cycle and 175 orbits per cycle (European Space Agency 2020).

The Sentinel-1 C-band sensor acquires data in four imaging modes (European Space Agency 2020) presented in Fig. 4.6. The Interferometric Wide Swath Mode (IW) is the primary acquisition mode over land (Bourbigot et al. 2016) and registers VV+VH polarisations; the Wave Mode (WV) registers VV polarisation over open ocean; the Extra Wide Swath Mode (EW) is primarily used for wide area coastal monitoring (e.g. ship traffic, oil spill and sea-ice monitoring); and Stripmap Mode (SM) is only used for small islands and on request for extraordinary events (European Space Agency 2020). SM, IW and EW Level-0 products can be processed to SAR Level-0, Level-1 SLC, Level-1 GRD and Level-2 OCN products.

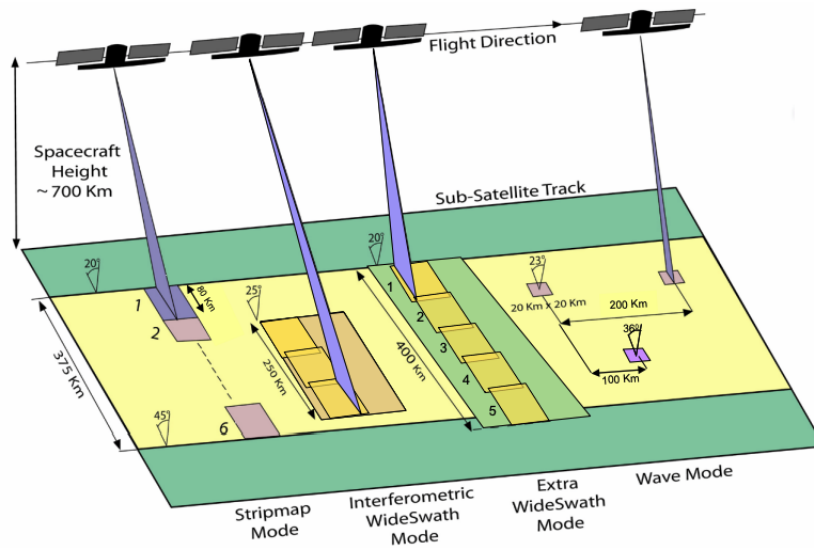


**Fig. 4.6** Sentinel-1 Acquisition Modes (from Bourbigot et al., 2016)

Level-1 products derived from raw Sentinel-1 signal data are georeferenced and time tagged (European Space Agency 2020). They are available in 2 formats: Single Look Complex (SLC) and Ground Range Detected (GRD). SLC products are images in the slant range that contain the phase and amplitude information, which is required for interferometric analysis. On the other hand, GRD includes only intensity data and is projected to ground range using an Earth ellipsoid model (Google 2021).

As the signal intensity is largely defined by the geometric properties of the surface that interacts with the wavelength, modifying the look angle also alters the interaction of the signal with the surface elements and therefore the image brightness (Flores et al. 2019). Fig. 4.7 shows the spatial variation of the S1 ascending and descending orbit look angles at the study area. With the available Sentinel-1 orbits, the studied plots lie at a look angle range of around  $42^\circ \pm 0.5^\circ$  in descending orbit and  $33.5^\circ \pm 0.5^\circ$  in ascending orbit. As the penetration of radar waves through vegetation is greater at smaller angles (Lillesand et al. 2015), images in the ascending orbit ( $33.5^\circ \pm 0.5^\circ$ ) will tend to look brighter compared to the descending orbit ( $42^\circ \pm 0.5^\circ$ ). Sentinel-1 products were grouped into ascending and descending orbit images to minimise the backscatter variation among acquisitions of the same polarisation due to differences in the look angle and prevent the anomaly detection method from being affected by these brightness variations.

**Table 4.3** SAR acquisition geometries

Pass direction	Relative orbit	Acquisition Time	Dates range
Descending	56	10:42	01/01/2018-31/03/2020
Ascending	39	23:13	01/01/2018-31/03/2020

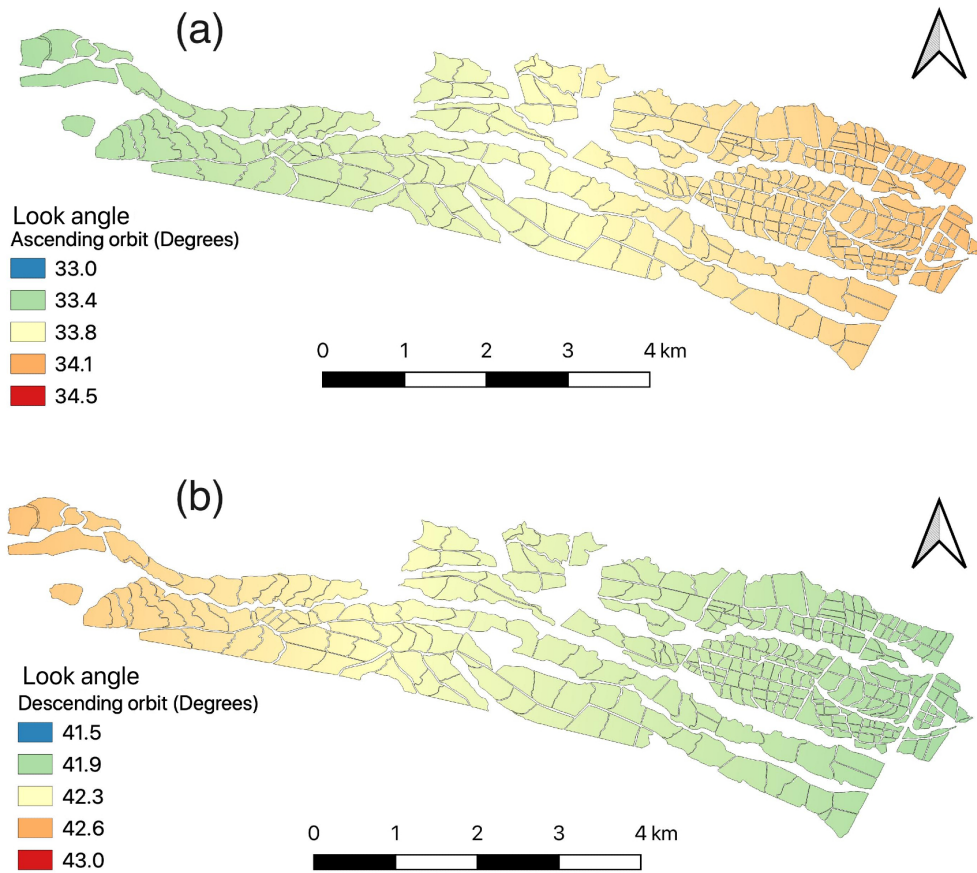


**Fig. 4.7** Spatial distribution of incidence angles in Sentinel-1 images over the study area. (a) Ascending orbit (b) Descending orbit

The S1 imagery used are Level-1 GRD data acquired in IW mode with dual-polarisation (VV and VH) that have been processed to backscatter coefficient  $\sigma^\circ$  in decibels (dB) (Bourbigot et al. 2016; Gorelick et al. 2017). The IW-GRD products are detected, multi-look products, with approximately square resolution cells (European Space Agency 2020). In the Sentinel-1 IW acquisition mode, the pixels are about 20 m x 5 m in extent, however, as part of the multi-looking procedure, five cells are incoherently averaged in the range direction to achieve approximate 20 m x 20 m resolution at the mid-range

value at mid-orbit altitude (Canty 2020). Multi-looking is a processing property in which the SAR processor splits the full synthetic aperture into several sub-apertures, each representing an independent look of the identical scene. The incoherent summing of these looks forms a multi-looking image. Multi-looking produces images with reduced speckle, but also with reduced resolution (Bourbigot et al. 2016)

## 4.2 Image pre-processing

Image preparation is critical for quantitative analyses of the Earth's surface using remote sensed data (Chakouri et al. 2020). Satellite imagery pre-processing operations comprise a set of geometric and radiometric corrections as well as coregistration operations that vary depending the type of sensor.

### 4.2.1 Optical Imagery

The purpose of optical satellite imagery pre-processing is to enhance the information available in the images. Data preparation includes atmospheric corrections, topographic and view angle normalisation, image sub-setting, co-registration, and cloud masking.

The application of atmospheric corrections before any optical-based satellite RS analysis is fundamental to reduce the effects of scattering and absorption by atmospheric molecules and aerosols on the measured reflectance (Song et al. 2001). Atmospheric corrections can either be absolute or relative. In relative corrections, the digital numbers in the corrected images represent the same reflectance, no matter the actual reflectance value on the ground (Chavez and Mackinnon 1994). Relative atmospheric correction techniques use information within the image to reduce noise by either normalising the pixel values between the different bands for a single scene or normalising the pixel values between similar bands in multi-date imagery. An example of relative atmospheric corrections is the retrieval of the spectral measurements of pseudo-invariant features PIFs to derive linear relationships between the image bands across time (Song et al. 2001).

In absolute atmospheric correction models, the digital numbers representing the Top

Of Atmosphere Reflectance (TOA) recorded by the sensor are converted into surface reflectance. The methods that model reflection, absorption and scattering by the atmosphere, such as 6S (Vermote et al. 1997), ATCOR (Schläpfer and Richter 2010), Fast Line-of-Sight Atmospheric Analysis of Spectral Hypercubes (FLAASH; Adler-Golden et al. 1999), Low-Resolution Atmospheric Transmission (LOWTRAN; Kneizys et al. 1988), and Moderate-Resolution Atmospheric Transmission (MODTRAN; Adler-Golden et al. 1999) , are examples of absolute correction techniques. These methods require information about both the sensor spectral profile and the atmospheric properties at the acquisition time.

The 6S model (Second Simulation of a Satellite Signal in the Solar Spectrum), is one of the most widely used and best documented RT codes in the remote-sensing community (Song et al. 2001). It is a physically based model that accounts for the main atmospheric effects (Vermote et al. 1997), and is used to make atmospheric corrections in the short wavelength region (between 0.25 and 4.0  $\mu\text{m}$ ) assuming a cloudless atmosphere (Zhao et al. 2001). It simulates the reflection of solar radiation for a wide range of spectral, geometric, and atmospheric conditions (Kotchenova et al. 2008) and uses the following parameters (Vermote et al. 1997):

- geometrical conditions
- atmospheric model for gaseous components
- aerosol model
- spectral condition
- ground reflectance

Modelled Atmospheric Correction Methods such as the 6S can be complex to apply as they require many parameters; however, they are the best solution for lower resolution imagery or areas where ground spectra targets are not available (Bunting 2018). Other absolute methods based on Dark Object Subtraction (DOS) do not require atmospheric measurements but they need radiative transfer codes to perform the radiometric corrections (El Hajj et al. 2008).

Cloud masking is also an essential pre-processing step for any optical satellite analysis as it helps identify the usable portion of the images. Clouds presence is a problem



for crop monitoring because unflagged clouds may be mapped as false changes and therefore provide misleading information about the temporal dynamics of crop growth (Coluzzi et al. 2018; Huang et al. 2010). Most common spectral classification techniques rely upon the presence of thermal bands to differentiate between clouds, and other land covers (Coluzzi et al. 2018). However, these methods cannot be applied over Sentinel-2 or PlanetScope imagery as they are not equipped with such bands. To overcome these limitations, some researchers have used parallax effects (Frantz et al. 2018) and supervised classification approaches (Shendryk et al. 2019).

The effects of topography on radiance have to be accounted for before any land monitoring application as they affect the radiance measured by satellite sensors (Holben and Justice 1980; Shepherd and Dymond 2003; Van Zyl and Kim 2010). For example, illumination is different for slopes facing the sun and slopes facing away from the sun (Holben and Justice 1980) and the proportion of energy reflected by a surface varies with the geometry of the sun, which in turn changes with topography (Teillet et al. 1982). Shepherd and Dymond (2003) proposed a method to produce standardised reflectance products, which are normalised for topography and the solar and sensor view angles. Regarding topographic corrections, this method only works for images where the solar elevation is between 50° and 70°. The equation for standardised reflectance, with respect to solar and view angles, as defined by Shepherd and Dymond (2003), is presented in Eq. 4.1.

$$\rho_h^{dir} = \frac{\pi L}{E^{dir} / \gamma + \beta E^{dif}} \quad (4.1)$$

Where:

$\rho_h^{dir}$  is the direct reflectance for a horizontal surface

$L$  is the radiance at the bottom of the atmosphere

$E^{dir}$  is the direct irradiance

$E^{dif}$  is the diffuse irradiance

$\beta$  can be evaluated from a bidirectional reflectance model, however, Shepherd and Dymond (2003) consider reasonable to set  $\beta$  to 1 for moderate sun elevations between 50° and 70°.

$\gamma$  is given by Eq. 4.2

$$\gamma = \frac{\cos(i) + \cos(e)}{\cos(i_h) + \cos(e_h)} \quad (4.2)$$

Where:

$i$  and  $e$  are the incidence and exitance angles on an inclined surface, respectively (See Fig 4.8)

$i_h$  and  $e_h$  are the incidence and exitance angles on a horizontal surface, respectively.

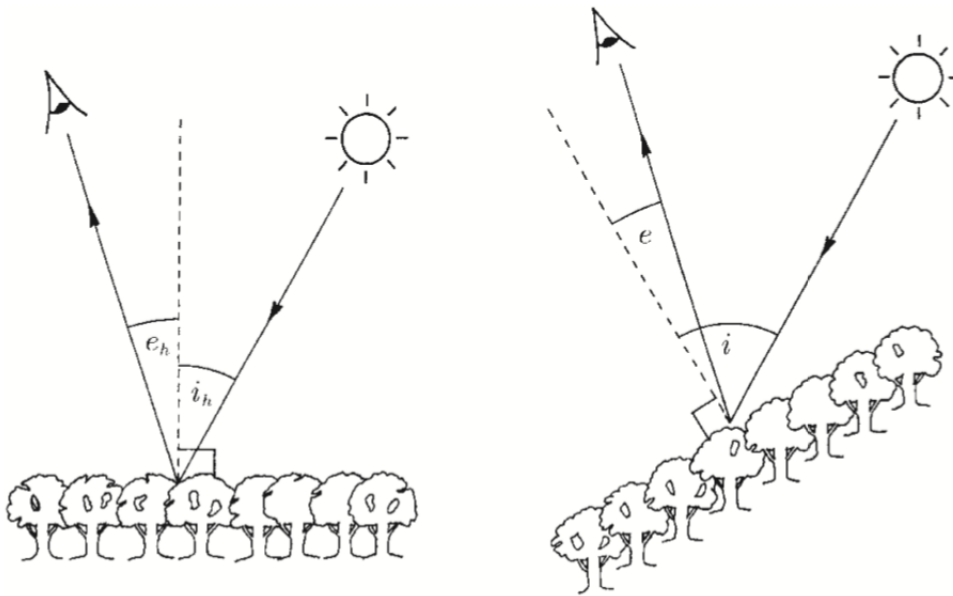


**Fig. 4.8** Scheme of the reflection angles of a vegetation canopy on a horizontal surface and an inclined surface (from Shepherd and Dymond, 2003).

Co-registration aims to ensure that all the images are spatially aligned into a common grid so that the features in one image overlap as well as possible its footprint in any other image in the time series (Gómez-Chova et al. 2011). Precise spatial alignment among the images within a time series is a prerequisite for the study of within-season dynamics in agricultural systems using satellite RS (Leprince et al. 2007). Particularly, in smallholder contexts, accurate image co-registration is a prerequisite to extract more precisely the temporal profiles of farm fields and characterise the within-field changes accurately over time (STARS project 2017). To corregister multiple images, first, all the images need to be projected and resampled onto a common reference system (Leprince et al. 2007). Typically, manual coregistration methods involve the identification of common tie points

between each pair of images to be registered. Similarly, classical automatic approaches identify and align matching features such as corners within the two images considered (Bunting et al. 2010).

#### 4.2.1.1 Sentinel-2

The pre-processing operations performed over the Sentinel-2 L1C data were applied in as automated fashion as possible using the Atmospheric and Radiometric Correction of Satellite Imagery (ARCSI) software (Bunting and Clewley 2018), the open-source Remote Sensing and GIS Software Library (RSGISLib; Bunting et al. 2014), and QGIS (QGIS.org 2021). These operations included atmospheric corrections, topographic and view angle normalisation, image sub-setting, co-registration, and cloud masking (See Fig. 4.9).

First, all Sentinel-2 L1C images were converted to surface reflectance using the 6S radiative transfer model in the ARCSI software (Bunting et al. 2018). The Coastal/Aerosols band (B1), the Atmospheric/Water Vapour band (B9), and the Cirrus band(10) were omitted from the analysis, as they do not contain information relevant for the current research. We chose the 6S model due to four reasons: 1) It is one of the most widely used and best documented RT codes in the remote-sensing community; 2) It is a physically based model that accounts for the main atmospheric effects; 3) It is not optimised on one specific satellite scene, location, or object class (Zhao et al. 2001); and 4) We did not have access to ground spectra targets.

After performing the atmospheric corrections, a 12.5 m Alos Palsar radiometrically terrain-corrected elevation model was used to build a lookup table (LUT) for correction with respect to altitude. It was applied subsequently to the input surface reflectance images to derive topographically corrected (standardised) reflectance products using the approach of Shepherd and Dymond (2003). In addition, all image bands were oversampled to 10 m x 10 m resolution using a nearest neighbour interpolation and were clipped to the study extent area.

Since automatic detection of clouds and cloud shadows in Sentinel-2 is difficult due to the lack of a thermal band, clouds and shadows are extracted through a supervised classification operation that uses an extra-trees classifier from the scikit-learn library

(Pedregosa et al. 2011).

After performing a visual inspection of control points recorded in the field, it was found that PlanetScope images were better georeferenced in the study area than Sentinel-2 images and better spatially aligned over time. For this reason, a PlanetScope image was selected as the reference to which all the Sentinel-2 images were aligned. First, the 3-meter resolution Planet Scope image was clipped and resampled to the extent and spatial resolution of the Sentinel-2 clipped images. The resampling operation was performed using the cubic convolution interpolation method in RSGISLib. Then, a Sentinel-2 scene was visually georeferenced to the previously resampled PlanetScope image using the georeferencing plugin from QGIS. The georeferenced Sentinel-2 scene was used as a reference to generate the tie points that matched each image using the basic registration algorithm available in the RSGISLib software (Pete Bunting and Daniel Clewley 2020). Finally, the gdalwarp (GDAL/OGR contributors 2021) utility was used to warp the images using the tie points generated previously.

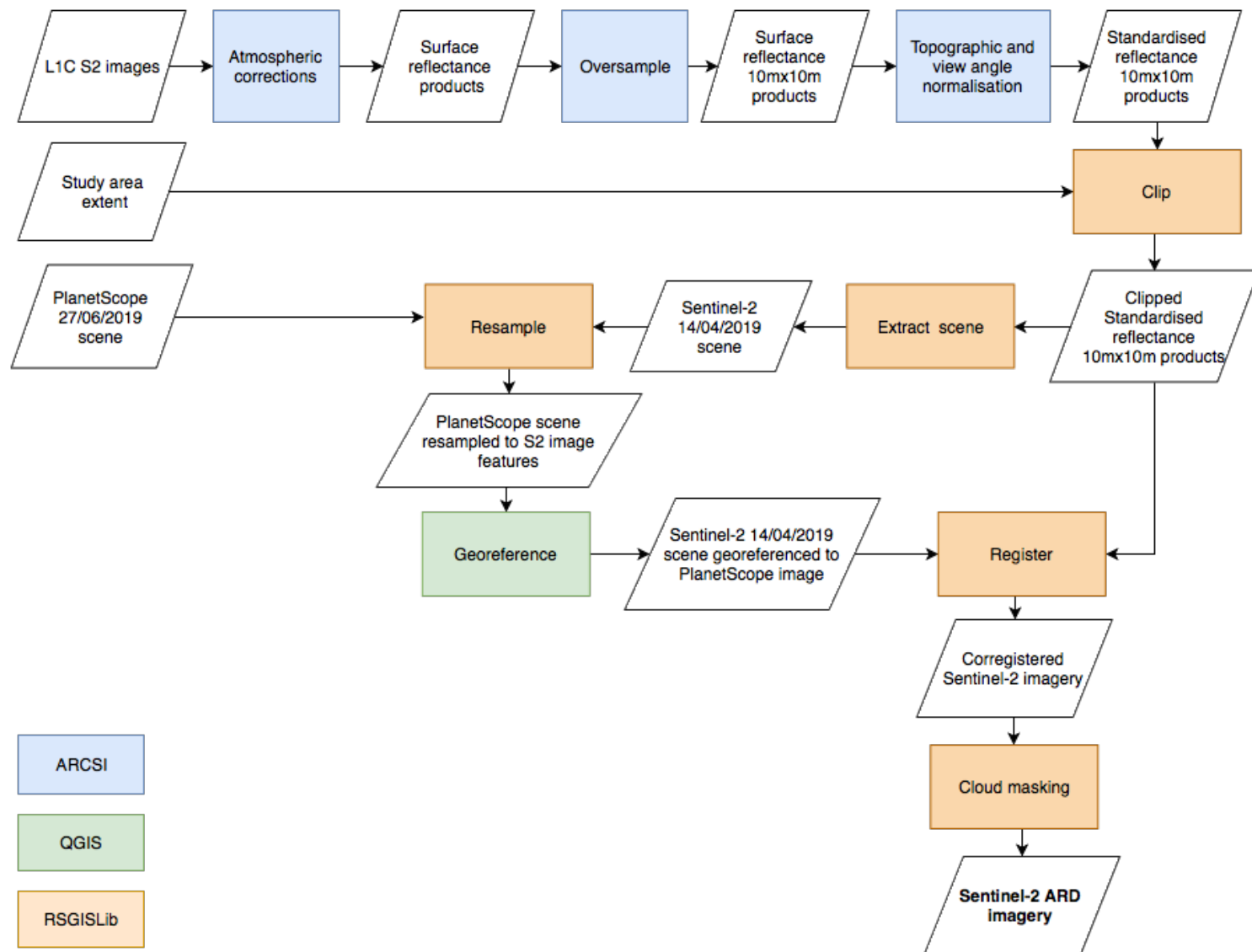


**Fig. 4.9** Flowchart of pre-processing operations performed over Sentinel-2 L1C products

#### 4.2.1.2 PlanetScope

The 15 PlanetScope 3B level products used in this research were accessed through the Planet Explorer browser. They are delivered as radiometrically and geometrically-corrected images. The atmospheric corrections of the 3B level products carried out by Planet Labs are performed using the 6S code. The inputs, such as AOD, water vapor and ozone inputs, are retrieved from MODIS near-real-time data (Planet Labs 2019).

PlanetScope images include an Unusable Data Mask (UDM) layer to flag candidate PlanetScope pixels contaminated by clouds/cloud shadows. However, the UDM layer is mainly used as a cloud coverage filter to browse imagery and is insufficient for accurate cloud/cloud shadow removal (Maohua 2001). For the study area, in particular, the unusable data mask provided with each PlanetScope image tended to overestimate the presence of non-usable pixels in both study locations. Therefore, clouds and shadows were identified with a supervised classification operation that used an extra-trees classifier from the scikit-learn library (Pedregosa et al. 2011), similarly, as it was done with Sentinel-2 imagery.

After performing a visual inspection of control points recorded in the field, PlanetScope images showed good accuracy and spatial co-registration, therefore no additional pre-processing operations were applied. The precise geolocation of PlanetScope imagery is determined by the integration of Ground Control Points (GCP) from sub-meter accuracy to USGS Landsat based ones: it allows to ensure a geolocation accuracy of below 10 m RMSE (Lemajic Blanka et al. 2018). Also, considering that the study area was relatively flat and that at the time at which the sensor acquired the images (15:05) the solar angle was outside the range of  $50^{\circ}$  and  $70^{\circ}$ , the products were not transformed into standardised reflectance and were left as surface reflectance products.

#### 4.2.2 Sentinel-1

Despite SAR imagery being less affected by atmospheric conditions, SAR data are very sensitive to imaging geometry and surface characteristics (Braun 2019; Van Zyl and Kim 2010). Creating an image where the value of each pixel is directly related to the backscatter of the surface is essential for quantitative analyses and comparing images acquired by different sensors, modalities, processors or times (Oliver and Quegan 2004).

Most common SAR image preprocessing operations include geometric and radiometric calibrations as well as speckle noise reduction.

GEE processes Sentinel-1 Level-1 GRD to generate calibrated products in the same way as the Sentinel-1 toolbox (S1TBX) does by applying the following steps (Google 2021):

- *Apply orbit File Operator* to update the orbit state vectors in the product metadata regarding satellite position and velocity.
- *Border Noise Removal* to remove low-intensity noise and invalid data on the scene edges (Filipponi 2019).
- *Thermal Noise Removal* to remove additive noise, in particular, normalising the backscatter signal within the S-1 scene.
- *Radiometric calibration* converts the backscatter intensity measured by the sensor into the backscatter coefficient ( $\sigma^\circ$ ) in each pixel. The backscatter coefficient ( $\sigma^\circ$ ), also known as differential scattering coefficient or normalised radar cross-section (Alexander et al. 2010) measures the strength of radar signals reflected by a target on the ground. It is a normalised dimensionless measurement, that compares the strength observed to that expected from an area of one square meter (European Space Agency 2020). Since the normalised radar cross-section can vary by several orders of magnitude, it is converted to decibels (dB) as  $10 \times \log_{10} \sigma^\circ$  (Google 2021). The radiometric correction is necessary for the comparison of Sentinel-1 A and B images (Tricht and Dries 2019). It has been argued that the based incidence angle approximations made by  $\sigma^\circ$  fails to account for important properties of radar backscatter in regions with significant topographic variation (Small 2011). Since the rice fields studied are located in a relatively flat area (slopes below 15%), it is possible to use the simplifying assumptions of  $\sigma^\circ$  to perform the radiometric calibration.
- *Terrain correction* converts each image from slant range or ground range geometry into a map coordinate system to correct for geometric distortions, such as foreshortening, layover and shadow (Braun and Veci 2021; Erika Podest 2017). The orthorectification is performed onto the WGS84 ellipsoid corrected using the Shuttle Radar Topography Mission digital elevation data (SRTM 30).

The presence of speckle in SAR imagery occurs due to the existence of many scatterers within each resolution cell (Ferretti et al. 2007). This salt and pepper effect makes

it complex to interpret SAR images because it reduces the effectiveness of the image for further analysis, such as segmentation, classification and multi-temporal analysis (Dekker 1998; Ferretti et al. 2007; Choudhury et al. 2007).

On top of the preprocessing operations performed on the GEE Sentinel-1 collection, a morphological mean reducer filter was applied to each SAR image using a 3x3 square kernel to reduce the speckle noise. Morphological filters have proved effective for image smoothing and boundary detection (Bovik 2009). Instead of having a convolution operation between the kernel and the region of the image, morphological filters use a small shape or template known as a structuring element (Wirth 2004). As morphological filters are based on morphological operations, the result is based on the spatial pattern of the input data values rather than on the values themselves (Fisher et al. 2014). The main limitation of using a mean filter on decibel scaled data is that by averaging logarithms, it provides the geometric mean rather than the arithmetic mean of the intensity Since  $\log A + \log B = \log AB$ , and  $\frac{1}{2}\log(AB) = \log(AB)^{1/2}$  (Woodhouse 2006). In future research, it is recommended to apply the noise reducer filters on the linear scaled data before transforming it into dB.

In addition to the VV and VH polarisations, the ratio VH-VV was estimated for all the ascending and descending images and included in the analysis. The result was a multi-band raster for each type of product presented in Table 4.4, where each band represented a different S-1 acquisition date.

**Table 4.4** Sentinel-1 products

S-1 product	Description
VH_asc	VH polarisation Pass direction: ascending
VV_asc	VV polarisation Pass direction: ascending
VV_div_VH_asc	VV/VH Pass direction: ascending
VH_des	VH polarisation Pass direction: descending



S-1 product	Description
VV_des	VV polarisation Pass direction: descending
VV_div_VH_des	VV/VH Pass direction: descending

#### 4.2.3 Vegetation Indices

The number of bands from optical satellite sensors is increasing, and the bandwidth is getting narrower (Xue and Su 2017). It makes more complex the analysis and interpretation of the reflectance registered by sensors for agricultural applications. For this reason, the resulting optical Analysis Ready Data (ARD) was used to calculate a suite of vegetation indices sensitive to a variety of crop properties (See Table 4.5). VIs were selected instead of all the spectral bands as the first synthesise and enhance the information in multispectral imagery in a single parameter related to vegetation traits (Coppin et al. 2004; Palacios-Orueta et al. 2012; Hatfield and Prueger 2010; Semeraro et al. 2019). Particularly, the chosen indices have shown to be good indicators of two main categories of crop biophysical properties: 1) Photosynthetic Pigments (PP) and 2) Vegetation and soil Water Content (VWC). The type and Common vegetation indices used in agricultural applications

The reduction of photosynthetic pigments due to plant stress is reflected in an increase in the visible portion of the reflectance spectra (Carter et al. 1992; McCann et al. 2017). Also, stress affects the internal structure of plant cells such that the reflectance spectra in the near-IR portion of the reflectance spectra decreases (Carter 1991; Li et al. 2005). Both effects associated with the photosynthetic pigments could be used as early indicators of anomalous vegetation (Carter and Knapp 2001; Eitel et al. 2011; McCann et al. 2017).

Canopy and soil water content are of vital significance to applications in agriculture such as crop yield estimation and irrigation (Xu et al. 2020). The spectral behaviour of green vegetation in the 0.9-2.5  $\mu\text{m}$  region is dominated by liquid water absorption and weakly affected by absorption due to other biochemical components (Gao 1996). For example,

Cibula et al. (1990) found that the reflectances for certain types of vegetation in the same region of the electromagnetic spectrum increased as leaf water content decreased.

Due to its relatively limited spectral capabilities, not all VIs were calculated using the PlanetScope imagery (five in total, compared to 24 for Sentinel-2). Sentinel-2 has more than one NIR and red-edge channels; therefore, all possible combinations of these VIs were considered (e.g. Normalised Difference Vegetation Index was calculated for Sentinel-2 twice: The first using band 8 and the second using band 8a). Table 4.5 shows the vegetation indices calculated from S2 and PlanetScope imagery that will be considered in this research.

**Table 4.5** Multi-spectral vegetation indices evaluated.

Index	Type	Formula	Convention/bands	
			Sentinel-2	PlanetScope
NDVI	PP	$\frac{\rho_{nir} - \rho_{red}}{\rho_{nir} + \rho_{red}}$	NDVI_b8 ( $\rho_{833}, \rho_{665}$ )	NDVI ( $\rho_{820}, \rho_{630}$ )
			NDVI_b8A ( $\rho_{865}, \rho_{665}$ )	
SAVI <sup>a</sup>	PP	$\frac{(1+L)(\rho_{nir} - \rho_{red})}{\rho_{nir} + \rho_{red} + L}$	SAVI_b8 ( $\rho_{833}, \rho_{665}$ )	SAVI ( $\rho_{820}, \rho_{630}$ )
			SAVI_b8A ( $\rho_{865}, \rho_{665}$ )	
EVI <sup>b</sup>	PP	$G \frac{\rho_{nir} - \rho_{red}}{\rho_{nir} + C_1 \rho_{red} - C_2 \rho_{blue} + L}$	EVI_b8 ( $\rho_{833}, \rho_{665}$ )	EVI ( $\rho_{820}, \rho_{630}$ )
			EVI_b8A ( $\rho_{865}, \rho_{560}$ )	
CI <sub>green</sub>	PP	$\frac{\rho_{nir}}{\rho_{green}} - 1$	CIg_b8 ( $\rho_{833}, \rho_{560}$ )	CIg ( $\rho_{820}, \rho_{545}$ )
			CIg_b8A ( $\rho_{865}, \rho_{560}$ )	
CI <sub>Red-edge</sub>	PP	$\frac{\rho_{nir}}{\rho_{red-edge}} - 1$	CIre_b8_5 ( $\rho_{833}, \rho_{704}$ )	
			CIre_b8_6 ( $\rho_{833}, \rho_{740}$ )	
			CIre_b8_7 ( $\rho_{833}, \rho_{783}$ )	

Index	Type	Formula	Convention/bands	
			Sentinel-2	PlanetScope
gNDVI	PP	$\frac{\rho_{nir} - \rho_{green}}{\rho_{nir} + \rho_{green}}$	CIre_b8A_5 ( $\rho_{865}, \rho_{704}$ )	
			CIre_b8A_6 ( $\rho_{865}, \rho_{740}$ )	
			CIre_b8A_7 ( $\rho_{865}, \rho_{783}$ )	
			GNDVI_b8 ( $\rho_{833}, \rho_{560}$ )	GNDVI ( $\rho_{820}, \rho_{545}$ )
			GNDVI_b8A ( $\rho_{865}, \rho_{560}$ )	
NDVI <sub>Red-edge</sub>	PP	$\frac{\rho_{nir} - \rho_{red-edge}}{\rho_{nir} + \rho_{red-edge}}$	RENDVI_b8_5 ( $\rho_{833}, \rho_{704}$ )	
			RENDVI_b8_6 ( $\rho_{833}, \rho_{740}$ )	
			RENDVI_b8_7 ( $\rho_{833}, \rho_{783}$ )	
			RENDVI_b8A_5 ( $\rho_{865}, \rho_{704}$ )	

Index	Type	Formula	Convention/bands	
			Sentinel-2	PlanetScope
NDII	VWC	$\frac{\rho_{nir} - \rho_{swir}}{\rho_{nir} + \rho_{swir}}$	RENDVI_b8A_6 ( $\rho_{865}, \rho_{740}$ )	
			RENDVI_b8A_7 ( $\rho_{865}, \rho_{783}$ )	
			NDII_b8_11 ( $\rho_{833}, \rho_{1610}$ )	
			NDII_b8_12 ( $\rho_{833}, \rho_{2186}$ )	
			NDII_b8A_11 ( $\rho_{865}, \rho_{1610}$ )	
			NDII_b8A_12 ( $\rho_{865}, \rho_{2186}$ )	

<sup>a</sup> For SAVI, the canopy background adjustment constant L accounts for differential near-infrared extinction through the canopy.

<sup>b</sup> For EVI, L is a soil adjustment factor, G is a gain factor, set to 2.5, and C1 and C2 are coefficients that describe the use of the blue band to correct the red channel for aerosol scattering (Set to 6 and 7.5, respectively)

### 4.3 Ground data

The ground data collected comprises climate data, agronomic data recorded per field and the anomalies registered during fieldwork campaigns.

#### 4.3.1 Weather data

Rainfall is the major climatic factor that influences crop growth (Brouwer and Heibloem 1986). Even irrigated crops require precipitation to recharge the water bodies or reservoirs used for irrigation. Extreme rainfall events affect crop growth and therefore productivity. For example, drought causes crop water stress and intensive rainfall events may cause floods and waterlogged soils (Alidoost et al. 2019; Lobell and Gourdji 2012).

To control for variations caused by climate and prevailing weather, the historical rainfall records between 1980-2010 for the study area were used to identify a period that was not considered extremely wet or dry conditions. The monthly precipitation data was acquired from the meteorological station of the Airport Perales in Ibagué, located at the coordinates 4.4241 °N, 75.1394° W (See Fig. 3.1). This weather station is managed by the Institute of Hydrology, Meteorology and Environmental Studies (IDEAM from its Spanish initials). IDEAM is a Colombian public institution that produces information on the state and dynamics of natural resources and the environment (IDEAM 2010). The weather data was downloaded through the DHIME geoportal (Instituto de Hidrología Meteorología y Estudios Ambientales de Colombia (IDEAM) 2021), which provides access to the time series of hydrometeorological data in Colombia.

Despite the importance of the series of meteorological observations, they are frequently contaminated by errors in the observations, their transmission or due to changes in the instruments used. These alterations, called inhomogeneities, may mislead the conclusions derived from the study of the series as they mask the real changes of climate (Guijarro 2014). Different authors have developed homogenisation methodologies to eliminate or reduce as much as possible these alterations (Aguilar et al. 2003; Peterson et al. 1998).

In this research, we used the R package *Climatol* (Guijarro 2019) to perform homogenisation and infilling of the missing data in the rainfall time series. First, *Climatol* corrects the

heterogeneities in the series by applying iteratively the Standard Normal Homogeneity Test (SNHT) proposed by Alexandersson (1986) at every series cycle, until no series is found inhomogeneous. Then, the missing data is filled using the method proposed by Paulhus and Kohler (1952) by averaging neighboring values and dividing them by their respective average rainfall. Finally, a quality control was performed using the test proposed by McCuen (2017), in which the difference between the series average and the infilled series is lower than 10%. Fig. 4.10 shows the homogenised rainfall data derived from the "Aeropuerto Perales" weather station.

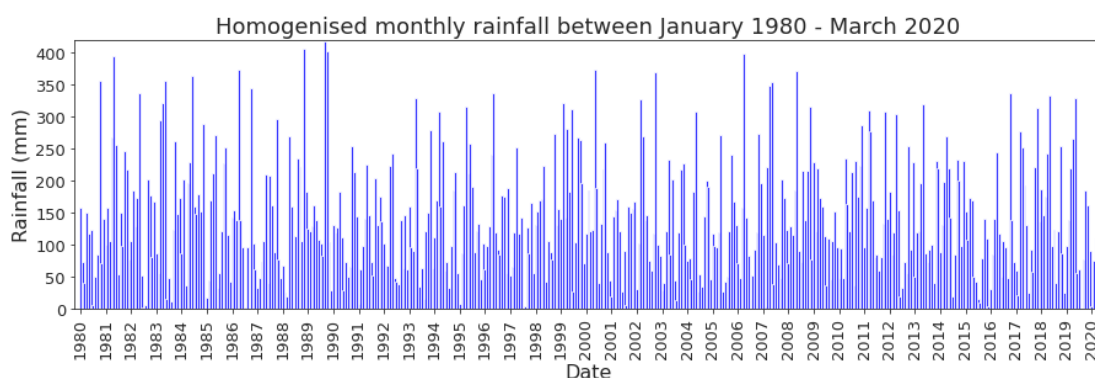


**Fig. 4.10** Homogenised rainfall data from the "Aeropuerto Perales" weather station

#### 4.3.2 Agronomic data

The agronomic data used in this study was collected in the Hacienda El Escobal farm, which is owned by the company Inversiones Agropecuarias Doima S.A.S. To solicit access to the data, these must be requested directly from the company <sup>1</sup>. A copy of the one-way data transfer agreement between Inversiones Agropecuarias Doima S.A.S. and Aberystwyth University can be found in Appendix A.

The agricultural features of the rice productive system used were recorded for two spatial units of analysis: Point and crop plot, as summarised in Table 4.6.

<sup>1</sup><https://elescobal.com/contactenos/>

**Table 4.6** Agronomic data available for the rice productive system

Spatial Unit	Variable	Frequency of measurement	Dates range
Plot	Agricultural plot boundaries	Once	–
Plot	Sowing date	Once per cycle	01/2018- 03/2020
Plot	Seedling emergence date	Once per cycle	01/2018- 03/2020
Plot	Crop variety	Once per cycle	01/2018- 03/2020
Plot	Harvest date	Once per cycle	01/2018- 03/2020
Plot	Average Yield	Once per cycle	01/2018- 03/2020
Plot	Wet grain yield per linear meter	Once per cycle	01/2018-03/2020
Point	Validation points	Once	06/2019 - 01/2020

- **Agricultural plot boundaries**, stored as polygonal shapefile layers. A negative 10 m buffer was applied over all of the plots to reduce edge effects and potential image alignment artefacts near the plot boundaries that remained after image co-registration. In addition, the buffered parcels with an area below 1000m<sup>2</sup> were excluded to avoid having a low number of pixels when performing the anomaly detection analysis.
- **Validation points** to assess the performance of the anomaly detection method. The set of validation points was selected using a 100 m regular grid over the study area between January 2018 and March 2020. A total of 36 reference points were recorded using the QField mobile app Version 1.2 on a mobile phone. At each location, we recorded the date, the presence/absence of visible anomalies, the type



of anomaly (when the observation was considered anomalous) and a photo of the location. The description of each validation point is presented in Appendix C. The identification of the presence/non-presence of anomalies in each point was performed visually by the farm agronomists, based on their expertise and crop knowledge.

- **Agronomic features** collected by the farm staff since 2016 are given per plot and include:

- *Harvest date*
- *Crop variety*
- *Sowing date* refers to the date when the seeds are planted
- *Seedling emergence date* refers to the date when at least 80% of the seedlings have emerged. The crop age is measured in days after the seedling emergence DAE.
- *Average yield* is given as average tons of paddy rice per hectare (t/ha). It is obtained by dividing the total rice weight per plot when entering the mill facilities.

- **Wet grain yield (t/ha) per linear meter.** The harvest is carried out with Massey Fergusson model 5650 combine harvesters. An impact plate Sensor and a moisture sensor Ag Leader brand are fitted to the combine. The rice grains are fed into the harvester's clean grain elevator, where a small amount enters the moisture sensor. An impact plate Sensor is mounted in the combine at the top of the elevator to measure the volume of the grain moving (Ag Leader 2019). The georeferenced yield and grain moisture data are recorded every second by a monitor mounted in the cab.

An inadequate calibration of the different sensors attached to the combine harvester can lead to erroneous crop yield maps. For example, the poor calibration of the yield monitor may lead to erroneously small yield values if the harvested swath width is less than the combine header width (Marchant et al. 2019). Also, an inaccurate definition of the position of the GPS antenna or errors introduced by the GPS may alter the location and the area over which the yield is averaged when building the yield surfaces (Marchant et al. 2019). The following calibration operations were performed to minimise the presence of errors associated with an inadequate calibration of the sensors (Ag Leader 2019):

- Enter the combine offsets (i.e., GPS antenna and combine head), and the headers data

- Enter the speed sources and calibrate the combine distance to guarantee that the distance registered by the monitor matches the actual length covered by the combine.
- Vibration calibration to disregard machine vibration in the grain flow measurement
- Temperature calibration to calculate moisture accurately
- Moisture calibration, which is done while harvesting. Three samples are extracted from one load of grain, and then each sample's moisture is measured using a handheld sampler. The samples' moisture values are averaged and entered into the monitor to correct the readings.
- Grain weight calibration. Initially, the combine is put to work empty, and then 3-4 calibration grain loads are collected and weighted. The weights obtained area entered into the monitor to correct any differences with the sensor estimation.

Data retrieved from yield monitors are inherently noisy and contain artefacts that have the potential to affect the analyses performed (Griffin 2010). For example, if the combine harvester stops, a flow of grain might still be recorded but the GPS signal indicates that an no area is being harvested. A similar situation occurs when the combine overlaps adjacent areas that were already harvested or in the headlands (Marchant et al. 2019). Previous research has identified the potential sources of artifacts in yield maps and have proposed different filters to to clean yield data (e.g., Marchant et al. 2019; Sudduth and Drummond 2007; Sun et al. 2013). To correct for possible artifacts in the yield data delivered in .csv format by the software Ag Leader, the following filters were applied:

- A Standard Deviation filter to remove yield data larger than a certain number of standard deviations from the plot mean (Sudduth and Drummond 2007). This filter has been proposed by other researches, using values of 2 (e.g., Thylen et al. 2000) and 3 (e.g., Ping and Dobermann 2005) standard deviations. In this research a number of 3 standard deviation was used to avoid excluding potentially low yield values due to anomalies in the field.
- A Standard Deviation filter to remove records with moisture values larger than a certain number of standard deviations from the plot mean. Similarly to yield, the number of standard deviations was set to 3 to avoid excluding anomalous moisture values due to the inner anomalies of the field.
- Exclusion of the yield data located within 10 m from the plot boundaries to

avoid including artifacts due to the headlands, as those are the areas used for turning around.

In future research it is recommended to include additional filters to remove other artifacts from the yield monitor data collected. For example, removing measurements that are extreme relative to their neighbours, such as the method proposed by Marchant et al. (2010) to detect local outliers.

The `gdal_grid` program from the GDAL translator library was used to build a raster surface out of the yield values. The raster was created using an inverse distance to a power algorithm, with a weighting power of 2 and a smoothing parameter of 0. Then, it was resampled to match the projection, extent and pixel size of the Sentinel-1 and Sentinel-2 products, using the bilinear interpolation method available in the RSGISLib Image Utilities Module. The yield values for all the plots were normalised between 0 and 1 to minimise the production variability among plots due to different management conditions.

## CHAPTER 5

### In-field Anomaly detection

*The analysis and results related to the methods described in Sections 5.2.2, 5.2.3, 5.2.4 , and 5.2.5 were already published in Castillo-Villamor et al. (2021b).*

#### 5.1 Introduction

The spatial variability of crop features is a natural condition of croplands. Agricultural fields are highly variable over space and time as a consequence of the interactions between different factors that include the biological life cycle of crops, management practices, and fluctuations in climate and soil properties (Basso et al. 2001; Shaw and Kelley 2005). Farmers establish tolerances for the variability of agronomic variables to identify anomalous regions that fall outside these tolerance ranges and implement corrective practices. Monitoring the within-field variability of different crop attributes is critical to identify anomalies at distinct points during the growing season (Chen et al. 2008) and implement corrective actions that sustainably optimise productivity.

Precision Agriculture (PA) technologies allow growers to treat the production field as the heterogeneous surface it is to support sustainable agriculture at a field level and across an ecosystem (Delgado et al. 2018). However, the adoption of PA has been slow (Joint Research Centre of the European Commission 2014), especially in developing countries. First, the high-tech nature of traditional PA technologies developed in advanced countries involves quantifying biophysical parameters to characterise the very particular conditions of an agricultural system. The reliance of these hard PA technologies on advanced sensor

systems often make these PA approaches site-specific and challenging to transfer to other agricultural systems (Delgado et al. 2019; Joint Research Centre of the European Commission 2014). However, rapid changes in the socio-economic of the developing world coupled with demands from specialised markets call for the development of softer PA approaches that are both scalable and transferable (Mondal and Basu 2009).

A more affordable approach to achieve PA goals is the implementation of agricultural practices based on Site-specific Management Zones (SSMZ; Gavioli et al. 2016; Koch et al. 2004; Méndez-Vázquez et al. 2019). SSMZ are conceived as areas with homogeneous properties known to impact crop yield (Ohana-Levi et al. 2019; Zhang et al. 2010). The definition of anomalous areas is closely related to the concept of SSMZ, as the delimitation of management zones implicitly allows for defining relatively homogeneous regions that show atypical characteristics compared to the behaviour of the majority of plants in a field. Delineation of management zones has been traditionally performed using cluster analysis techniques on agronomic variables that vary along the field, such as crop yield or soil chemical and physical properties (Gavioli et al. 2019). For example, Assis Silva et al. (2021) presented satisfactory results in outlining management zones for cocoa plantations based on the crop productivity and the apparent soil electrical conductivity using the fuzzy k-means algorithm. Also, Moral et al. (2010) measured soil physical variables from soil samples to generate potential management zones using principal component analysis and the Fuzzy C-means algorithm.

In-field anomalies can be caused by the presence of different levels of plant stress or species within the same area, different soil properties differences or management practices (Carter et al. 2008; McCann et al. 2017). Identifying these anomalies at distinct points during the growing season facilitates their management with site-specific practices to optimise agricultural productivity and profitability (Shaw and Kelley 2005) and reduce the overuse of supplies that can result in contamination of groundwater and surface water. However, the early detection of crop anomalies is difficult due to the complex correlations and spatial variability of nutrient concentration and soil properties (Chlingaryan et al. 2018). In addition, the sporadic nature of these anomalies and lack of clearly visible symptoms without close observation (Shaw and Kelley 2005) demand frequent and detailed ground inspection.

The temporal and spatial nature of satellite remote sensing has demonstrated great potential to monitor croplands variability over space and time (Basso et al. 2001; Battude et al. 2016; Chen et al. 2008). Spectral reflectance provided by multi-temporal optical

remotely sensed data has been used in different applications such as crop mapping (Dheeravath et al. 2010; Nguyen et al. 2012), crop phenology extraction (Palacios-Orueta et al. 2012), growth monitoring (Gao et al. 2017), or climate change impacts on croplands (Vrieling et al. 2008). Additionally, the use of SAR imagery is potentially significant for agricultural applications due to their ability to monitor under almost all weather conditions and the sensitivity of the microwave signal to the dielectric and geometrical properties of surfaces, including vegetation canopies (McNairn and Shang 2016). SAR products have been used for multiple agricultural studies, such as crop classification (e.g. Inglada et al. 2016; Denize et al. 2019; McNairn et al. 2009a) or phenology characterisation (e.g. Canisius et al. 2018; Mandal et al. 2020; McNairn et al. 2018).

Satellite EO has the potential to support the delimitation of in-field anomalous regions, thereby reducing frequent detailed scouting. However, satellite EO has mainly been used to detect anomalous zones at regional scales due to its relatively coarse spatial resolution, ignoring in-field variability. For example, medium spatial resolution satellite imagery, such as Landsat (30 m), have been used primarily to map land cover change within agricultural areas rather than monitoring anomalies within crops (e.g. Dutrieux et al. 2016). Also, studies that analyse temporal patterns of crop growth are typically implemented using higher frequency imagery, such as the Moderate Resolution Imaging Spectroradiometer (MODIS) and SPOT Vegetation (SPOT-VGT) data (e.g. Bolton and Friedl 2013; Eerens et al. 2014; Funk and Budde 2009; Lasaponara 2006; Rembold et al. 2019). Such studies sacrifice spatial resolution (MODIS:250 m, SPOT-VGT: 1000 m) and are therefore limited to making assessments at regional and global scales (Bolton and Friedl 2013; Eerens et al. 2014; Lasaponara 2006), rather than informing sub-plot farm management decisions. To reduce this gap between temporal and spatial resolution, authors such as Gao et al. (2017) and Hilker et al. (2009) have evaluated multi-sourced imagery integration. However, the level of consistency between multi-source reflectance inputs can affect the accuracy of the data fusion (Gao et al. 2017).

The pixel-based nature of the current approaches to detect in-field anomalous regions, mainly applied to aerial imagery and near-ground sensors, is sensitive to noise (producing a salt and pepper effect) and makes it difficult to account for contextual information (Chen et al. 2012). Such limitations have been resolved using kernel filters or moving windows that allow considering the pixels contextual information (Tewkesbury et al. 2015). For these approaches, often hard thresholds are applied to spectral data in a plot based on statistical metrics retrieved from the distribution of the data within a moving

window. For example, McCann et al. (2017) mapped local anomalies based on the number of Median Absolute Deviations (MADS) for a given pixel area surrounding a centre pixel. Although it proved to locate anomalies with accuracies up to 70%, the method accuracy varied between highly depending on the window size, growth stage and number of MADS chosen (McCann et al. 2017). The lack of standard criteria to choose the thresholds makes it necessary to tailor each set of thresholds to a particular crop location, growth stage or agricultural system.

Rather than using variable kernels to define anomalous pixels, object-based image analysis (OBIA) offers an opportunity to use the agricultural plot as a fixed spatial unit of analysis. It eliminates the window size variable and is especially relevant for in-field anomaly detection, given the fact that agricultural management decisions are usually made on a per-field basis (Belgiu and Csillik 2018; Long et al. 2013). Nevertheless, the object-based approach is only preferred if the objects of interest are significantly larger than the pixels of the imagery (Gilbertson and Niekerk 2017; Blaschke 2010). Thus, the potential to apply OBIA relies on the pixel size and the relative size of the agricultural field. This, therefore, excludes the use of coarse spatial resolution sensors such as MODIS and SPOT-VGT for in-field anomaly detection and restricts the use of Landsat when monitoring plots smaller than 4 ha, as there would not be a sufficient number of pixels to carry out a robust analysis.

Thresholding spectral data to determine whether pixels are anomalous is also challenging and current research is still limited. This is because each crop plot has its particular characteristics (e.g. soil properties, plant species, phenological stage, weather conditions, or management practices) that need to be accounted for independently. For example, the spectral behaviour of an area, flagged as anomalous within one field, might not be considered atypical in other crop plots, where most of the plants share this "unusual behaviour". An optimal threshold should consider the particular distribution within each field, as those properties are expected to be similar within the plot but different among fields. A thresholding method that considers these dynamics should be sensitive to the distribution of the pixel values contained within each plot and be transparent to any observer. Several studies have developed methods that use ground truth data to train the anomaly detection models or tune the value of the threshold point to produce higher accuracies (e.g. Liang et al. 2021; Kanjir et al. 2018; McCann et al. 2017; Mouret et al. 2021). Authors such as Rembold et al. (2019) have developed methods to flag as anomalous those pixels which value was larger than a specified number of standard deviations away from the mean. Nevertheless, these hard thresholding approaches have

limitations when assessing in-field crop anomalies. First, the distribution of each parcel is different, as it depends on features such as phenological stage, plant variety, irrigation routines, or planting date that vary over space and time. Thus, the number of standard deviations that separate anomalous from non-anomalous pixels will differ for each parcel depending on its particular conditions. In addition, the location of anomalous pixels in relation to the mean will vary on the quantity of anomalous and non-anomalous values within the distribution.

With constantly improving sensor technology, satellite EO can develop transferable, scalable, and low-cost PA solutions to detect in-field crop anomalies and implement corrective actions that maximise the production along the crop cycle. It requires methods that automatically tune the threshold values for each crop plot, considering its particular biophysical conditions.

Evidence from other EO application areas have successfully used automatic, histogram-based thresholding techniques that do not require training. For instance, Thomas et al. (2018) successfully deployed this approach to detect changes in mangrove forest extent with spectral change being defined where there is a change in the distribution of data within a segmented object. This approach has potential for use in crop anomaly detection but has yet to be explored.

The increased temporal and spatial resolutions of Sentinel-2 and PlanetScope imagery provide a promising direction for monitoring within crop anomalies from an object-based perspective, considering the crop plot as the spatial unit of analysis. The object-based approach is essential in crop monitoring and for decision-makers, given the fact that management decisions are generally made at the level of agricultural parcels (Long et al. 2013; Belgiu and Csillik 2018). Currently, the applications of satellite SAR in agriculture are primarily focused on studies at the field level (Bhogapurapu et al. 2021). However, the higher revisit frequency and spatial resolution of Sentinel-1 (12-day repeat cycle) over other SAR missions such as ERS-1/2 and ENVISAT ASAR might offer new opportunities for in-field monitoring, considering their ability to see through clouds (Mandal et al. 2020) and the sensitivity to the dielectric and geometrical properties of the surfaces (McNairn and Shang 2016).

This chapter presents a novel approach for detecting in-field crop anomalies over space and time using optical (Sentinel-2 and PlanetScope) and SAR (Sentinel-1) imagery. The Earth Observation-based Anomaly Detection (EOAD) approach implements a



simple histogram analysis technique for delineating potentially anomalous pixels and draws comparisons with field observations. First, the chapter describes the methods implemented to 1) detect in-field anomalies; and 2) assess the accuracy and capacity of the method to discriminate between anomalous and non-anomalous areas. Then, it presents the results of the implementation of the EOAD over rice plots in the Ibagué Plateau, Colombia and the discussion around those results. It finalises presenting the main conclusions drawn from the analysis performed. The analysis and results related to the methods described in Sections 5.2.2, 5.2.3, 5.2.4 , and 5.2.5 were already published in Castillo-Villamor et al. (2021b)

## 5.2 Methods

The Earth Observation-based Anomaly Detection (EOAD) approach implements a simple histogram analysis technique for delineating potentially anomalous pixels using Sentinel-2, PlanetScope and Sentinel-1 products. The technique was tested over rice plots in the Ibagué Plateau, Colombia, comparing field observations of anomalous areas and final yield data.

The method derives the histogram of the pixels values within a crop parcel and defines dynamic thresholds to classify them into three classes: high-anomalous values, low-values and non-anomalous values. The thresholds for the pixels within each plot are defined by removing the atypical values in increments from the tails towards the median until the distribution is normal. The distribution normality is assessed based upon measures of skewness and kurtosis for each iteration.

The EOAD method was applied to the individual rice plots at each date for VIs, and SAR products available. The accuracy of the technique was assessed using a confusion matrix to compare the predicted anomalies with a set of validation points collected on four dates in January 2020. Then, the mean values of the anomalous pixels per plot were compared with the mean values of the non-anomalous pixels per plot at different growth stages to identify particular points in the growing cycle that may be better suited to discriminate anomalous pixels.

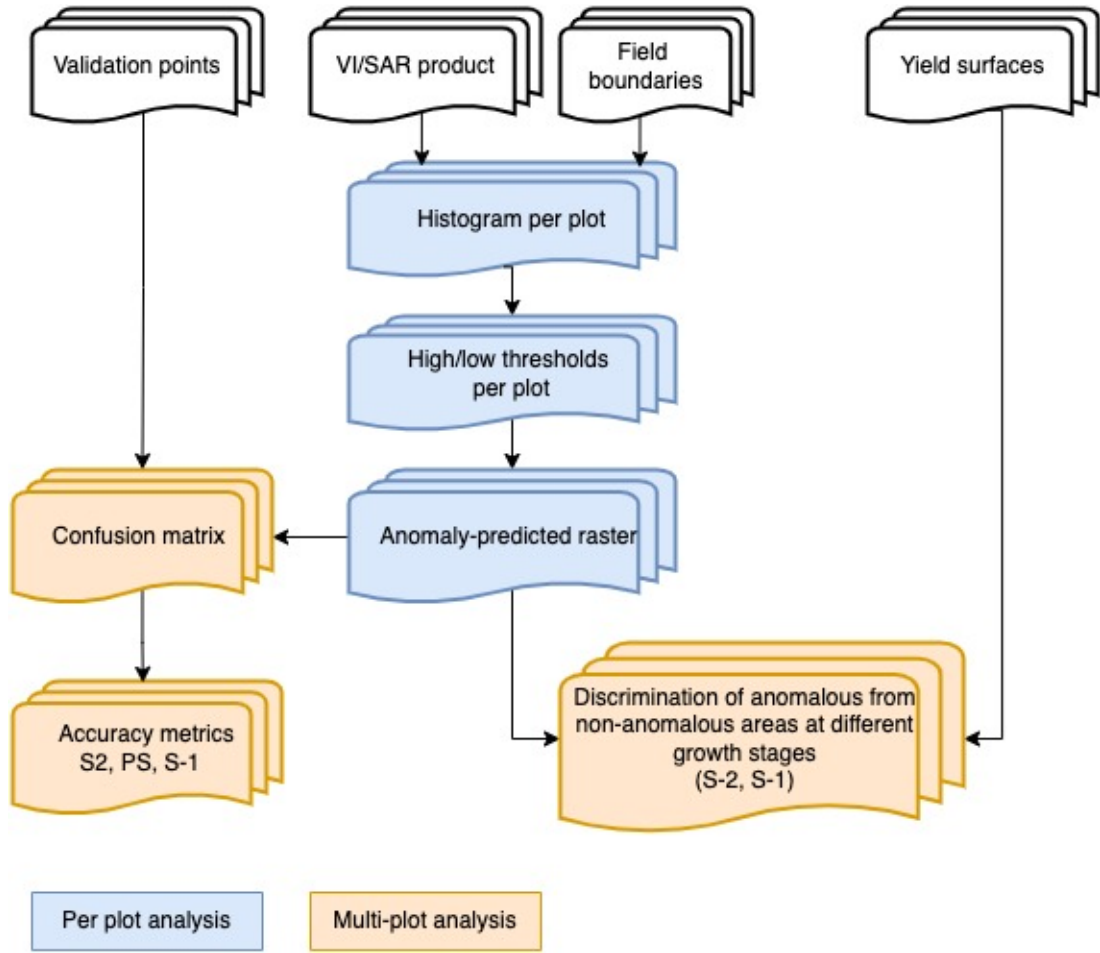


**Fig. 5.1** Flowchart describing the processes involved in the Earth EOAD method and assessment.

### 5.2.1 Datasets Description

This research used 47 Sentinel-2, 15 PlanetScope, 39 Sentinel-1 GRD ascending and 56 Sentinel-1 GRD descending images acquired over 2018-2020. Fig. 4.1 shows graphically the availability of both Optical and SAR images over time. As described in Section 4.2.1, optical images were prepared to generate the VIs presented in Table 4.5. The Ground Range Detected (GRD) dual-polarized SAR images (vertical-vertical VV, and vertical-horizontal VH polarisations) acquired by the Sentinel-1 satellites in interferometric wide swath mode (IW) were retrieved and pre-processed for speckle using the Google Earth Engine Code Editor as described in Section 4.2.2. Both VIs and SAR polarisation products were used as input for the EOAD method to assess its performance and potential impact on the crop yield.

The ground data used include:

- **Historical monthly rainfall data** retrieved from the Aeropuerto Perales station during the period 1980-2020.
- **Crop field boundaries** in shapefile format.
- **Crop features per field**
  - Sowing date
  - Seedling emergence date
  - Harvest date
  - Crop variety
  - Average yield
- **Validation points** to assess the performance of the EOAD technique to identify true anomalies observed in the field. The field visit was carried out between June and July 2019. It comprised multiple knowledge exchange sessions to explain the agricultural system's functioning, train the farm staff to collect georeferenced data and define the protocols to register the validation points. Pictures of the rice production system, management practices and activities carried out during the field visit are presented in Appendix B. Due to time and resources limitations, the validation points could not be collected during the field visit. Instead, they were registered by the farm staff between January 2018 and March 2020.

The set of validation points was selected using a 100 m regular grid over the study area between January 2018 and March 2020. The grid was designed in the software QGIS Version 3.4 and later synchronised with the QField mobile app Version 1.2, previously installed on a mobile phone. The grid was used to identify the location of the points to visit. The agronomist assessed a spatial footprint of 10 x 10 metres at each of the 36 observation points visited and visually identified atypical areas in the field. At each location, we recorded the date, the presence/absence of visible anomalies, the type of anomaly (when the observation was considered anomalous) and a photo of the location. The identification of the presence/non-presence of anomalies in each point was performed visually by the farm agronomists, based on their expertise and crop knowledge.

In order to collect representative validation points while generating a minimum disruption in the activities carried out by the farm staff, the sampling strategy considered not only the grid sampling design but also that the chosen plots fulfilled two main requirements:

- The plot should be in a productive status for the date of the image acquisition. Finally, the chosen plot had to be younger than 90 DAE, when it was still possible to implement corrective actions and avoid mechanical damage to the plants, which would negatively impact the harvest operation's efficiency.
- The plot should be located in a farm area scheduled to be visited as part of the farm agricultural management plan.

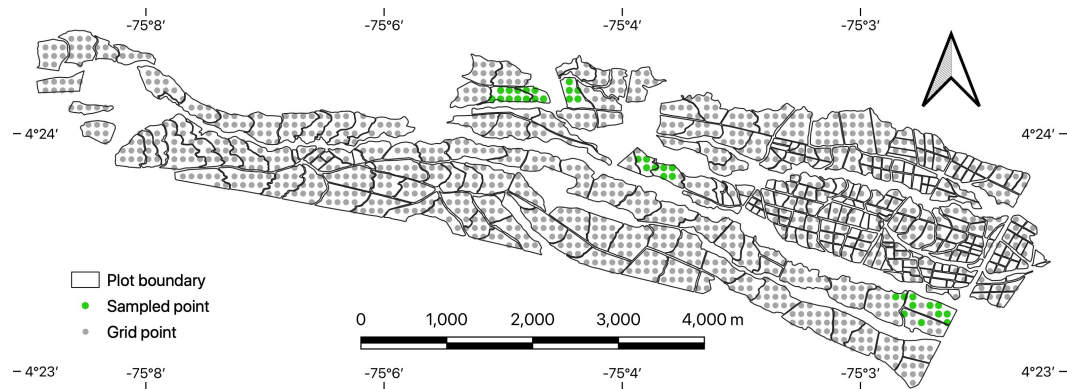


**Fig. 5.2** Distribution of sample points used for validation

- **Wet grain yield (t/ha) surface** derived from the wet grain yield per linear meter recorded by the rice combine harvester. The calibrations performed to the yield monitor and the pre-processing operations applied to build the yield surface are described in section 4.3.2.

### 5.2.2 The Earth Observation-based Anomaly Detection (EOAD) Technique

The technique is based on thresholding the histogram of EO data (i.e. VI values and SAR products) within a crop plot which boundaries are known. The python algorithm to implement the EOAD method can be found in a GitHub repository available at Castillo-Villamor et al. (2021a), under a GNU General Public License v3.0. There are two critical assumptions that EOAD is based on: i) VI values for non-anomalous pixels will be normally distributed in a crop plot, and ii) pixel values that deviate from this normal distribution are considered anomalous (i.e. significantly high or significantly low values).

The normal distribution of a homogeneous crop area was validated by assessing the pixel value distribution of homogeneous regions in the field. The normality test was applied over the pixels located within two areas identified as homogeneous in plant density,

height, health and nutrition characteristics. The field identification of these areas was performed in companion with local rice experts.

The thresholding process used by EOAD is illustrated in Fig. 5.3. Here, pixels are excluded by iteratively removing the tail bins of the histogram associated with each plot until normality is achieved. The degree of normality is based on measures of kurtosis and skewness, where the iteration that produced the lowest kurtosis and skewness represents the most normal distribution. As the second assumption is that the pixel values that deviate from the normal distribution are considered anomalous, most of the values representing non-anomalous pixels will be close to the median, and those representing anomalous pixels will be far from it. Thus, the upper and lower bin values are extracted, representing corresponding thresholds for determining whether a pixel is considered high-anomalous or low-anomalous, the rest remaining as non-anomalous. The Histogram Bin Width (BW) is defined independently for each plot following Freedman and Diaconis (1981), using the interquartile range (IQR), where  $n$  is the number of available values (See Eq. 5.1). A similar analysis was developed by Thomas et al. (2018) to assess mangrove extent change, adequately detecting changes in image classes (>90%), irrespective of the geographic location of the land cover class.

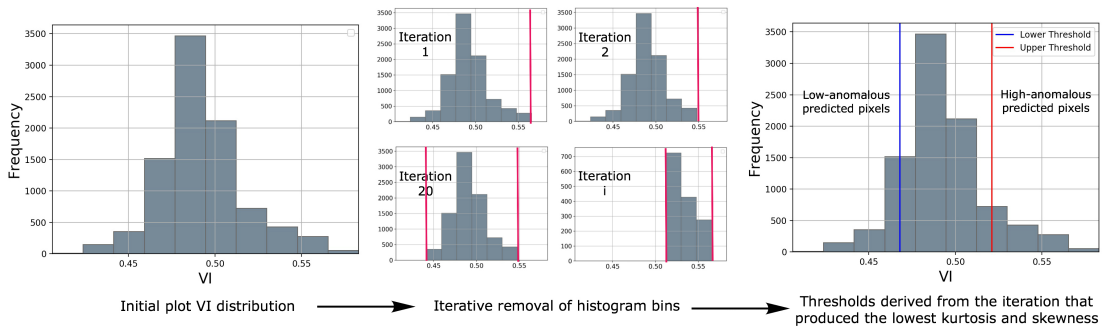


**Fig. 5.3** Extraction of thresholds using the histogram analysis approach

$$BW = (2 \times IQR \times n^{-1/3}) \quad (5.1)$$

The thresholding method proposed hereby aims to overcome the limitations observed in previous hard-thresholding anomaly-detection techniques by establishing dynamic thresholds, sensitive to the statistics of each parcel pixel distribution, independently of the variability that may occur between parcels as a consequence of different management practices.

A worked example of how the EOAD technique automatically splits the plot pixels' histogram into high-anomalous, low-anomalous and non-anomalous pixels is given in Fig. 5.4. The minimum and maximum thresholds were identified as the centre value of the furthest left bin and the centre value of the furthest right bin that remained in the iteration that produced the most normal distribution. Thus, a different pair of thresholds is retrieved from each parcel, based on the particular features of its pixel distribution.

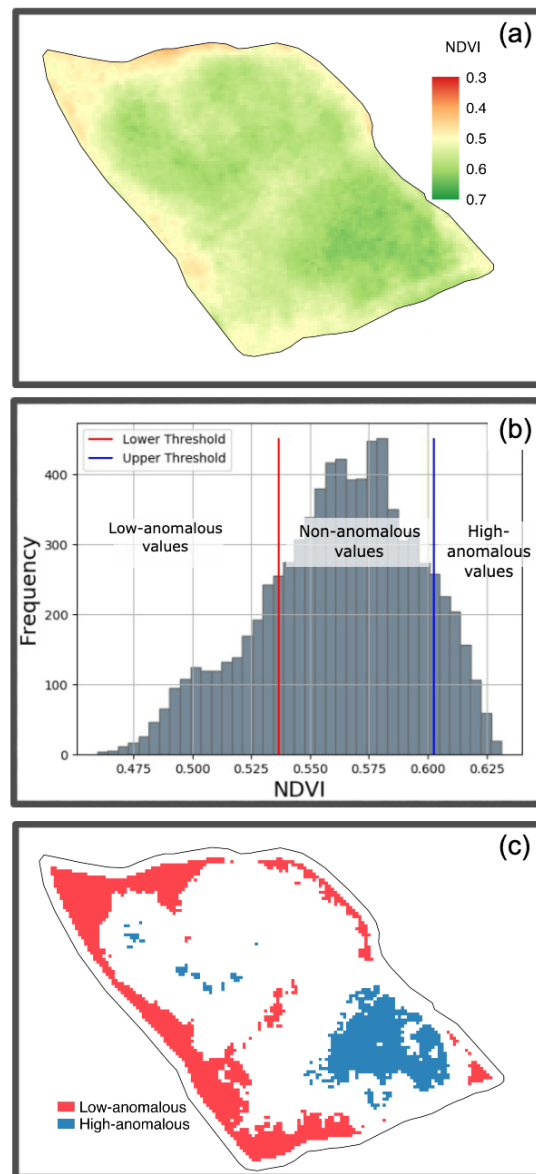


**Fig. 5.4** Example of the histogram analysis performed over one rice field. (a) The NDVI raster, (b) thresholds that produced the lowest kurtosis and skewness, (c) anomaly-predicted surface.

### 5.2.3 Accuracy Assessment

The EOAD was applied to all crop plots at the study site using the VIs outlined in Table 4.5 and the SAR products presented in Table 4.4. Its performance was validated against field observations to determine which VIs or SAR products could map anomalies more accurately.

The method validation is based upon the fundamental assumption that the validity of the anomalies in the productive system is less than 8 days. This is the approximate time that takes to the anomalous areas detected in the field to reach a condition similar to the majority of the field. For example, after a water shortage is detected at any area in the field, the irrigation is fixed within the next 4 days after the anomaly is detected. However, it takes around 5 days for the affected area to recover from the stress caused by the lack of water and to have a condition similar to that of the rest of the rice field that does not present anomalies. The presence of anomalous areas associated with a nutrient deficiency or poor soil health can remain along the crop cycle, as they might not be fully fixed after implementing corrective practices. However, to assess the method's accuracy in detecting anomalies, the anomalies identified visually in the field are assumed to last for eight days. This assumption is made to avoid marking as true anomalies those regions that are no longer atypical because the problem was already corrected (e.g., dry areas where water supply was already fixed).

For the studied rice plots, the 36 reference points were found in four (4) S2 and four (4) PlanetScope cloud/shadow-free images within  $\pm 8$  days, resulting in 78 and 72 observations, respectively. Each image was checked visually to assess the presence of clouds and shadows. For S1 imagery, the 36 reference points matched 2 ascending and 2 descending images, resulting in 64 and 42 observations, respectively.

For each observation, the EO-derived anomaly status was compared against the anomaly status recorded in the field using a confusion matrix, thereby summarising the number of true positives (TP), false positives (FP), false negatives (FN) and true negatives (TN) cases predicted by the method (See Table 5.1). TP values correspond to true anomalous points identified correctly as anomalous by the algorithm; FP correspond to the number of non-anomalous points classified incorrectly as anomalous; FN is the number of the anomalous points incorrectly identified as non-anomalous; and TN represents the number of the non-anomalous points correctly classified as non-anomalous. Table 5.1 presents

the structure of the confusion matrix. This approach was chosen as it has been used to compare species distribution model outputs and field observations when the model gives a binary result, such as species presence or absence, or pest risk models and maps (USDA Forest Service 2015).

		Validation data set	
		Anomalous	Non- anomalous
<b>AOAD prediction</b>	Anomalous (True)	TP	FP
	Non- anomalous (False)	FN	TN

**Table 5.1** Confusion matrix used to evaluate the anomaly detection method accuracy.

Two standard metrics were derived from the confusion matrix: The overall accuracy and the True Skill statistic (TSS). The overall accuracy is the proportion of correctly predicted sites and therefore is commonly quoted as an indicator of how well the methods perform. It is defined as the ratio between the correctly classified points to the total number of points (Sokolova et al. 2006; Tharwat 2021). However, this measure has been criticised due to its dependence on prevalence that introduces statistical artefacts to the accuracy estimates, especially when the dataset is imbalanced (Allouche et al. 2006; Gonzalez-Abril et al. 2014).

The most popular measure to correct the overall accuracy of the model by the accuracy expected to occur by chance is Cohen's kappa (Cohen 1960; Segurado and Araújo 2004). However, despite its wide use, authors such as Segurado and Araújo (2004) and Allouche et al. (2006) found that this metric is dependent on prevalence, introducing bias and statistical artefacts. Instead, the TSS was used, as it corrects for the dependence mentioned above while still keeping all the advantages of Kappa when predictions are expressed as presence-absence maps (Allouche et al. 2006). TSS, also known as the Hanssen-Kuipers discriminant, compares the number of correct predictions minus those attributable to random guessing to a hypothetical set of perfect predictions. The TSS is used to correct the model's overall accuracy by the accuracy expected to occur by chance (Allouche et al. 2006).

Similarly to Kappa, TSS ranges from -1 to +1, where +1 indicates perfect agreement between predictions and observations; values of 0 or less indicate agreement no better than random (Allouche et al. 2006; Zhang et al. 2015a). The same ranges proposed Landis and Koch 1977 to interpret Kappa were used by to interpret the strength of agreement of TSS statistics (See Table 5.3).



Metric	Formula
Overall accuracy	$\frac{TP+TN}{TP+TN+FP+FN}$
TSS	$\frac{(TP \times TN) - (FP \times FN)}{(TP+FN) \times (FP+TN)}$

**Table 5.2** Performance metrics derived from the confusion matrix

TSS statistic	Strength of Agreement
<0.00	Poor
0.0-0.2	Slight
0.21-0.4	Fair
0.41-0.6	Moderate
0.61-0.8	Substantial
0.81-1.0	Almost perfect

**Table 5.3** Thresholds used to interpret the strength of agreement of TSS statistics

#### 5.2.4 Typical Rainfall Period

To control for variations caused by climate and prevailing weather, satellite data analysed in the onward sections were acquired during a period that was not considered to be extremely wet or dry using the Standardised Precipitation Index (McKee et al. 1993). The Standardised Precipitation Index (SPI) was calculated for each month in the period comprised between January 2016 and March 2020 using historical rainfall records from the meteorological station of the Perales Airport. The SPI is used to determine the time-lapse to assess the impact of the predicted anomalies over the yield and test if particular points in the growing cycle may be better suited to discriminate anomalous pixels at different phenological stages. The aim is to avoid biases caused by extreme VIs and SAR values due to very humid or dry weather conditions.

The SPI is based on the probability of precipitation for any time scale, which is transformed into a normalised index. It fits the historic long-term precipitation record to a probability distribution and transforms it into a normal distribution so that the mean SPI

for the location and desired period is zero (World Meteorological Organization 2012). Positive monthly SPI values indicate that precipitation is greater than the median for that specific month, and negative values indicate that it is lower than median precipitation (Edwards and McKee 1997).

In this study, the historical monthly precipitation data between 1980-2020 from the meteorological station of the Airport Perales in Ibagué was used to estimate the monthly SPI values. Fig. 5.5 shows the location of the weather station in relation to the study area. Monthly rainfall during the period for which there are available S2 and S1 images (January 2018 and March 2020) is compared to what is typical for the respective month, based on the historical records. The typical rainfall period was defined as the set of consecutive months that showed SPI values between -1.5 and 1.5. Hereafter, we will refer to this as the typical rainfall period.

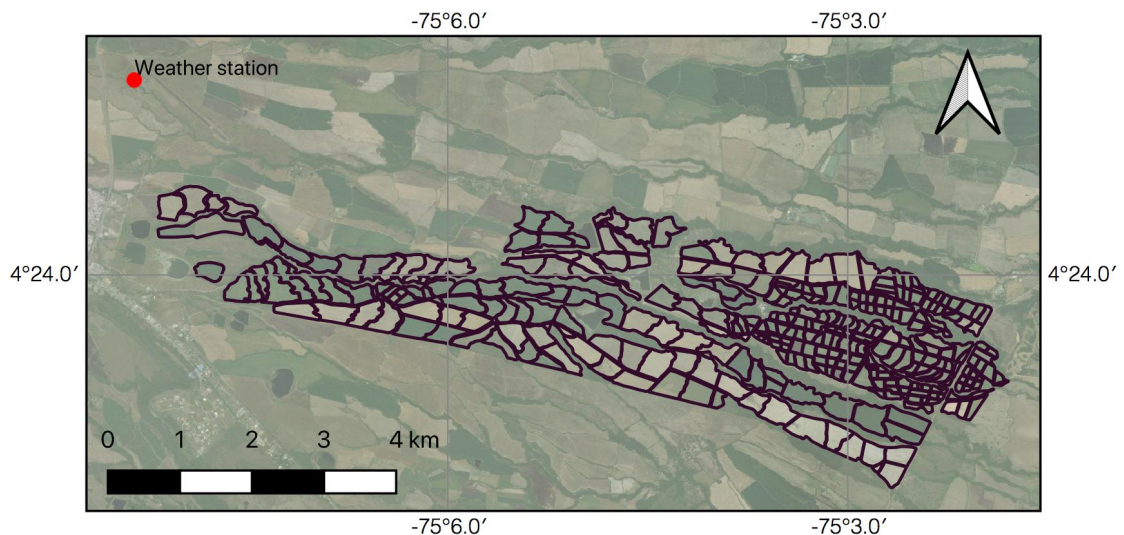


**Fig. 5.5** Location of the Perales Airport weather station in relation to the study area

#### 5.2.5 Discrimination of Anomalous from Non-anomalous Areas at Different Growth Stages

Particular points in the growing cycle may be better suited to discriminate anomalous pixels. To test this, the average value of the anomalous and non-anomalous pixels per plot were compared at each growth stage using an independent two-sample t-test or a Welch-Satterthwaite test when the samples did not have similar variance (Student 1908). The comparisons were made using the S2 and S1 products derived from images acquired during the typical rainfall period.

The Student's t-test for two samples is used to test if the means of a measurement variable are different in two groups (McDonald 2014). The original t-test has four main assumptions: 1) The observations within each group are normally distributed; 2) the observations in the samples are independent of each other; 3) data are collected from a random sample from the population of interest, and 4) equal variances in the two groups (homoscedasticity). However, when the variances of the two groups are not equal, the Welch-Satterthwaite test (Welch 1947) can be implemented instead.

In this research, the Student's t-test is used to determine if the average value of the anomalous pixels in a plot is different from the average value of the non-anomalous pixels in a field. The original Student's t-test was used when the two datasets variances were equal and the Welch-Satterthwaite test when the condition of homoscedasticity was not met. Variance homogeneity was defined using Levene's test (Levene 1960). Each individual in the anomalous sample represented the average value of the anomalous pixels in a plot. Similarly, each individual in the non-anomalous sample represented the average value of the non-anomalous pixels in a plot. Only those plots with a percentage of anomalous pixels greater than 0.001% were considered in this analysis to guarantee a minimum number of pixels to average for each category (i.e. anomalous and non-anomalous). An independent test was performed at each phenological stage using all the VIs and SAR anomaly products. The null hypothesis  $H_0$  is tested against the alternative hypothesis  $H_1$  as follows:

$H_0$ : There is no difference between the average value of anomalous pixels per plot and the average value of non-anomalous pixels per plot.

$H_1$ : There is a difference between the average value of anomalous pixels per plot and the average value of non-anomalous pixels per plot.

### 5.3 Results

A worked example of the implementation of the EOAD technique over Sentinel-1 products and Sentinel-2/PlanetScope NDVI for a rice field at the tillering stage (BBCH 21 - BBCH 30) is presented in Fig. 5.6. The optical images were acquired with one day difference (i.e., PlanetScope at 28 DAE and Sentinel-2 at 29 DAE), which explains the similarity of the NDVI distributions. Despite their likeness, the PlanetScope NDVI values

tended to be larger than Sentinel-2, which produced higher thresholds for PlanetScope. These discrepancies seem to be caused by differences in the spectral sensitivity of the red channels rather than due to changes in the crop condition. The smaller pixel size of PlanetScope showed an improved capability to capture smaller atypical areas. However, PlanetScope NDVI seemed more susceptible to saturate, which is reflected in fewer atypical areas highlighted above the higher threshold. Decibel scaled radar intensity shows a more normal distribution than the optical products. Fewer anomalous pixels are detected using decibel scaled VH, which seems to be caused by two main reasons:

- The lower spatial resolution of S1 does not capture the spatial variability of the crop condition in areas smaller than 400  $m^2$  properly.
- The log transformation of radar intensity makes data approximately conform to normality and reduces data variability, especially in datasets that include outlying observations. (Feng et al. 2014).

Overall, EOAD, applied to various VIs, detected the presence of anomalies within rice crop plots with accuracies ranging between 58% and 80%. In contrast, the accuracy obtained with the Sentinel-1 products had a maximum overall accuracy of 60%.

### 5.3.1 Accuracy assessment

Among the 36 validation points visited in the field, 16 were defined as anomalous in relation with the majority of the plot. Most of these anomalies ( $\approx 87\%$ ) were associated to two main factors: 1) water shortages and 2) lower plant density. Fig. 5.7 shows the types of anomalies identified in the field. In terms of growth, 75% of field-observed anomalies were registered between 33 and 44 DAE, during the tillering stage. The remaining 25% anomalous points were identified during the booting stage (70 days). All areas identified as having a water shortage also presented lower plant development and in some cases lower plant density than the majority of the plot.

Overall, those VIs that showed the highest accuracies ( $>70\%$ ), in terms of correctly identifying anomalous points in a plot, were related to normalised difference indices that use NIR bands, i.e. NDVI, SAVI and gNDVI. The complete accuracy statistics are presented in Fig. 5.8. Furthermore, the accuracies of these NIR-based VIs seemed

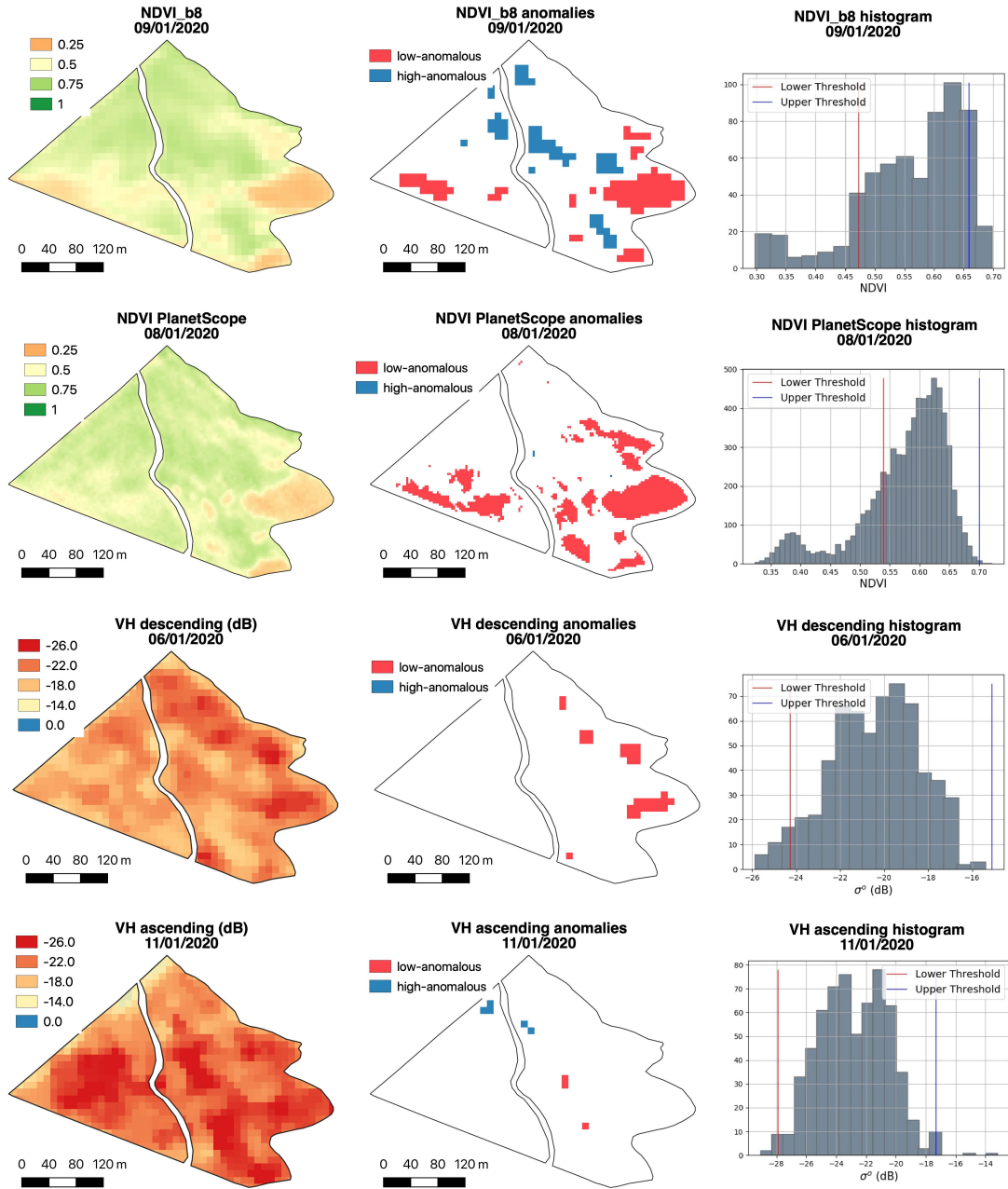


**Fig. 5.6** Examples of anomaly surfaces built after applying the EOAD technique over Sentinel-2/PlanetScope NDVI and Sentinel-1 VH products for a rice plot at the tillering stage (BBCH 21 - BBCH 30). The field's emergence date is 11/12/2019

to remain consistent between Sentinel-2 and PlanetScope, demonstrating their relative robustness to represent anomalous areas in a crop plot accurately. For example, there is no significant difference in the accuracy obtained using the NDVI when calculated by either Sentinel-2 band 8 (10 m), Sentinel-2 band 8a (20 m) or PlanetScope (3 m), suggesting that spatial scale is not a controlling factor, at least for this particular VI.

For Sentinel-2, the indices SAVI\_b8, gNDVI\_b8, reNDVI\_b8\_5 and NDVI\_b8 showed

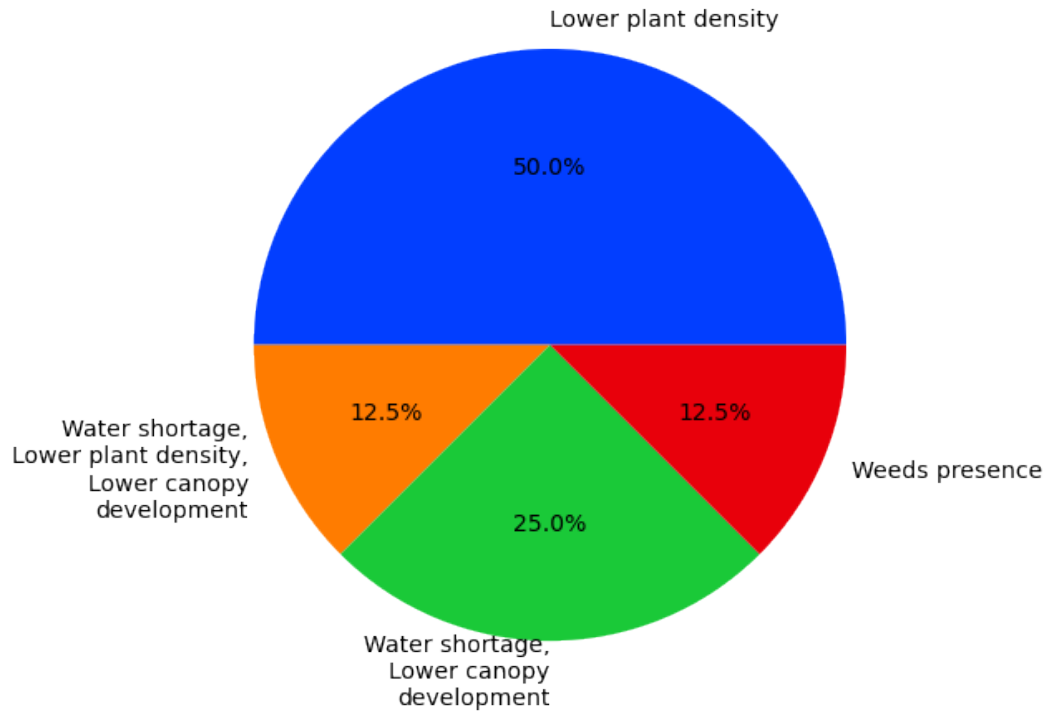


**Fig. 5.7** Types of anomalies identified in the rice fields

overall accuracies above 70% and TSS greater than 0.5. Interestingly, those Sentinel-2 VIs that employed the red-edge channels ( $n = 3$ ) only obtained accuracies above 70% when the red-edge band 5 was used. In fact, the lowest accuracies recorded were obtained with VIs that included the red-edge bands 6 and 7. Similarly, those VIs centred on chlorophyll (i.e.  $CI_{green}$  and  $CI_{Red-edge}$ ) also performed poorly ( $<60\%$ ). For PlanetScope, on the other hand, the NDVI, EVI and SAVI showed the highest overall accuracies and TSS. For all these indices, recorded true-positives were exclusively related to low-anomalies. As such, analysis from this point only relates to detected low-anomalies.

Fig. 5.9 shows the accuracy metrics obtained for SAR products. None of the SAR polarisations produced accuracies above 70% or TSS above 0.4. The overall accuracy was similar for the SAR products assessed, still, the accuracy obtained with the VH polarisation tended to be larger than VV in both ascending and descending passes. The TSS values showed larger discrepancies among polarisations and orbits. Descending VH imagery evidenced a larger TSS score than the other SAR products while negative scores were obtained for the VH/VV polarisation ratio products, indicating that the number of observations wrongly classified was larger than the number of observations correctly classified.

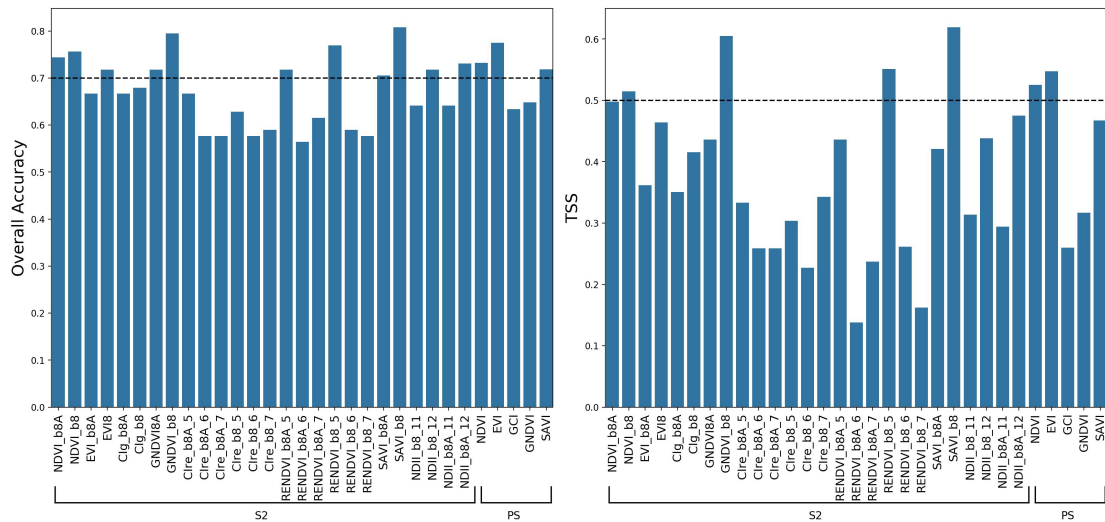


**Fig. 5.8** Anomaly detection accuracy metrics obtained with the optical vegetation indices

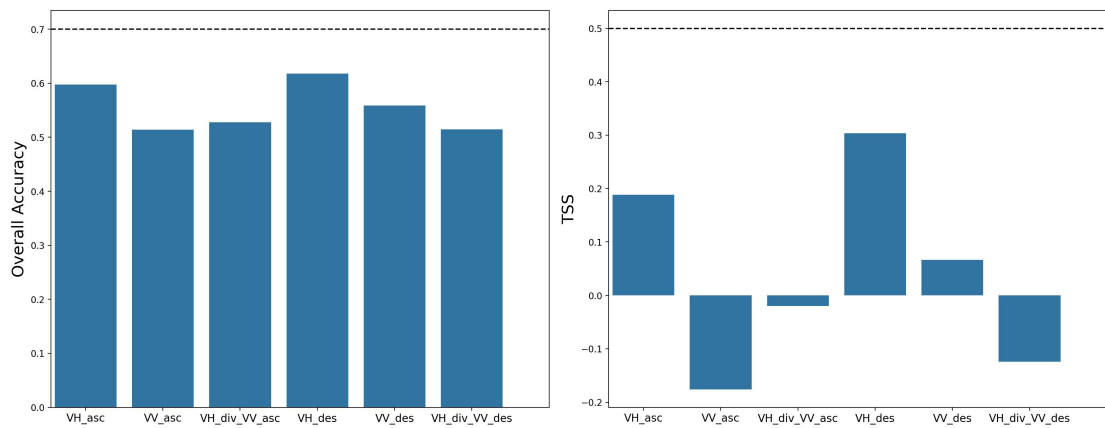


**Fig. 5.9** Anomaly detection accuracy metrics obtained with the Sentinel-1 products

The accuracy of the EOAD to effectively detect different types of anomalies varied across the VIs and SAR products analysed. Table 5.4 presents the number of field observations correctly marked as anomalous per type of anomaly identified in the field. Over 62% percent of the anomalies identified in the ground were related with lower plant density (). This relation is also reflected in the number of true-positives detected by the EOAD, as most of them are associated to . The NDVI\_b8, the SAVI\_b8 and the reNDVI\_b8A\_5 detected the highest number of true-positives associated exclusively to , however, other normalised difference indices such as the NDVI\_b8A showed slightly lower results. Overall, the areas which experienced lower plant density accounted for more than 75% of the true positives detected with the EOAD using the VIs that produced the highest accuracies (i.e SAVI\_b8A, gNDVI\_b8 and reNDVI\_b8\_5). Water shortages were the type of anomalies with the second highest number of correctly classified records. Those areas affected by water shortage also experienced lower canopy development () and in some cases lower plant density as result of the water stress. In particular, the NDVI\_b8A

detected correctly the highest number of anomalies associated to water shortage WS using optical imagery. Due to the low accuracies obtained using the SAR products, the number of true-positive anomalies was also lower than VIs. However, despite the water shortage areas represented only 37.5% of the total anomalies identified, over 50% of the true-positives detected using the SAR products corresponded to this type of problem (ie. WS+LCD an WS+LPD+LCD). The weeds presence (WP) was the least common type of anomaly found in the field, which was also reflected in the lower number of true-positives registered.

**Table 5.4** Correctly predicted anomalies per type of problem identified in the field using PS, S1 and S2 imagery

Sensor	VI/Product	LPD	WS + LCD	WS + LPD + LCD	WP
S2	CIg_b8	9	4	4	0
	CIg_b8A	9	3	3	4
	CIre_b8A_5	12	5	3	2
	CIre_b8A_6	4	0	1	2
	CIre_b8A_7	4	2	1	0
	CIre_b8_5	9	3	0	2
	CIre_b8_6	6	0	0	2
	CIre_b8_7	4	1	0	2
	EVI_b8	14	3	2	2
	EVI_b8A	10	3	3	2
	NDII_b8A_11	11	4	3	0
	NDII_b8A_12	12	5	4	2
	NDII_b8_11	10	3	1	2
	NDII_b8_12	12	7	3	2
	NDVI_b8	16	7	4	2
S2	NDVI_b8A	17	9	4	0
	SAVI_b8	17	3	4	4
	SAVI_b8A	13	3	4	2
	gNDVI_b8	14	6	4	2
	gNDVI_b8A	14	7	4	2
	reNDVI_b8A_5	16	5	4	2
	reNDVI_b8A_6	6	0	1	4
	reNDVI_b8A_7	10	7	0	0



Sensor	VI/Product	LPD	WS + LCD	WS + LPD + LCD	WP
	reNDVI_b8_5	13	6	4	2
	reNDVI_b8_6	7	2	0	0
	reNDVI_b8_7	9	2	0	2
PS	EVI	12	5	4	2
	GCI	8	5	4	1
	GNDVI	10	5	4	2
	NDVI	15	6	4	1
	SAVI	13	5	4	2
S1	VH_asc	12	7	3	4
	VH_des	12	5	2	2
	VV_asc	12	7	3	4
	VV_des	12	5	2	2
	VH_div_VV_asc	12	7	3	4
	VH_div_VV_des	12	5	2	2

LPD: Lower plant density  
WS: Water shortage  
LCD: lower canopy development  
WP: Weeds presence

### 5.3.2 Typical Rainfall Period

The SPI was estimated for each month between January 2016 and March 2020, using the historical data of the Aeropuerto Perales weather station. The typical-rainfall period was set between January 2018 and July 2019 despite the SPI in December 2017 being lower than 1.5. These dates were selected to avoid the effects of the high SPI in November 2017 on the plants' growth. Fig. 5.10 shows the monthly SPI values for this period and the thresholds ( $SPI = \pm 1.5$ ) used to determine the typical rainfall period.

In total, 5 PlanetScope, 35 Sentinel-2, 21 Sentinel-1 ascendant, and 35 Sentinel-1 descendent images were available for this typical rainfall period (See Fig. 4.1).

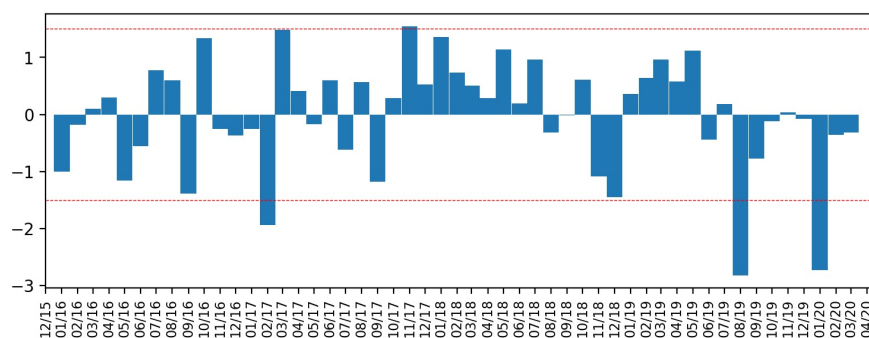


**Fig. 5.10** SPI values from January 2016 until March 2020

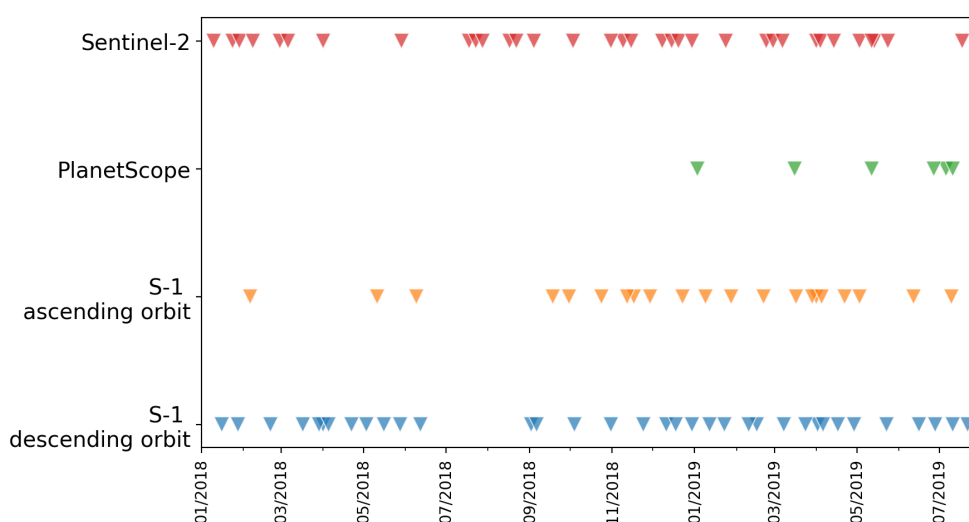


**Fig. 5.11** Optical and SAR imagery available for the typical-rainfall period

### 5.3.3 Discrimination of Anomalous from Non-anomalous Areas at Different Growth Stages

Independent two-sample t-tests and Welch-Satterthwaite tests were performed to see whether imagery from a particular stage in the growing cycle would provide better discrimination between anomalous and non-anomalous pixels. Table 5.5 shows the t-scores obtained for each pairwise comparison of all VI/SAR products at different phenological stages. Similarly, Fig. 5.12 presents the box plots of the average plot values for anomalous and non-anomalous pixels. The t-scores were marked with "NaN" when not enough samples were available to perform the test (less than 30 plots with a minimum of anomalous pixels to compare).

**Table 5.5** t-scores for comparing the average plot values of VI/SAR-products for non-anomalous and anomalous areas at different growth stages.

VI/SAR product	Seedling	Tillering	Panicle formation	Booting	Ripening
NDVI_b8A	-6.4**	-7.1**	-6.8**	-7**	-7.5**
NDVI_b8	-5.7**	-7.1**	-7.4**	-7.2**	-7.7**
EVI_b8A	-6.4**	-8**	-7.4**	-9.1**	-9.2**
EVI_b8	-5.8**	-8.7**	-8.4**	-10.1**	-9.8**
CIg_b8A	-8.8**	-8.5**	-8.3**	-8.4**	-8.7**
CIg_b8	-6.8**	-8.6**	-9.2**	-8.8**	-8.9**
GNDVI_b8A	-8.3**	-7.2**	-6.8**	-7.5**	-8.2**
GNDVI_b8	-6.4**	-7.1**	-7.5**	-8.1**	-8**
CIre_b8A_5	-6**	-8.6**	-8.4**	-11**	-7.6**
CIre_b8A_6	-11.3**	-12**	-7.6**	-12.2**	-13.4**
CIre_b8A_7	-12.9**	-24.1**	-18.5**	-20.5**	-16**
CIre_b8_5	-6.9**	-9.6**	-8.9**	-11.3**	-8.3**
CIre_b8_6	-15.6**	-18.5**	-10.7**	-15**	-17**
CIre_b8_7	NaN	NaN	NaN	-22.1**	-27.3**
RENDVI_b8A_5	-6.2**	-7.1**	-7.5**	-10**	-7.4**
RENDVI_b8A_6	-10.4**	-11.7**	-8.2**	-12.3**	-13.1**
RENDVI_b8A_7	-13.2**	-23.7**	-16.1**	-20.3**	-15.9**
RENDVI_b8_5	-6.9**	-7.6**	-7.7**	-10.1**	-7.6**
RENDVI_b8_6	-15.8**	-17.5**	-10.6**	-14.2**	-16.3**
RENDVI_b8_7	NaN	NaN	NaN	-22.7**	-27.2**
SAVI_b8A	-7**	-7.7**	-8.6**	-8.8**	-9.5**
SAVI_b8	-6.9**	-8.1**	-8.6**	-9.6**	-10.1**
NDII_b8_11	NaN	-9.7**	-7.6**	-10.4**	-9.7**
NDII_b8_12	-5.4**	-7.6**	-7.4**	-8.2**	-8.7**
NDII_b8A_11	NaN	-8.4**	-7.3**	-10.1**	-9.3**
NDII_b8A_12	-4.5**	-6.9**	-7**	-8**	-8.6**
VH_asc	9.7**	20.3*	21.3**	25.7**	30.8**
VV_asc	12.6**	21.4**	14.8**	18.3**	23.0**
VH/VV_asc	16.5**	27.2**	22.7**	36.1**	41.4**
VH_des	13.1**	35.0**	25.0**	26.4**	35.2**
VV_des	15.6**	30.5**	15.7**	23.9**	30.4**

VI/SAR product	Seedling	Tillering	Panicle formation	Booting	Ripening
VH/VV_des	31.2**	38.7**	28.3**	47**	69.2**

\*\* Significant at  $\alpha = 0.05$

The greener the cell of a specific product, the more significant the difference between the average plot VI/backscatter values of anomalous and non-anomalous pixels.

In general, the mean VI values were significantly different ( $\alpha = 0.05$ ) between anomalous and non-anomalous areas across all VIs tested. However, significance tended to be lower during the seedling stage for most normalised difference indices. This seems a consequence of the short size of plants at this stage, where most of the energy is reflected by the bare soil. The variance of the average pixel values per plot is larger for those fields at the tillering stage for most of the VIs, except the chlorophyll indices (i.e. CI<sub>re</sub>, CI<sub>g</sub>) and those VIs that included the red-edge bands 6 and 7. This can be a consequence of the longer length of this stage and the fact that the LAI values change the most due to the tillering development. As presented in Fig. 5.12, the average pixel values of anomalous and non-anomalous plots remained low and stable along the crop cycle for those VIs that included the red-edge band 7. These low values are consequence of the closeness of the reflectance values measured in channel 7 and the values measured in the NIR bands 8 and 8A. In particular, the pixel values for those VIs that included the NIR band 8 and the red-edge band 7 (i.e. CI<sub>re\_b8\_7</sub> and RE<sub>NDVI\_b8\_7</sub>) were homogeneous for plots at early stages, to the extent that not enough plots had a minimum of anomalous pixels to perform the comparison.

Similarly to optical imagery, the pixel values between anomalous and non-anomalous areas in SAR products were significantly different at  $\alpha = 0.05$  across all polarisations and phenological stages. However, the significance of the differences between anomalous and non-anomalous average values per plot tended to be higher for SAR imagery than for optical products. In general, rice VV backscatter tended to be higher than VH and decreased as the crop developed and reached the booting stage, where it remained almost constant until the rice was harvested. VH scatter, on the other hand, tended to rise during the early and late stages, being relatively constant in the middle. The ratio between VH and VV backscatter tended to increase steadily until the crop reached the booting stage, stabilising until the field was harvested. In contrast to the accuracy assessment, the mean backscatter values for each polarisation had similar trends in the ascending and descending acquisitions.

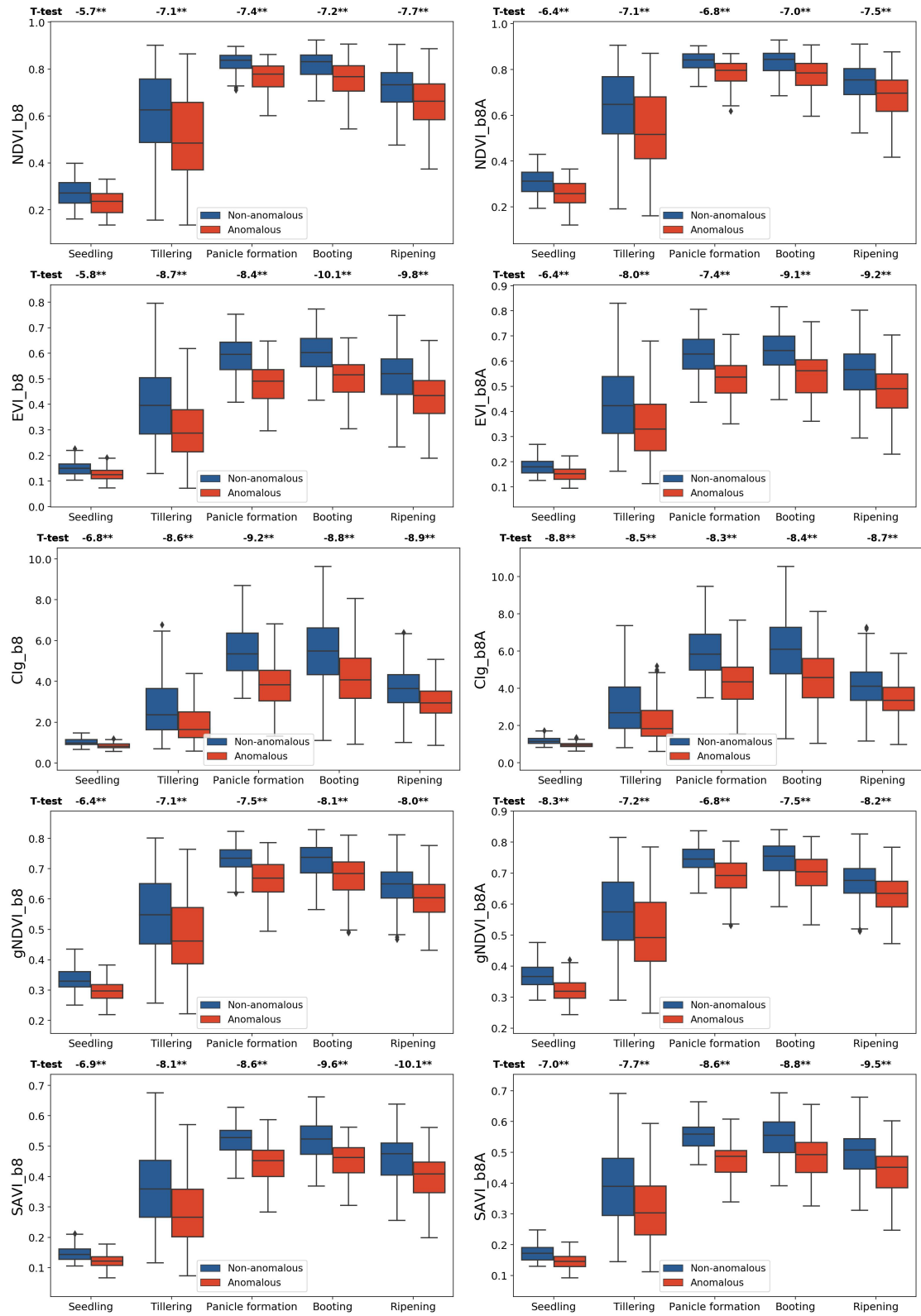


**Fig. 5.12** Box plots of the average plot values of VI/SAR-products for non-anomalous and anomalous areas at different growth stages and t-statistic obtained for each independent two-sample t-test.

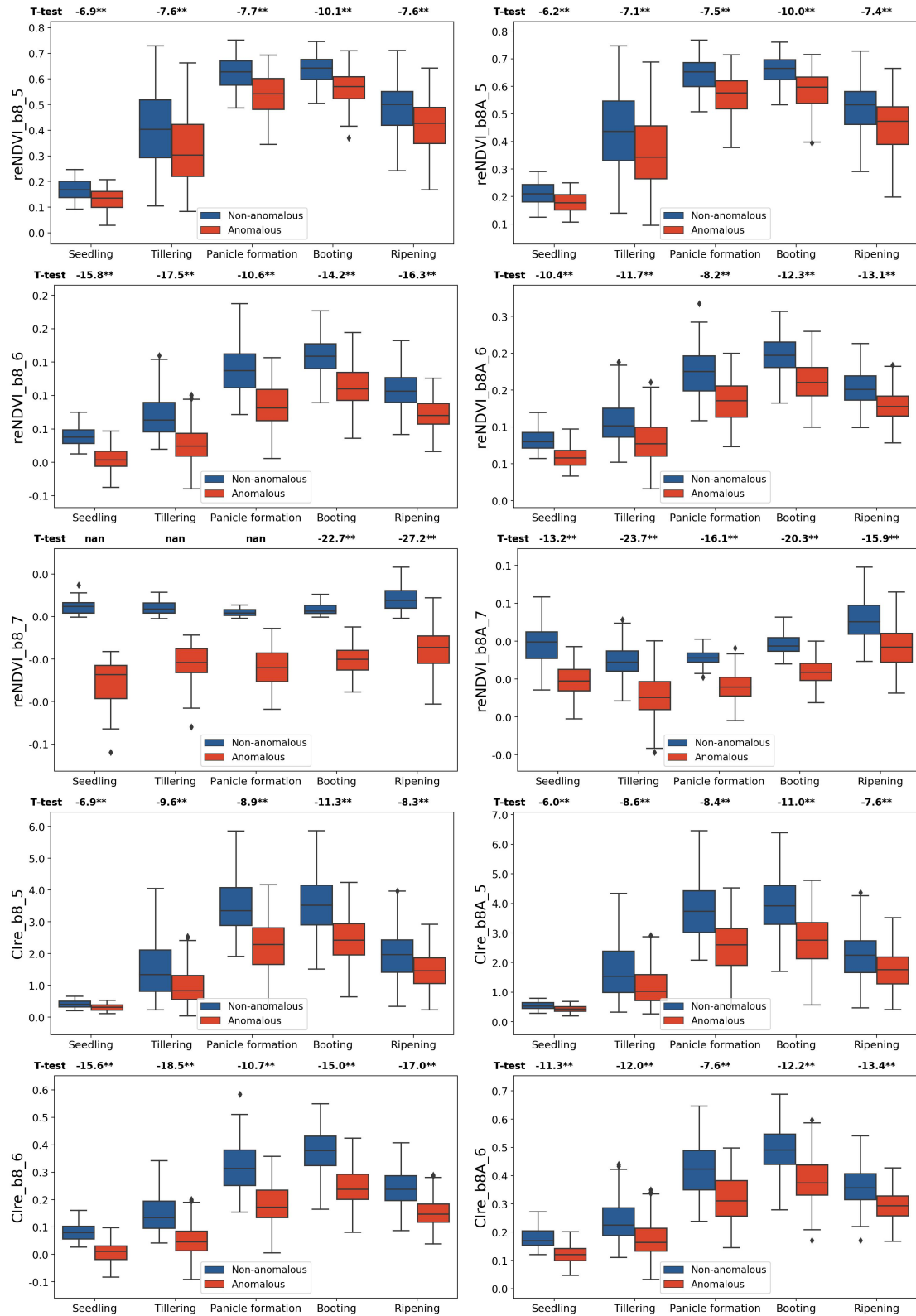


**Fig. 5.12 (cont.)** Box plots of the average plot values of VI/SAR-products for non-anomalous and anomalous areas at different growth stages and t-statistic obtained for each independent two-sample t-test.

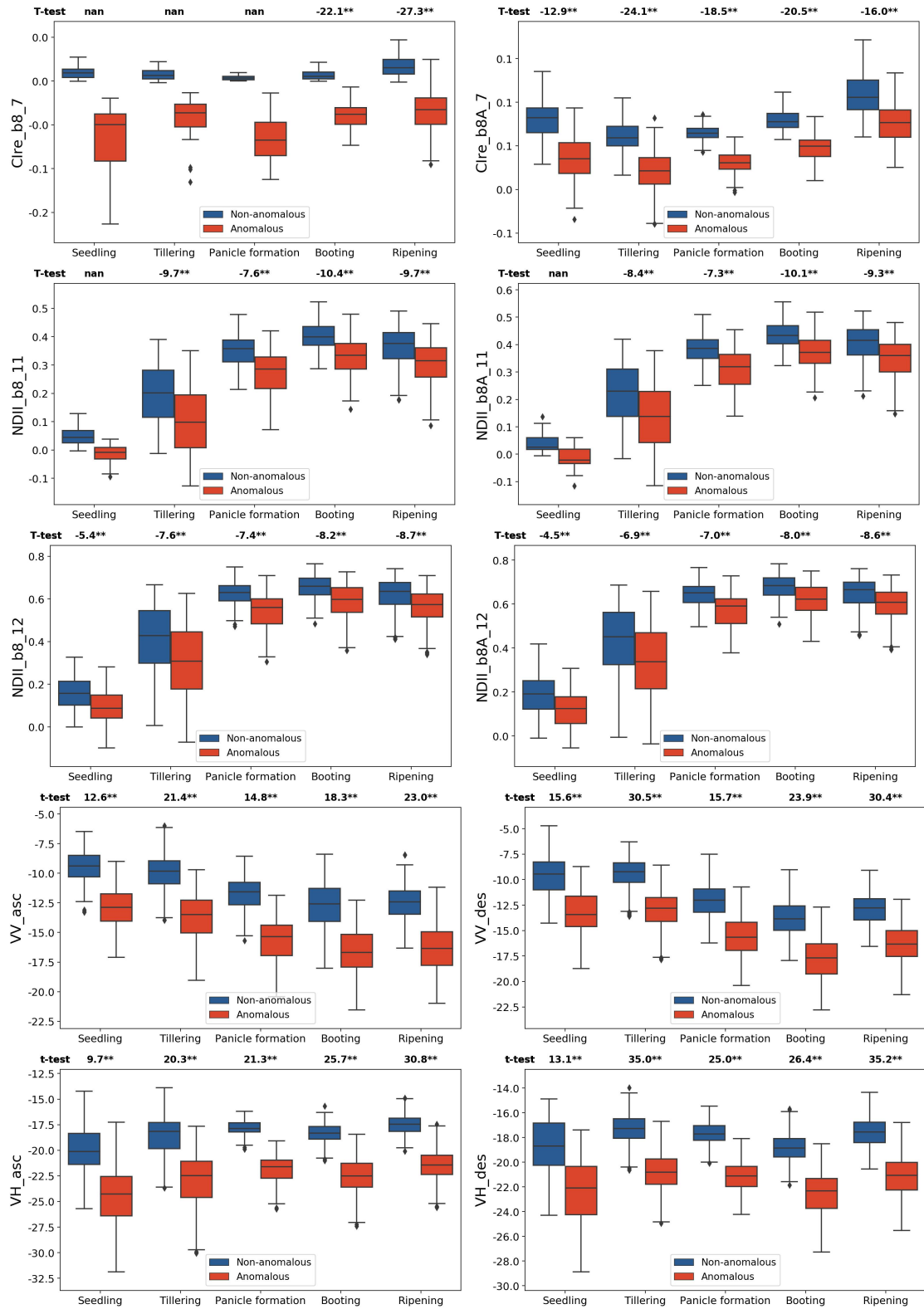


**Fig. 5.12 (cont.)** Box plots of the average plot values of VI/SAR-products for non-anomalous and anomalous areas at different growth stages and t-statistic obtained for each independent two-sample t-test.

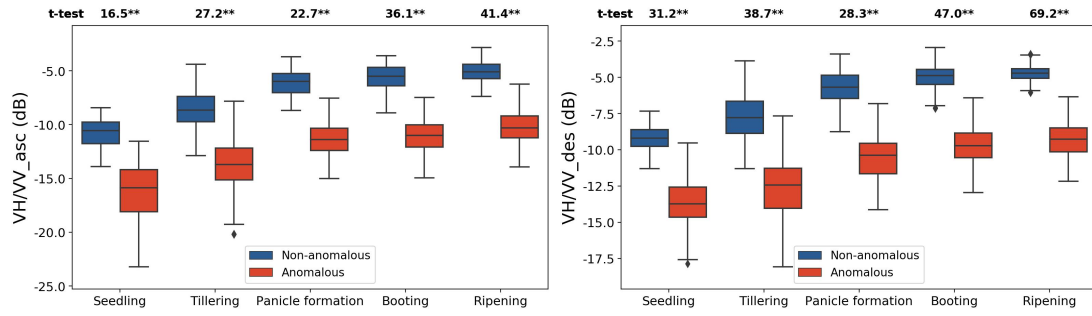


**Fig. 5.12 (cont.)** Box plots of the average plot values of VI/SAR-products for non-anomalous and anomalous areas at different growth stages and t-statistic obtained for each independent two-sample t-test.

## 5.4 Discussion

The proposed EOAD method was able to identify and map crop anomalies with accuracy scores up to 80% comparing favourably with other anomaly detection approaches. A drawback of optical EO imagery is the dependence on cloud-free conditions, but the consistency in performance over the two sensors investigated offers the potential to detect anomalies in relatively large (>5 ha) crop plots using different systems, e.g. Sentinel-2 and Landsat, meaning a greater frequency of revisit, a higher chance of making cloud-free observations and increases the monitoring frequency throughout the growing cycle. To overcome the limitations of cloud presence, the EOAD technique was also tested on Sentinel-1 images, however the accuracy metrics were low for all the polarisations assessed. Despite literature that address anomaly detection using SAR polarimetry is limited, other authors such as (Belenguer-Plomer et al. 2019) obtained similar results for anomaly detection in grasslands. However, rather than using unique scenes, they detected burned areas based on temporal series of C-band backscatter coefficient.

Intelligent management of water throughout the crop cycle is essential for overall profitability, management of diseases, nutrient management and development of rice plants (Henry et al. 2018), such as those found at the study site on the Ibagu Plateau. In these contour-levee irrigation schemes, the level of homogeneity in water distribution along the plot is defined when the "irrigator" sets the levees breaks during the field preparation (Okada and Lopez-Galvis 2018). When the rainfall or the wet bulbs of nearby irrigated areas do not fully cover the crop water requirements after sowing, the rice seeds do not germinate or emerge homogeneously along the field. However, in later crop stages, the lack of adequate water supply affects not only the plant growth but also the activation of products applied such as fertilisers or herbicides (Henry et al. 2018;



Vories et al. 2017).

Such heterogeneity tends to manifest itself in reduced final yields but also in grain quality, leading to a reduction in price (Marchesi et al. 2010). The sooner in-field anomalies are identified and fixed, the more homogeneously the plants will grow along the field. The EOAD approach can be used to detect anomalies related to soil moisture but also patches with lower plant density due to other factors such as seed quality and sowing/soil heterogeneity in order to re-sow the seeds (Jarrod Hardke et al. 2018). In the present study, anomalous-detected areas were targeted by farm staff to detect dry patches and fix the water supply or identify the areas with lower plant density for site-located re-sowing.

Although the EOAD approach was only demonstrated for rice crops, the approach is based on the variability in reflectance as an indicator of biophysical properties of the crops. This is not unique to rice crops, and therefore there is clear potential to be applied to different crop types and different agricultural systems. The intention of EOAD is not to provide a definitive prediction or estimate of biophysical properties, but its simplicity and reliance on freely available EO data means that it can be used as a convenient alternative for systematic anomaly screening that is fundamental in crop management, i.e. decision-makers can focus attention towards areas identified as anomalous and perform site-specific practices based on their expertise and knowledge about the crop and its context. This is especially important in relatively resource-poor regions where farm data monitoring networks that supply spatial and temporal information on the biophysical properties of agricultural systems are prohibitively expensive.

#### 5.4.1 Accuracy assessment

The proposed EOAD method was able to identify and map crop anomalies with accuracy scores up to 80% comparing favourably with other anomaly detection approaches reporting accuracies of 50-70% (e.g. McCann et al. 2017). As the EOAD is based on a simple automatic thresholding approach applied to the distribution of VI values within a crop plot. This automated approach offers procedural advantages over other approaches, such as McCann et al. (2017) that detected anomalies by applying manually set thresholds to Median Absolute Deviation (MAD) values calculated over a moving window. Furthermore, because McCann et al. (2017) employs a moving window, thereby taking advantage of the relatively high spatial resolution aerial or drone imagery to which

it was applied, the size of the anomalous area detected is limited to the size of the kernel i.e. areas smaller than the kernel will be missed, whereas EOAD can detect anomalous areas at the pixel level making it better suited to relatively coarse satellite EO data.

For Sentinel-2, EOAD performed best when VIs were used that relate to LAI and vegetation coverage, namely, the SAVI and gNDVI indices (accuracy  $\approx 80\%$ ). Although EOAD is able to detect both high and low anomalies, true positive matches with field observations were exclusively low-anomalous areas associated with lower canopy density and lower vegetation coverage. Specifically, the success of gNDVI aligns with other studies that identified the gNDVI as better to predict LAI in rice than the conventional NDVI (Wang et al. 2007). As the majority of the field validation points were registered during the tillering phase, the higher accuracy of SAVI reflects its ability to minimise soil brightness that characterises canopies with intermediate levels of vegetation cover (Huete 1988), such as rice during the tillering stage.

The results using optical imagery demonstrate that the EOAD approach is transferable across different optical EO systems and data types. In the present study, the accurate detection (overall accuracy  $>70\%$ ) of anomalous pixels using both Sentinel-2 and PlanetScope imagery was demonstrated. Most of the Sentinel-2 VIs that produced the highest accuracies are transferable to other systems such as Landsat and PlanetScope, except the reNDVI. This consistency among different vegetation indices demonstrates the potential for applying the approach to a range of broadband EO systems. However, the spectral responses of the sensor's bands should be compared before applying the technique on VIs derived from different sensors. The results of this study showed that slightly different accuracy scores were achieved when applying the EOAD on VIs derived from Sentinel-2 and PlanetScope. Specifically, the PlanetScope gNDVI did not perform as well as the equivalent for S2. This is likely due to the difference in spectral response curve for the green channel, with the PlanetScope channel being much broader (500-590 nm) compared to Sentinel-2 (542-578 nm) (Fig. 5.13). An accuracy assessment using a sample of field points will identify those VIs that produce the best results for anomaly detection in different agricultural systems when the spectral responses among sensors differ significantly.

A number of the poorer performing VIs are designed to be sensitive to specific absorption features that may be indicative of leaf chemistry or pigments. However, the ground truth data used in this study related mainly to observations of canopy coverage. Further research should draw comparisons with variables such as Chlorophyll content to assess

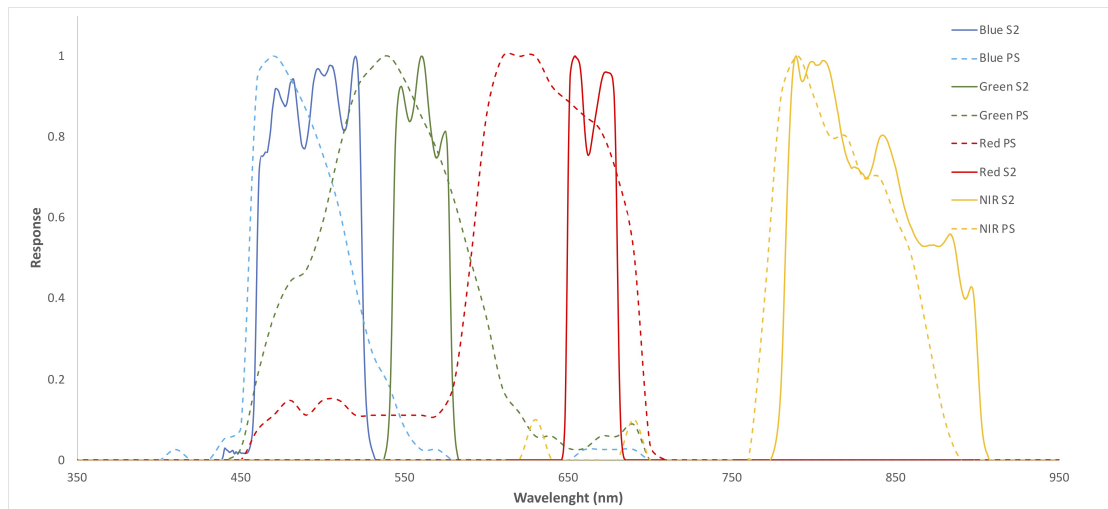


**Fig. 5.13** Sentinel-2 and Planet Scope spectral response functions

the capability of the EOAD to indicate, for instance, Nitrogen deficiency, that is known to affect crop productivity as it enhances and stabilises crop growth and yield production (Kuenzer and Knauer 2013; Wang et al. 2012). In addition, the field observations used to assess the method accuracy were collected mostly during the tillering stage, therefore, limited conclusions can be drawn regarding the method performance at other crop ages. Future work should consider collect validation observations along the whole crop cycle to identify the best age to detect anomalies using the EOAD technique.

Unlike optical satellite imagery, most Sentinel-1 products, showed poor accuracies at detecting field anomalies. It seems to be a consequence of three main factors. First, the coarse spatial resolution of the Sentinel-1 imagery together with the morphological reducer filter applied to reduce the speckle noise make it difficult to detect anomalies that are much smaller than S1 spatial resolution, which is defined as 20x22 at mid-orbit altitude in the range and azimuth direction. However, the spatial resolution for SAR systems is not as straightforward to interpret as it is for optical systems. Radar speckle introduces stochastic fluctuations in intensity that, for a single-look image, lead to an expected error of 100% (Woodhouse et al. 2011). While multi-look processing reduces speckle to improve the separability between targets by gaining a better estimate of the underlying radar cross section, the increase in ENL reduces the spatial resolution. The 4.4-look S1 GRD images still seem to be dominated by speckle and are not comparable to an optical image with a 20 x 22 spatial resolution. Moreover, the filter applied to reduce the remaining effect of speckle reduced even further the spatial resolution, making more difficult to differentiate the anomalies identified in the field at a spatial footprint of 10 x 10 metres.

Secondly, the 'COPERNICUS/S1\_GRD' Sentinel-1 image collection in GEE are processed to backscatter coefficient  $\sigma^o$  in decibels (dB) as  $10 \times \log_{10} \sigma^o$ , distorting the original distribution of pixel values within a homogeneous area. This factor is key as the logarithmic scale of the images expressed in decibels affects the pixels distribution for a homogeneous region, and therefore the method applicability. In addition, authors have shown that the Gamma distribution is more suitable to describe radar intensity in a multi-look SAR image from homogeneous regions rather than Gaussian distributions (Hajnsek and Desnos 2021; Chitroub et al. 2002). This is because the natural spatial variation of the radar cross-section is generally not perfectly homogeneous for pixels that belong to one thematic class (Anfinsen et al. 2009), in our case a crop plot. This last factor is also fundamental, as the main assumption of the EOAD is that the plot pixels follow a normal distribution. The IW GRD Sentinel-1 products used in this research are multilooked only in the range direction (i.e. 5 looks; ESA 2021). In a further stage, it is recommended to implement the anomaly-detection method on linear-scaled  $\sigma^o$  imagery, which can be more adequate to fulfil the normality distribution for pixels that belong to homogeneous areas. It is also recommended to perform multi-looking in azimuth and range directions, which will increase the number of ENL. In this case, the probability density function (pdf) of a homogeneous area can be approximated by the Gaussian pdf (Fang et al. 2018; Hajnsek and Desnos 2021).

The echo returning from rice fields to the sensor is a combination of the three basic scattering mechanisms. Further research should consider assessing the accuracy of the EOAD on the elementary scattering mechanisms extracted from the SAR polarisations by means of polarimetric decomposition. The main objective of the scattering decomposition techniques (e.g., Cloude and Pottier 1997; Freeman and Durden 1998; Touzi 2007) is to break down the polarimetric backscattering of distributed scatterers into the elementary scattering contributions (Moreira et al. 2013). Decomposition approaches have shown improved crop rice classification accuracies and in general better descriptions of the target surfaces (Li et al. 2014). Polarimetric decomposition techniques have also been successfully to improve soil moisture content estimation by separating and removing the effect of disturbing vegetation (Moreira et al. 2013).

#### 5.4.2 Typical Rainfall Period

The SPI was estimated to define a typical rainfall period and reduce variations caused by extreme climate effects. However, soil water availability also depends on the Evapotran-

spiration (ET), the combination of the water lost from the soil surface by evaporation and from the crop by transpiration (Allen et al. 1998). In this sense, identifying extreme soil moisture conditions by considering evapotranspiration, rather than just the precipitation, will potentially provide better discrimination of atypical periods for crop development. Further research should perform a soil water balance to identify typical periods of drought or extreme wet conditions. For example, the Palmer Drought Severity Index (PDSI) is a measurement of dryness based on recent precipitation and temperature (Palmer 1965). The FAO Penman-Monteith method (Allen et al. 1998) is the most common soil water balance model for determining reference evapotranspiration  $ETo$ . It uses as input radiation, air temperature, air humidity, wind speed data and soil physical properties. However, as the FAO Penman-Monteith method also requires information about soil physical properties, this data is not always available at in-field scale and would require carrying out an additional soil survey or making assumptions about the soil properties in the study area.

#### 5.4.3 Discrimination of anomalous from non-anomalous areas for different growth stages

In general, the method showed clearly discriminate anomalous from non-anomalous areas within crop plots for most of the optical VIs and polarisations considered. In particular, the method showed superior discrimination capabilities at the ripening and booting stages. The relatively lower significant differences between the values of anomalous and non-anomalous pixels at the seedling and panicle formation stages can be an indicator of the presence of overlapping values between the two categories. This situation can increase the probability of obtaining miss-classified pixels especially for those values close to the threshold set by the method and reduce the accuracy of the EOAD during these phenological phases.

Only the VIs calculated with the red-edge band 7 and NIR band 8 (i.e.  $CI_{re\_b8\_7}$  and  $RENDVI_{b8\_7}$ ) did not show good capabilities to detect anomalies in the studied plots at more than one stage, marking as anomalous only very few pixels within each field. The low sensitivity to discriminate anomalous vs non-anomalous pixels is related with the lower values of these VIs compared to the same indices estimated with the red edge band 5 (See Fig. 5.12). Such low values are due to the closeness of the reflectance values measured in channels 7 and 8, making the difference and ratio between these bands small and therefore hindering the anomaly detection.

Despite most of the assessed products showed to discriminate well between anomalous and anomalous pixels, many VIs such as NDVI started saturating during the panicle formation stage. In this sense, Vis such as the C<sub>Ir</sub>\_b6 or NDII\_b8\_11 can be better options to estimate anomalies in fields that are already in the booting phase. Also, as the SAR VV backscatter showed lower saturation problems during the panicle formation and booting stages, it could provide a good alternative to optical products if higher spatial resolutions are available.

Analysing the patterns of SAR polarisations at different growth stages, in general, rice VV backscatter tended to be higher than VH (See Fig. 5.12). This difference, reported by authors such as Pang et al. (2021) and Yang et al. (2021), is explained by the vertical structure of the rice plants (Brown et al. 2003; Veloso et al. 2017). Fig. 5.12 shows that the VH  $\sigma^0$  saturated at an early crop age, and the asymptotic maximum did not change significantly during most of the crop development. This pattern shows coincidences with the relationship between the C-band VH  $\sigma^0$  and total dry biomass (DW) reported by Inoue et al. (2014) and presented in Fig. 5.14. Based on these results, the rice growth stage at which the  $\sigma^0$  saturates corresponds approximately to the end of the tillering phase, similarly to the behaviour evidenced in this research for the VH backscatter (See Fig. 5.12). The variation of VH  $\sigma^0$  during the crop development described in this research confirms the findings of other authors about the usability of SAR backscatter as an indicator of rice growth. However, the early asymptotic behaviour of the VH backscatter coefficient provides hints about the limited usability of this polarisation for anomaly detection when the anomalies are related to differences in the total biomass content.

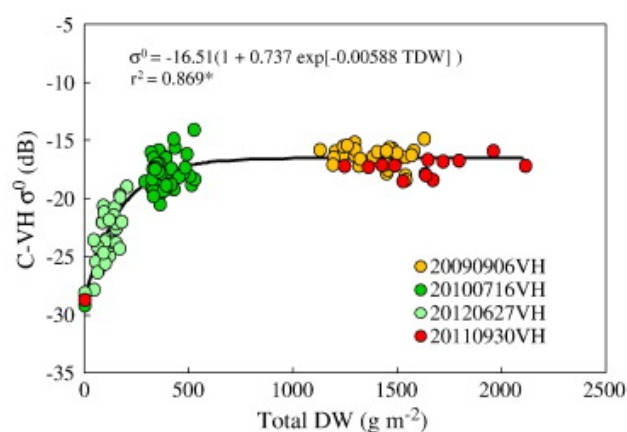


**Fig. 5.14** Relationship between C-band  $\sigma^0$  and total dry biomass (from Inoue et al., 2014).

During the soil preparation and the seedling stage predominates the surface scattering and

double bounce. Scattering from smooth to medium rough surfaces does not depolarise the wave and more energy is received by in the co-polarised channel (VV) (Vreugdenhil et al. 2020). During most of the growth cycle of grass-type crops (e.g. rice or barley), the VH backscatter is dominated by the double-bounce and volume scattering mechanisms, causing  $\sigma^0$  to increase until it saturates (Lopez-Sanchez et al. 2013; Veloso et al. 2017; Wiseman et al. 2014). Unlike the VH  $\sigma^0$ , the VV backscatter, dominated by the direct contribution from the ground and the canopy, decreases over time due to the increased attenuation from the predominantly vertical structure of the plant stems (Brown et al. 2003; Veloso et al. 2017). These temporal patterns of VV  $\sigma^0$  differ from the temporal patterns described by other authors, such as Pang et al. (2021), which state that both VV  $\sigma^0$  and VH  $\sigma^0$  rise after the rice plants emerge. These differences may lie in the type of production system implemented as the backscatter mechanisms are different for flooded areas. Fig. 5.15 shows the temporal variation of VV and VH  $\sigma$  for a rice pixel under flood irrigation conditions.

No notable differences in backscatter were evidenced between ascending and descending orbit images for the VV polarisation. One notable finding of this analysis is the peculiar relationship between the incidence angle and the VH backscatter compared to what was observed in past studies. Most studies have reported that the rice VH backscatter during the early crop stages tends to decrease as the incidence angle increases (Kuenzer and Knauer 2013). However, in this study, the descending VH backscatter showed to be higher than the ascending during the seedling stage. This discrepancy can be explained by the micro-topography created by the dikes in rice production systems with contour-levee irrigation, which generate different backscattering mechanisms than completely flat surfaces.

The fact that most of the VIs and SAR products analysed showed good capabilities to discriminate anomalous from non-anomalous plots suggests that the discrimination capability of a specific VI does not represent a criterion to prefer using a specific VI. The selection of the most adequate satellite product to detect problematic anomalies in the crop rather relies on the impacts that such anomalies have on the final yield and the phenological stage at which such anomalies occur.

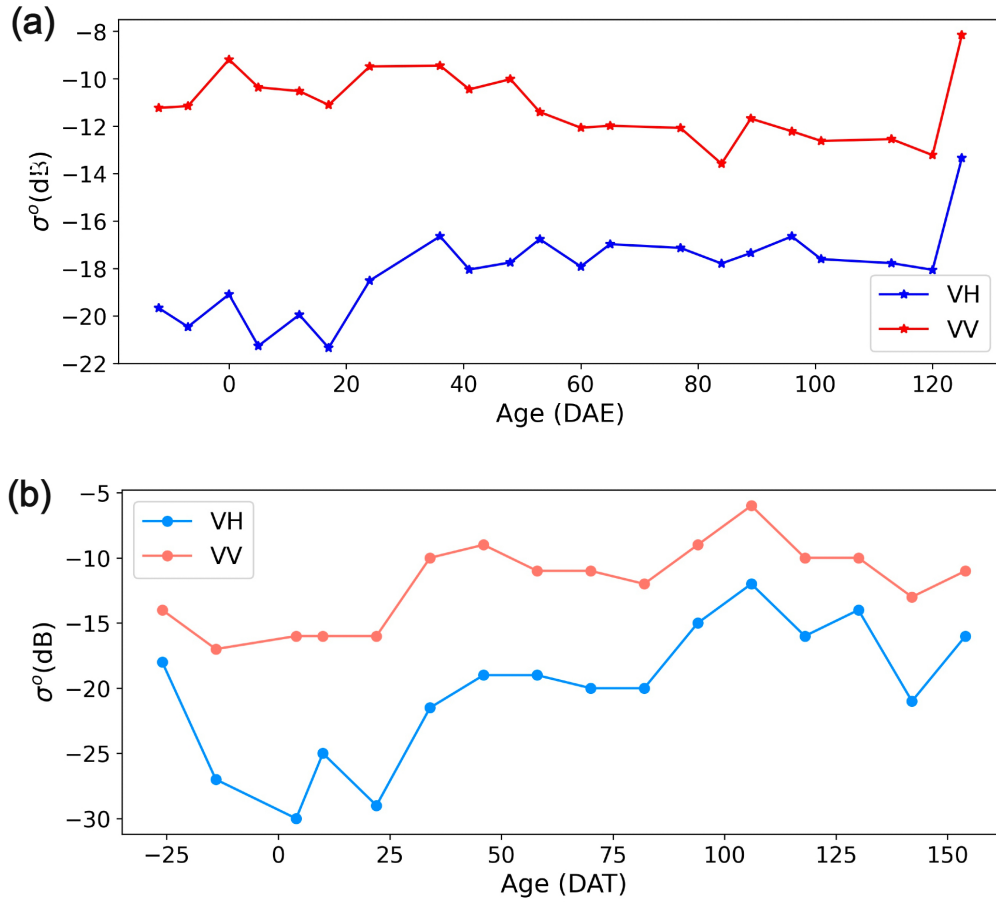


**Fig. 5.15** Temporal variation of VV and VH for two types of rice productive systems. (a) Temporal variation of the SAR intensity for a rice pixel in Hacienda El Escobal (Crop age is expressed as DAE). (b) VV and VH temporal variation of a rice pixel under flood irrigation conditions in Fujin City in Heilongjiang, province of China. (Crop age is expressed as Days after transplant (DAE)). Source: Pang et al. (2021).

## 5.5 Conclusions

The EOAD method presented in this thesis was able to map anomalies at sub-plot level in rice crops in Colombia. Detected anomalies can be used to direct farmers to areas of fields to determine what strategy needs to be put in place, such as fixing water supply, to correct for these anomalies bringing about and ultimately an overall improvement to crop yields.

In this study, EOAD was applied to different VIs and SAR products. For the rice crops studied, VIs such as gNDVI performed consistently well. Although this study tested EOAD using just two EO optical data sources, Sentinel-2 and PlanetScope, VIs like



gNDVI employ spectral channels common across many EO systems, meaning the EOAD can potentially be applied to imagery from multiple sources, increasing the frequency of anomaly detection. As such, EOAD's ability to be applied to a number of commonly used EO systems means greater observations, thereby providing greater confidence when informing decision-makers on the ground. Due to the broad resolution of Sentinel-1 imagery, the implementation of EOAD over SAR products did not show high accuracies at detecting in-field anomalies. Especially because such anomalies were much smaller (less than 100m<sup>2</sup>) than the spatial resolution of Sentinel-1 imagery.

Ultimately, the EOAD is designed to be a simple technique, without the need for manual calibration, or indeed, prior expertise in spectral analysis of crops. In this respect, EOAD is applied to histogram data for individual crop plots, in this instance, with data from commonly used VIs (e.g. NDVI, SAVI, gNDVI etc.), derived from freely available optical EO data. As such, the EOAD approach represents an efficient and low-cost means of collecting PA information almost anywhere in the world. If coupled with automatic approaches for field delineation, this represents an exciting and tractable tool for informing agricultural practices, especially in relatively resource-poor regions of the world where food security is paramount.

The usefulness of different Vegetation indices to best capture agricultural characteristics imply the need to use multiple vegetation indices at different phenological stages (Hatfield and Prueger 2010). In this sense, further studies should focus on assessing the accuracy of different VI at different crop growth stages. Specifically, the images that were used in this study to relate to yield data were captured during the reproductive phenological phases of rice (i.e. booting and panicle formation), where VIs such as NDVI (Liu et al. 2014) and reNDVI (Zhang et al. 2019a) have shown to be more related to grain yield. Therefore, although single observations of anomalies may be valuable, greater confidence in the EOAD outputs can be gained by making more observations, which could be achieved for many areas by integrating imagery from different systems.

Most of the VIs and SAR products analysed showed good capabilities to discriminate anomalous from non-anomalous, which suggests that the discrimination capability of a specific VI does not represent a criterion to prefer using a specific VI. The selection of the most adequate satellite product to detect problematic anomalies should rely on the accuracy to detect anomalies, the impacts that such anomalies have on the final yield and the phenological stage at which such anomalies occur.

## CHAPTER 6

### Effects of in-field anomalies on crop yield

#### 6.1 Introduction

As presented in Chapter 5, the EOAD method was able to identify and map in-field crop anomalies with accuracy scores up to 80% comparing favourably with other anomaly detection approaches that require manual calibration. Detected anomalies can be used to direct farmers to potentially problematic areas. Once the anomaly is found, the farmer assesses the nature of the problem, its potential implications for crop productivity and determines the strategy to be put in place. However, farmers mostly need to prioritise those crop plots and in-field regions that are most likely to experience yield losses. By identifying the anomalies that are more prone to negatively affect crop yield and the growing stages at which they occur, farmers can implement timely corrective practices.

Multiple studies have used satellite imagery to detect anomalies in vegetated areas and croplands at national, regional and global scales. Most of these approaches use historical data to model VIs typical time series and compare new observations with their corresponding predicted values to detect potential anomalies (e.g. Beck et al. 2006; Meroni et al. 2019; Verbesselt et al. 2012). They can compare current pixel values with historical average values (GEOGLAM 2018), changes in temporal patterns of VIs (Campos and Di Bella 2012) or extract phenological metrics, such as start-of-season or end-of-season to compare their behaviour over time (Jönsson and Eklundh 2004; Zhang et al. 2003). For example, the GEOGLAM crop monitor uses MODIS and VIIRS products to derive NDVI anomalies. These anomalies are defined as the difference between the averages NDVI over a specific time step compared to the average NDVI for

the same time step across a range of years that varies between 5 and 20 (GEOGLAM 2017).

Campos and Di Bella (2012) applied a discrete wavelet transform (DWT) to smooth the time-series data and disaggregated the signal into its component frequencies (e.g. gradual change, seasonal change). The resulting signals for a pixel that had experienced changes were compared with those belonging to a pixel that provided a control signal using the mean and standard deviation of specific periods within the time series. This method proved capable of detecting deforestation related to soybean and planted pasture expansion in Argentina between 2002 and 2006 and studying seasonal inundation in the Mekong Delta. Kanjir et al. (2018) developed a similar approach for land cover anomaly detection in croplands using Sentinel-2 imagery. They performed a pixel-based time series analysis over NDVI products using the BFAST Monitor, a method for change analysis based on time series. The technique proved to detect anomalies in croplands, however, it overestimated the number of anomalies and had to be supplemented with an analysis of the NDVI temporal development curve for each potentially anomalous field using basic descriptive statistics per plot (i.e. mean, standard deviation).

Despite the power of time-series analysis, reliable methods for detecting anomalous crop fields using optical data can be challenging to implement for different reasons. For example, the lack of historical data, asymmetrical availability of images over time and annual crop differences associated with crop rotation systems that disturb the seasonal observations (Kanjir et al. 2018; Lambert et al. 2018). It has led authors such as Mouret et al. (2021) to propose approaches that overcome many of these limitations and detect abnormal parcels within a growing season, rather than detecting inter-annual abnormalities. Mouret et al. (2021) trained an isolation forest algorithm over a set of S1 and S2 derived indices at different crop ages to detect anomalous fields within a growing season. This approach considers the temporal variation of the crop status along the cycle and does not require historical agronomic data or prior knowledge on the expected behaviour of the parcels, however, it relies on the availability of satellite products at the same ages for all plots. Such conditions can be found in temperate regions where seasonal climatic thresholds are drivers of the spatial patterns in planting dates, however, in equatorial regions, there is a considerable spread in these climatic features (Sacks et al. 2010). In addition, as it is warm throughout the year, farmers plant new fields during the whole year, causing each plot's growth pattern to be different from others depending on the date when its cycle starts (Perfetti et al. 2013).

The studies mentioned above implicitly assume that the detected anomalies impact crop yield but do not statistically assess this relationship. For example, negative NDVI anomalies are considered to be a good indicator of poor crop conditions or a slower growth rate of the crop in the GEOGLAM Crop Monitor (GEOGLAM 2017). Mostly meteorological-related studies have established relationships between the presence of weather anomalies with yield losses (e.g. Schwalbert et al. 2020). However, no studies were found that explicitly assessed the impact of the satellite-detected anomalies with changes in crop yield.

The EOAD was shown to be successful in detecting infield anomalies - this chapter investigates the method's potential to support informed agricultural practices that lead to increased yield. It analyses how the outputs of the EOAD, combined with basic agronomic data, can help prioritise the implementation of corrective actions on crop plots and in-field areas that are prone to experience losses in yield. First, it describes the methods implemented to 1) evaluate the impact of the frequency of anomalies on productivity; 2) assess the impact of in-field anomalies over yield in different moments along the crop cycle; and 3) detect underperforming plots at early stages using the metrics derived from the EOAD. Then, it presents the results of the analyses described in the Methods section and the discussion around those results. It finalises by presenting the main conclusions regarding the potential of using EOAD's outputs for the early detection of underperforming areas. The objective is to identify to which extent the EOAD can provide additional information that helps the farmer prioritise crop plots and in-field areas that require immediate attention based on identifying those anomalies that can negatively affect crop yield.

## 6.2 Methods

The EOAD approach was able to accurately identify and map in-field crop anomalies using optical VIs. This next work package will evaluate the implications of these anomalies on final yield and how the severity of such impacts change when anomalous pixels are detected at different growing stages. This section describes the techniques used to 1) assess the relationship between the EOAD anomalies and crop yield and 2) identify to which extent the outputs of the EOAD can help identify those fields more vulnerable to suffer yield losses.

The Sentinel-2 VIs and Sentinel-1 GRD products were analysed further to determine whether EOAD-observed anomalies were related to crop yield. The methodological workflow is presented in Fig. 6.1. Firstly, the anomaly-frequency surfaces were compared with the yield to determine whether the frequency of anomalies along the cycle impacted the final yield. Then, the anomaly-predicted surfaces derived from Sentinel-2 VIs were compared with the crop yield to identify if they affected productivity differently at distinct growth stages. Finally, the percentage of anomalous area per plot was integrated with agronomic data from each field to assess how the anomaly detection technique can support the detection of underperforming plots in early crop stages. This was explored using a training a classifier to predict underperforming plots.

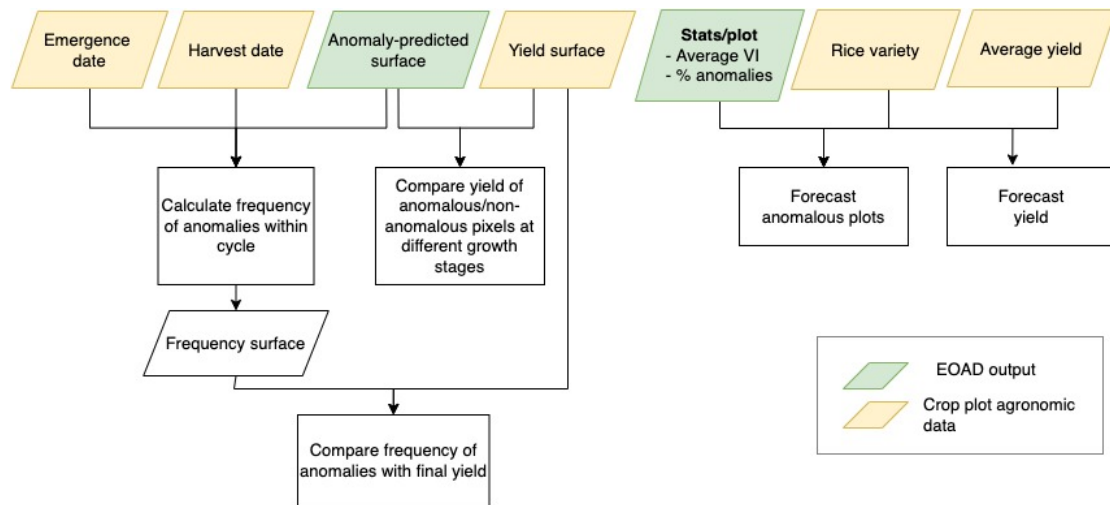


**Fig. 6.1** Flowchart describing the analysis performed on each plot to assess the effects of in-field anomalies on crop yield

### 6.2.1 Datasets Description

Three types of datasets were considered for the analyses described in this chapter: EO surfaces, agronomic features recorded per plot and EO metrics derived from the EO surfaces. All datasets were acquired during the typical rainfall period (January 2018 and July 2019). The typical rainfall period was previously estimated in Section 5.2.4. Table 6.1 presents the variables and metrics registered per plot.

**Table 6.1** Datasets registered per plot.

Type	Dataset	Description
EO data	VI surfaces	VI surfaces built from the Sentinel-2 scenes
	Anomaly-predicted surfaces	Output surfaces of the EOAD method.
EO derived metrics	Mean VI	Average of the VI values within the plot
	VI Standard deviation (std VI)	Standard deviation of the VI values within the plot
	Percentage of anomalous area per plot (% anomalies)	Percentage of anomalous pixels in the plot
	Mean non-anomalous VI	Average of the non-anomalous VI values within the plot
	Mean anomalous VI	Average of the anomalous VI values within the plot
Agronomic features	Seedling emergence month	Month in which at least 80% of the seedlings have emerged.
	Variety	Rice variety planted in the plot
	Average plot yield	Average tons of paddy rice per hectare (t/ha).
	Normalised yield surface	Yield surface built using the data recorded by the harvester sensor (Values range between 0 and 1).

A set of metrics was derived from the EO surfaces for each plot. It included the average and standard deviation of the VI pixel values within each plot, percentage of anomalous area, and average VI values of anomalous/non-anomalous pixels. The agronomic features recorded per plot include the emergence month, rice variety, and average yield per plot. The latter refers to the average tons of paddy rice per hectare. (t/ha). It is obtained by dividing the total rice weight per plot when entering the mill facilities. In addition, a normalised yield surface was built for each plot, using the data recorded by the harvester

sensor. The details of the processing operations implemented to derive the yield surfaces are described in Section 4.3.2.

### 6.2.2 Impact of Frequency of Anomalies on Yield

After assessing the accuracy of the EOAD approach, the frequency of occurrence of predicted anomalies within a crop cycle was compared against the yield distribution for different plots. The aim was to determine EOAD's potential for directly informing agricultural practices that lead to increases in yield. First, the number of images acquired during the crop cycle was estimated for those plots which growth cycle fell entirely within the typical rainfall period. The growth cycle begins on the planting date and finishes on the harvest. The analysis was performed using S2 and S1 imagery only on those plots for which there were available  $\geq 7$  images during the whole cycle. PlanetScope products were not considered in this analysis, as there was not enough imagery to cover multiple crop development stages within the crop cycle. Then, an anomaly-frequency surface was built by calculating the number of images in which each pixel was marked as anomalous within each crop cycle. Fig. 6.2 presents an example of the frequency surface built for a rice field for one crop cycle.

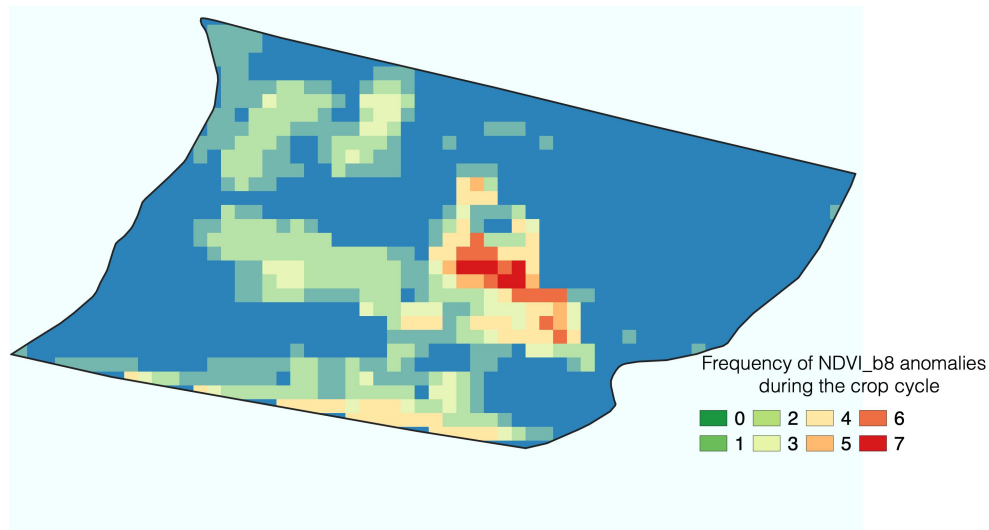


**Fig. 6.2** Example of the frequency surface built for a rice field using the NDVI\_b8 anomaly surface for one crop cycle.

Once the frequency surfaces were extracted, a Kruskal-Wallis test was applied to a sample of pixels to determine whether any significant difference could be found between the yield for different frequencies of anomalies. Then, the a Dunn's test was performed as a *post hoc* test to assess the individual differences between each pair of frequencies.

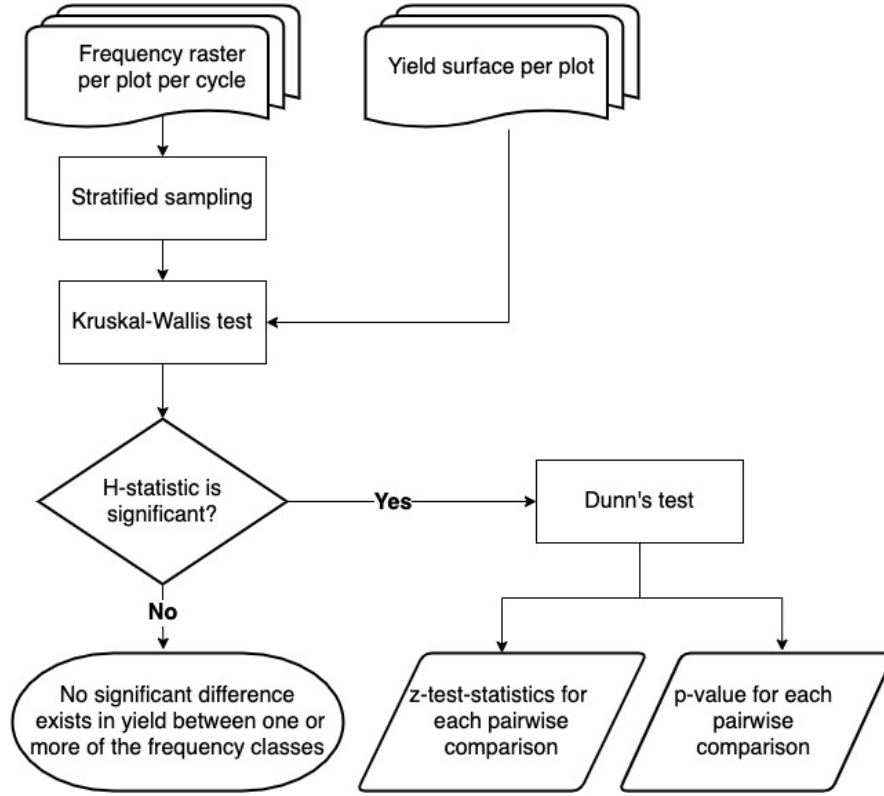


**Fig. 6.3** Flowchart describing the processes involved in the analysis of frequency

#### 6.2.2.1 Sample extraction

The analysis was performed over a sample extracted from all the pixels falling within those plots that met the conditions indicated above, using a stratified approach. The stratified sample was preferred to ensure that each frequency class in all the plots received proper representation within the sample. In stratified random sampling, the population is partitioned into strata, and a sample is selected randomly within each stratum (Chris B. Murphy and Margaret James 2021).

First, the total sample size was estimated by using the Eq. 6.1 (Hogg 2014). Then, the normality of the samples for each satellite product was tested using the Shapiro-Wilk test (Shapiro and Wilk 1965).

$$n = \frac{Z_{\alpha/2}^2 \times p \times (1 - p)}{e^2} \quad (6.1)$$

Where:



$Z_{\alpha/2}^2$  is the Z-score associated with a level of confidence. For this analysis, the level of confidence chosen was 99.5

$p$  is the probability of having a specific frequency class in the population (50%).

$\epsilon$  is the margin of error (0.03)

Once the sample size was estimated, stratified random sampling was performed. Each stratum was defined as the sets of pixels depicted as anomalous 0, 1, 2, 4, 5, 6, or 7 times during the cycle. Then, a random sample was selected independently within each stratum. The total sample size was allocated proportionally to the stratum size using Eq. 6.2. Finally, the random sample from each stratum was extracted by using the function `DataFrame.sample` available in the Pandas Python library (Reback et al. 2021).

$$n_i = n \frac{N_i}{N} \quad (6.2)$$

Where:

$n_i$  is the sample size within the stratum  $i$

$n$  is the total sample size as defined in Eq. 6.1

$N_i$  is the total stratum size

$N$  is the total number of pixels available for all strata

#### 6.2.2.2 Hypothesis testing

Since the samples' distribution for most of the satellite products did not have a normal distribution, the non-parametric Kruskal-Wallis test was applied to determine whether any significant difference could be found between yield and frequencies of anomalies. The Kruskal-Wallis test (Kruskal and Wallis 1952) is aimed to test the hypothesis of group differences when the data is divided into three or more independent categories (Verma and Abdel-Salam 2019). The Kruskal-Wallis computation begins by combining all of the samples and rank ordering the values together. The H statistic is determined

using the Eq. 6.3 and compared with a table of critical values to examine the groups for significant differences (Corder and Foreman 2014). The null hypothesis  $H_0$  is tested against the alternative hypothesis  $H_1$  as follows:

$H_0$ : There is no significant difference between the mean yield of pixels that are marked as anomalous in 1, 2, 3, 4, 5, 6 and 7 scenes within a crop cycle.

$H_1$ : There is a significant difference between the mean yield of pixels that are marked as anomalous in 1, 2, 3, 4, 5, 6 and 7 scenes within a crop cycle.

$$H = \frac{12}{N(N+1)} \sum_{i=1}^k \frac{R_i^2}{n_i} - 3(N+1) \quad (6.3)$$

Where:

$N$  is the number of values from all combined samples

$R_i$  is the sum of the ranks from a particular sample

$n_i$  is the number of values from the corresponding rank-sum

When the Kruskal-Wallis H-statistic is significant, at least one of the samples is different from the other samples. However, it does not tell which pairs of groups are different (Verma and Abdel-Salam 2019). In order to determine which frequencies were significantly different from others, the Dunn's test was conducted as *post-hoc* testing. The Dunn's test performs pairwise comparisons between each independent class to indicate which groups are statistically significantly different at some level of  $\alpha$ . For example, is the yield significantly lower for a pixel registered as anomalous five times compared to the yield of a pixel that has been registered as anomalous only once?.

For each pairwise comparison, the null hypothesis is that the probability of observing a randomly selected value from one class that is larger than a randomly selected value from another class equals one-half (Alexis Dinno 2017). However, when making multiple comparisons at once, the probability of getting a false positive increases. A common approach to control the family-wise error rate is to adjust the p-values that result from

the multiple comparisons. Different adjustment methods have been proposed to adjust the p-values and control the type I error (e.g. Benjamini and Hochberg 1995; Dunn 1961; Hochberg 1988; Holm 1979; Sidak 1967).

The Dunn's test was performed in the R software (R Core Team 2018) using the `dunnTest` function available in the `FSA` package. The Benjamini-Hochberg method was used to adjust the p-value for multiple comparisons, and the nominal level of significance used in the multiple comparisons procedures was set to 0.05. For each pairwise comparison, the null hypothesis  $H_0$  is tested against the alternative hypothesis  $H_1$  as follows:

$H_0$ : There is no significant difference between the yield of pixels that are marked as anomalous  $m$  times within a crop cycle and the yield of those pixels that are marked as anomalous  $n$  times within a crop cycle

$H_1$ : There is a significant difference between the yield of pixels that are marked as anomalous  $m$  times within a crop cycle and the yield of those pixels that are marked as anomalous  $n$  times within a crop cycle

As the Dunn's test generates p-values for each pairwise comparison, the output tables of p-values produced by the algorithm were condensed into a compact letter display format. In the output, groups are separated by letters. Those classes sharing the same letter are not significantly different. Fig. 6.4 and Fig. 6.5 present a working example of the output table with the results of the Dunn's test and the compact letter display, respectively. Both figures show the results for the NDVI\_b8A\_6 frequency pixels. From both figures, it is possible to conclude that, for example, there are no significant differences between the yield values obtained when a pixel is marked as anomalous once during the crop cycle compared to the yield of a pixel that is marked anomalous three times during the growth cycle.

### 6.2.3 Impact of anomalies at different crop stages over yield

The anomaly-predicted S2 surfaces were compared with the final yield to identify if the presence of such anomalies at distinct growth stages impacted the productivity differently. To test this, the yield of a sample of anomalous plots was compared with the yield of a sample of non-anomalous plots at each of the five growth stages. The comparisons were

	Comparison	Z	P.unadj	P.adj
1	F_0 - F_1	6.9291707	4.233148e-12	1.269945e-11
2	F_0 - F_2	7.7092979	1.265118e-14	7.590708e-14
3	F_1 - F_2	3.0364252	2.394015e-03	3.591023e-03
4	F_0 - F_3	0.5706102	5.682639e-01	5.682639e-01
5	F_1 - F_3	-1.7579204	7.876106e-02	9.451327e-02
6	F_2 - F_3	-3.3449659	8.229270e-04	1.645854e-03

**Fig. 6.4** example of the Dunn's multiple comparison output for the NDVI\_b8A\_6 frequency pixels. The "Comparison" column describes each pairwise comparison (e.g. F\_1 - F\_2 compares the yields of those plots that were marked anomalous once and those that were marked as anomalous twice during the cycle); the Column "Z" contains the Z statistic for the difference between the two frequencies; The column "P.unadj" presents the original p-values calculated by the test. The column "P.adj" contains the p-values adjusted with the Benjamini-Hochberg method.

	Group	Letter	MonoLetter
1	F_0	a	a
2	F_1	b	b
3	F_2	c	c
4	F_3	ab	ab

**Fig. 6.5** example of the compact letter display format to present the result of the Dunn's test for the NDVI\_b8A\_6 frequency pixels. Those frequencies sharing the same letter are not significantly different at  $\alpha = 0.05$ .

made using the S2 and S1 products derived from images acquired during the typical rainfall period. The analysis was performed over a sample extracted from the pixels in 13 plots sown with four rice varieties. The selected plots were those whose growth cycle fell entirely within the typical period. The growth cycle begins on the planting date and finishes on harvest.

#### 6.2.3.1 Sample extraction

The sample was extracted using a stratified sampling approach applied over all the pixels in 13 plots which growth cycle fell completely within the typical period. The stratified sample was preferred to ensure that each growing stage received proper representation within the sample. In stratified random sampling, the population is partitioned into strata,

and a sample is selected randomly within each stratum (Chris B. Murphy and Margaret James 2021).

The sample size was estimated by using the Eq. 6.1 (Hogg 2014). Then, the normality of the samples for each satellite product was tested using the Shapiro-Wilk test (Shapiro and Wilk 1965). The values of  $Z_{\alpha/2}^2$ ,  $p$  and  $\epsilon$  were set to 99.5, 50%, and 0.03, respectively. Once the sample size was estimated, the stratified random sampling was performed. Each stratum represented a phenological stage (i.e. seedling, tillering, panicle formation, booting, and ripening). Then, a random sample was selected independently within each stratum. The total sample size was allocated proportionally to the stratum size using Eq. 6.2. Finally, the random sample from each stratum was extracted by using the function `DataFrame.sample` available in the Pandas Python library (Reback et al. 2021).

#### 6.2.3.2 Hypothesis testing

Anomalies occurring at particular points in the growing cycle may affect differently final yield. To test this, the yield for anomalous and non-anomalous pixels at each of the five growth stages was compared using an independent two-sample t-test when the two samples variances were equal. The Student's t-test for two samples was selected, as it is used to test whether the means of a measurement variable are different in two groups (McDonald 2014) and a Welch-Satterthwaite test when the variances were unequal (Student 1908). The analysis was performed over the sample extracted from the pixels in 13 plots sown with four rice varieties. The original t-test has four main assumptions: 1) The observations within each group are normally distributed; 2) the observations in the samples are independent of each other; 3) data are collected from a random sample from the population of interest, and 4) equal variances in the two groups (homoscedasticity). However, when the variances of the two groups were not equal, the Welch-Satterthwaite test was implemented instead (Welch 1947). Variance homogeneity was defined using Levene's test (Levene 1960).

Each individual in the anomalous sample represented the yield of a pixel pointed as anomalous at a specific growth stage by the EOAD. Similarly, each individual in the non-anomalous sample represented the yield of a pixel pointed as non-anomalous at a specific growth stage. An independent test was performed at each phenological stage using all the VI anomaly-predicted products. The null hypothesis  $H_0$  was tested against

the alternative hypothesis  $H_1$  for all the phenological stages as follows:

$H_0$ : There is no significant difference between the mean yield of pixels marked as anomalous at the stage M and the mean yield of pixels marked as non-anomalous at the stage M.

$H_1$ : There is a significant difference between the mean yield of pixels marked as anomalous at the stage M and the mean yield of pixels marked as non-anomalous at the stage M.

#### 6.2.4 Early detection of underperforming plots

The detection of anomalies can provide crucial information for plot-level management decisions; however, often, PA is focused on the ability of data to indicate or even predict yield. This section describes how the outputs of the EOAD, combined with crop agronomic data, were used to predict underperforming plots at early stages using ML approaches. If this relationship proves true, the EOAD might also help prioritise those fields that require more immediate attention.

First, two sets of variables were proposed as predictors of a classification model to predict underperforming plots. Both groups included agronomic features and metrics per plot derived from the VI surfaces, but the second group also included the percentage of the anomalous area detected with the EOAD in the plot. The aim was to determine whether including the metrics derived from the EOAD anomaly-predicted surfaces improved the predictability of underperforming plots. The continuous predictors were assessed for collinearity to select the independent features in the prediction model. Then, the historical farm yields were classified into high and low-performing, choosing 4 different thresholds. The resulting datasets for each threshold considered were balanced using an oversampling approach. The open-source Automated Machine Learning (AutoML) system TPOT was used to design the ML classifier pipeline to predict underperforming plots using the NDVI\_b8 data during the booting stage. TPOT automatically compares several machine learning techniques and tune the models' hyperparameters to find the best-performing algorithm using genetic programming (Le et al. 2020). The best pipeline obtained was trained for all VIs using the data available at each phenological stage for the two groups of predictors. The model performance was evaluated on the balanced

datasets for each threshold and VI at each growth stage using cross-validation for the Area under the ROC Curve (AUC-ROC).

#### 6.2.4.1 Model Predictors

Two sets of variables that included agronomic features, metrics derived from the VI surfaces, and the percentage of anomalous pixels within the plot were proposed to predict underperforming plots at each single growth stage. Agronomic features and vegetation indices have been used for crop yield estimation, either empirically or mechanistically, as input of crop models (Panda et al. 2010; Weiss et al. 2020). No previous studies have used variables related to the presence of in-field anomalies as predictors of crop yield; however, in this research, the percentage of anomalies within the plot was included to determine whether the anomalies detected with the EOAD improved the predictability of underperforming plots. The two sets of proposed predictors per plot are presented in Table 6.2.

**Table 6.2** Two sets of predictors per plot proposed to predict underperforming plots

Predictor	Set A	Set B
Mean VI per plot	X	X
Standard deviation of VI values within the plot (std VI)	X	X
Average of the non-anomalous VI values within the plot (Mean non-anomalous VI)	X	X
Average of the anomalous VI values within the plot (Mean anomalous VI )	X	X
Rice cultivar	X	X
Emergence month	X	X
Percentage of the anomalous area in the plot (% anomalies)		X

#### 6.2.4.2 Multicollinearity and feature selection

A multicollinearity diagnosis was performed among the continuous predictors proposed to guarantee no linear correlations between the explanatory variables and select the independent features in the prediction model. Although ML algorithms such as Random Forest have shown to be less sensitive to collinearity, a strong degree of correlation between variables can impact the models' stability and limit their prediction capabilities because highly correlated predictors can lead the models to overfit (Montgomery et al. 2012; Rosipal et al. 2001). Accounting for multicollinearity is particularly important when modelling variables in agricultural systems as many of them are often highly correlated with and within each other (Jeong et al. 2016).

The multicollinearity among continuous variables at each phenological stage was assessed using a Pearson correlation matrix. The aim was to determine the explanatory variables for which there were no linear correlations at any of the phenological stages studied. Correlation values larger than  $|0.70|$  indicated substantial collinearity between two variables.

#### 6.2.4.3 Yield thresholding

A set of thresholds were established to classify the historical farm yield into high and low. These are the two categories that the classifier will predict. The thresholds were chosen in terms of the different number of standard deviations away from the farm yield mean, as presented in Table 6.3. This thresholding strategy was chosen due to its simplicity as it only relies on historical yield records; however, it can be adapted based on the requirements of each agricultural system.

**Table 6.3** Yield thresholds.

Threshold	1	2	3	4
Value	$\bar{X}$	$0.5 \sigma$	$\sigma$	$1.5 \sigma$



#### 6.2.4.4 Balancing data

In many classification problems, the data are imbalanced; that is, the classes are not represented equally (Awad and Khanna 2015). For most machine learning techniques, a minor imbalance is not a problem. However, if the minority class has many fewer samples than the majority class, imbalanced data presents a significant challenge for classification algorithms as the model will be biased towards the majority class. The training data was balanced for high/low yields at each threshold by random oversampling to reduce the problems that imbalanced data can create in the classification (Japkowicz and Stephen 2002). Balancing was done independently for each VI and threshold at the different growth stages.

Undersampling and oversampling methods are the most used approaches to deal with imbalanced data. Undersampling methods randomly eliminate instances of the majority class, reducing the number of observations from the majority class and balancing the dataset. It is recommended only when the datasets are very large as undersampling results in information loss for the majority class (Awad and Khanna 2015). Oversampling methods randomly duplicate records from the minority class (Risal et al. 2021). This technique is more suitable for small datasets, however, it might increase the chances of overfitting when the dataset is severely imbalanced (Fernandez et al. 2018).

In this research, the dataset was balanced by randomly oversampling the minority yield class with replacement using the resampling module from Scikit-Learn (Pedregosa et al. 2011). Oversampling with replacement means that the examples from the minority class chosen and added to the new "more balanced" dataset can be selected more than once. The minority yield class varied depending on the thresholds used to classify the crop plots into high and low-performing (See Section 6.2.4.3).

#### 6.2.4.5 Model Selection

The Tree-based Pipeline Optimisation Tool (TPOT) was used to design the ML classifier pipeline to predict underperforming plots. Building a ML classification model is a time-consuming experimentation process as it involves performing repetitive operations such as hyperparameter tuning, implementing a range of modelling algorithms/approaches with a range of parameter sets. TPOT was selected because it automatically compares

several machine learning techniques and tunes the models' hyperparameters to find the best-performing one using less time than is required if these operations were coded manually. TPOT (Le et al. 2020) is an open-source genetic programming-based Automated Machine Learning (AutoML) system that optimises automatically a series of preprocessing operations and machine learning models to maximise the classification accuracy (Olson and Moore 2019). TPOT is a wrapper for the Python scikit-learn package (Pedregosa et al. 2011). A wrapper is a Python module that allows using Python to interface with programs written in other programming languages through the Application Programming Interface (API) of those programs (Toms 2015).

The TPOT classifier class (TPOTClassifier) was used over the two groups of predictors using the NDVI\_b8 data during the booting stage. These phenological states were selected for the definition of the model because the anomalies found during such age showed to affect the crop yield (See section 6.3.2) significantly. The aim was to define the classifier trained on each set of variables retrieved from all the VI at each phenological stage. The TPOT classifier was run using the hyperparameters presented in Table 6.4. The pipelines performance was assessed at each growth stage using a K-fold cross-validation for the AUC-ROC (Bradley 1997; Hanley and McNeil 1982). The AUC-ROC was chosen over other metrics such as the classification accuracy because it represents better the classifier performance as it is independent of the classification threshold selected and does not depend on the imbalance of the training set (Kołcz et al. 2003; Rokach and Maimon 2008). The dataset used to train the models was divided so that 75% would be used as the training set while the remaining 25% would be used as the test set.

**Table 6.4** Parameters entered in TPOT to find the best pipeline to predict the high/low yield classes using the NDVI\_b8 data at the seedling and booting stages

Parameter	Description	Value
generations	number of iterations to the run pipeline optimisation process.	50
population_size	number of individuals to retain in the genetic programming population every generation	50
offspring_size	number of offspring to produce in each genetic programming generation.	Population size (default)

Parameter	Description	Value
mutation_rate	Mutation rate for the genetic programming algorithm in the range. This parameter tells the GP algorithm how many pipelines to apply random changes to every generation.	0.9 (default)
crossover_rate	Crossover rate for the genetic programming algorithm in the range. This parameter tells the genetic programming algorithm how many pipelines to "breed" every generation.	0.1 (default)
scoring	Function used to evaluate the quality of a given pipeline for the classification problem.	Area under the ROC Curve (AUC-ROC)
cv	Number of cross-validation folds	5

#### 6.2.4.6 Model training and validation at multiple growth stages

The resulting best pipeline from executing the TPOTClassifier was trained for all VIs using the data available at each phenological stage using the two groups of predictors. The model performance was evaluated for each threshold and VI at each growth stage using a K-fold cross-validation for the AUC-ROC (Bradley 1997; Hanley and McNeil 1982). Similar to model selection, the AUC-ROC was selected because it represents better the classifier performance as it is independent of the classification threshold selected and does not depend on the imbalance of the training set (Kołcz et al. 2003; Rokach and Maimon 2008).

The cross-validation was carried out using the Stratified K-Folds cross-validator from the ScikitLearn library. Each dataset was split into five (5) folds. The mean and standard deviation of the resulting 5 AUC-ROC curves were calculated and compared among the

multiple VI at each growth stage. The cross-validation testing was chosen because it avoids the instability that can bring the process of a single split of sampling when the experiment is repeated with a new division, providing a more reliable perspective on how the model is expected to perform on out of sample data (Azzalini and Scarpa 2012).

## 6.3 Results

### 6.3.1 Impact of frequency of anomalies on yield

A Kruskal-Wallis test was conducted to evaluate differences in yield among multiple frequencies of S1 and S2 anomalies detected during the growing season. Table 6.5 shows the Kruskal-Wallis metrics derived from comparing yield among pixels with different frequencies of anomalies using S2 and S1 products.

**Table 6.5** Kruskal-Wallis metrics derived from the comparison of yield for pixels with different frequencies of anomalies using S2 and S1 products.

Product type	VI/SAR product	df	H-statistic <sup>a</sup>
S2	CIg_b8	4	47.83**
S2	CIg_b8a	4	49.3**
S2	CIre_b8_5	4	75.7**
S2	CIre_b8_6	4	94.28**
S2	CIre_b8_7	6	55.85**
S2	CIre_b8a_5	5	42.38**
S2	CIre_b8a_6	3	58.74**
S2	CIre_b8a_7	3	25.4**
S2	EVI_b8	6	92.94**
S2	EVI_b8a	6	111.92**
S2	GNDVI_b8	5	101.98**
S2	GNDVI_b8a	5	72.27**
S2	NDII_b8_11	6	298.11**
S2	NDII_b8_12	6	168.8**
S2	NDII_b8a_11	6	243.59**
S2	NDII_b8a_12	6	214.96**

Product type	VI/SAR product	df	H-statistic <sup>a</sup>
S2	NDVI_b8	6	79.34**
S2	NDVI_b8a	6	146.6**
S2	RENDVI_b8_5	5	86.04**
S2	RENDVI_b8_6	6	94.76**
S2	RENDVI_b8_7	6	48.07**
S2	RENDVI_b8a_5	5	68.94**
S2	RENDVI_b8a_6	3	101.67**
S2	RENDVI_b8a_7	3	30.27**
S2	SAVI_b8	6	119.31**
S2	SAVI_b8a	6	96.53**
S1	VH_asc	3	1.39
S1	VH_des	3	5.36
S1	VV_asc	4	2.86
S1	VV_des	3	6.63
S1	VV_div_VH_asc	3	3.24
S1	VV_div_VH_des	3	13.74**

\*\* Significant at  $\alpha = 0.005$

<sup>a</sup> The greener the cell, the more significant the difference among the yield of the different frequencies for a particular VI or SAR product.

The optical VIs showed a significant difference ( $\alpha = 0.05$ ) in yield for pixels identified as anomalous on multiple occasions using all VIs tested. The frequency of detected anomalies during the crop cycle using SAR products was lower than those obtained using optical VIs. Although it was possible to retrieve up to 13 SAR products within a cycle, no pixel was found anomalous in more than four (4) scenes. In contrast with optical VIs, most SAR products did not show differences in yield between pixels that experienced different frequencies of anomalies. Only the descending VV/VH product showed a statistically significant difference in yield among different frequencies along the cycle.

Despite the significant differences in yield among different frequencies of anomalies during the cycle for most products, there are no clear yield variation trends in relation to the number of scenes in which a pixel was flagged as anomalous. The results of

the pairwise comparisons using Dunn's test were summarised using a compact letter display and presented in the top axes of the box plots in Fig. 6.6. They evidence that there are no significant differences between several pairs of frequencies. Those classes sharing the same letter are not significantly different. For example, the Kruskal-Wallis test showed significant differences among the yield of pixels marked anomalous in multiple NDVI\_b8 scenes. However, the yield for those pixels that were never detected as anomalous was not significantly different from those marked 3 or 6 times anomalous during the growth cycle.

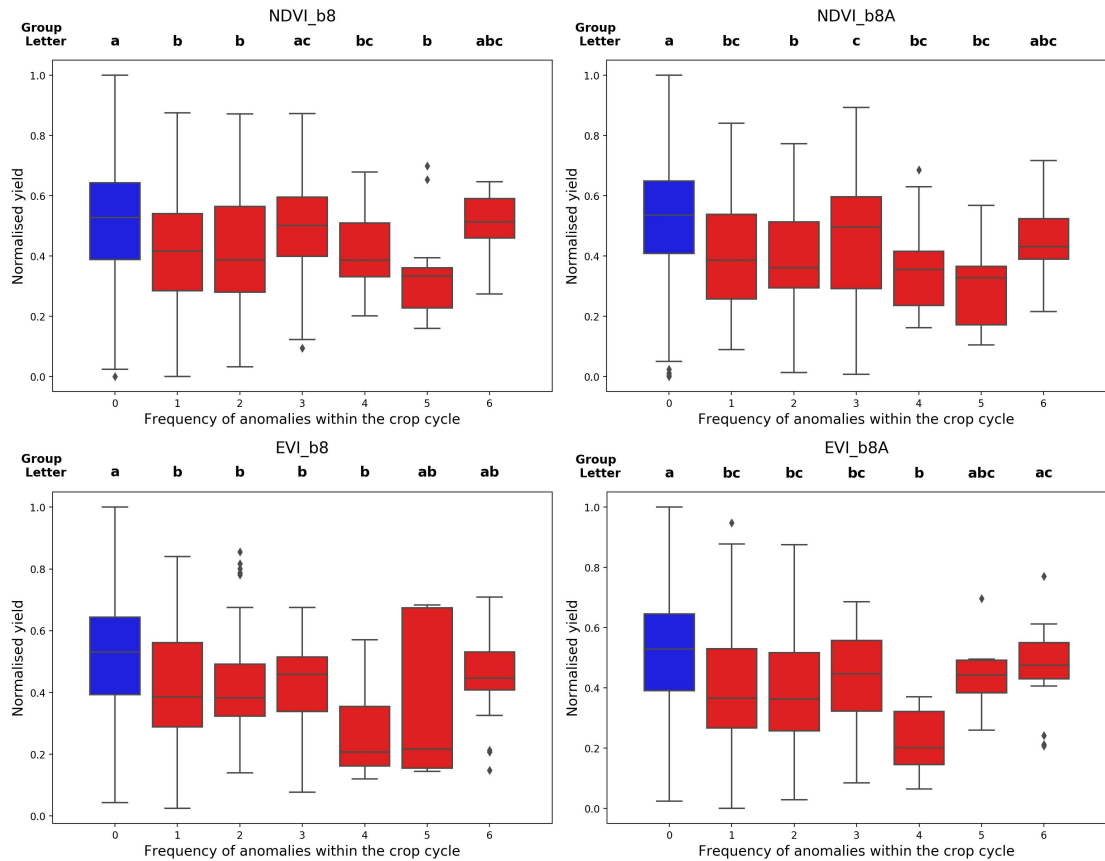


**Fig. 6.6** Box plots of yield per number of scenes in which the pixels are predicted anomalous within one crop cycle. Groups of data sharing the same letter are not significantly different.

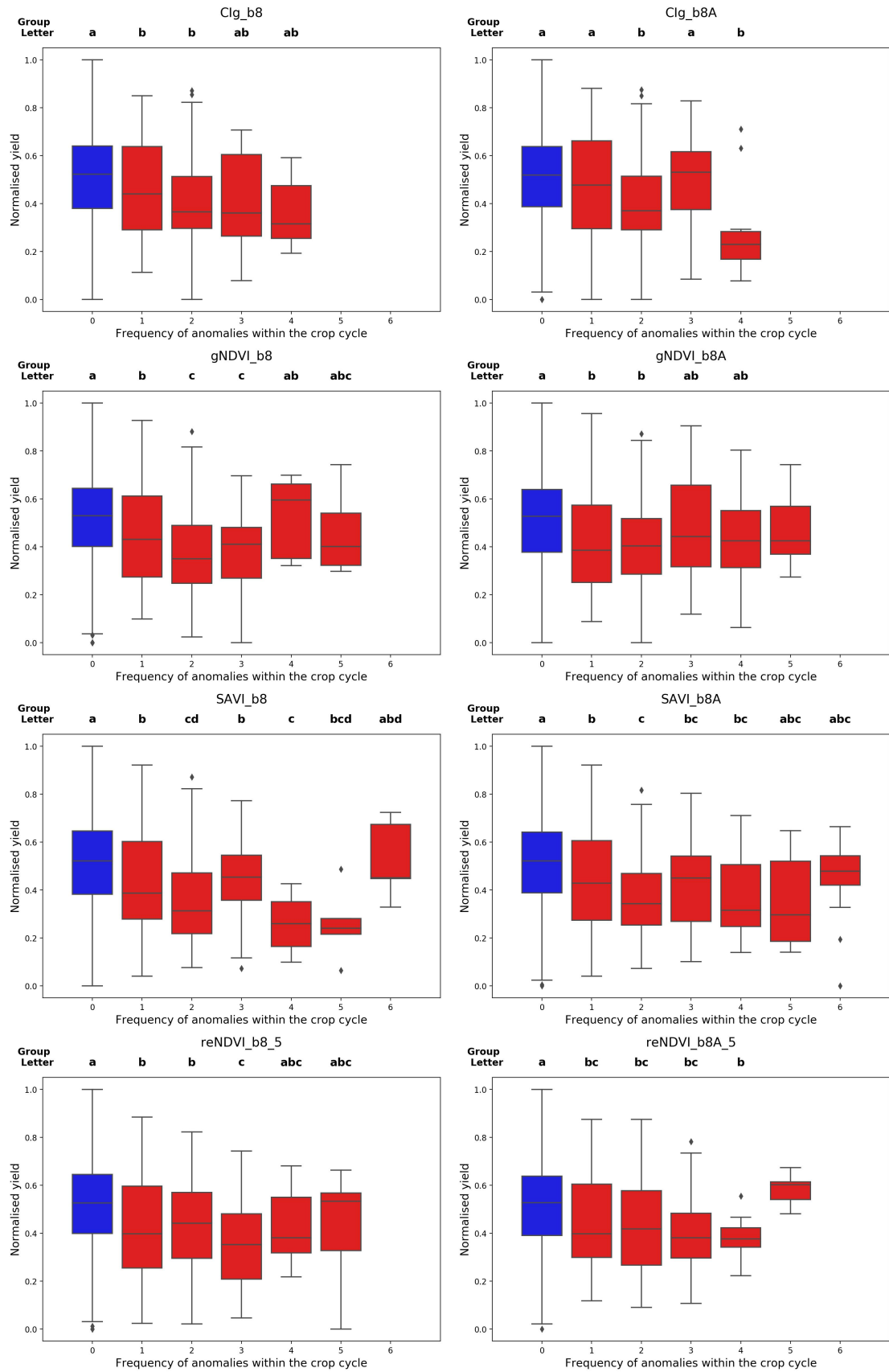


**Fig. 6.6 (cont.)** Box plots of yield per number of scenes in which the pixels are predicted anomalous within one crop cycle. Groups of data sharing the same letter are not significantly different.

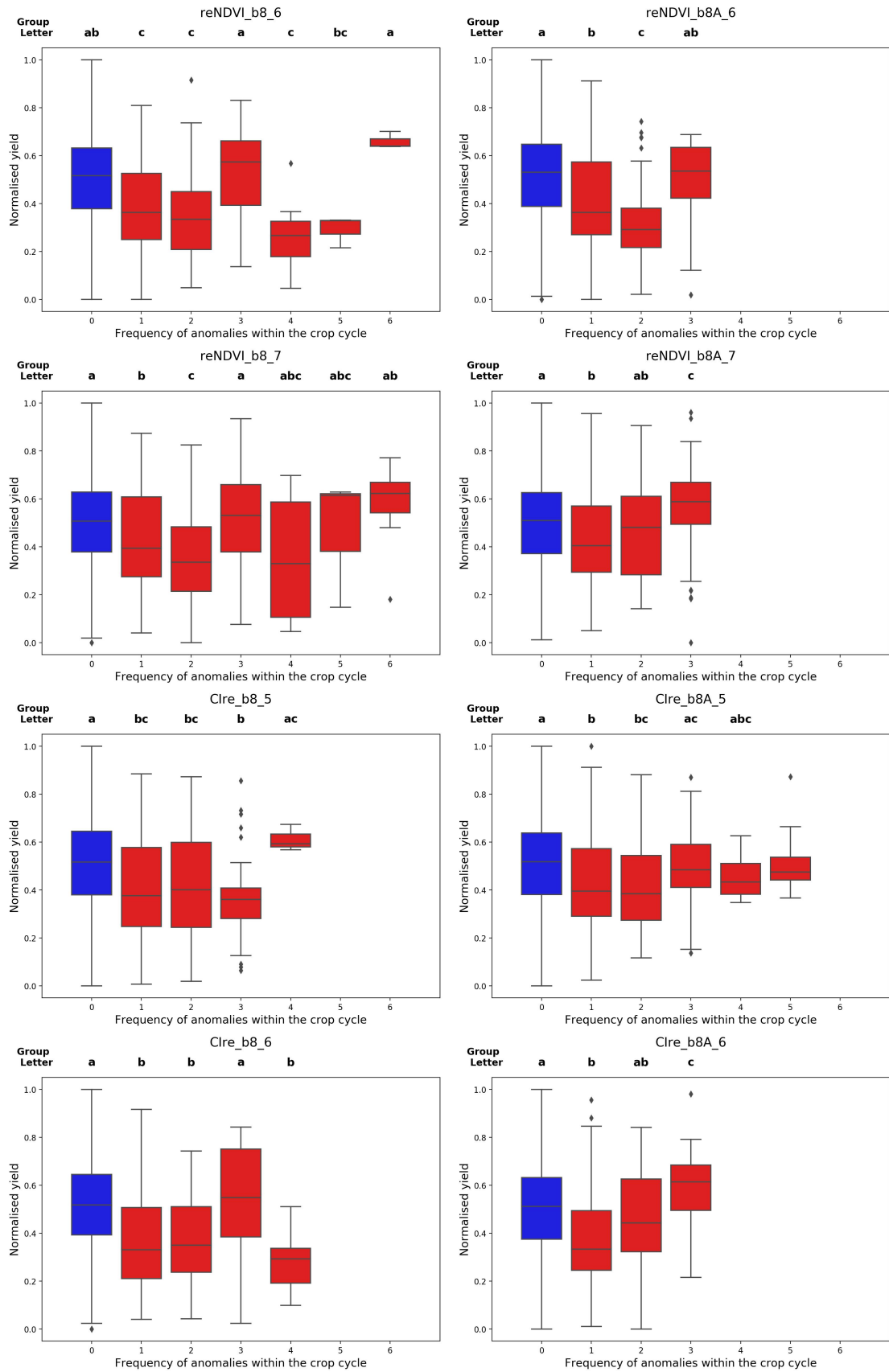


**Fig. 6.6 (cont.)** Box plots of yield per number of scenes in which the pixels are predicted anomalous within one crop cycle. Groups of data sharing the same letter are not significantly different.



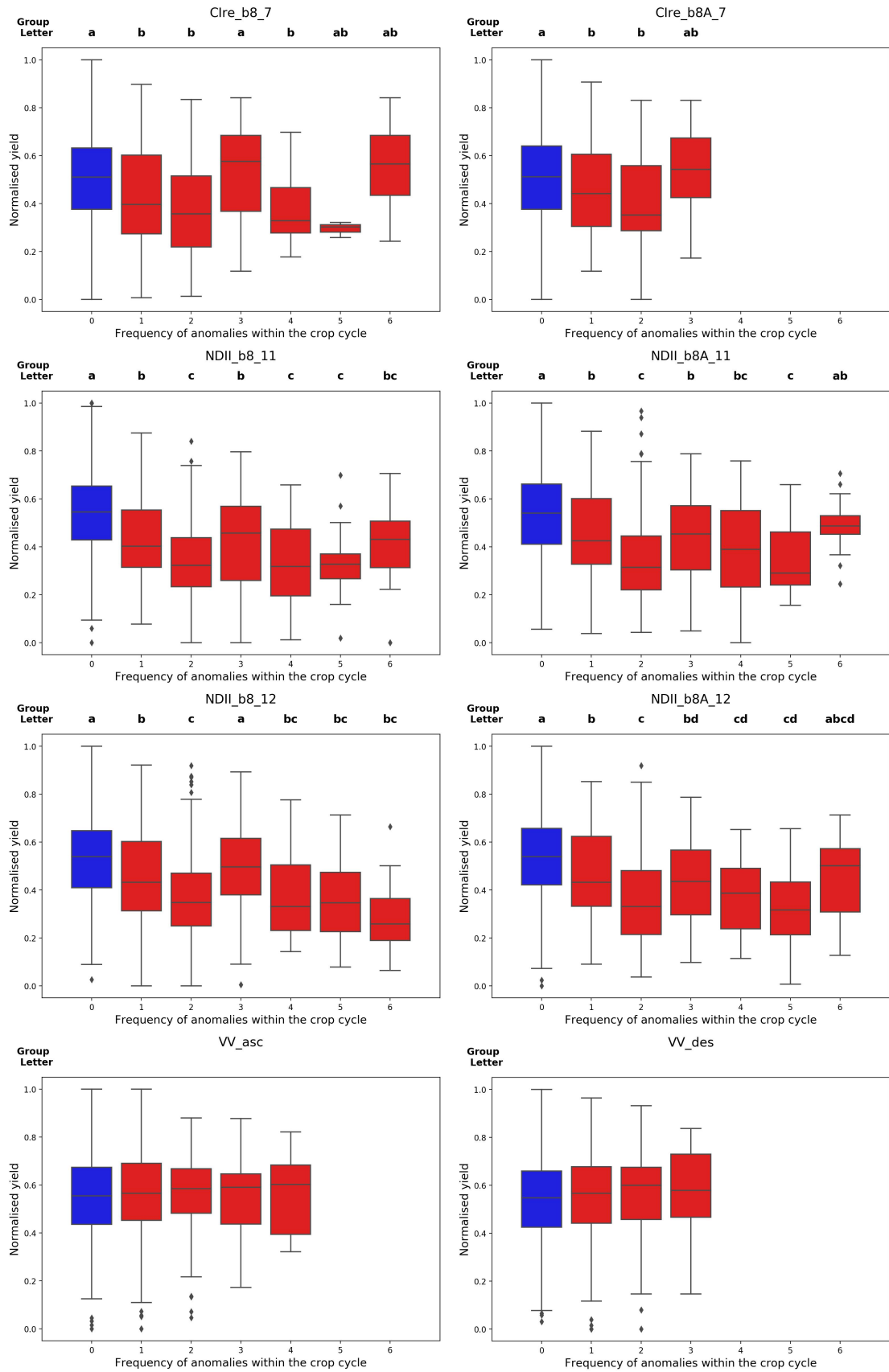


**Fig. 6.6 (cont.)** Box plots of yield per number of scenes in which the pixels are predicted anomalous within one crop cycle. Groups of data sharing the same letter are not significantly different.

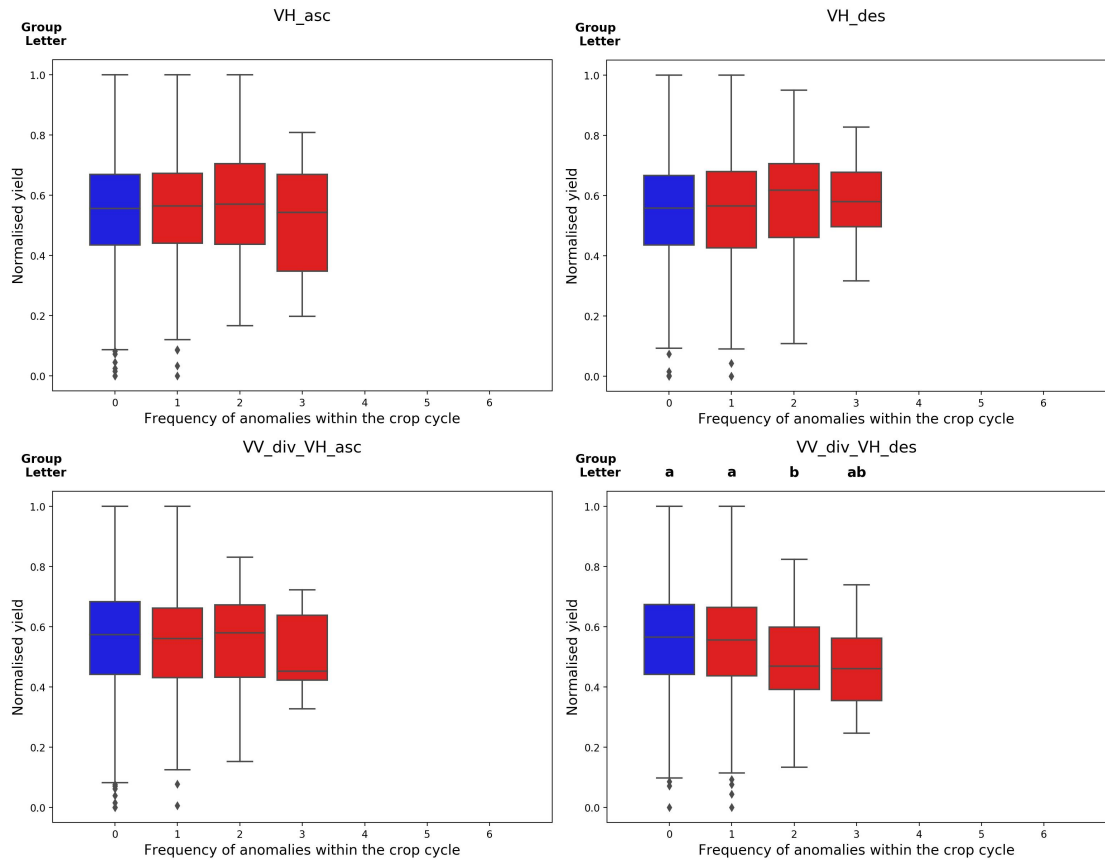


**Fig. 6.6 (cont.)** Box plots of yield per number of scenes in which the pixels are predicted anomalous within one crop cycle. Groups of data sharing the same letter are not significantly different.

### 6.3.2 Impact of anomalies at different crop stages over yield

Fig. 6.7 shows the normalised yield obtained for anomalous and non-anomalous pixels detected by applying the EOAD on different VIs. It also presents the t-scores from comparing the yield between anomalous and non-anomalous pixels. In general, most of the anomalies detected using the narrow NIR band VIs provided a better explanation of yield compared with those indices estimated with the band 8.

The booting stage showed to be consistently the phase at which the anomalies detected had a more significant impact on yield. For 35% of the VIs assessed, the anomalies detected at this stage showed a significant impact on yield at  $\alpha = 0.005$ . The most significant differences in yield between anomalous and non-anomalous pixels during the booting stage were obtained when applying the EOAD over the `RENDVI_b8A_6` and

the GNDVI\_b8A surfaces.

The shortwave infrared-based index NDII calculated with the band 8 showed significant differences ( $\alpha = 0.005$  and  $\alpha = 0.05$ ) in yield between anomalous and non-anomalous areas occurring during the seedling stage. Yields for anomalous pixels found with the NDII (band 8) tended to be higher. The NDII values of anomalous pixels were primarily positive and associated with areas with a higher soil and plant water content, based on the visual observations in the field. NDII is a well-known indicator of water content, in particular, the region of 2190 nm (Sentinel-2 band 12) has shown to be more sensitive to soil moisture than band 11 at 1640 nm (Wang et al. 2008). At the tillering stage, only the anomalies detected with the RENDVI\_b8A\_6 and RENDVI\_b8\_6 showed a significant impact on final productivity at  $\alpha = 0.005$ . However, at a lower level of significance ( $\alpha = 0.05$ ), the anomalies detected at this stage significantly impacted yield in 42% of the VIs assessed. The panicle formation stage was the only growth phase at which none of the VIs produced anomalies that impacted rice productivity significantly ( $\alpha = 0.005$ ).

As expected, for those indices that demonstrated lower accuracies at detecting in-field anomalies, the pixels marked as anomalous were not significantly associated with the final yield at any of the crop growth phases. They include the vegetation indices aimed for chlorophyll content estimation (i.e.  $CI_{green}$ ,  $CI_{Red-edge}$ ) and those that used the S2 band 7. Surprisingly, despite the higher accuracy shown by the SAVI to detect in-field anomalies, such anomalies did not impact productivity at any phenological stage.

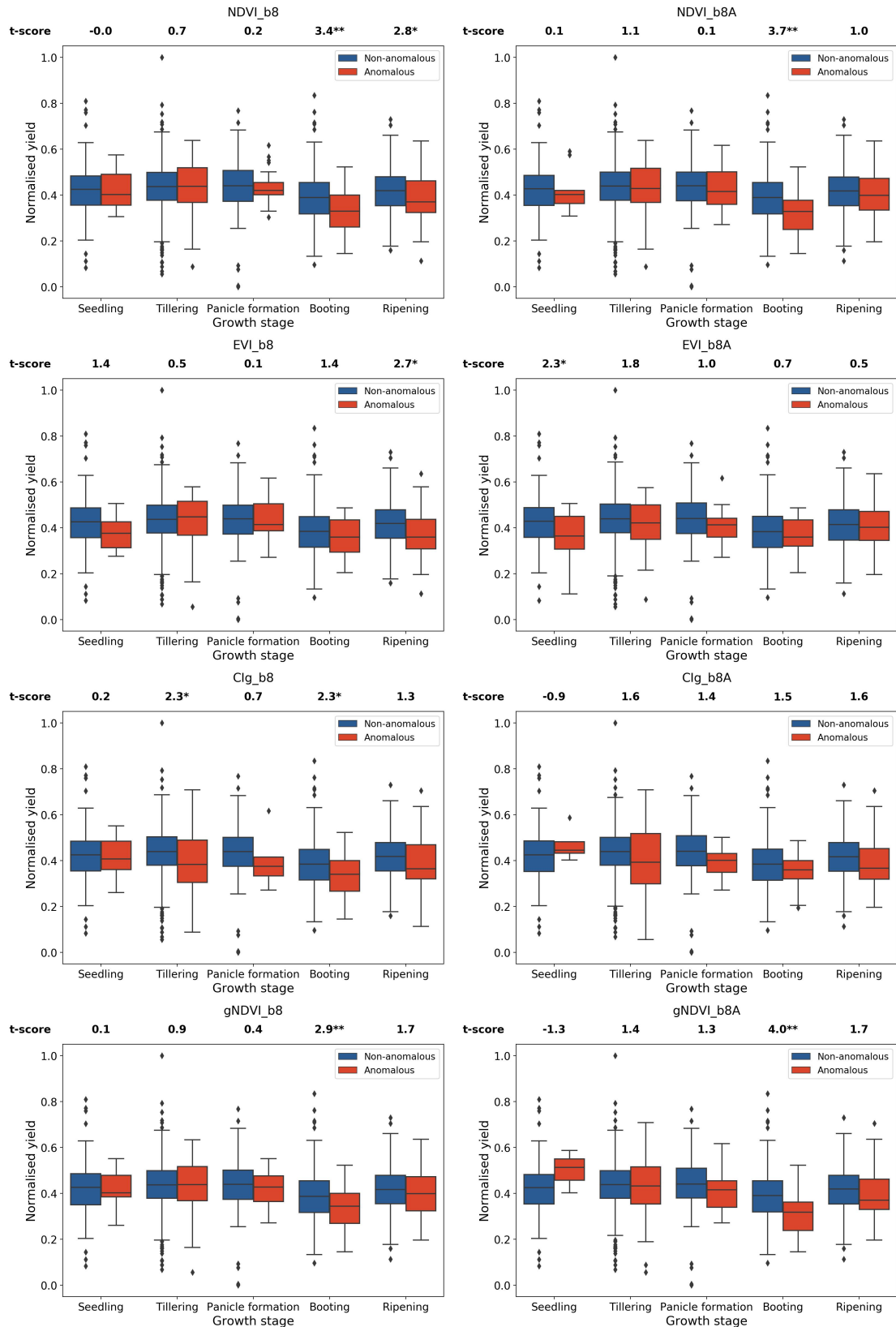


**Fig. 6.7** Box plots of yield obtained for anomalous and non-anomalous pixels values at different growth stages. The t-test values correspond to each pairwise comparison between pixels predicted as non-anomalous (blue box-plot) and those predicted as anomalous (red box-plots) \*\* Significant at  $\alpha = 0.005$ ; \* Significant at  $\alpha = 0.005$

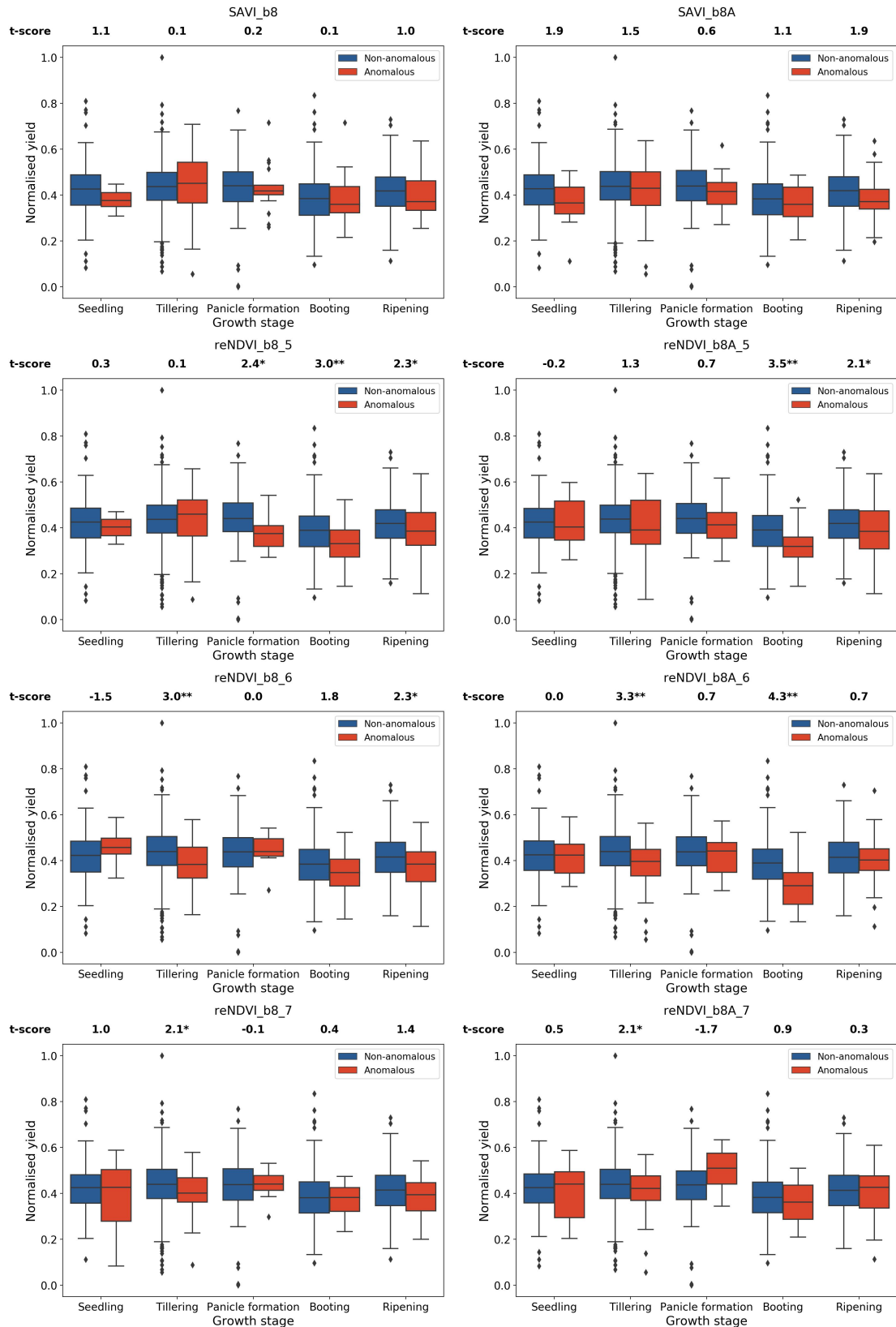


**Fig. 6.7 (cont.)** Box plots of yield obtained for anomalous and non-anomalous pixels values at different growth stages. The t-test values correspond to each pairwise comparison between pixels predicted as non-anomalous (blue box-plot) and those predicted as anomalous (red box-plots) \*\* Significant at  $\alpha = 0.005$ ; \* Significant at  $\alpha = 0.05$ .

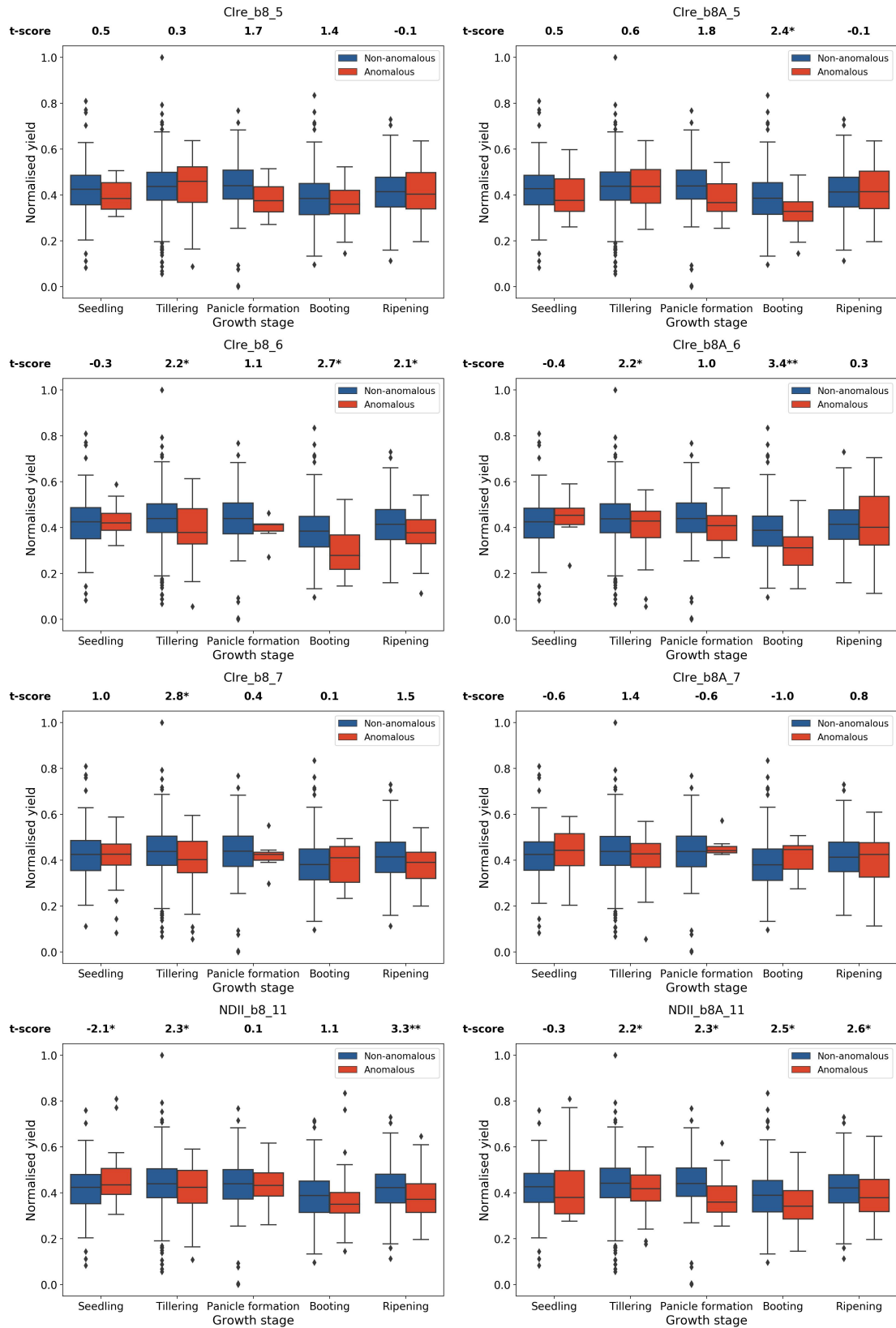


**Fig. 6.7 (cont.)** Box plots of yield obtained for anomalous and non-anomalous pixels values at different growth stages. The t-test values correspond to each pairwise comparison between pixels predicted as non-anomalous (blue box-plot) and those predicted as anomalous (red box-plots) \*\* Significant at  $\alpha = 0.005$ ; \* Significant at  $\alpha = 0.05$ .

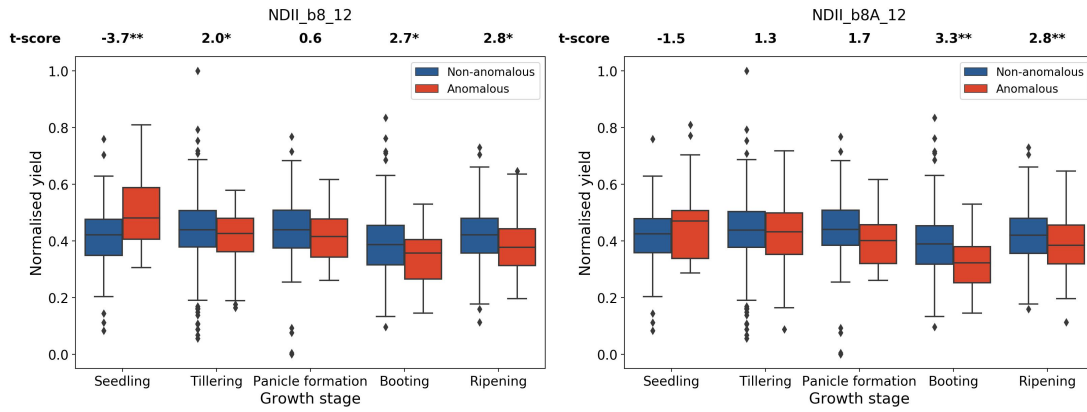


**Fig. 6.7 (cont.)** Box plots of yield obtained for anomalous and non-anomalous pixels values at different growth stages (VIs that showed the highest accuracy and TSS). The t-test values correspond to each pairwise comparison between pixels predicted as non-anomalous (blue box-plot) and those predicted as anomalous (red box-plots) \*\* Significant at  $\alpha = 0.005$ ; \* Significant at  $\alpha = 0.05$ .

### 6.3.3 Early detection of underperforming plots

#### 6.3.3.1 Multicollinearity and feature selection

Building upon performance improvements offered by the metrics derived from the VI surfaces and the anomalies detected with the EOAD, further RS variables were explored to maximise the prediction of underperforming plots. Figures 6.8 - 6.12 present a Pearson's coefficient heatmap, demonstrating collinearity between continuous variables. Stronger collinearity between the metrics derived from the VI surfaces is present, most prominently between the average VI values of the plot and the mean values of anomalous and non-anomalous pixels. The only variable that did not show collinearity with any other proposed predictor was the percentage of anomalies derived from the anomaly-predicted rasters.

Based on the results for the collinearity evaluation, the mean VI per plot is the only VI-derived metric to be considered as a predictor for the yield classification model. This, as the mean VI per plot provides a better overall perspective of the whole plot status than other metrics. Although the VI standard deviation per plot was correlated with other variables on fewer occasions than the other VI-derived metrics, it showed a strong correlation ( $\geq |0.7|$ ) with the mean VI per plot for some indices during the tillering stage (e.g.  $CI_{green}$ ,  $CI_{Red-edge}$ ).

As no collinearity evaluation was performed for the agronomic variables (i.e. emergence month and crop variety), they were kept as predictors. The two sets of definitive predictors used for the classification model are presented in Table 6.6.

**Table 6.6** Two sets of definitive predictors to be used in the yield classification model

Predictor	Set A	Set B
Mean VI per plot	X	X
Rice cultivar	X	X
Emergence month	X	X
Percentage of anomalous area in the plot (% anomalies)		X



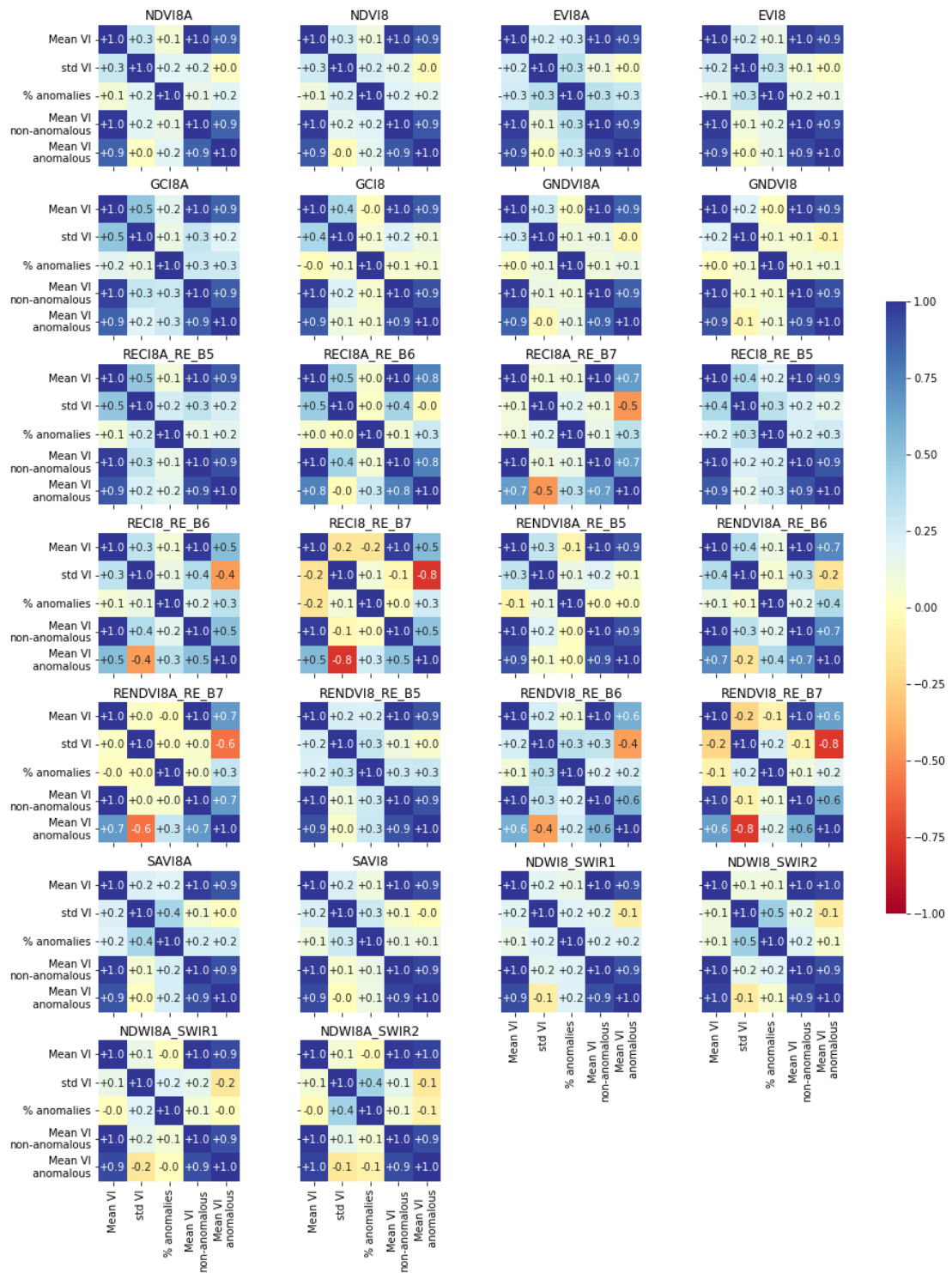


**Fig. 6.8** Heat maps presenting Pearson's correlation analysis of proposed variables to predict underperforming plots using different VIs during the seedling stage.

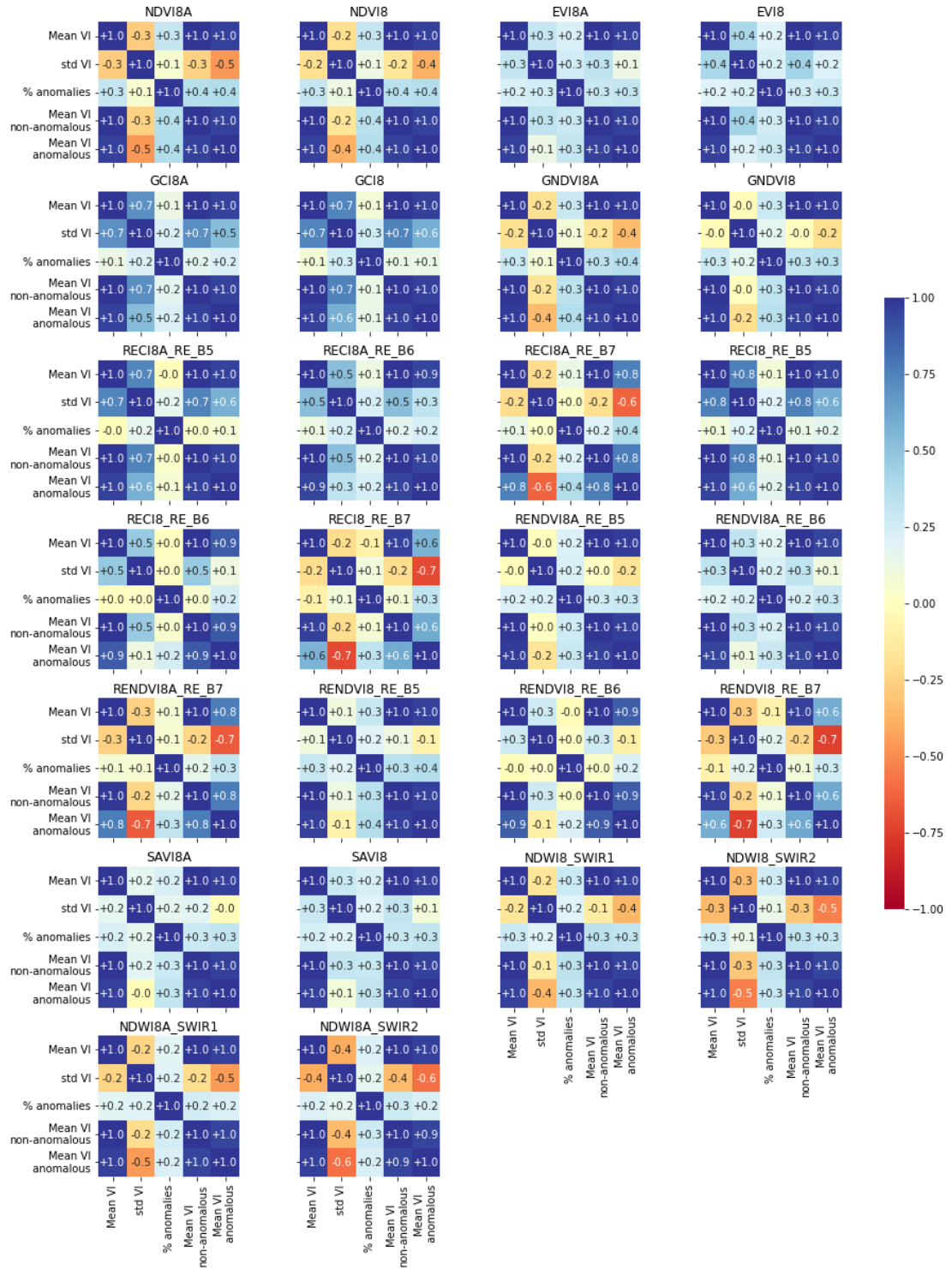


**Fig. 6.9** Heat maps presenting Pearson's correlation analysis of proposed variables to predict underperforming plots using different VIs during the tillering stage.

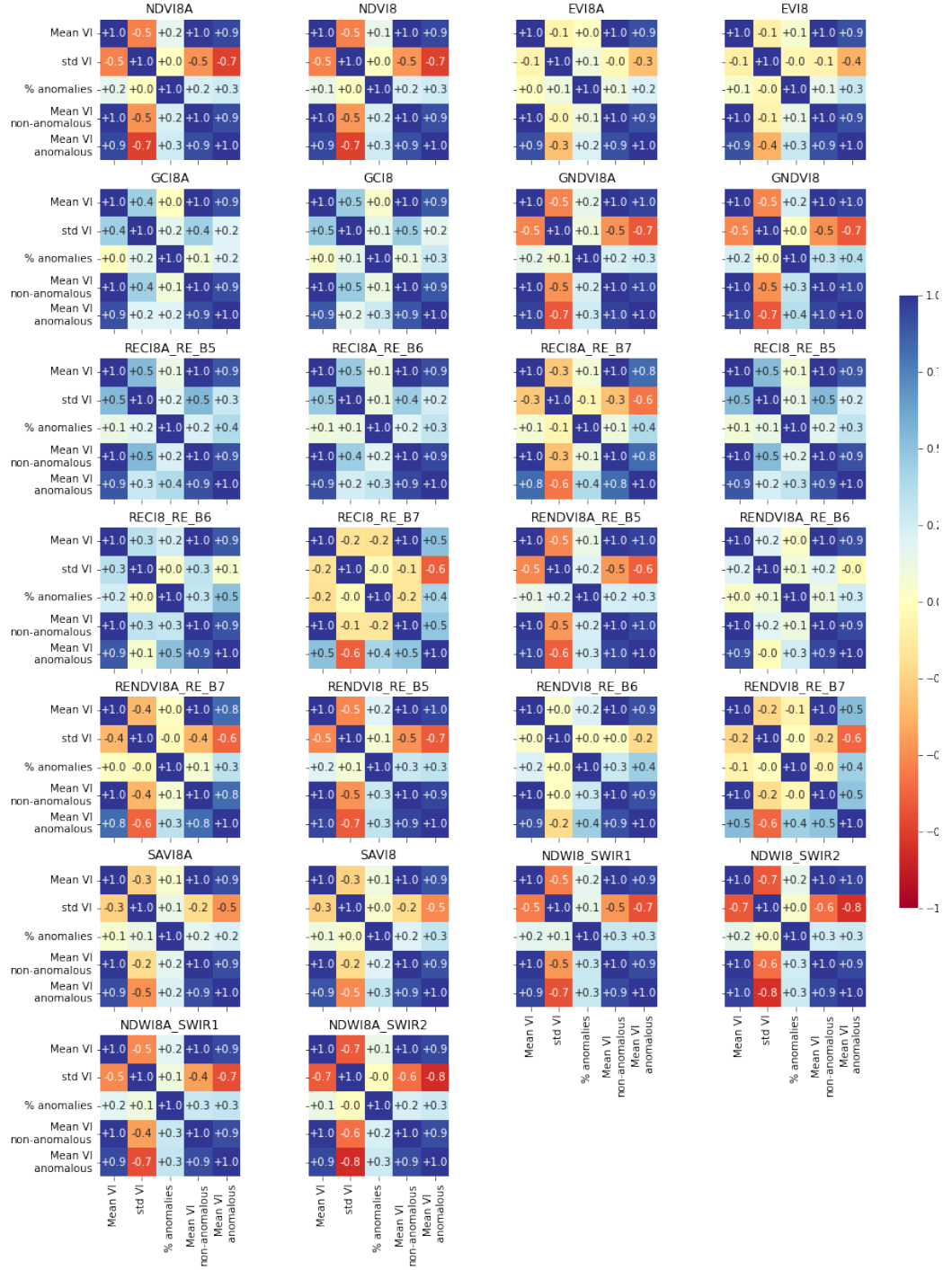


**Fig. 6.10** Heat maps presenting Pearson's correlation analysis of proposed variables to predict underperforming plots using different VIs during the panicle formation stage.

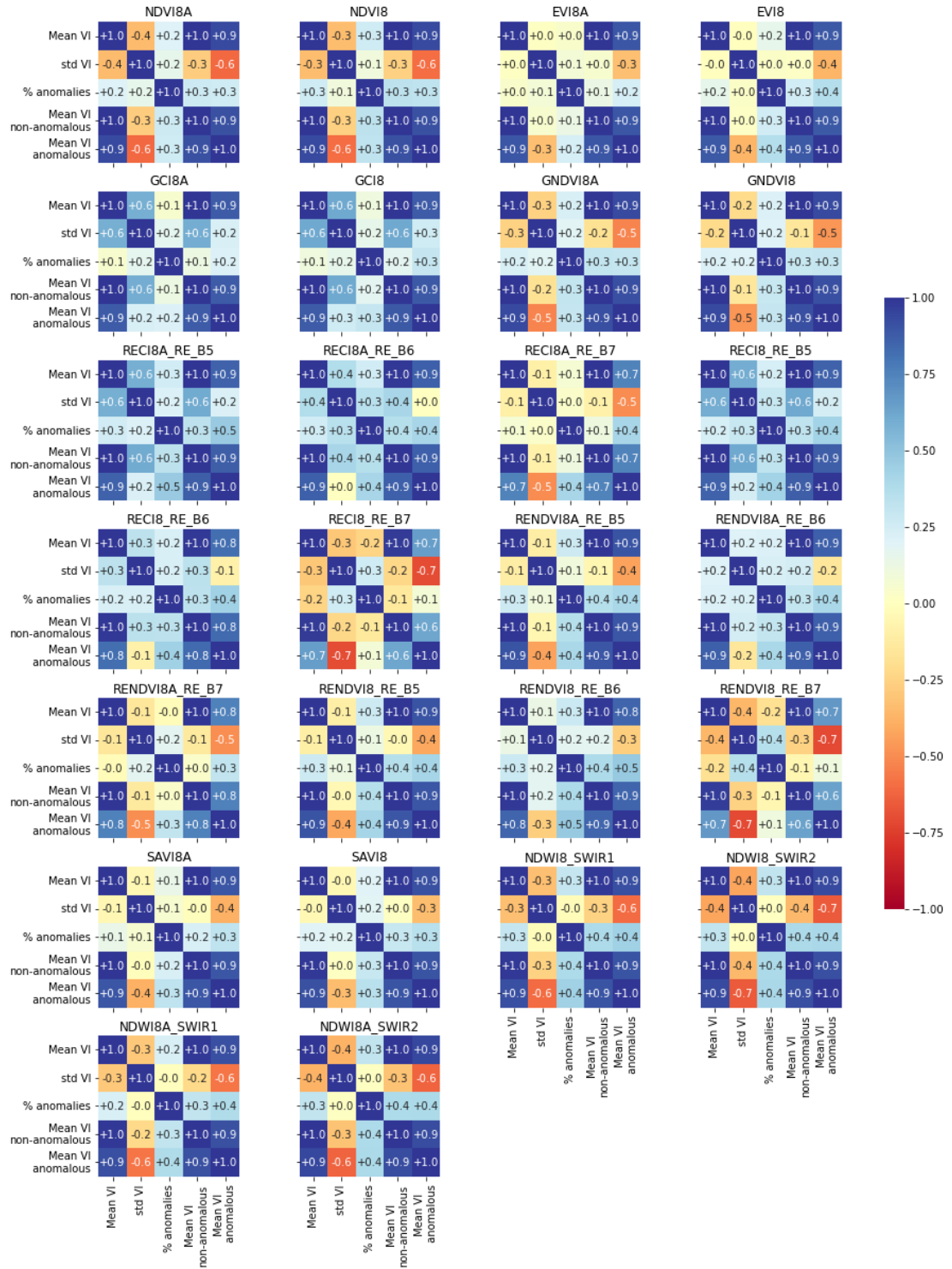


**Fig. 6.11** Heat maps presenting Pearson's correlation analysis of proposed variables to predict underperforming plots using different VIs during the booting stage.

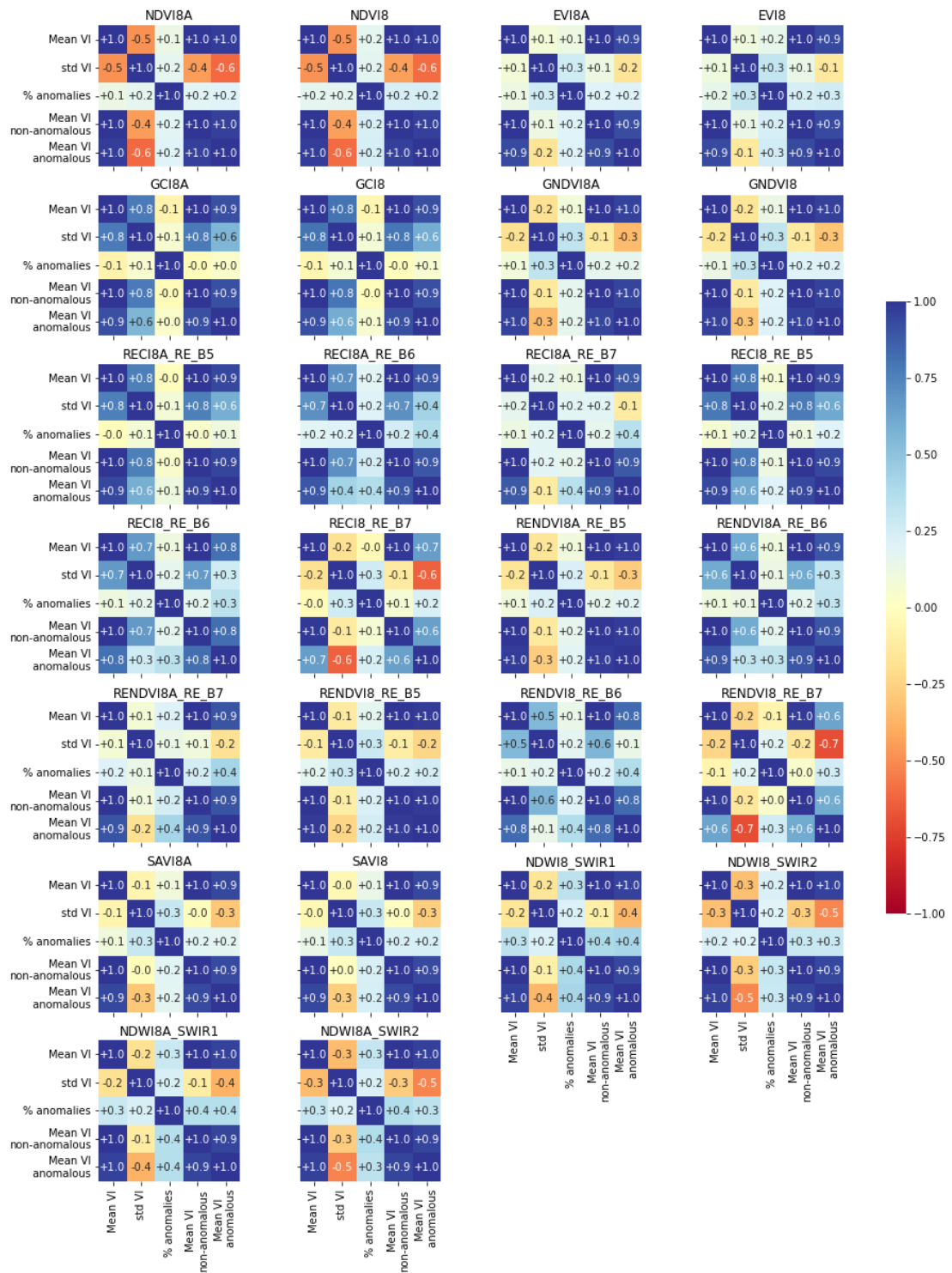


**Fig. 6.12** Heat maps presenting Pearson's correlation analysis of proposed variables to predict underperforming plots using different VIs during the ripening stage.

### 6.3.3.2 Yield thresholding

The histogram of the historical average plot yields in the farm and the four thresholds defined to classify plots into high and low performing are presented in Fig. 6.13. The

farm historical yields per plot follow a normal distribution, with a mean value of 8.3 t/ha. The thresholds selected were all larger or equal to the mean historical values. This, as the farmers aim to constantly obtain yields above the average and early detect those plots that might not comply with such high productivity expectations. Fig. 6.7 presents the number of plots per yield category for each threshold that will be used to train and test the predicting model.

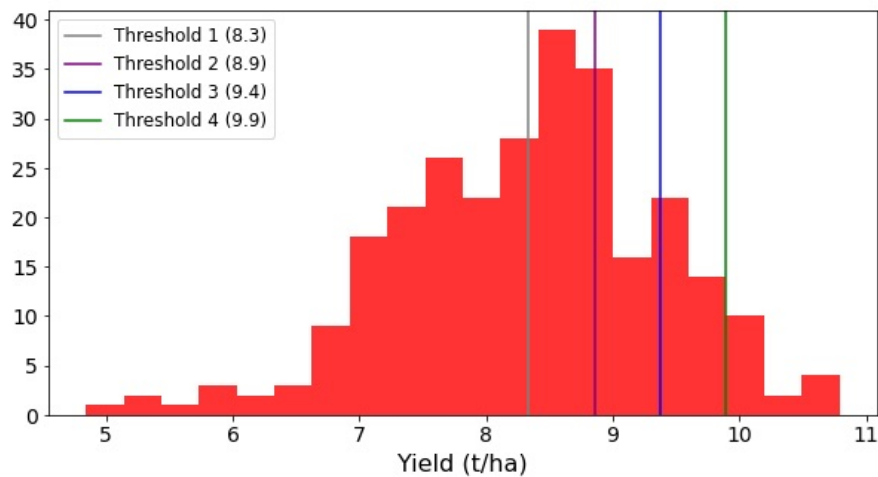


**Fig. 6.13** Histogram of farm average yield values per plot and thresholds used to classify the fields into high and low performing.

**Table 6.7** Number of high and low performing plots per threshold

Threshold	Number of plots	
	High-yield	Low-yield
$\bar{X}$ (8.3)	151	127
$0.5 \sigma$ (8.9)	90	188
$\sigma$ (9.4)	45	233
$1.5 \sigma$ (9.9)	16	262

### 6.3.3.3 Model Selection

The TPOT classifier was run for the two sets of predictors using the NDVI\_b8 data at the booting stage and the four(4) thresholds. The AUC-ROC values obtained after validating each pipeline on the test set are presented in table 6.8.

**Table 6.8** AUC-ROC values obtained from TPOT for the yield threshold at the booting stage using the NDVI\_b8

Threshold	Set of predictors	AUC
Threshold 4 (9.9)	B	0.99
Threshold 3 (9.4)	B	0.97
Threshold 2 (8.9)	A	0.89
Threshold 1 (8.3)	B	0.72
Threshold 4 (9.9)	A	0.87
Threshold 3 (9.4)	A	0.86
Threshold 2 (8.9)	B	0.77
Threshold 1 (8.3)	A	0.65

A Gradient Boosting Classifier (GBC) with the hyperparameters presented in Table 6.9 was selected as the most suitable model to predict high and low performing plots using TPOT over the NDVI\_b8 products during the booting stage. The model produced the highest AUC-ROC (0.99) for the threshold 4 (9.9 t/ha) and the set of predictors B, that is, the variables that included the percentage of anomalous pixels in the plot.

**Table 6.9** Hyperparameters of the Gradient Boosting Classifier selected by TPOT as the best pipeline to predict underperforming plots using the NDVI\_b8 during the booting stage

Parameter	Description	Value
ccp_alpha	Complexity parameter used for Minimal Cost-Complexity Pruning.	0 (No pruning is performed)
criterion	The function to measure the quality of a split.	Mean squared error with improvement score by Friedman (friedman_mse).
learning_rate	Learning rate	0.5
max_depth	The maximum depth of the individual regression estimators. The maximum depth limits the number of nodes in the tree	8
max_leaf_nodes	Maximum number of leaf nodes. If None, there is an unlimited number of leaf nodes.	None
min_impurity_decrease	A node will be split if this split induces a decrease of the impurity greater than or equal to this value.	0
min_impurity_split	threshold for early stopping in tree growth. A node will split if its impurity is above the threshold, otherwise, it is a leaf.	None
min_samples_leaf	The minimum number of samples required at a leaf node.	19
min_samples_split	The minimum number of samples required to split an internal node.	4
min_weight_fraction_leaf	The minimum weighted fraction of the sum total of weights (of all the input samples) required to be at a leaf node.	0



Parameter	Description	Value
n_estimators	number of boosting stages to perform.	100
n_iter_no_change	parameter used to decide if early stopping will be used to terminate training when validation score is not improving.	None (disable early stopping)
random_state	Controls the random seed given to each tree estimator at each boosting iteration	None
subsample	fraction of samples to be used for fitting the individual base learners	0.75
tol	Tolerance for the early stopping. The training stops when the loss is not improving by at least tol for n_iter_no_change iterations.	0.0001
init	An estimator object that is used to compute the initial predictions.	None (a DummyEstimator predicting the classes priors is used.)
loss	The loss function to be optimised	'deviance'
max_features	The number of features to consider when looking for the best split	0.5
validation_fraction	The proportion of training data set aside as validation set for early stopping.	0.1
warm_start	It is possible to reuse aspects of the model learned from the previous parameter value when fitting an estimator repeatedly on the same dataset but for multiple parameter values. When warm_start is true, the existing fitted model attributes are used to initialise the new model.	False

#### 6.3.3.4 Model training and validation at multiple growth stages

The Gradient Boosting Classifier model was fitted to each of the two sets of predictors using the hyperparameters listed in Table 6.9. The cross-validated mean AUC-ROC values of the GBC for all the VIs at different growth stages are presented in Fig. 6.14. In general, the classifier performance improved as the yield thresholds moved away from the mean. Adding the percentage of anomalous pixels within the plot improved the model's performance for all the thresholds above the yield mean. In both sets of variables, the model fit to the booting and ripening data showed cross-validated mean AUC values above 90% and above 80% when fit to the seedling and tillering data for the thresholds above the yield mean. Despite the high performance at predicting high/low yield plots at the ripening stage, it is too late to implement actions that optimise crop productivity.

The increased performance of the model fitted to the booting and ripening data is also evidenced in the variability of the cross-validated mean AUC values. Fig. 6.15 shows that the mean AUC variability for the model, fitted on the set of variables B, is lower at booting and ripening stages. In contrast, the panicle formation presents the lowest CV mean AUC-ROC values and the larger standard deviation.

Fig. 6.16 shows the cross-validated AUC-ROC values computed for the GBC fitted on the dataset B using multiple VIs at each threshold for different rice stages. Using the threshold 1 (mean), only the RECI8A\_RE\_B6 and the SAVI\_b8 produced AUC-ROC values above 0.75 at the seedling and panicle formation stages, respectively. For the threshold 2, the highest AUC-ROCs were obtained during the booting phase using the data from the RENDVI8A\_RE\_B6, GNDVI\_b8, and GNDVI\_b8A surfaces. In general, 69% of the VIs assessed during the booting stage produced AUC-ROC values above 0.9, while no VI produced such accuracy when assessed during the panicle formation and tillering stage. Only 4 VIs evaluated during the seedling stage using the threshold 2 produced AUC-ROCs above 0.9 (i.e. RECI8A\_RE\_B5, RENDVI8A\_RE\_B7, RENDVI8\_RE\_B7, RECI8A\_RE\_B7). For the thresholds 3 and 4, almost all the VIs produced Cross-validated AUC values above 0.9, except the NDVI\_b8 and the NDVI\_b8A during the panicle formation stage, still, their values were always above 0.8. In fact, the mean AUC-ROC values obtained for threshold 3 were above 0.95 in more than 70% of the VIs assessed at all phenological stages, except the panicle formation. All the VIs produced AUC values above 0.95 at the five phases when the threshold 4 was chosen.

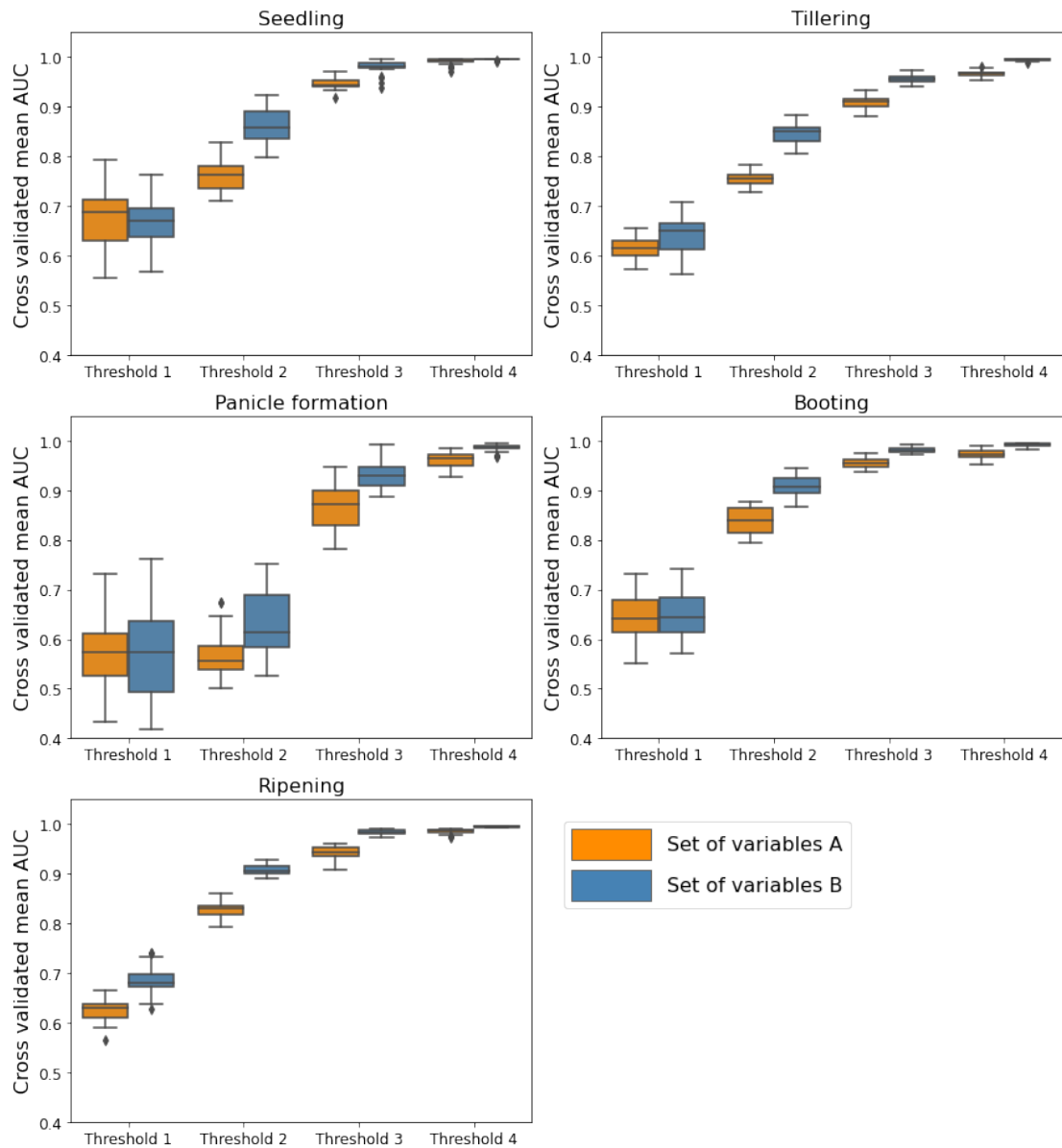


**Fig. 6.14** Cross validated mean AUC values of the GB classifier for all the VIs at different growths stages using the set of predictors A and B

## 6.4 Discussion

Although the detection of anomalies can provide crucial information for plot-level management decisions, often, PA is focused on the ability of data to indicate or even predict yield. The EOAD proved helpful for detecting infield anomalies and supporting informed agricultural practices that lead to increased yield. The occurrence of crop anomalies at certain stages had a more significant impact on final yield than the frequency of anomalies within a crop cycle. Particularly, the anomalies detected during the booting

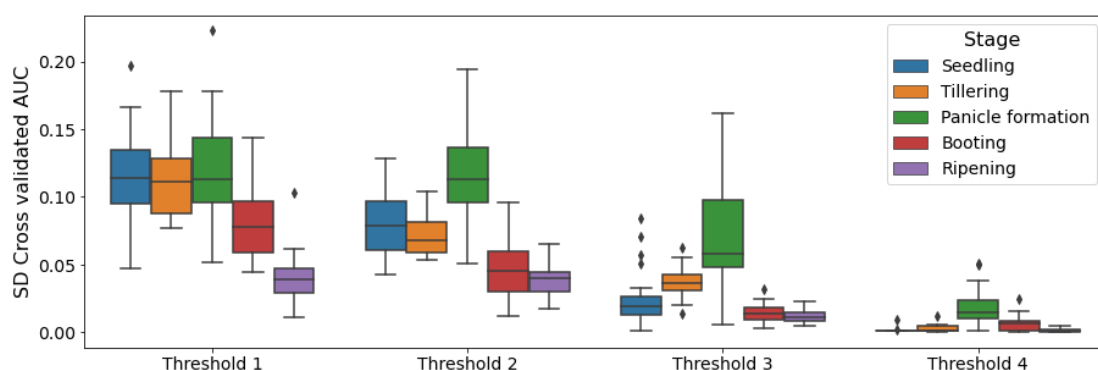


**Fig. 6.15** Standard deviation of cross-validated AUC values of the GB classifier fit to the set of variables B at different crop growth stages for the VIs presented in Table 4.5

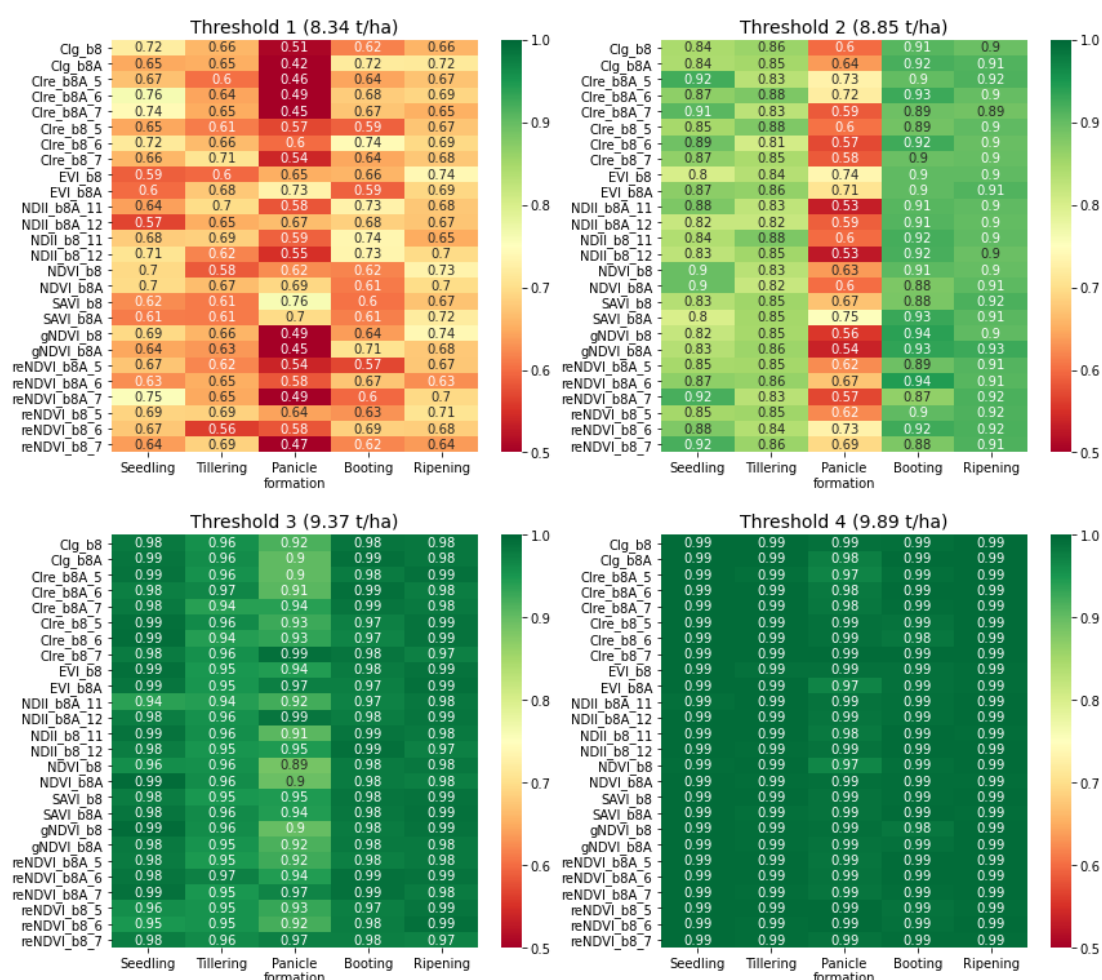


**Fig. 6.16** Heat maps presenting the cross-validated AUC-ROC values computed for the classifier trained and validated on the set of predictors B at different rice stages and the 4 thresholds.

and ripening phases showed to affect more significantly yield than the anomalies detected at other phenological stages. In addition, the percentage of in-field anomalies proved to

be an useful predictor to forecast underperforming plots at early growth stages.

#### 6.4.1 Impact of frequency of anomalies on yield

The main aim of the EOAD is to identify problem areas that might affect crop productivity or quality and implement timely corrections that maximise production and optimise the use of agricultural supplies. To assess the potential impact that the anomalies detected with the EOAD might have on yield, we first tested whether the pixels marked as anomalous in a higher number of scenes within the crop cycle yielded lower productivity.

No previous studies were found that related the frequency or prevalence of RS detected anomalies with reductions in agricultural yields. However, multiple studies have investigated how the frequency of events that produce stress in crops affect their yield. These studies analyse mostly weather variables that register data equally distributed along the crop cycle (e.g. hourly, daily, monthly), allowing to accurately calculate indicators such as the length and frequency of extreme weather spells. The periodical nature of the weather data also allow to identify those phenological stages in which the prevalence of anomalies affected more the crop productivity. For example, Abhishek et al. (2021) found that, despite stress conditions for rice plantations in Cambodia mostly occurred during the initial months, the subsequent alleviation of these conditions at the onset of the growing season allowed the crop to recover and the yield was not affected significantly.

In this research, the optical VIs assessed showed a significant difference in yield for pixels identified as anomalous on multiple occasions. However, no trend indicated that a higher number of anomaly occurrences was associated with a further decrease in yield. In contrast with meteorological data, which are recorded periodically, the dates of optical image acquisitions are not equally spaced along the growth cycle due to cloud cover. This is reflected in a different number of images per cycle for multiple plots in spite that the duration of the cycle is the same for all fields. The unequal availability of Sentinel-2 imagery along the crop cycle also implies that the phenological stages at which the images are taken are different for each plot, making difficult to perform meaningful comparisons among multiple fields. For SAR imagery, where the number of image acquisitions are equally distributed along the crop cycle, the weak link between anomalies frequency and yield can be explained by the lower performance of the method to detect anomalies using S1 imagery, compared to optical VIs. This is mostly due to

the lower spatial resolution of SAR images, which was much broader than the average size of the anomalies identified in the ground. The lower performance of S1 products to detect in-field anomalies is reflected in the relatively lower frequency of anomalies found in comparison with the use of optical VIs (i.e. No pixel was marked as anomalous more than 4 times within the crop cycle).

#### 6.4.2 Impact of anomalies at different crop stages over yield

The occurrence of crop anomalies at different stages impacted the final yield differently. In general, the anomalies identified with the EOAD during later growth stages, using normalised difference indices that included the NIR bands, tended to have a larger impact on the yield for most optical VIs. These results coincide with Cao et al. (2016) which found that at early rice stages the red-based vegetation indices resulted in better relations with rice grain yield, but, as the plant approached the maturity stage, red-edge-based ratio indices performed better. The SAVI and EVI are an exception of this behaviour as the anomalies detected with these indices did not show a significant impact on yield at any growth stage. These findings for SAVI are especially surprising as it showed a relative higher accuracy to detect in-field anomalies, compared to other VIs. A possible explanation for such behaviour is that as SAVI is an index used to correct for soil effects (Huete 1988), however, during the later crop stages, where the presence of anomalies shows a higher impact on yield, the crop canopy is covering the bare soil.

Most of the anomalies that showed a significant impact on yield were detected using the narrow NIR band VIs rather than the NIR band 8. Since the band 8A from S2 has the same band center wavelength as the Landsat-8's band 5, the EOAD constitutes a promising tool to detect anomalies that impact crop yield using Landsat-8 OLI imagery. This is especially important for regions where cloud cover limits a frequent imagery acquisition. The availability of two sources of data increases the chances of retrieving cloud-free imagery and improve the data acquisition frequency.

The anomalies that occurred at the booting stage tended to produce significant yield differences between anomalous and non-anomalous pixels using indices sensitive to chlorophyll. This coincides with the findings of authors such as Zhang et al. (2019a) that indicated a strong relationship between yield and crop condition at the booting stage. This relationship is consequence of the high Nitrogen (N) absorption rate occurring

during this stage (Liu et al. 2016; Xiang et al. 2013). It is typically during the booting stage that farmers apply nitrogen fertilisers as rice crops demand adequate N supply to maximise yield.

The most significant differences in yield between anomalous and non-anomalous pixels during the booting stage were obtained when applying the EOAD on  $RENDVI_{b8A\_6}$  and  $GNDVI_{b8A}$  surfaces. Similar results were obtained in studies that used reflectance data collected with near-ground sensors. For example, Cao et al. (2016) found that, compared with red-based indices (e.g. NDVI), the red-edge-based ratio indices resulted in better relations with rice grain yield as the plant approached the maturity stage (booting phase). Also, Kanke et al. (2016) found that the  $NDVI_{Red-edge}$  estimated with the NIR ( $0.78\ \mu m$ ) and red-edge ( $0.73\ \mu m$ ) bands had a stronger degree of relationship with N uptake, and grain yield compared with red-based indices during the booting stage.

Ideally, diagnostic information for nitrogen management in rice should be obtained just before the panicle formation stage, however, none of the anomalies detected with the chlorophyll sensitive indices during the seedling and panicle formation stages showed a significant impact on yield. Rather, the anomalies detected using the NDII, an indicator of vegetation and soil water content seemed to have a significant impact on productivity when detected during the seedling stage. Specifically yields for anomalous pixels detected during the seedling stage with the  $NDII_{b8\_12}$  surfaces tended to be higher than yields for non-anomalous pixels. The farm agronomist explained this behaviour occurs due to a deeper water layer that delays the emergence of rice plants. However, once the plants emerge, they remain wetter during the whole crop cycle and produce higher yields. Negative NDII values for areas with low LAI can also be indicators or dry patches and therefore be equally presented as anomalies. Therefore, it is required to contrast the  $NDII_{b8\_12}$  surfaces and the anomalous-predicted pixels during the seedling stage to see if the values are positive or negative, the latter representing dry areas that require immediate irrigation.

As it was expected, for those VI surfaces that showed less capabilities to detect in-field anomalies, the pixels marked as anomalous were not significantly associated with the final yield at any of the crop growth phases. They include the vegetation indices aimed for chlorophyll content estimation (i.e.  $CI_{green}$ ,  $CI_{Red-edge}$ ) and those that used the S2 band 7. In section 5, the low performance of those indices to detect in-field anomalies was associated to the lack of ground truth along the whole crop cycle. However the low capacity of the method to detect anomalies that have an actual impact on the final

yield using these indices can be an indicator of their low suitability for in-field anomaly detection using the EOAD. Further research should draw comparisons between anomaly-predicted surfaces using these two groups of VIs and other variables such as nitrogen content that are drivers of rice productivity (Kuenzer and Knauer 2013; Wang et al. 2012). Authors such as Schlemmer et al. (2013) and Zheng et al. (2016) have previously discussed the linear relationship between the  $CI_{Red-edge}$  and  $CI_{green}$  with N uptake in maize and rice crops. For example, Brinkhoff et al. (2021) consistently obtained accurate estimations of rice Nitrogen uptake when using the  $CI_{green}$ .

#### 6.4.3 Early detection of underperforming plots

In general, the inclusion of the percentage of anomalies detected with the EOAD improved the prediction of high/low yield plots using the GBC. The selection of the two sets of predictors was made using the results of a Pearson multicollinearity analysis performed on the continuous variables. Further research should consider using a different metric such as the Generalised Variance Inflation Factor (GVIF) proposed by Fox and Monette in 1992 to assess multicollinearity. It will allow to drop variables confidently, as the correlations computed between categorical and continuous variables are comparable. Although Gradient Boosting Trees are considered to be relatively tolerant to Collinearity (Breiman 2001; Friedman et al. 2000) it is a good practice to remove any redundant features from the dataset used for training and reduce the risk of overfitting (Read 1994; Zaghloul et al. 2021).

The classifier performance improved as the yield thresholds moved away from the mean. The reason for selecting yield thresholds larger or equal to the mean historical values is that farmers constantly aim to obtain yields above the average and detect timely those plots that might not comply with such high productivity expectations. However, these thresholds can be adapted to the needs of the agricultural system. For example, they can be moved to the left to focus on those plots that might produce yields below the historical mean value. Special care has to be taken with the selection of extreme thresholds to avoid the presence of extremely unbalanced datasets that can lead to overfitted models. The random oversampling method used to balance the datasets may increase the likelihood of occurring overfitting, especially under the presence of extreme disproportion among the number of examples of each class. This can occur, because random oversampling makes exact copies of the minority class instances. (Fernandez et al. 2018). In this study, adding the percentage of anomalous pixels within the plot improved the model's



performance for all the thresholds above the yield mean (i.e. Thresholds 2-4), producing generalised high accuracies at the most extreme threshold (4). Further research should investigate the predicting capability of the explanatory variables to forecast plots with lower yields than the historical farm yield.

The significant effect of crop condition over yield during the booting stage was also evidenced in the use of VI-derived metrics to predict high/low yield fields. In both sets of variables, the model fitted to the booting data showed cross-validated mean AUC values above 0.9 for the thresholds above the yield mean. This coincides with the findings of authors such as Chang et al. (2005), Zhang et al. (2019a), and Zhou et al. (2017) that indicated a strong relationship between yield and crop condition at the booting stage. This relationship is a consequence of the high N absorption rate occurring during this stage (Liu et al. 2016; Xiang et al. 2013). In fact, it is during the booting stage that farmers apply nitrogen fertilisers as rice crops demand adequate N supply to maximise yield. Site-specific N management is also important to improve crop N use efficiency and reduce risks of natural resources contamination (Cao et al. 2016). Previous studies have demonstrated that the position of red edge channel is closely related to the chlorophyll and Nitrogen content of various plants. For example, Clevers and Gitelson (2013) found that the red-edge bands in the range of 720-740 nm provide better information about N content for erectophile canopies, specifically maize and grass. These findings can explain why the indices that included the channel 6 (740 nm) performed better at the booting than those VIs that used other red-edge bands. In fact, the `RENDVI_b8A_6` was the VI that showed the best potential to detect underperforming plots. This confirms the significant relationship between the `RENDVI_b8A_6` and grain yield that was previously evidenced in Section 6.3.2.

Also, the use of GNDVI indices presented a relative better performance in comparison to other VIs to predict low/yield plots during the booting stage. This results coincide with the findings reported in Section 6.3.2, according to which GNDVI was one of the two VIs that evidenced the most significant differences in yield between anomalous and non-anomalous pixels at the booting stage. The GNDVI was also reported as to have a high correlation with grain yield at the booting stage by other authors such as Saberioon et al. (2013) and Duan et al. (2019).

Detecting anomalies during the booting stage helps identify those plots that require more immediate attention, however, ideally, diagnostic information for N management in rice should be obtained just before the panicle formation stage (Kanke et al. 2016), this is

the end of tillering phase. For the dataset that included the percentage of anomalies per plot, the model fitted to the tillering phase data showed cross-validated mean AUC values above 0.8 from threshold 2 onwards. Predicting underperforming plots during the tillering stage with such level of accuracy is useful to identify those plots that might require diagnostic information for nitrogen management, which is reported by literature as fundamental to optimise productivity. Particularly, the  $CI_{Ire\_b8\_7}$  showed a superior performance than other VIs at the thresholds 1, 2, and 3. The  $CI_{Red-edge}$  has shown to be one of the best indices to estimate canopy chlorophyll or N content (Clevers and Kooistra 2012), however, the position of the spectral bands affected the accuracy of the classification during the tillering stage. Clevers and Gitelson (2013) reported that the choice of the red-edge band showed to be more critical than the choice of the NIR band to estimate or Nitrogen content. Still, further research, agronomic data and validation points are needed to identify whether the anomalies detected at the tillering and booting stages are related to N deficiency issues, and how the predictions are affected by data recorded at different ages during the tillering, the longest rice phenological stage.

The reflectance measurements registered during the seedling phase are expected to be highly affected by the soil and the soil water content. This, as only the first internode, has elongated and pushed the tip of the rice coleoptile through the soil surface (Moldenhauer et al. 2013). Despite the Vegetation and soil Water Content indices (i.e. NDII) showed Cross-validated AUC mean values above 0.8 for the thresholds above the mean historical farm yields during the seedling stage, they did not produce the highest AUC-ROC values at this phase. Instead, the highest AUC mean values were produced when the classifier was fitted to datasets that included the NDVI and those VIs estimated using the red-edge channels. These results are not in line with the findings in section 6.3.2, according to which the pixels detected as anomalous during the seedling phase using the NDII indices had a more significant impact on the final yield than other VIs. This can be the result of fitting a classifier model that was selected using the results for the booting stage datasets. Further research should choose the most adequate classifier pipeline for each phenological stage to clarify whether such differences are due to the ML model used or plant physiological features.

Consistent with the results in Section 6.3.2, the panicle formation stage presented the lowest capability to predict underperforming plots. The relatively larger variation of the five cross-validated AUC-ROC values indicates that the model fitted to the panicle formation datasets have a higher risk to overfit compared to other stages. This relatively poor relationship between crop condition and grain yield during the panicle formation

phase disagrees with the findings of other authors which reported a high correlation between N and grain yield in panicle formation stage (Gholizadeh et al. 2017). It is difficult to identify the source of such differences because no ground measurements of Nitrogen or leaf chlorophyll content were taken in this study. However, this discrepancy can be explained by the lower number of samples available for the panicle formation stage in comparison to other phenological stages that last longer and provide more sample points to train the classifier.

TPOT was successful in selecting the machine-learning classifier and the optimal input parameters to predict underperforming plots by evaluating different types of possible pipelines automatically. Although the resulting pipelines often tend to become complex and hard to interpret (Sokolova et al. 2022), the pipeline produced was composed by a Gradient Boosting Classifier exclusively. Gradient Boosted Regression Models (GBR) have showed superior performance at predicting crop yield in different studies. For example found that the GBC fitted and validated on Sentinel-2 weather, soil moisture and topographic data outperformed linear regression models and RF. Only a limited number of studies have focused on predicting yield classes, however those found in the literature have used RF, Support Vector Machine (SVM), Artificial Neural Network (ANN) and k-means instead (e.g., Pantazi et al. 2016; Yoosefzadeh-Najafabadi et al. 2021).

Fitting and validating the selected classifier on the datasets for the different VIs and phenological stages allowed to have a better perspective of the predicting capability of the explanatory variables and the extent at which the anomalies detected with the EOAD can help identifying potentially under-performing plots. Some authors such as Sokolova et al. (2022) argue that TPOT can lead to model overfitting, however, in order to detect possible overfitting a 75/25 split was employed to train and test the model using a 5-fold cross-validation. The datasets with the highest risk of overfit were identified as those with the larger standard deviations among the 5 cross-validated AUC-ROC.

## 6.5 Conclusions

The EOAD method was able to map in-field anomalies that showed a significant impact on rice yield for specific VIs. Thus, the EOAD method also allows identifying plots that require more immediate attention and then assessing the more problematic areas within the field.

When analysing the impact of the prevalence of anomalies on yield, no trend indicated that a higher number of anomaly occurrences was associated with a further decrease in yield. For optical images, the presence of clouds, plus the fact that the plots are sowed on different dates, lead to an uneven availability of imagery along the crop cycle and unequal availability of RS data among plots. As the crop age at which the images are acquired and the number of images per cycle varies largely among different plots, it becomes difficult to establish comparisons among multiple fields and derive meaningful conclusions. For SAR polarisations, the weak link between EOAD anomalies frequency and yield is associated with the low capability of the method to detect anomalies. This is reflected in the relatively low frequency of anomalies found (i.e. No pixel was marked as anomalous more than four times within the crop cycle).

The occurrence of crop anomalies at different stages impacted the final yield differently. The anomalies identified with the EOAD at later growth stages, using normalised difference indices that included the NIR bands, tended to impact the yield significantly for most optical VIs. The SAVI was an exception to this behaviour, which is surprising as it showed relatively higher accuracy in detecting in-field anomalies than other VIs. A possible explanation for such behaviour is that as SAVI is an index used to correct for soil effects, during the later crop stages, where the presence of anomalies seems to produce a higher impact on yield, the rice canopy is fully developed, and the SAVI might not be a good indicator of the crop status.

The occurrence of crop anomalies at different stages significantly impacted final yield than the frequency of anomalies within a crop cycle. In particular, including the percentage of anomalies detected within the fields using the eoad increased the accuracy to detect low-yield plots at early stages, including seedling, tillering and booting.

In general, the booting stage was the earliest phase in which the crop condition provided better productivity indicators using chlorophyll sensitive indices. The significant relationship between crop condition and yield during the booting is related to the high N absorption rate occurring during this phase. Site-specific N management is essential to maximise productivity and reduce risks of natural resources contamination.

The GNDVI\_b8A and the RNDVI\_b8A6 consistently showed a higher relation between crop status at the booting stage, delivering the best forecasts of yield classes. The cross-validated mean AUC values of the GBC to predict low-yield plots using the GNDVI\_b8A and the RNDVI\_b8A6 datasets were above 0.94 for the thresholds larger

than the average farm yield. As the GNDVI can be estimated using imagery from other missions such as Landsat or PlanetScope, the presented techniques can be transferred to other sensors. This is especially important in regions with a constant presence of clouds, as the availability of two data sources improves the data acquisition frequency by increasing the chances of retrieving cloud-free imagery.

Higher accuracy to predict low-yield plots was achieved at the ripening stage, which the farmers consider late to implement corrective practices. However, identifying those plots that are likely to yield low-productivity during the ripening phase allows farmers to make early gross estimates of rice production to negotiate more favourable prices with their customers and better plan the harvesting and transport operations.

Diagnostic information for optimal N management in rice should be obtained by the end of the tillering phase. The GBC fitted and validated to the tillering phase data produced cross-validated mean AUC values above 0.8. Although the AUC values at the tillering stage are lower than those obtained during the booting, such accuracy gives further confidence that the EOAD can add value to farming operations by early identifying those plots that might require further diagnostic for nitrogen management using freely available EO data.

Further research will require identifying whether the anomalies detected at the tillering and booting stages are related to N deficiency issues by collecting field measurements of chlorophyll content and relating them to VIs known for providing indicators of Photosynthetic Pigments. Measurements taken at different times during the tillering will allow identifying how yield predictions are affected by different crop ages during the longest rice growth stage.

Among all the rice growth stages, the crop status during the panicle formation showed the lowest relationship with grain yield and the lowest capability to predict underperforming plots. With the information available in this study, it is difficult to identify why such results do not coincide with some of the previous studies about rice. Further studies should record leaf chlorophyll content during the crop cycle to establish more precise relationships between N content, the anomalies detected using different VIs at different growth phases, and grain yield.

In this study, first, the yield of anomalous and non-anomalous pixels was compared

to identify significant differences among them. The positive results obtained in this analysis led to investigating to which extent the percentage of anomalous area per plot could support the detection of underperforming plots. In general, the results of both analyses corroborate each other portraying common conclusions; however, the two studies showed notable differences in two aspects. First, the indices that included the narrow NIR band (8A) presented more significant differences in yield between anomalous and non-anomalous areas in most of the cases. However, those indices that included the S2 band 8A did not perform better to forecast low-yield plots than those estimated with the band 8. Secondly, despite the significant differences in yield between anomalous and non-anomalous plots detected at the seedling stage using the NDII indices, the predictive power of these VIs to forecast low-yield plots was low, compared to other indices.

## **CHAPTER 7**

### **Conclusions**

Global agricultural land is expected to keep expanding in the coming years, especially in Sub-Sahara Africa and Latin American countries (Bruinsma 2009). Despite precision agriculture has the potential to contribute to long-term sustainable agricultural production in these countries, many existing PA techniques are challenging to implement as they rely on prohibitively expensive crop monitoring systems. Agricultural practices based on Site-specific Management Zones (SSMZ) offer a more affordable approach to achieving PA goals in limited-resources regions. Still, most methods proposed to identify homogeneous management regions require a significant amount of crop, soil and weather data that is expensive to collect. Delimitation of SSMZ using a reduced amount of agronomic data and resources presents a unique challenge to developing affordable solutions that guide site-specific practices and maximise agricultural productivity in regions where the implementation of traditional PA techniques is prohibitively expensive. Satellite remote sensing has the potential to support the delimitation of SSMZ as it offers an inexpensive and non-destructive way of providing frequent information systematically at different spatial scales.

The primary aim of this thesis was to develop an automated approach to detecting in-field anomalies using freely available EO data. The EOAD is a novel system for detecting in-field anomalies through automatic thresholding of EO imagery, based on their deviation from a normal distribution. Detected anomalies can be used to direct farmers towards potentially abnormal areas and determine what strategy needs to be put in place, such as fixing water supply, to correct for these anomalies bringing about and ultimately an overall improvement to crop yields.

In this study, the EOAD was applied to different VIs and SAR products to detect anomalies in rice plots. The method was able to identify and map crop anomalies at the sub-plot level with accuracy scores up to 80% using optical VIs, comparing favourably with other anomaly detection approaches that require calibration using agronomic data or near-ground sensors. As the field observations used to assess the method accuracy were collected mainly during the tillering stage, the accuracies reported are primarily associated with the crop status at this phase and limited conclusions can be drawn regarding the method performance at other crop ages. However, the results obtained for optical VIs like the NDVI, which performed consistently well for the two types of optical imagery analysed, provide valuable insights to develop further research and assess the method performance at different growth stages.

The implementation of EOAD to SAR data was not sufficiently accurate to provide useful information regarding in-field anomalies. However, the relatively higher performance of the Sentinel-1 VH polarisation in the ascending and descending orbits suggests that there is also potential on applying the EOAD on radar data. A number of routes can be suggested for further work in this regard: Firstly, the relatively coarse resolution of SAR compared to the footprint of the anomalies identified in the field and the speckle present in the S1 GRD images makes difficult to discriminate confidently between anomalous and non-anomalous areas. As such, application of the approach to farms with larger fields may find more success. Secondly, the Sentinel-1 GRD imagery used is already processed to backscatter coefficient  $\sigma^0$  in decibels (dB), distorting the original distribution of pixel values within a homogeneous area and affecting the distribution of the pixels for homogeneous regions and therefore could affect the method's efficiency. Implementing the EOAD on linear-scaled  $\sigma^0$  imagery can improve the anomaly-detection process. Thirdly, exploring a Gamma distribution may be more suitable for describing radar intensity in homogeneous regions and is therefore likely to have affected the method's performance using SAR imagery as the primary assumption of the EOAD is that the plot pixels have a normal distribution. Finally, the combination of the multiple scattering mechanisms registered by the SAR sensor could also reduce the EOAD capacity to detect anomalous areas. Implementing decomposition techniques to isolate the multiple scattering mechanisms (including those related directly to canopy structure) registered by the SAR sensor might improve the EOAD capacity to detect anomalous areas.

There was a significant difference between the values of anomalous and non-anomalous pixels for all of the optical and SAR products considered. In particular, greatest discrimination was found at the ripening and booting stages and relatively lower significant



differences between the values of anomalous and non-anomalous pixels at the seedling and panicle formation stages. An accuracy assessment that includes anomalies registered across the full cycle will provide more definitive results about the performance of the method at different growth phases. However, the method's capability to separate anomalous from non-anomalous pixels can provide an initial estimation of its accuracy at different growth stages, when no validation points are available.

The selection of the most suitable satellite product to detect problematic anomalies on a particular crop should rely on the accuracy to detect in-field anomalies and the degree to which detected anomalies impact on the final yield. Crop anomalies at specific growth stages had a more significant impact on final yield than the number of anomaly occurrences registered within a crop cycle. The relatively weak link between frequency and yield is due to the presence of clouds and the different sowing dates among multiple plots in the farm. It leads to an uneven availability of imagery along the crop cycle and unequal availability of RS data among plots, making it difficult to perform meaningful comparisons among fields.

Integrating the percentage of anomalies detected within the fields, the VI metrics per plot and basic agronomic data allowed predicting low-yield plots more accurately than using only VI values, especially during the booting and ripening. Although the ripening stage can be considered late for implementing corrective practices, identifying those plots that are likely to yield low productivity allows farmers to make early gross estimates of rice production, negotiate more favourable prices with their customers, and better plan the harvesting and transport operations. The gNDVI indices, particularly the GNDVI\_b8A, showed a higher performance than other indices to predict anomalous areas in rice fields and forecast underperforming areas at early crop stages. As the gNDVI can be estimated using imagery from other missions such as Landsat or PlanetScope, such consistently high performance demonstrate that the EOAD approach is transferable across different optical sensors, e.g. Sentinel-2 and Landsat. This is especially important in regions with a constant presence of clouds, as the availability of two data sources improves the data acquisition frequency by increasing the chances of retrieving cloud-free imagery, leading to a higher chance of making cloud-free observations throughout the growing cycle, providing greater confidence when informing decision-makers on the ground. Also, as the EOAD does not require more data than the field boundaries to be implemented, there is potential for application on other crop types. The method transferability to other agricultural systems requires an initial assessment to identify the satellite products that produce higher accuracies and the growth stages at which the presence of these

anomalies have a larger impact on yield.

The significantly higher relationship between crop condition and grain yield and the accurate forecasts of under-performing plots obtained during the booting can be explained by the high N absorption rate occurring at this stage. Site-specific N management is essential to maximise productivity and reduce risks of natural resources contamination. While the anomalies detected at the booting stage can provide a good overview of potentially under-performing areas, ideally, diagnostic information for N management in rice should be obtained by the end of the tillering stage, just before the panicle formation (Kanke et al. 2016). The GBC tested on the tillering phase data produced cross-validated mean AUC values slightly lower than those obtained at the ripening and booting stages. Such accuracy gives further confidence that the EOAD can add value to farming operations by early identifying those plots that might require further diagnostic for nitrogen management using freely available EO data. Further research should test different classifier models on the tillering datasets to identify which one generates better estimations of low-performing plots.

Ultimately, the EOAD is designed to be a simple technique, without the need for manual calibration, or indeed, prior expertise in spectral analysis of crops. The EOAD was applied to histogram data for individual crop plots, in this instance, with data from commonly used VIs (e.g. NDVI, gNDVI), derived from freely available optical satellite data, showing outstanding potential to detect in-field anomalies that affect grain yield negatively. Currently, there is a limited offer of methods that detect in-field anomalies in croplands under low agronomic data availability scenarios and even fewer reports of the actual impacts of these anomalies on yield. As such, the EOAD approach represents a novel, efficient and low-cost means of collecting PA information almost anywhere in the World. If coupled with automatic approaches for field delineation, this represents an exciting and tractable tool for informing agricultural practices, especially in relatively resource-poor regions of the world where food security is paramount.

## 7.1 Future Work

This thesis contributes to the growing research on satellite earth observation for precision agriculture applications. The results presented show the potential of a satellite imagery-based technique that does not require manual calibration to detect anomalous areas in

croplands. It is hoped that the research presented in this thesis will inspire future research towards the development of affordable satellite-based precision agriculture techniques that can be easily transferred among agricultural systems.

#### 7.1.1 In-field Anomaly detection

This thesis presents the Earth Observation-based Anomaly Detection (EOAD), a novel approach for detecting in-field crop anomalies using optical and SAR imagery. The EOAD method does not require manual calibration as it implements a simple histogram analysis technique that automatically delineates potentially anomalous pixels. The EOAD was applied to different VIs and SAR products, and it was able to identify and map crop anomalies at the sub-plot level with accuracy scores up to 80% using optical VIs. This accuracy was obtained using validation data captured during the reproductive phenological phases of rice (i.e. booting and panicle formation), therefore, limited conclusions were drawn about the method performance at other crop ages. Further studies should focus on assessing the accuracy of the different VIs using validation data recorded across the whole crop cycle to identify the satellite products that best capture the inconsistencies within agricultural fields.

In general, the EOAD allowed detecting anomalies with accuracy that compared favourably with other anomaly detection approaches that require calibration using agronomic data or near-ground sensors. Once the anomaly is detected, the farmer assesses the nature of the problem and potential implications for crop productivity and determines the strategy to be implemented. Identifying the nature of crop anomalies will require further research, in which other variables that affect crop yield are characterised. For example, establishing relationships between Nitrogen deficiency and the presence of anomalies using particular VIs will demand the collection of chlorophyll content data using handheld devices. Also, keeping continuous records of leaf chlorophyll content across the crop cycle will allow establishing more precise relationships between N content, the presence of anomalies detected with different VIs at different growth phases and grain yield.

Although radar data did not perform as well as optical data at detecting in-field anomalies, the implementation of the EOAD on SAR imagery should be explored further. Radar ability to monitor the earth surface under almost all weather conditions and the sensitivity of the microwave signal to the dielectric and geometrical properties of the surfaces

represent a convenient alternative to monitor croplands in persistently cloudy areas. In a further stage, it is recommended to perform multi-looking to the linear-scaled SAR intensity data. The increase in the number of looks results in a more accurately estimated radar cross section, which can be related to the capacity of discriminating between anomalous and non-anomalous areas. However, the increase of ENL has to be carefully addressed as it leads to a decrease in spatial resolution, which may be a critical factor over smaller fields. It is also recommended to compare the results of implementing the EOAD on linear-scaled  $\sigma^0$  imagery and decibel-scaled  $\sigma^0$ . The logarithmic scale of the images expressed in decibels affects the pixels distribution for a homogeneous region, and therefore it might affect the method applicability. However, the log transformation of radar intensity makes data approximately conform to normality, a main assumption to implement the EOAD. Finally, as the combination of the multiple scattering mechanisms registered by the radar sensor could also reduce the EOAD capacity to detect anomalous areas, implementing decomposition techniques to isolate the multiple scattering mechanisms can improve the EOAD capacity to detect anomalous areas using SAR.

### 7.1.2 Effects of in-field anomalies on crop yield

Chapter 6 investigated to which extent the anomalies detected with the EOAD can be used to identify crop plots and in-field areas that are prone to experience losses in yield. After a first analysis that demonstrated the significant relationship between anomalies at certain phenological stages and grain yield, a Gradient Boosting Classifier (GBC) was trained to predict low-yield plots using the percentage of anomalies per plot and basic agricultural data as predictors. To reduce the amount of time required to test multiple models on each dataset, the chosen pipeline was designed using the open-source library TPOT on the NDVI\_b8 data during the booting stage and then fitted to each of the available datasets. Therefore, the Gradient Boosting Classifier (GBC) implemented was not the optimal pipeline to predict underperforming plots for all the VI and growth stages. In order to maximise the predictive power of the anomalies detected and clarify whether the differences in accuracy evidenced in this study are due to the ML model used or plant physiological features, further research should choose an optimal classifier pipeline for each phenological stage and VI.

The percentage of anomalous pixels within the plot improved the classifier's performance to detect low-yield plots for all the thresholds above the yield mean (i.e. Thresholds 2-4).

Future research can investigate the predicting capability of the explanatory variables to forecast plots with lower yields than the historical farm yield. It can help the farmer identify those plots in a critical condition and implement timely corrective actions.

### 7.1.3 Transferability

The EOAD simplicity and reliance on the basic statistics of a field/plot's pixels mean that it has the potential to be transferred to any VI or, indeed, any geographically continuous data and crop type. Future work could investigate validating the EOAD using other types of satellite imagery such as Landsat and different crops to evaluate the method's transferability among satellite sensors and agricultural systems.

## 7.2 Wider importance

Substantial improvements in resource-use efficiency and resource conservation must be implemented within agricultural systems around the world to meet the growing food demand and limit environmental degradation. Although Precision Agriculture has been used for the last few decades to improve the productivity and sustainability of agricultural production, the adoption of these technologies remains reliant on the availability of field sensors at a cost prohibitive to many farmers, particularly in those resource-poor regions where most agricultural expansion is forecast to take place. Incorporating freely accessible EO products into crop monitoring can support the development of softer and affordable precision agriculture approaches such as the delimitation of site-specific management zones. The Earth Observation-based Anomaly Detection method devised in Chapter 5 has provided evidence of its ability to automatically delimit in-field anomalous zones without the need for manual calibration, or prior expertise in spectral analysis of crops. It provides a potentially powerful tool for resource-poor regions, enabling growers to adopt environmentally sustainable cropping systems that optimise resource-use efficiency, making agriculture more resilient, productive and sustainable, and ultimately safeguard the global food supplies.

## REFERENCES

- Abdi, H (2003). “Partial Least Squares (PLS) Regression.” In: *Encyclopedia of Social Sciences Research Methods*.
- Abhishek, Abhijeet et al. (2021). “Evaluating the impacts of drought on rice productivity over Cambodia in the Lower Mekong Basin”. In: *Journal of Hydrology* 599, p. 126291. doi. 10.1016/j.jhydrol.2021.126291.
- Aboelghar, Mohamed, Abdel-Raouf Ali, and Sayed Arafat (2012). “Spectral wheat yield prediction modeling using SPOT satellite imagery and leaf area index”. In: *Arabian Journal of Geosciences* 2012 7:2 7.2, pp. 465–474. doi. 10.1007/s12517-012-0772-6.
- Adler-Golden, Steven M et al. (1999). “Atmospheric correction for shortwave spectral imagery based on MODTRAN4”. In: *Imaging Spectrometry V*. Ed. by Michael R Descour and Sylvia S Shen. Vol. 3753. International Society for Optics and Photonics. SPIE, pp. 61–69. doi. 10.1117/12.366315.
- Ag Leader (2019). *Components of Yield Monitors*.
- Aguilar, Enric, Ingeborg Auer, Manola Brunet, T C Peterson, and J Wieringa (2003). “Guidelines on climate metadata and homogenization”. In: *WMO-TD No. 1186* 1186.
- Alexander, Cici, Kevin Tansey, Jörg Kaduk, David Holland, and Nicholas J. Tate (2010). “Backscatter coefficient as an attribute for the classification of full-waveform airborne laser scanning data in urban areas”. In: *ISPRS Journal of Photogrammetry and Remote Sensing* 65.5, pp. 423–432. doi. 10.1016/j.isprsjprs.2010.05.002.
- Alexandersson, Hans (1986). “A homogeneity test applied to precipitation data”. In: *Journal of Climatology* 6.6, pp. 661–675. doi. 10.1002/joc.3370060607.
- Alexandratos, Nikos and Jelle Bruinsma (2012). “World Agriculture Towards 2030/2015: The 2012 Revision”. Rome.
- Alexis Dinno (2017). *Dunn’s Test of Multiple Comparisons Using Rank Sums*. Tech. rep.
- Ali, Iftikhar, Felix Greifeneder, Jelena Stamenkovic, Maxim Neumann, and Claudia Notarnicola (2015). “Review of Machine Learning Approaches for Biomass and Soil

- Moisture Retrievals from Remote Sensing Data”. In: *Remote Sensing 2015, Vol. 7, Pages 16398-16421* 7.12, pp. 16398–16421. doi. 10.3390/rs71215841.
- Alidoost, Fakhreh, Zhongbo Su, and Alfred Stein (2019). “Evaluating the effects of climate extremes on crop yield, production and price using multivariate distributions: A new copula application”. In: *Weather and Climate Extremes* 26, p. 100227. doi. 10.1016/j.wace.2019.100227.
- Allen, Richard G., Luis S. Pereira, Dirk Raes, and Martin Smith (1998). *Crop evapotranspiration - Guidelines for computing crop water requirements - FAO Irrigation and drainage paper 56*. Rome, Italy.
- Allouche, Omri, Asaf Tsoar, and Ronen Kadmon (2006). “Assessing the accuracy of species distribution models: prevalence, kappa and the true skill statistic (TSS)”. In: *Journal of Applied Ecology* 43.6, pp. 1223–1232. doi. 10.1111/j.1365-2664.2006.01214.x.
- Alpaydin, Ethem and Francis Bach (2014). *Introduction to Machine Learning*. Cambridge, United States: MIT Press.
- Anfinson, Stian Normann, Anthony P. Doulgeris, and Torbjorn Eltoft (2009). “Estimation of the Equivalent Number of Looks in Polarimetric Synthetic Aperture Radar Imagery”. In: *IEEE Transactions on Geoscience and Remote Sensing* 47.11, pp. 3795–3809. doi. 10.1109/tgrs.2009.2019269.
- Aragon, Bruno, Rasmus Houborg, Kevin Tu, Joshua B. Fisher, and Matthew McCabe (2018). “CubeSats Enable High Spatiotemporal Retrievals of Crop-Water Use for Precision Agriculture”. In: *Remote Sensing 2018, Vol. 10, Page 1867* 10.12, p. 1867. doi. 10.3390/rs10121867.
- Arai, Kohei (2008). “Nonlinear mixture model of mixed pixels in remote sensing satellite images based on Monte Carlo simulation”. In: *Advances in Space Research* 41.11, pp. 1715–1723. doi. 10.1016/j.asr.2007.04.096.
- Arumugam, Ponraj, Abel Chemura, Bernhard Schauburger, and Christoph Gornott (2021). “Remote Sensing Based Yield Estimation of Rice (*Oryza Sativa* L.) Using Gradient Boosted Regression in India”. In: *Remote Sensing 2021, Vol. 13, Page 2379* 13.12, p. 2379. doi. 10.3390/rs13122379.
- Arvor, Damien, Milton Jonathan, Margareth Simões Penello Meirelles, Vincent Dubreuil, and Laurent Durieux (2011). “Classification of MODIS EVI time series for crop mapping in the state of Mato Grosso, Brazil”. In: *International Journal of Remote Sensing* 32.22, pp. 7847–7871. doi. 10.1080/01431161.2010.531783.
- Aschbacher, J, A Pongsrihadulchai, S Karnchanasutham, C Rodprom, D R Paudyal, and Thuy Le Toan (1995). “Assessment of ERS-1 SAR data for rice crop mapping and monitoring”. In: vol. 3, 2183 –2185 vol.3. doi. 10.1109/igarss.1995.524142.

- Assis Silva, Samuel de, Railton Oliveira dos Santos, Daniel Marçal de Queiroz, Julião Soares de Souza Lima, Levi Fraga Pajehú, and Caique Carvalho Medauar (2021). “Apparent soil electrical conductivity in the delineation of management zones for cocoa cultivation”. In: *Information Processing in Agriculture*. doi. 10.1016/j.inpa.2021.04.004.
- Avitabile, Valerio, Alessandro Baccini, Mark A. Friedl, and Christiane Schmullius (2012). “Capabilities and limitations of Landsat and land cover data for aboveground woody biomass estimation of Uganda”. In: *Remote Sensing of Environment* 117, pp. 366–380. doi. 10.1016/j.rse.2011.10.012.
- Awad, Mariette. and Rahul. Khanna (2015). *Efficient Learning Machines Theories, Concepts, and Applications for Engineers and System Designers*. 1st ed. 20. The expert’s voice in machine learning. Berkeley, CA: Apress. doi. 10.1007/978-1-4302-5990-9.
- Azzalini, Adelchi and Bruno Scarpa (2012). *Data Analysis and Data Mining : An Introduction*. Cary, United States: Oxford University Press USA - OSO.
- Badhwar, G D (1984). “Use of LANDSAT-derived profile features for spring small-grains classification”. In: *International Journal of Remote Sensing* 5.5, pp. 783–797. doi. 10.1080/01431168408948860.
- Bai, Yun et al. (2021). “On the use of machine learning based ensemble approaches to improve evapotranspiration estimates from croplands across a wide environmental gradient”. In: *Agricultural and Forest Meteorology* 298-299, p. 108308. doi. 10.1016/j.agrformet.2020.108308.
- Baret, F., V. Houlès, and M. Guérif (2007). “Quantification of plant stress using remote sensing observations and crop models: The case of nitrogen management”. In: *Journal of Experimental Botany* 58.4, pp. 869–880. doi. 10.1093/jxb/er1231.
- Basso, B., J.T. Ritchie, F.J. Pierce, R.P. Braga, and J.W. Jones (2001). “Spatial validation of crop models for precision agriculture”. In: *Agricultural Systems* 68.2, pp. 97–112. doi. 10.1016/S0308-521X(00)00063-9.
- Battude, Marjorie et al. (2016). “Estimating maize biomass and yield over large areas using high spatial and temporal resolution Sentinel-2 like remote sensing data”. In: *Remote Sensing of Environment* 184, pp. 668–681. doi. 10.1016/j.rse.2016.07.030.
- Becerra, I. et al. (2020). *Plan de ordenamiento productivo del arroz en Colombia 2020-2038*. Bogota: UPRA.
- Beck, Pieter S.A., Clement Atzberger, Kjell Arild Høgda, Bernt Johansen, and Andrew K. Skidmore (2006). “Improved monitoring of vegetation dynamics at very high latitudes: A new method using MODIS NDVI”. In: *Remote Sensing of Environment* 100.3, pp. 321–334. doi. 10.1016/j.rse.2005.10.021.



- Becker-Reshef, I., E. Vermote, M. Lindeman, and C. Justice (2010a). “A generalized regression-based model for forecasting winter wheat yields in Kansas and Ukraine using MODIS data”. In: *Remote Sensing of Environment* 114.6, pp. 1312–1323. doi. 10.1016/j.rse.2010.01.010.
- Becker-Reshef, Inbal et al. (2010b). *Monitoring Global Croplands with Coarse Resolution Earth Observations: The Global Agriculture Monitoring (GLAM) Project*. doi. 10.3390/rs2061589.
- Belenguier-Plomer, Miguel A., Mihai A. Tanase, A. Fernandez-Carrillo, and Emilio Chuvieco (2019). “Burned area detection and mapping using Sentinel-1 backscatter coefficient and thermal anomalies”. In: *Remote Sensing of Environment* 233, p. 111345. doi. 10.1016/j.rse.2019.111345.
- Belgiu, Mariana and Ovidiu Csillik (2018). “Sentinel-2 cropland mapping using pixel-based and object-based time-weighted dynamic time warping analysis”. In: *Remote Sensing of Environment* 204. January 2017, pp. 509–523. doi. 10.1016/j.rse.2017.10.005.
- Bellvert, J., P. J. Zarco-Tejada, J. Girona, and E. Fereres (2014). “Mapping crop water stress index in a ‘Pinot-noir’ vineyard: Comparing ground measurements with thermal remote sensing imagery from an unmanned aerial vehicle”. In: *Precision Agriculture* 15.4, pp. 361–376. doi. 10.1007/s11119-013-9334-5.
- Bengio Yoshua (2009). “Learning Deep Architectures for AI”. In: *Foundations and Trends® in Machine Learning* 2.1, pp. 1–27. doi. 10.1561/22000000006.
- Benhamou, Latifa, Vincent Giard, Mehdi Khoulood, Pierres Fenies, and Frédéric Fontane (2020). “Reverse Blending: An economically efficient approach to the challenge of fertilizer mass customization”. In: *International Journal of Production Economics* 226, p. 107603. doi. 10.1016/j.ijpe.2019.107603.
- Benjamini, Yoav and Yosef Hochberg (1995). “Controlling the False Discovery Rate: A Practical and Powerful Approach to Multiple Testing”. In: *Journal of the Royal Statistical Society: Series B (Methodological)* 57.1, pp. 289–300. doi. <https://doi.org/10.1111/j.2517-6161.1995.tb02031.x>.
- Berry, Michael W and Murray Browne (2006). *Lecture Notes In Data Mining*. Singapore, SINGAPORE: World Scientific Publishing Company.
- Bhogapurapu, Narayanarao et al. (2021). “Dual-polarimetric descriptors from Sentinel-1 GRD SAR data for crop growth assessment”. In: *ISPRS Journal of Photogrammetry and Remote Sensing* 178, pp. 20–35. doi. 10.1016/j.isprsjprs.2021.05.013.
- Blaschke, T. (2010). “Object based image analysis for remote sensing”. In: *ISPRS Journal of Photogrammetry and Remote Sensing* 65.1, pp. 2–16. doi. 10.1016/j.isprsjprs.2009.06.004.

- Bolton, Douglas K. and Mark A. Friedl (2013). “Forecasting crop yield using remotely sensed vegetation indices and crop phenology metrics”. In: *Agricultural and Forest Meteorology* 173, pp. 74–84. doi. 10.1016/j.agrformet.2013.01.007.
- Bondell, Howard D. and Brian J. Reich (2008). “Simultaneous Regression Shrinkage, Variable Selection, and Supervised Clustering of Predictors with OSCAR”. In: *Biometrics* 64.1, pp. 115–123. doi. 10.1111/j.1541-0420.2007.00843.x.
- Bonilla Alvis, Andrea, Omar Enrique Peláez Martínez, Oscar Giovanni Linares Triviño, and Juan Carlos Reyes Palma (2012). *Estructura Ecológica Principal Municipal*. Tech. rep. Ibagué, Colombia: Alcaldía Municipal de Ibagué, p. 356.
- Bontemps, Sophie; et al. (2019). *Sen4CAP - Sentinels Agricultural Policy System Software User Manual for Common*. Tech. rep. 1, pp. 1–134.
- Boschetti, M., D. Stroppiana, P. A. Brivio, and S. Bocchi (2009). “Multi-year monitoring of rice crop phenology through time series analysis of MODIS images”. In: *International Journal of Remote Sensing* 30.18, pp. 4643–4662. doi. 10.1080/01431160802632249.
- Boser, Bernhard E., Isabelle M. Guyon, and Vladimir N. Vapnik (1992). “Training algorithm for optimal margin classifiers”. In: *Proceedings of the Fifth Annual ACM Workshop on Computational Learning Theory*, pp. 144–152. doi. 10.1145/130385.130401.
- Bourbigot, Matthieu, Harald Johnsen, and Riccardo Piantanida (2016). *Sentinel-1 Product definition*. Tech. rep.
- Bovik, Alan C (2009). “Chapter 4 - Basic Binary Image Processing”. In: *The Essential Guide to Image Processing*. Ed. by Al Bovik. Boston: Academic Press, pp. 69–96. doi. <https://doi.org/10.1016/b978-0-12-374457-9.00004-4>.
- Boydell, B. and A. B. McBratney (2002). “Identifying Potential Within-Field Management Zones from Cotton-Yield Estimates”. In: *Precision Agriculture 2002 3:1* 3.1, pp. 9–23. doi. 10.1023/a:1013318002609.
- Bradley, Andrew P. (1997). “The use of the area under the ROC curve in the evaluation of machine learning algorithms”. In: *Pattern Recognition* 30.7, pp. 1145–1159. doi. 10.1016/s0031-3203(96)00142-2.
- Braun, Andreas (2019). “Radar satellite imagery for humanitarian response. Bridging the gap between technology and application”. PhD thesis. Universität Tübingen. doi. 10.15496/publikation-32698.
- Braun, Andreas and Luis Veci (2021). *Sentinel-1 Toolbox SAR Basics Tutorial*. Tech. rep. ESA.
- Breiman, Leo (2001). “Random Forests”. In: *Machine Learning 2001 45:1* 45.1, pp. 5–32. doi. 10.1023/a:1010933404324.

- Breiman, Leo, Jerome H. Friedman, Richard A. Olshen, and Charles J. Stone (1984). “Classification And Regression Trees”. In: *Classification and Regression Trees*, pp. 1–358. doi. 10.1201/9781315139470.
- Breunig, Fábio Marcelo et al. (2020). “Delineation of management zones in agricultural fields using cover–crop biomass estimates from PlanetScope data”. In: *International Journal of Applied Earth Observation and Geoinformation* 85, p. 102004. doi. 10.1016/j.jag.2019.102004.
- Brinkhoff, James, Brian W. Dunn, and Andrew J. Robson (2021). “Rice nitrogen status detection using commercial-scale imagery”. In: *International Journal of Applied Earth Observation and Geoinformation* 105, p. 102627. doi. 10.1016/j.jag.2021.102627.
- Brouwer, C. and M. Heibloem (1986). *Irrigation Water Management: Irrigation Water Needs*. Rome, Italy: FAO.
- Brown, S C M, S Quegan, K Morrison, J C Bennett, and G Cookmartin (2003). “High-resolution measurements of scattering in wheat canopies - Implications for crop parameter retrieval”. In: *IEEE Transactions on Geoscience and Remote Sensing* 41.7 PART I, pp. 1602–1610. doi. 10.1109/tgrs.2003.814132.
- Bruinsma, Jelle (2003). *World agriculture: Towards 2015/2030: An FAO Study*, pp. 1–431. doi. 10.4324/9781315083858.
- (2009). “The Resource Outlook to 2050. By how much do land, water use and crop yields need to increase by 2050?” In: *Expert Meeting on How to Feed the World in 2050*. Rome, Italy.
- Bueno, Marcos, Alexssandra Dayane Soares De Campos, Jaqueline Trombetta Da Silva, Lessandro Coll Faria, Fabricio Da Silva Terra, and Jose Maria Barbat Parfitt (2019). “Demarcation of levees in irrigated rice fields: Laser technology vs. gnss-rtk”. In: *Applied Engineering in Agriculture* 35.3, pp. 431–437. doi. 10.13031/aea.13012.
- Bunting, Pete (2018). *Introduction to ARCSI for generating Analysis Ready Data (ARD)*. Tech. rep. Aberystwyth: Aberystwyth University.
- Bunting, Pete and Dan Clewley (2018). *About — ARCSI*.
- Bunting, Pete et al. (2018). “The global mangrove watch - A new 2010 global baseline of mangrove extent”. In: *Remote Sensing* 10.10. doi. 10.3390/rs10101669.
- Bunting, Peter, Frédéric Labrosse, and Richard Lucas (2010). “A multi-resolution area-based technique for automatic multi-modal image registration”. In: *Image and Vision Computing* 28.8, pp. 1203–1219. doi. 10.1016/j.imavis.2009.12.005.
- Bunting, Peter, Daniel Clewley, Richard M. Lucas, and Sam Gillingham (2014). “The Remote Sensing and GIS Software Library (RSGISLib)”. In: *Computers and Geosciences* 62, pp. 216–226. doi. 10.1016/j.cageo.2013.08.007.

- Calera, A., I. Campos, A. Osann, G. D'Urso, and M. Menenti (2017). "Remote sensing for crop water management: From ET modelling to services for the end users". In: *Sensors (Switzerland)* 17.5. doi. 10.3390/s17051104.
- Camacho, Fernando et al. (2021). "Crop specific algorithms trained over ground measurements provide the best performance for GAI and fAPAR estimates from Landsat-8 observations". In: *Remote Sensing of Environment* 260, p. 112453. doi. 10.1016/j.rse.2021.112453.
- Campos, Isidro, Christopher M.U. Neale, Timothy J. Arkebauer, Andrew E. Suyker, and Ivo Z. Gonçalves (2018). "Water productivity and crop yield: A simplified remote sensing driven operational approach". In: *Agricultural and Forest Meteorology* 249, pp. 501–511. doi. 10.1016/j.agrformet.2017.07.018.
- Campos, Nicolás Alfredo and Carlos Marcelo Di Bella (2012). "Multi-Temporal Analysis of Remotely Sensed Information Using Wavelets". In: *Journal of Geographic Information System* 04.04, pp. 383–391. doi. 10.4236/jgis.2012.44044.
- Canisius, Francis et al. (2018). "Tracking crop phenological development using multi-temporal polarimetric Radarsat-2 data". In: *Remote Sensing of Environment* 210, pp. 508–518. doi. 10.1016/j.rse.2017.07.031.
- Canty, Mort (2020). *Detecting Changes in Sentinel-1 Imagery* | Google Earth Engine.
- Cao, Qiang et al. (2016). "Improving in-season estimation of rice yield potential and responsiveness to topdressing nitrogen application with Crop Circle active crop canopy sensor". In: *Precision Agriculture* 17.2, pp. 136–154. doi. 10.1007/s11119-015-9412-y/tables/3.
- Carolan, Michael (2020). "Acting like an algorithm: digital farming platforms and the trajectories they (need not) lock-in". In: *Agriculture and Human Values* 2020 37:4 37.4, pp. 1041–1053. doi. 10.1007/s10460-020-10032-w.
- Carter, Gregory A. (1991). "Primary and Secondary Effects of Water Content on the spectral reflectance of leaves". In: *American Journal of Botany* 78.7, pp. 916–924. doi. 10.1002/j.1537-2197.1991.tb14495.x.
- Carter, Gregory A. and Alan K. Knapp (2001). "Leaf optical properties in higher plants: linking spectral characteristics to stress and chlorophyll concentration". In: *American Journal of Botany* 88.4, pp. 677–684. doi. 10.2307/2657068.
- Carter, Gregory A, Robert J Mitchell, Arthut H Chappelka, and Charles H Brewer (1992). "Response of Leaf Spectral Reflectance in Loblolly Pine to Increased Atmospheric Ozone and Precipitation Acidity". In: *Journal of Experimental Botany* 43.4, pp. 577–584. doi. 10.1093/jxb/43.4.577.
- Carter, Paul G, Christian J Johannsen, and Bernard A Engel (2008). "Recognizing Patterns Within Cropland Vegetation: A Crop Anomaly Classification System". In: *Journal of Terrestrial Observation* 1.1, pp. 38–49.

- Carvalho, Leila M.V., Charles Jones, and Brant Liebmann (2004). “The South Atlantic convergence zone: Intensity, form, persistence, and relationships with intraseasonal to interannual activity and extreme rainfall”. In: *Journal of Climate* 17.1, pp. 88–108. doi. 10.1175/1520-0442(2004)017<0088:tsaczi>2.0.co;2.
- Castillo-Villamor, Liliana, Peter Bunting, and Andrew Hardy (2021a). *Earth Observation-based Anomaly Detection (EOAD) system*. Aberystwyth. doi. 10.5281/zenodo.4753348.
- Castillo-Villamor, Liliana et al. (2021b). “The Earth Observation-based Anomaly Detection (EOAD) system: A simple, scalable approach to mapping in-field and farm-scale anomalies using widely available satellite imagery”. In: *International Journal of Applied Earth Observation and Geoinformation* 104, p. 102535. doi. <https://doi.org/10.1016/j.jag.2021.102535>.
- Chaherli, Nabil and John Nash (2013). “Agricultural Exports from Latin America and the Caribbean : Harnessing Trade to Feed the World and Promote Development”. In: *World Bank Other Operational Studies* 16048.
- Chakouri, Mohcine, Rachid Lhissou, Abderrazak El Harti, Soufiane Maimouni, and Zakaria Adiri (2020). “Assessment of the image-based atmospheric correction of multispectral satellite images for geological mapping in arid and semi-arid regions”. In: *Remote Sensing Applications: Society and Environment* 20, p. 100420. doi. 10.1016/j.rsase.2020.100420.
- Chang, Kuo Wei, Yuan Shen, and Jeng Chung Lo (2005). “Predicting rice yield using canopy reflectance measured at booting stage”. In: *Agronomy Journal* 97.3, pp. 872–878. doi. 10.2134/agronj2004.0162.
- Chavez, P S and D J Mackinnon (1994). “Automatic detection of vegetation changes in the southwestern United States using remotely sensed images”. English. In: 60.
- Chen, C. and H. McNairn (2007). “A neural network integrated approach for rice crop monitoring”. In: <http://dx.doi.org/10.1080/01431160500421507> 27.7, pp. 1367–1393. doi. 10.1080/01431160500421507.
- Chen, Gang, Geoffrey J. Hay, Luis M.T. T Carvalho, and Michael A. Wulder (2012). “Object-based change detection”. In: *International Journal of Remote Sensing* 33.14, pp. 4434–4457. doi. 10.1080/01431161.2011.648285.
- Chen, Jing-Wen, Chang-Hua Chen, and Sheng-Chi Chen (2005). “Application of Fuzzy K-mean Cluster And Fuzzy Similarity In Soil Classification”. In: vol. All Days. International Ocean and Polar Engineering Conference.
- Chen, J.M et al. (2002). “Derivation and validation of Canada-wide coarse-resolution leaf area index maps using high-resolution satellite imagery and ground measurements”. In: *Remote Sensing of Environment* 80.1, pp. 165–184. doi. 10.1016/s0034-4257(01)00300-5.

- Chen, X., J. Ma, H. Qiao, D. Cheng, Y. Xu, and Y. Zhao (2007). “Detecting infestation of take-all disease in wheat using Landsat Thematic Mapper imagery”. In: *International Journal of Remote Sensing* 28.22, pp. 5183–5189. doi. 10.1080/01431160701620683.
- Chen, Zhongxin et al. (2008). “Monitoring and Management of Agriculture with Remote Sensing”. In: *Advances in Land Remote Sensing: System, Modeling, Inversion and Application*. Ed. by Shunlin Liang. Dordrecht: Springer Netherlands, pp. 397–421. doi. 10.1007/978-1-4020-6450-0{\\_}15.
- Chica, Jaqueline, Yeimy Carolina Tirado, and Joan Manuel Barreto (2016). “Indicadores de competitividad del cultivo del arroz en Colombia y Estados Unidos”. In: *Revista de Ciencias Agrícolas* 33.2, pp. 16–31. doi. 10.22267/rcia.163302.49.
- Chitroub, Salim, Amrane Houacine, and Boualem Sansal (2002). “Statistical characterisation and modelling of SAR images”. In: *Signal Processing* 82.1, pp. 69–92. doi. 10.1016/s0165-1684(01)00158-x.
- Chlingaryan, Anna, Salah Sukkarieh, and Brett Whelan (2018). *Machine learning approaches for crop yield prediction and nitrogen status estimation in precision agriculture: A review*. doi. <https://doi.org/10.1016/j.compag.2018.05.012>.
- Choudhury, Indrani and M. Chakraborty (2006). “SAR signature investigation of rice crop using RADARSAT data”. In: *International Journal of Remote Sensing* 27.3, pp. 519–534. doi. 10.1080/01431160500239172.
- Choudhury, Indrani, M Chakraborty, and J Parihar (2007). “Estimation of rice growth parameter and crop phenology with conjunctive use of radarsat and ENVISAT”. In: *Envisat Symposium*. ESA.
- Chris B. Murphy and Margaret James (2021). *Pros and Cons of Stratified Random Sampling*.
- Cibula, W. G., E. F. Zetka, and D. L. Rickman (1990). “Response of thematic mapper bands to plant water stress”. In: <http://dx.doi.org/10.1080/01431169208904236> 13.10, pp. 1869–1880. doi. 10.1080/01431169208904236.
- Cichocki, Andrzej (2014). *Unsupervised Learning Algorithms and Latent Variable Models: PCA/SVD, CCA/PLS, ICA, NMF, etc.* Vol. 1. Elsevier Masson SAS, pp. 1151–1238. doi. 10.1016/b978-0-12-396502-8.00021-8.
- Cisternas, Isabel, Ignacio Velásquez, Angélica Caro, and Alfonso Rodríguez (2020). “Systematic literature review of implementations of precision agriculture”. In: *Computers and Electronics in Agriculture* 176, p. 105626. doi. 10.1016/j.compag.2020.105626.
- Clauss, Kersten, Marco Ottinger, Patrick Leinenkugel, and Claudia Kuenzer (2018). “Estimating rice production in the Mekong Delta, Vietnam, utilizing time series of

- Sentinel-1 SAR data”. In: *International Journal of Applied Earth Observation and Geoinformation* 73.March, pp. 574–585. doi. 10.1016/j.jag.2018.07.022.
- Clevers, J.G.P.W. and A.A. Gitelson (2013). “Remote estimation of crop and grass chlorophyll and nitrogen content using red-edge bands on Sentinel-2 and -3”. In: *International Journal of Applied Earth Observation and Geoinformation* 23.1, pp. 334–343. doi. 10.1016/j.jag.2012.10.008.
- Clevers, J.G.P.W. and L Kooistra (2012). “Using hyperspectral remote sensing data for retrieving canopy chlorophyll and nitrogen content”. In: *IEEE Journal of Selected Topics in Applied Earth Observations and Remote Sensing* 5.2, pp. 574–583. doi. 10.1109/jstars.2011.2176468.
- Cloude, Shane Robert and Eric Pottier (1997). “An entropy based classification scheme for land applications of polarimetric SAR”. In: *IEEE Transactions on Geoscience and Remote Sensing* 35.1, pp. 68–78. doi. 10.1109/36.551935.
- Cohen, Jacob (1960). “A Coefficient of Agreement for Nominal Scales”. In: *Educational and Psychological Measurement* 20.1, pp. 37–46. doi. 10.1177/001316446002000104.
- Coluzzi, Rosa, Vito Imbrenda, Maria Lanfredi, and Tiziana Simoniello (2018). “A first assessment of the Sentinel-2 Level 1-C cloud mask product to support informed surface analyses”. In: *Remote Sensing of Environment* 217, pp. 426–443. doi. 10.1016/j.rse.2018.08.009.
- Cooley, W and P R Lohnes (1971). “Multivariate Data Analysis”. In: *Journal of the Royal Statistical Society* 136. doi. 10.2307/2344428.
- Coppin, P, I Jonckheere, K Nackaerts, B Muys, and E Lambin (2004). “Review Article Digital change detection methods in ecosystem monitoring: a review”. In: *International Journal of Remote Sensing* 25.9, pp. 1565–1596. doi. 10.1080/0143116031000101675.
- Corder, Gregory W and Dale I Foreman (2014). *Nonparametric Statistics : A Step-By-Step Approach*. Somerset, United States: John Wiley and Sons, Incorporated.
- Dash, Jadunandan and Booker O. Ogutu (2016). “Recent advances in space-borne optical remote sensing systems for monitoring global terrestrial ecosystems:” in: *Progress in Physical Geography: Earth and Environment* 40.2, pp. 322–351. doi. 10.1177/0309133316639403.
- David Dalpiaz (2021). *Chapter 15 Collinearity | Applied Statistics with R*.
- Davidson, Andrew M., Thierry Fisette, Heather McNairn, and Bahram Daneshfar (2014). “Handbook on remote sensing for agricultural statistics”. In: *Handbook on Remote Sensing for Agricultural Statistics* August, Chapter 4. doi. 10.13140/rg.2.2.13259.69920.
- Defourny, Pierre et al. (2019). “Near real-time agriculture monitoring at national scale at parcel resolution: Performance assessment of the Sen2-Agri automated system

- in various cropping systems around the world”. In: *Remote Sensing of Environment* 221, pp. 551–568. doi. 10.1016/j.rse.2018.11.007.
- Dekker, R J (1998). “Speckle filtering in satellite SAR change detection imagery”. In: *International Journal of Remote Sensing* 19.6, pp. 1133–1146. doi. 10.1080/014311698215649.
- Delegido, J., J. Verrelst, C. M. Meza, J. P. Rivera, L. Alonso, and J. Moreno (2013). “A red-edge spectral index for remote sensing estimation of green LAI over agroecosystems”. In: *European Journal of Agronomy* 46, pp. 42–52. doi. 10.1016/j.eja.2012.12.001.
- Delgado, J.A., G.F. Sassenrath, and T. Mueller, eds. (2018). *Precision Conservation: Geospatial Techniques for Agricultural and Natural Resources Conservation*. English. Madison, WI: American Society of Agronomy and Crop Science Society of America, Inc. doi. 10.2134/precisionconservation.2018.frontmatter.
- Delgado, Jorge A, Nicholas M Short, Daniel P Roberts, and Bruce Vandenberg (2019). “Big Data Analysis for Sustainable Agriculture on a Geospatial Cloud Framework”. In: *Frontiers in Sustainable Food Systems* 3, p. 54. doi. 10.3389/fsufs.2019.00054.
- Delgado, Martha, Cristian Samir, Ulloa Juan, and Mauricio Ramírez (2015). *La Economía del Departamento del Tolima: Diagnóstico y Perspectivas de Mediano Plazo-forme elaborado por*. Tech. rep. Bogota: Fedesarrollo.
- Delgado, William (2009). “Caracterización del proceso de transferencia y adopción tecnológica de pequeños y medianos productores de cebolla (*Allium cepa* L.) en el municipio de Pasca (Cundinamarca)”. PhD thesis, p. 119.
- Delloye, Cindy, Marie Weiss, and Pierre Defourny (2018). “Retrieval of the canopy chlorophyll content from Sentinel-2 spectral bands to estimate nitrogen uptake in intensive winter wheat cropping systems”. In: *Remote Sensing of Environment* 216, pp. 245–261. doi. 10.1016/j.rse.2018.06.037.
- Denize, Julien, Laurence Hubert-Moy, Julie Betbeder, Samuel Corgne, Jacques Baudry, and Eric Pottier (2019). “Evaluation of using sentinel-1 and -2 time-series to identify winter land use in agricultural landscapes”. In: *Remote Sensing* 11.1. doi. 10.3390/rs11010037.
- Departamento Administrativo Nacional de Estadísticas (DANE) and Federacion Nacional de Arroceros (FEDEARROZ) (2017). *Boletín Técnico. Censo Nacional Arrocero*. Tech. rep. Bogota, Colombia, p. 35.
- Dheeravath, V. et al. (2010). “Irrigated areas of India derived using MODIS 500 m time series for the years 2001-2003”. In: *ISPRS Journal of Photogrammetry and Remote Sensing* 65.1, pp. 42–59. doi. 10.1016/j.isprsjprs.2009.08.004.



- Dong, Jinwei et al. (2015). “Tracking the dynamics of paddy rice planting area in 1986-2010 through time series Landsat images and phenology-based algorithms”. In: *Remote Sensing of Environment* 160, pp. 99–113. doi. 10.1016/j.rse.2015.01.004.
- Dong, Taifeng et al. (2019). “Assessment of red-edge vegetation indices for crop leaf area index estimation”. In: *Remote Sensing of Environment* 222, pp. 133–143. doi. 10.1016/j.rse.2018.12.032.
- Dormann, Carsten F. et al. (2013). “Collinearity: A review of methods to deal with it and a simulation study evaluating their performance”. In: *Ecography* 36.1, pp. 27–46. doi. 10.1111/j.1600-0587.2012.07348.x.
- Draper, Norman R and Harry Smith (1998). *Applied Regression Analysis*. Newy York, United States: John Wiley and Sons, Incorporated.
- Drummond, S. T., K. A. Sudduth, A. Joshi, S. J. Birrell, and N. R. Kitchen (2003). “Statistical and neural methods for site-specific yield prediction”. In: *Transactions of the ASAE* 46.1, pp. 5–. doi. 10.13031/2013.12541.
- Duan, Bo et al. (2019). “Remote estimation of rice yield with unmanned aerial vehicle (uav) data and spectral mixture analysis”. In: *Frontiers in Plant Science* 10, p. 204. doi. 10.3389/fpls.2019.00204/bibtex.
- Dunn, Olive Jean (1961). “Multiple Comparisons Among Means”. In: *Journal of the American Statistical Association* 56.293, pp. 52–64. doi. 10.2307/2282330.
- Duquette, Jacques and Jennifer A. Kimball (2020). “Phenological stages of cultivated northern wild rice according to the BBCH scale”. In: *Annals of Applied Biology* 176.3, pp. 350–356. doi. 10.1111/aab.12588.
- Dutrieux, Loïc P., Catarina C. Jakovac, Siti H. Latifah, and Lammert Kooistra (2016). “Reconstructing land use history from Landsat time-series: Case study of a swidden agriculture system in Brazil”. In: *International Journal of Applied Earth Observation and Geoinformation* 47, pp. 112–124. doi. 10.1016/j.jag.2015.11.018.
- Edwards, Daniel C. and Thomas B. McKee (1997). *Characteristics of 20th century drought in the United States at multiple time scales*. Tech. rep. Fort Collins, USA: Colorado State University. Department of Atmospheric Science.
- Eerens, Herman, Dominique Haesen, Felix Rembold, Ferdinando Urbano, Carolien Tote, and Lieven Bydekerke (2014). “Image time series processing for agriculture monitoring”. In: *Environmental Modelling and Software* 53, pp. 154–162. doi. 10.1016/j.envsoft.2013.10.021.
- Eitel, Jan U.H. et al. (2011). “Broadband, red-edge information from satellites improves early stress detection in a New Mexico conifer woodland”. In: *Remote Sensing of Environment* 115.12, pp. 3640–3646. doi. 10.1016/j.rse.2011.09.002.

- El Hajj, Mahmoud, Agnès Bégué, Serge Guillaume, and Jean François Martiné (2009). “Integrating SPOT-5 time series, crop growth modeling and expert knowledge for monitoring agricultural practices — The case of sugarcane harvest on Reunion Island”. In: *Remote Sensing of Environment* 113.10, pp. 2052–2061. doi. 10.1016/j.rse.2009.04.009.
- El Hajj, Mohamad, Agnès Bégué, Bruno Lafrance, Olivier Hagolle, Gérard Dedieu, and M Rumeau (2008). “Relative Radiometric Normalization and Atmospheric Correction of a SPOT 5 Time Series”. In: *Sensors (Basel, Switzerland)* 8. doi. 10.3390/s8042774.
- Elith, J., J. R. Leathwick, and T. Hastie (2008). “A working guide to boosted regression trees”. In: *Journal of Animal Ecology* 77.4, pp. 802–813. doi. 10.1111/j.1365-2656.2008.01390.x.
- Erika Podest (2017). *SAR Processing and Data Analysis*.
- ESA (2013). *User Guides - Sentinel-2 MSI - Processing Levels - Sentinel Online*.  
— (2021). *IW GRD Resolutions*.
- European Space Agency (2020). *Sentinel-1 SAR Technical Guide*.
- Fall, Cheikh Modou Noreyni, Christophe Lavaysse, Hervé Kerdiles, Mamadou Simina Dramé, Philippe Roudier, and Amadou Thierno Gaye (2021). “Performance of dry and wet spells combined with remote sensing indicators for crop yield prediction in Senegal”. In: *Climate Risk Management* 33, p. 100331. doi. 10.1016/j.crm.2021.100331.
- Fang, Jing, Shaohai Hu, and Xiaole Ma (2018). “A Boosting SAR Image Despeckling Method Based on Non-Local Weighted Group Low-Rank Representation”. In: *Sensors* 18.10. doi. 10.3390/s18103448.
- Federico, Giovanni (2008). *Feeding the World : An Economic History of Agriculture, 1800-2000*. Princeton, United States: Princeton University Press.
- Feng, Changyong et al. (2014). “Log-transformation and its implications for data analysis”. In: *Shanghai Archives of Psychiatry* 26.2, p. 105. doi. 10.3969/j.issn.1002-0829.2014.02.009.
- Fernandez, Alberto, Salvador Garcia, Mikel Galar, Ronaldo Prati, Bartosz Krawczyk, and Francisco Herrera (2018). *Learning from Imbalanced Data Sets*. Springer, Cham, pp. XVIII, 377. doi. 10.1007/978-3-319-98074-4.
- Ferretti, Alessandro et al. (2007). *InSAR Principles: Guidelines for SAR Interferometry Processing and Interpretation*. Ed. by Karen Fletcher. February. Frascati, Italy: European Space Agency. doi. 10.1073/pnas.81.17.5399.
- Filipponi, Federico (2019). “Sentinel-1 GRD Preprocessing Workflow”. In: *Proceedings* 18.1, p. 11. doi. 10.3390/ecrs-3-06201.

- Fisher, Robert B et al. (2014). *Dictionary of Computer Vision and Image Processing*. Somerset, UNITED KINGDOM: John Wiley and Sons, Incorporated.
- Fleming, K L, D G Westfall, D W Wiens, and M C Brodahl (2000). “Evaluating Farmer Defined Management Zone Maps for Variable Rate Fertilizer Application”. In: *Precision Agriculture* 2.2, pp. 201–215. doi. 10.1023/a:1011481832064.
- Flores, A., K. Herndon, R. Thapa, and E. Cherrington (2019). “SAR Handbook: Comprehensive Methodologies for Forest Monitoring and Biomass Estimation”. In: *The SAR Handbook Comprehensive Methodologies for Forest Monitoring and Biomass Estimation*, pp. 1–307. doi. 10.25966/nr2c-s697.
- Food and Agriculture Organization (FAO) (2017). *The future of food and agriculture - Trends and challenges*. Rome, Italy.
- (2018). *The future of food and agriculture – Alternative pathways to 2050*. Rome: Food and Agriculture Organization of the United Nations, p. 60.
- (2020). *Digital Innovation for promoting Agriculture 4.0 in the Near East and North Africa*. Tech. rep. February. Muscat, Sultanate of Oman: FAO, pp. 1–9.
- Food and Agriculture Organization (FAO) and UN Environment Programme(UNEP) (2020). *The State of the World’s Forests*. 2020th ed. Rome, Italy: FAO and UNEP, p. 214.
- Food Security and Nutrition Analysis Unit and FSNAU (2013). “Food Security and Nutrition Analysis Post Deyr 2012/13”. In: *FSNAU Technical Series Report No VI. 50 March 5, 2013 Vi*, p. 174.
- Fox, John and Georges Monette (1992). “Generalized Collinearity Diagnostics”. In: *Journal of the American Statistical Association* 87.417, pp. 178–183. doi. 10.1080/01621459.1992.10475190.
- Fraisse, C W, K A Sudduth, and N R Kitchen (2001). “Delineation of site-specific management zones by unsupervised classification of topographic attributes and soil electrical conductivity”. In: *Transactions of the American Society of Agricultural Engineers* 44.1, pp. 155–166.
- Franco-Solís, Alberto and Claudia V. Montanía (2021). “Dynamics of deforestation worldwide: A structural decomposition analysis of agricultural land use in South America”. In: *Land Use Policy* 109, p. 105619. doi. 10.1016/j.landusepol.2021.105619.
- Franke, Jonas and Gunter Menz (2007). “Multi-temporal wheat disease detection by multi-spectral remote sensing”. In: *Precision Agriculture* 8.3, pp. 161–172. doi. 10.1007/s11119-007-9036-y.
- Frantz, David, Erik Haß, Andreas Uhl, Johannes Stoffels, and Joachim Hill (2018). “Improvement of the Fmask algorithm for Sentinel-2 images: Separating clouds from

- bright surfaces based on parallax effects”. In: *Remote Sensing of Environment* 215, pp. 471–481. doi. 10.1016/j.rse.2018.04.046.
- Franzen, David W., David H. Hopkins, Michael D. Sweeney, Michael K. Ulmer, and Ardell D. Halvorson (2002). “Evaluation of Soil Survey Scale for Zone Development of Site-Specific Nitrogen Management”. In: *Agronomy Journal* 94.2, pp. 381–389. doi. 10.2134/agronj2002.3810.
- Freedman, David and Persi Diaconis (1981). “On the maximum deviation between the histogram and the underlying density”. In: *Zeitschrift für Wahrscheinlichkeitstheorie und Verwandte Gebiete* 58.2, pp. 139–167. doi. 10.1007/bf00531558.
- Freeman, Anthony and Stephen L. Durden (1998). “A three-component scattering model for polarimetric SAR data”. In: *IEEE Transactions on Geoscience and Remote Sensing* 36.3, pp. 963–973. doi. 10.1109/36.673687.
- Freund, Rudolf J, William J Wilson, and Ping Sa (2006). *Regression Analysis : Statistical Modeling of a Response Variable*. Burlington, United States: Elsevier Science and Technology.
- Friedman, Jerome, Trevor Hastie, and Robert Tibshirani (2000). “Additive logistic regression: A statistical view of boosting”. In: *Annals of Statistics* 28.2, pp. 337–407. doi. 10.1214/aos/1016218223.
- Friedman, Jerome H (1991). “Multivariate Adaptive Regression Splines”. In: *The Annals of Statistics* 19.1, pp. 1–67.
- Friedman, Jerome H. (2001). “Greedy function approximation: A gradient boosting machine.” In: <https://doi.org/10.1214/aos/1013203451> 29.5, pp. 1189–1232. doi. 10.1214/aos/1013203451.
- Frogbrook, Z L and M A Oliver (2007). “Identifying management zones in agricultural fields using spatially constrained classification of soil and ancillary data”. In: *Soil Use and Management* 23.1, pp. 40–51. doi. 10.1111/j.1475-2743.2006.00065.x.
- Funk, Chris and Michael E. Budde (2009). “Phenologically-tuned MODIS NDVI-based production anomaly estimates for Zimbabwe”. In: *Remote Sensing of Environment* 113.1, pp. 115–125. doi. 10.1016/j.rse.2008.08.015.
- Gao, Bo Cai (1996). “NDWI—A normalized difference water index for remote sensing of vegetation liquid water from space”. In: *Remote Sensing of Environment* 58.3, pp. 257–266. doi. 10.1016/s0034-4257(96)00067-3.
- Gao, Feng et al. (2017). “Toward mapping crop progress at field scales through fusion of Landsat and MODIS imagery”. In: *Remote Sensing of Environment* 188, pp. 9–25. doi. 10.1016/j.rse.2016.11.004.
- Garbulsky, Martin F., Josep Peñuelas, John Gamon, Yoshio Inoue, and Iolanda Filella (2011). *The photochemical reflectance index (PRI) and the remote sensing of leaf,*

- canopy and ecosystem radiation use efficiencies. A review and meta-analysis*. doi. 10.1016/j.rse.2010.08.023.
- Gavioli, A., E. G. Souza, C. L. Bazzi, N. M. Betzek, K. Schenatto, and H. Beneduzzi (2016). “Delineation of site-specific management zones using spatial principal components and cluster analysis”. In: *SA13th International Conference on Precision Agriculture, St. Luis Missouri, USA*, pp. 1–11.
- Gavioli, Alan, Eduardo Godoy de Souza, Claudio Leones Bazzi, Kelyn Schenatto, and Nelson Miguel Betzek (2019). “Identification of management zones in precision agriculture: An evaluation of alternative cluster analysis methods”. In: *Biosystems Engineering* 181, pp. 86–102. doi. 10.1016/j.biosystemseng.2019.02.019.
- GDAL/OGR contributors (2021). *{GDAL/OGR} Geospatial Data Abstraction software Library*.
- Ge, Y., J.A. Thomasson, and R. Sui (2011). “Remote sensing of soil properties in precision agriculture: A review”. In: *Frontiers of Earth Science* 5.3, pp. 229–238. doi. 10.1007/s11707-011-0175-0.
- GEOGLAM (2017). *Crop Monitor*.
- (2018). *Crop Monitor Early Warning*. Tech. rep. GEGOLAM.
- Gholizadeh, Asa, Mohammadmehdi Saberioon, Luboš Borůvka, Aimrun Wayayok, and Mohd Amin Mohd Soom (2017). “Leaf chlorophyll and nitrogen dynamics and their relationship to lowland rice yield for site-specific paddy management”. In: *Information Processing in Agriculture* 4.4, pp. 259–268. doi. 10.1016/j.inpa.2017.08.002.
- Gilbertson, Jason Kane and Adriaan van Niekerk (2017). “Value of dimensionality reduction for crop differentiation with multi-temporal imagery and machine learning”. In: *Computers and Electronics in Agriculture* 142, pp. 50–58. doi. 10.1016/j.compag.2017.08.024.
- Gili, Adriana, Cristian Álvarez, Ramiro Bagnato, and Elke Noellemeyer (2017). “Comparison of three methods for delineating management zones for site-specific crop management”. In: *Computers and Electronics in Agriculture* 139, pp. 213–223. doi. 10.1016/j.compag.2017.05.022.
- Gim, Hyeon Ju, Chang Hoi Ho, Sujong Jeong, Jinwon Kim, Song Feng, and Michael J. Hayes (2020). “Improved mapping and change detection of the start of the crop growing season in the US Corn Belt from long-term AVHRR NDVI”. In: *Agricultural and Forest Meteorology* 294, p. 108143. doi. 10.1016/j.agrformet.2020.108143.
- Gitelson, Anatoly and Mark N Merzlyak (1994). “Spectral Reflectance Changes Associated with Autumn Senescence of *Aesculus hippocastanum* L. and *Acer platanoides*

- L. Leaves. Spectral Features and Relation to Chlorophyll Estimation”. In: *Journal of Plant Physiology* 143.3, pp. 286–292. doi. 10.1016/s0176-1617(11)81633-0.
- Gitelson, Anatoly A., Yoram J. Kaufman, and Mark N. Merzlyak (1996). “Use of a green channel in remote sensing of global vegetation from EOS-MODIS”. In: *Remote Sensing of Environment* 58.3, pp. 289–298. doi. 10.1016/s0034-4257(96)00072-7.
- Gitelson, Anatoly A., Andrés Viña, Timothy J. Arkebauer, Donald C. Rundquist, Galina Keydan, and Bryan Leavitt (2003). “Remote estimation of leaf area index and green leaf biomass in maize canopies”. In: *Geophysical Research Letters* 30.5, n/a–n/a. doi. 10.1029/2002gl016450.
- Glenn, Edward P., Christopher M. U. Neale, Doug J. Hunsaker, and Pamela L. Nagler (2011). “Vegetation index-based crop coefficients to estimate evapotranspiration by remote sensing in agricultural and natural ecosystems”. In: *Hydrological Processes* 25.26, pp. 4050–4062. doi. 10.1002/hyp.8392.
- Global Rice Science Partnership (2013). *Rice Almanac*. 4th. Los Baños, Philippines: International Rice Research Institute, p. 283.
- Gómez, Diego, Pablo Salvador, Julia Sanz, and José Luis Casanova (2021). “Regional estimation of garlic yield using crop, satellite and climate data in Mexico”. In: *Computers and Electronics in Agriculture* 181, p. 105943. doi. 10.1016/j.compag.2020.105943.
- Gómez-Chova, Luis, Ral Zurita-Milla, Luis Alonso, Julia Amorós-López, Luis Guanter, and Gustavo Camps-Valls (2011). “Gridding artifacts on medium-resolution satellite image time series: MERIS case study”. In: *IEEE Transactions on Geoscience and Remote Sensing* 49.7, pp. 2601–2611. doi. 10.1109/tgrs.2011.2108660.
- Gonzalez-Abril, L., H. Nuñez, C. Angulo, and F. Velasco (2014). “GSVM: An SVM for handling imbalanced accuracy between classes in bi-classification problems”. In: *Applied Soft Computing Journal* 17, pp. 23–31. doi. 10.1016/j.asoc.2013.12.013.
- Gonzalez-Sanchez, A, J Frausto-Solis, and W Ojeda-Bustamante (2014). “Predictive ability of machine learning methods for massive crop yield prediction”. In: *Spanish Journal of Agricultural Research* 12.2, pp. 313–328. doi. 10.5424/sjar/2014122-4439.
- Google (2021). *Sentinel-1 Algorithms* | Google Earth Engine.
- Gorelick, Noel, Matt Hancher, Mike Dixon, Simon Ilyushchenko, David Thau, and Rebecca Moore (2017). “Google Earth Engine: Planetary-scale geospatial analysis for everyone”. In: *Remote Sensing of Environment* 202, pp. 18–27. doi. 10.1016/j.rse.2017.06.031.

- Graesser, Jordan and Navin Ramankutty (2017). “Detection of cropland field parcels from Landsat imagery”. In: *Remote Sensing of Environment* 201, July, pp. 165–180. doi. 10.1016/j.rse.2017.08.027.
- Griffin, T W (2010). “The Spatial Analysis of Yield Data”. In: *Geostatistical Applications for Precision Agriculture*. Ed. by M A Oliver. Dordrecht: Springer Netherlands, pp. 89–116. doi. 10.1007/978-90-481-9133-8{\\_}4.
- Groher, Tanja, Katja Heitkämper, Achim Walter, Frank Liebisch, and Christina Umstätter (2020). “Status quo of adoption of precision agriculture enabling technologies in Swiss plant production”. In: *Precision Agriculture* 2020 21:6 21.6, pp. 1327–1350. doi. 10.1007/s11119-020-09723-5.
- Guijarro, Jose A. (2019). *CRAN - Package climatol*.
- Guijarro, José A. (2014). “Quality Control and Homogenization of Climatological Series”. In: *Handbook of Engineering Hydrology*. CRC Press, pp. 501–513. doi. 10.1201/b15625-28.
- Guzinski, Radoslaw and Héctor Nieto (2019). “Evaluating the feasibility of using Sentinel-2 and Sentinel-3 satellites for high-resolution evapotranspiration estimations”. In: *Remote Sensing of Environment* 221, pp. 157–172. doi. 10.1016/j.rse.2018.11.019.
- Haghverdi, Amir, Brian G. Leib, Robert A. Washington-Allen, Paul D. Ayers, and Michael J. Buschermohle (2015). “Perspectives on delineating management zones for variable rate irrigation”. In: *Computers and Electronics in Agriculture* 117, pp. 154–167. doi. 10.1016/j.compag.2015.06.019.
- Haghverdi, Amir, Robert A. Washington-Allen, and Brian G. Leib (2018). “Prediction of cotton lint yield from phenology of crop indices using artificial neural networks”. In: *Computers and Electronics in Agriculture* 152, pp. 186–197. doi. 10.1016/j.compag.2018.07.021.
- Hajnssek, Irena and Yves-Louis Desnos, eds. (2021). *Polarimetric Synthetic Aperture Radar Principles and Application*. 1st ed. Cham, Switzerland: Springer International Publishing, pp. XIV, 294. doi. 10.1007/978-3-030-56504-6.
- Han, Jiawei, Jian Pei, and Micheline Kamber (2011). *Data Mining: Concepts and Techniques : Concepts and Techniques*. Saint Louis, United States: Elsevier Science and Technology.
- Hanley, J. A. and B. J. McNeil (1982). “The meaning and use of the area under a receiver operating characteristic (ROC) curve”. In: *Radiology* 143.1, pp. 29–36. doi. 10.1148/radiology.143.1.7063747.
- Harrell, Frank E. (2001). *Regression Modeling Strategies*. 1st ed. New York: Springer, pp. XXIV, 572. doi. 10.1007/978-1-4757-3462-1.

- Hatfield, J. L., Anatoly A. Gitelson, James S. Schepers, and C. L. Walthall (2008). "Application of Spectral Remote Sensing for Agronomic Decisions". In: *Papers in Natural Resources*. doi. 10.2134/agronj2006.0370c.
- Hatfield, Jerry L. and John H. Prueger (2010). "Value of using different vegetative indices to quantify agricultural crop characteristics at different growth stages under varying management practices". In: *Remote Sensing* 2.2, pp. 562–578. doi. 10.3390/rs2020562.
- Hayes, Andrew F (2005). *Statistical Methods for Communication Science*. Mahwah, United States: Taylor and Francis Group.
- Henrich, V., A. Jung, C. Götze, C. Sandow, D. Thürkow, and C. Gläßer (2009). "Development of an online indices database: motivation, concept and implementation". In: *6th EARSeL Imaging Spectroscopy SIG Workshop Innovative Tool For Scientific And Commercial Environment Applications*. Tel Aviv, Israel.
- Henry, Chris, Mike Daniels, Mike Hamilton, and Jarrod Hardke (2018). "Water Management". In: *Rice production handbook*. Ed. by Jarrod T. Hardke. Little Rock, Arkansas: University of Arkansas- Division of Agriculture. Chap. 10.
- Heremans, Stien, Qinghan Dong, Beier Zhang, Lieven Bydekerke, and Jos Van Orshoven (2015). "Potential of ensemble tree methods for early-season prediction of winter wheat yield from short time series of remotely sensed normalized difference vegetation index and in situ meteorological data". In: *Journal of Applied Remote Sensing* 9.1, p. 097095. doi. 10.1117/1.jrs.9.097095.
- Heung, Brandon, Hung Chak Ho, Jin Zhang, Anders Knudby, Chuck E. Bulmer, and Margaret G. Schmidt (2016). "An overview and comparison of machine-learning techniques for classification purposes in digital soil mapping". In: *Geoderma* 265, pp. 62–77. doi. 10.1016/j.geoderma.2015.11.014.
- Hilker, Thomas et al. (2009). "A new data fusion model for high spatial- and temporal-resolution mapping of forest disturbance based on Landsat and MODIS". In: *Remote Sensing of Environment* 113.8, pp. 1613–1627. doi. 10.1016/j.rse.2009.03.007.
- Hochberg, Yosef (1988). "A Sharper Bonferroni Procedure for Multiple Tests of Significance". In: *Biometrika* 75.4, pp. 800–802. doi. 10.2307/2336325.
- Hoerl, Arthur E and Robert W Kennard (1970). "Ridge Regression: Biased Estimation for Nonorthogonal Problems". In: *Technometrics* 12.1, pp. 55–67. doi. 10.1080/00401706.1970.10488634.
- Hogg, Robert V (2014). *Probability and statistical inference*. Pearson Education.
- Holben, Brent N and Christopher O Justice (1980). "The topographic effect on spectral response from nadir-pointing sensors". In:



- Holm, Sture (1979). "A Simple Sequentially Rejective Multiple Test Procedure". In: *Scandinavian Journal of Statistics* 6.2, pp. 65–70.
- Houborg, Rasmus and Matthew F. McCabe (2016). "High-Resolution NDVI from Planet's Constellation of Earth Observing Nano-Satellites: A New Data Source for Precision Agriculture". In: *Remote Sensing 2016, Vol. 8, Page 768* 8.9, p. 768. doi. 10.3390/rs8090768.
- (2018). "A Cubesat enabled Spatio-Temporal Enhancement Method (CESTEM) utilizing Planet, Landsat and MODIS data". In: *Remote Sensing of Environment* 209, pp. 211–226. doi. 10.1016/j.rse.2018.02.067.
- Houborg, Rasmus, Joshua B. Fisher, and Andrew K. Skidmore (2015). "Advances in remote sensing of vegetation function and traits". In: *International Journal of Applied Earth Observation and Geoinformation* 43, pp. 1–6. doi. 10.1016/j.jag.2015.06.001.
- Huang, Chengquan et al. (2010). "Automated masking of cloud and cloud shadow for forest change analysis using Landsat images". In: *International Journal of Remote Sensing* 31.20, pp. 5449–5464. doi. 10.1080/01431160903369642.
- Huang, Jianxi et al. (2019). "Assimilation of remote sensing into crop growth models: Current status and perspectives". In: *Agricultural and Forest Meteorology* 276-277, p. 107609. doi. 10.1016/j.agrformet.2019.06.008.
- Huete, A., K. Didan, T. Miura, E. P. Rodriguez, X. Gao, and L. G. Ferreira (2002). "Overview of the radiometric and biophysical performance of the MODIS vegetation indices". In: *Remote Sensing of Environment* 83.1-2, pp. 195–213. doi. 10.1016/s0034-4257(02)00096-2.
- Huete, A.R (1988). "A soil-adjusted vegetation index (SAVI)". In: *Remote Sensing of Environment* 25.3, pp. 295–309. doi. 10.1016/0034-4257(88)90106-x.
- Hunt, E Raymond and Craig S T Daughtry (2018). "What good are unmanned aircraft systems for agricultural remote sensing and precision agriculture?" In: *International Journal of Remote Sensing* 39.15-16, pp. 5345–5376. doi. 10.1080/01431161.2017.1410300.
- Hunt, E. Raymond, Li Li, M. Tugrul Yilmaz, and Thomas J. Jackson (2011). "Comparison of vegetation water contents derived from shortwave-infrared and passive-microwave sensors over central Iowa". In: *Remote Sensing of Environment* 115.9, pp. 2376–2383. doi. 10.1016/j.rse.2011.04.037.
- Hunt, Merryn L., George Alan Blackburn, Luis Carrasco, John W. Redhead, and Clare S. Rowland (2019). "High resolution wheat yield mapping using Sentinel-2". In: *Remote Sensing of Environment* 233, p. 111410. doi. 10.1016/j.rse.2019.111410.
- IDEAM (2010). *Acerca de la identidad*.

- Ihuoma, Samuel O. and Chandra A. Madramootoo (2019). "Sensitivity of spectral vegetation indices for monitoring water stress in tomato plants". In: *Computers and Electronics in Agriculture* 163. doi. 10.1016/j.compag.2019.104860.
- Inglada, Jordi, Arthur Vincent, Marcela Arias, and Claire Marais-Sicre (2016). "Improved early crop type identification by joint use of high temporal resolution sar and optical image time series". In: *Remote Sensing* 8.5. doi. 10.3390/rs8050362.
- Inoue, Y et al. (2002). "Season-long daily measurements of multifrequency (Ka, Ku, X, C, and L) and full-polarization backscatter signatures over paddy rice field and their relationship with biological variables". In: *Remote Sensing of Environment* 81.2, pp. 194–204. doi. 10.1016/s0034-4257(01)00343-1.
- Inoue, Yoshio, Eiji Sakaiya, and Cuizhen Wang (2014). "Capability of C-band backscattering coefficients from high-resolution satellite SAR sensors to assess biophysical variables in paddy rice". In: *Remote Sensing of Environment* 140, pp. 257–266. doi. 10.1016/j.rse.2013.09.001.
- Instituto de Hidrología Meteorología y Estudios Ambientales de Colombia (2020). *Sistema de Información para la Gestión de Datos de Hidrología y Meteorología*.
- Instituto de Hidrología Meteorología y Estudios Ambientales de Colombia (IDEAM) (2021). *Consulta y Descarga de Datos Hidrometeorológicos*.
- International Society of Precision Agriculture (2019). *Precision Agriculture Definition*.
- Isaksson, A., M. Wallman, H. Göransson, and M. G. Gustafsson (2008). "Cross-validation and bootstrapping are unreliable in small sample classification". In: *Pattern Recognition Letters* 29.14, pp. 1960–1965. doi. 10.1016/j.patrec.2008.06.018.
- Jakubauskas, Mark E., David R. Legates, and Jude H. Kastens (2003). "Crop identification using harmonic analysis of time-series AVHRR NDVI data". In: *Computers and Electronics in Agriculture* 37.1-3, pp. 127–139. doi. 10.1016/s0168-1699(02)00116-3.
- Japkowicz, Nathalie and Shaju Stephen (2002). "The class imbalance problem: A systematic study". In: *Intelligent Data analysis*, pp. 429–449.
- Jarrold Hardke, Yeshe Wamishe, Gus Lorenz, and Nick Bateman (2018). "Rice Stand Establishment". In: *Rice production handbook*. Little Rock, Arkansas: University of Arkansas- Division of Agriculture. Chap. 4.
- Jensen, Elaine, Kerrie Farrar, Sian Thomas-Jones, Astley Hastings, Iain Donnison, and John Clifton-Brown (2011). "Characterization of flowering time diversity in *Miscanthus* species". In: *GCB Bioenergy* 3.5, pp. 387–400. doi. 10.1111/j.1757-1707.2011.01097.x.
- Jensen, Jhon (2007). *Remote sensing of the environment: an earth resource perspective*. United States of America: Pearson Prentice Hall.

- Jensen, John R (2014). *Remote sensing of the environment an earth resource perspective*. Second edi. Pearson Custom Library. Harlow, Essex, England: Pearson Education Limited.
- Jeong, Jig Han et al. (2016). “Random Forests for Global and Regional Crop Yield Predictions”. In: *PLOS ONE* 11.6, e0156571. doi. 10.1371/journal.pone.0156571.
- Ji-Hua, M, W Bing-Fang, and L Qiang-Zi (2006). “A Global Crop Growth Monitoring System Based on Remote Sensing”. In: *2006 IEEE International Symposium on Geoscience and Remote Sensing*, pp. 2277–2280. doi. 10.1109/igarss.2006.589.
- Jiang, Zhangyan, Alfredo R. Huete, Kamel Didan, and Tomoaki Miura (2008). “Development of a two-band enhanced vegetation index without a blue band”. In: *Remote Sensing of Environment* 112.10, pp. 3833–3845. doi. 10.1016/j.rse.2008.06.006.
- Johnson, Michael D., William W. Hsieh, Alex J. Cannon, Andrew Davidson, and Frédéric Bédard (2016). “Crop yield forecasting on the Canadian Prairies by remotely sensed vegetation indices and machine learning methods”. In: *Agricultural and Forest Meteorology* 218-219, pp. 74–84. doi. 10.1016/j.agrformet.2015.11.003.
- Joint Research Centre of the European Commission (2014). *Precision Agriculture: An opportunity for EU farmers - Potential support with the CAP 2014-2020*. Tech. rep. European Parliament.
- Jolliffe, Ian T. (1982). “A Note on the Use of Principal Components in Regression”. In: *Applied Statistics* 31.3, p. 300. doi. 10.2307/2348005.
- Jones, Hamlyn and Robin Vaughan (2010). *Remote sensing of vegetation: principles, techniques and applications*. United States: Oxford University Press Inc.
- Jönsson, Per and Lars Eklundh (2004). “TIMESAT - A program for analyzing time-series of satellite sensor data”. In: *Computers and Geosciences* 30.8, pp. 833–845. doi. 10.1016/j.cageo.2004.05.006.
- Joshi, Neha et al. (2016). “A review of the application of optical and radar remote sensing data fusion to land use mapping and monitoring”. In: *Remote Sensing* 8.1, pp. 1–23. doi. 10.3390/rs8010070.
- JRC et al. (2017). *Discussion document on the introduction of monitoring to substitute OTSC*. doi. 10.2760/258531.
- Kanjir, Urska Urška, Nataša Đurić, Tatjana Veljanovski, Natasa Duric, and Tatjana Veljanovski (2018). “Sentinel-2 based temporal detection of agricultural land use anomalies in support of common agricultural policy monitoring”. In: *ISPRS International Journal of Geo-Information* 7.10. doi. 10.3390/ijgi7100405.

- Kanke, Yumiko, Brenda Tubaña, Marilyn Dalen, and Dustin Harrell (2016). “Evaluation of red and red-edge reflectance-based vegetation indices for rice biomass and grain yield prediction models in paddy fields”. In: *Precision Agriculture* 17.5, pp. 507–530. doi. 10.1007/s11119-016-9433-1/tables/7.
- Karlson, Martin et al. (2020). “The Potential of Sentinel-2 for Crop Production Estimation in a Smallholder Agroforestry Landscape, Burkina Faso”. In: *Frontiers in Environmental Science* 0, p. 85. doi. 10.3389/fenvs.2020.00085.
- Kern, Anikó et al. (2018). “Statistical modelling of crop yield in Central Europe using climate data and remote sensing vegetation indices”. In: *Agricultural and Forest Meteorology* 260-261, pp. 300–320. doi. 10.1016/j.agrformet.2018.06.009.
- Khan, Ahmad et al. (2018). “Evaluating Landsat and RapidEye Data for Winter Wheat Mapping and Area Estimation in Punjab, Pakistan”. In: *Remote Sensing 2018, Vol. 10, Page 489* 10.4, p. 489. doi. 10.3390/rs10040489.
- Khan, M. R., C. A.J.M. J M de Bie, H. van Keulen, E. M.A. A Smaling, and R. Real (2010). “Disaggregating and mapping crop statistics using hypertemporal remote sensing”. In: *International Journal of Applied Earth Observation and Geoinformation* 12.1, pp. 36–46. doi. 10.1016/j.jag.2009.09.010.
- Khan, Mohammad Saleem, Manoj Semwal, Ashok Sharma, and Rajesh Kumar Verma (2019). “An artificial neural network model for estimating Mentha crop biomass yield using Landsat 8 OLI”. In: *Precision Agriculture 2019 21:1* 21.1, pp. 18–33. doi. 10.1007/s11119-019-09655-9.
- Khanal, Sami, John Fulton, Andrew Klopfenstein, Nathan Douridas, and Scott Shearer (2018). “Integration of high resolution remotely sensed data and machine learning techniques for spatial prediction of soil properties and corn yield”. In: *Computers and Electronics in Agriculture* 153, pp. 213–225. doi. 10.1016/j.compag.2018.07.016.
- Khosla, R and M M Alley (1999). “Soil-specific nitrogen management on Mid-Atlantic Coastal Plain soils”. In: *Better Crops* 83.3, pp. 6–7.
- Kim, Yi Hyun, S. Young Hong, and Hoonyol Lee (2008). “Radar backscattering measurement of a paddy rice field using multi-frequency(l, c and x) and full-polarization”. In: *International Geoscience and Remote Sensing Symposium (IGARSS)* 4.1. doi. 10.1109/igarss.2008.4779781.
- King, Lee Ann et al. (2017). “A multi-resolution approach to national-scale cultivated area estimation of soybean”. In: *Remote Sensing of Environment* 195, pp. 13–29. doi. 10.1016/j.rse.2017.03.047.

- Kirova, Maria et al. (2019). *Megatrends in the agri-food sector: global overview and possible policy response from an EU perspective*. Tech. rep. Brussels: European Parliament, Policy Department for Structural and Cohesion Policies.
- Klompenburg, Thomas van, Ayalew Kassahun, and Cagatay Catal (2020). “Crop yield prediction using machine learning: A systematic literature review”. In: *Computers and Electronics in Agriculture* 177, p. 105709. doi. 10.1016/j.compag.2020.105709.
- Kneizys, F, Eric Shettle, L Abreu, J Chetwynd, and G Anderson (1988). “User guide to LOWTRAN 7”. In: p. 146.
- Knudsen, Marie, Niels Halberg, Jørgen Olesen, John Byrne, Venkatesh Iyer, and Noah Toly (2006). “Global trends in agriculture and food systems”. In: *Global development of organic agriculture: challenges and prospects*. CABI. doi. 10.1079/9781845930783.0001.
- Koay, Jun Yi et al. (2007). “Paddy fields as electrically dense media: Theoretical modeling and measurement comparisons”. In: *IEEE Transactions on Geoscience and Remote Sensing* 45.9, pp. 2837–2849. doi. 10.1109/tgrs.2007.902291.
- Koch, B., R. Khosla, W. M. Frasier, D. G. Westfall, and D. Inman (2004). “Economic Feasibility of Variable-Rate Nitrogen Application Utilizing Site-Specific Management Zones”. In: *Agronomy Journal* 96.6, pp. 1572–1580. doi. 10.2134/agronj2004.1572.
- Kołcz akolcz, Aleksander, ieegeorg Abdur Chowdhury, and Joshua Alspector (2003). “Data duplication: an imbalance problem ?” In: *Workshop on Learning from Imbalanced Datasets II*. Washington.
- Kotchenova, Svetlana Y., Eric F. Vermote, Robert Levy, and Alexei Lyapustin (2008). “Radiative transfer codes for atmospheric correction and aerosol retrieval: intercomparison study”. In: *Applied Optics, Vol. 47, Issue 13, pp. 2215-2226* 47.13, pp. 2215–2226. doi. 10.1364/ao.47.002215.
- Kowalik, Wanda, Katarzyna Dabrowska-Zielinska, Michele Meroni, Teresa Urszula Raczka, and Allard de Wit (2014). “Yield estimation using SPOT-VEGETATION products: A case study of wheat in European countries”. In: *International Journal of Applied Earth Observation and Geoinformation* 32.1, pp. 228–239. doi. 10.1016/j.jag.2014.03.011.
- Kross, Angela, Heather McNairn, David Lapen, Mark Sunohara, and Catherine Champagne (2015). “Assessment of RapidEye vegetation indices for estimation of leaf area index and biomass in corn and soybean crops”. In: *International Journal of Applied Earth Observation and Geoinformation* 34.1, pp. 235–248. doi. 10.1016/j.jag.2014.08.002.

- Kruskal, William H. and W. Allen Wallis (1952). “Use of Ranks in One-Criterion Variance Analysis”. In: *Journal of the American Statistical Association* 47.260, pp. 583–621. doi. 10.1080/01621459.1952.10483441.
- Kuenzer, Claudia and Kim Knauer (2013). “Remote sensing of rice crop areas”. In: *International Journal of Remote Sensing* 34.6, pp. 2101–2139. doi. 10.1080/01431161.2012.738946.
- Kutner, Michael, Christopher Nachtsheim, John Neter, and William Li (2005). *Applied Linear Statistical Models*. 5th ed. New York: McGraw-Hill.
- Lambert, Marie-Julie, Pierre C. Sibiry Traoré, Xavier Blaes, Philippe Baret, and Pierre Defourny (2018). “Estimating smallholder crops production at village level from Sentinel-2 time series in Mali’s cotton belt”. In: *Remote Sensing of Environment* 216, pp. 647–657. doi. 10.1016/j.rse.2018.06.036.
- Landis, J Richard and Gary G Koch (1977). *The Measurement of Observer Agreement for Categorical Data*. Tech. rep. 1, pp. 159–174.
- Larose, Daniel T (2004). *Discovering Knowledge in Data : An Introduction to Data Mining*. Hoboken, United States: John Wiley and Sons, Incorporated.
- Lasaponara, R. (2006). “On the use of principal component analysis (PCA) for evaluating interannual vegetation anomalies from Spot/Vegetation NDVI temporal series”. In: *Ecological Modelling* 194.4, pp. 429–434. doi. 10.1016/j.ecolmodel.2005.10.035.
- Le, Trang T., Weixuan Fu, and Jason H. Moore (2020). “Scaling tree-based automated machine learning to biomedical big data with a feature set selector”. In: *Bioinformatics* 36.1, pp. 250–256. doi. 10.1093/bioinformatics/btz470.
- Le Toan, T et al. (1997). “Rice crop mapping and monitoring using ERS-1 data based on experiment and modeling results”. In: *IEEE Transactions on Geoscience and Remote Sensing* 35.1, pp. 41–56. doi. 10.1109/36.551933.
- Lemajic Blanka, Slavko, Vajsova Pär, and Johan Åstrand (2018). “New sensors benchmark report on PlanetScope Geometric benchmarking test for Common Agricultural Policy (CAP) purposes”. In: doi. 10.2760/178918.
- Leones Bazzi, Claudio, Eduardo Godoy De Souza, Kelyn Schenatto, Nelson Miguel Betzek, and Alan Gavioli (2019). “A software for the delineation of crop management zones (SDUM)”. In: *Australian Journal of Crop Science*. doi. 10.21475/ajcs.19.13.01.p1026.
- Leprince, Sébastien, Student Member, Sylvain Barbot, François Ayoub, and Jean-Philippe Avouac (2007). “Automatic and Precise Orthorectification, Coregistration, and Subpixel Correlation of Satellite Images, Application to Ground Deformation Measurements”. In: *IEEE TRANSACTIONS ON GEOSCIENCE AND REMOTE SENSING* 45.6. doi. 10.1109/tgrs.2006.888937.

- Leslie, Colin R, Larisa O Serbina, and Holly M Miller (2017). *Landsat and agriculture—Case studies on the uses and benefits of Landsat imagery in agricultural monitoring and production*. English. Tech. rep. Reston, VA, p. 34. doi. 10.3133/ofr20171034.
- Levene, Howard (1960). “Robust tests for equality of variances”. English. In: *Contributions to probability and statistics; essays in honor of Harold Hotelling*. Stanford, Calif.: Stanford University Press.
- Li, Kun, Brian Brisco, Shao Yun, and Ridha Touzi (2014). “Polarimetric decomposition with RADARSAT-2 for rice mapping and monitoring”. In: <http://dx.doi.org/10.5589/m12-024> 38.2, pp. 169–179. doi. 10.5589/m12-024.
- Li, Lin, Susan L. Ustin, and Mui Lay (2005). “Application of AVIRIS data in detection of oil-induced vegetation stress and cover change at Jornada, New Mexico”. In: *Remote Sensing of Environment* 94.1, pp. 1–16. doi. 10.1016/j.rse.2004.08.010.
- Li, Qingting, Cuizhen Wang, Bing Zhang, and Linlin Lu (2015). “Object-Based Crop Classification with Landsat-MODIS Enhanced Time-Series Data”. In: *Remote Sensing* 7.12, pp. 16091–16107. doi. 10.3390/rs71215820.
- Li, Wei et al. (2019). “Generating Red-Edge Images at 3 M Spatial Resolution by Fusing Sentinel-2 and Planet Satellite Products”. In: *Remote Sensing 2019, Vol. 11, Page 1422* 11.12, p. 1422. doi. 10.3390/rs11121422.
- Li, Xueyong et al. (2003). “Control of tillering in rice”. In: *Nature* 422.6932, pp. 618–621. doi. 10.1038/nature01518.
- Li, Zhan, Daniel Scheffler, Nicholas C. Coops, Nicholas Leach, and Torsten Sachs (2021). “Towards analysis ready data of optical CubeSat images: Demonstrating a hierarchical normalization framework at a wetland site”. In: *International Journal of Applied Earth Observation and Geoinformation* 103, p. 102502. doi. 10.1016/j.jag.2021.102502.
- Liang, Haoran, Lei Song, Jianxing Wang, Lili Guo, Xuzhi Li, and Ji Liang (2021). “Robust unsupervised anomaly detection via multi-time scale DCGANs with forgetting mechanism for industrial multivariate time series”. In: *Neurocomputing* 423, pp. 444–462. doi. 10.1016/j.neucom.2020.10.084.
- Lillesand, Thomas M., Ralph W. Kiefer, and Jonathan W. Chipman (2015). *Remote Sensing and Image Interpretation. 7th Edition*. Seventh. Vol. 81. 8. Wiley, pp. 615–616. doi. 10.14358/pers.81.8.615.
- Lin, Hui and Ming Li (2021). *Introduction to Data Science*.
- Lin, Shangrong, Jing Li, Qinhua Liu, Longhui Li, Jing Zhao, and Wentao Yu (2019). “Evaluating the effectiveness of using vegetation indices based on red-edge reflectance from Sentinel-2 to estimate gross primary productivity”. In: *Remote Sensing* 11.11. doi. 10.3390/rs11111303.

- Liu, Chang an, Zhong xin Chen, Yun Shao, Jin song Chen, Tuya Hasi, and Hai zhu Pan (2019). *Research advances of SAR remote sensing for agriculture applications: A review*. doi. 10.1016/s2095-3119(18)62016-7.
- Liu, Kailou, Yazhen Li, and Huiwen Hu (2014). “Estimating the effect of urease inhibitor on rice yield based on NDVI at key growth stages”. In: *Frontiers of Agricultural Science and Engineering* 1.2, pp. 150–157. doi. 10.15302/j-fase-2014028.
- Liu, Lingling, Xiaoyang Zhang, Yunyue Yu, Feng Gao, and Zhengwei Yang (2018). “Real-Time Monitoring of Crop Phenology in the Midwestern United States Using VIIRS Observations”. In: *Remote Sensing 2018, Vol. 10, Page 1540* 10.10, p. 1540. doi. 10.3390/rs10101540.
- Liu, Xiaowei et al. (2016). “Effect of N Fertilization Pattern on Rice Yield, N Use Efficiency and Fertilizer-N Fate in the Yangtze River Basin, China”. In: doi. 10.1371/journal.pone.0166002.
- Liu, Zhengjia et al. (2017). “Spring green-up date derived from GIMMS3g and SPOT-VGT NDVI of winter wheat cropland in the North China Plain”. In: *ISPRS Journal of Photogrammetry and Remote Sensing* 130, pp. 81–91. doi. 10.1016/j.isprsjprs.2017.05.015.
- Lobell, David B and Sharon M Gourdj (2012). “The Influence of Climate Change on Global Crop Productivity”. In: *Plant Physiology* 160.4, pp. 1686–1697. doi. 10.1104/pp.112.208298.
- Lobell, David B., J. Ivan Ortiz-Monasterio, Adam M. Sibley, and V. S. Sohu (2013). “Satellite detection of earlier wheat sowing in India and implications for yield trends”. In: *Agricultural Systems* 115, pp. 137–143. doi. 10.1016/j.agsy.2012.09.003.
- Londoño, Jose Luis (2016). *Resolución por la cual se resuelve la solicitud de declaración de protección y delegación de facultad para autorizar el uso de una Denominación de Origen*.
- Long, John A., Rick L. Lawrence, Mark C. Greenwood, Lucy Marshall, and Perry R. Miller (2013). “Object-oriented crop classification using multitemporal ETM+ SLC-off imagery and random forest”. In: *GIScience and Remote Sensing* 50.4, pp. 418–436. doi. 10.1080/15481603.2013.817150.
- López-Granados, F (2011). “Weed detection for site-specific weed management: mapping and real-time approaches”. In: *Weed Research* 51.1, pp. 1–11. doi. 10.1111/j.1365-3180.2010.00829.x.
- Lopez-Sanchez, J M, S R Cloude, and J D Ballester-Berman (2012). “Rice Phenology Monitoring by Means of SAR Polarimetry at X-Band”. In: *IEEE Transactions on Geoscience and Remote Sensing* 50.7, pp. 2695–2709. doi. 10.1109/tgrs.2011.2176740.



- Lopez-Sanchez, J M, F Vicente-Guijalba, J D Ballester-Berman, and S R Cloude (2014). “Polarimetric Response of Rice Fields at C-Band: Analysis and Phenology Retrieval”. In: *IEEE Transactions on Geoscience and Remote Sensing* 52.5, pp. 2977–2993. doi. 10.1109/tgrs.2013.2268319.
- Lopez-Sanchez, J.M., F. Vicente-Guijalba, J.D. Ballester-Berman, and S.R. Cloude (2013). “Estimating Phenology of Agricultural Crops from Space”. In: *ESA Living Planet Symposium*. Edinburgh, UK.
- Maclean, J. L., D. C. Dawe, B. Hardy, and G. P. Hettel, eds. (2002). *Rice Almanac: source book for the most important economic activity on earth*. 3rd ed. CABI. doi. 10.1079/9780851996363.0000.
- Mahlein, Anne-Katrin (2016). “Plant Disease Detection by Imaging Sensors – Parallels and Specific Demands for Precision Agriculture and Plant Phenotyping”. In: *The American Phytopathological Society* 100.2, pp. 241–254. doi. 10.1094/pdis-03-15-0340-fe.
- Maitra, Sanjit, Micheal G. Gartley, Jason Faulring, and John P. Kerekes (2013). “Characterization of basic scattering mechanisms using laboratory based polarimetric synthetic aperture radar imaging”. In: *International Geoscience and Remote Sensing Symposium (IGARSS)*, pp. 4479–4482. doi. 10.1109/igarss.2013.6723830.
- Maki, Masayasu and Koki Homma (2014). “Empirical regression models for estimating multiyear leaf area index of rice from several vegetation indices at the field scale”. In: *Remote Sensing* 6.6, pp. 4764–4779. doi. 10.3390/rs6064764.
- Mandal, Dipankar et al. (2020). “Dual polarimetric radar vegetation index for crop growth monitoring using sentinel-1 SAR data”. In: *Remote Sensing of Environment* 247.January, p. 111954. doi. 10.1016/j.rse.2020.111954.
- Mandanici, Emanuele and Gabriele Bitelli (2016). “Preliminary comparison of sentinel-2 and landsat 8 imagery for a combined use”. In: *Remote Sensing* 8.12. doi. 10.3390/rs8121014.
- Maohua, Wang (2001). “Possible adoption of precision agriculture for developing countries at the threshold of the new millennium”. In: *Computers and Electronics in Agriculture* 30.1-3, pp. 45–50. doi. 10.1016/s0168-1699(00)00154-x.
- Marchant, B. P., N. P.A. Saby, R. M. Lark, P. H. Bellamy, C. C. Jolivet, and D. Arrouays (2010). “Robust analysis of soil properties at the national scale: Cadmium content of French soils”. In: *European Journal of Soil Science* 61.1, pp. 144–152. doi. 10.1111/j.1365-2389.2009.01212.x.
- Marchant, Ben et al. (2019). “Establishing the precision and robustness of farmers’ crop experiments”. In: *Field Crops Research* 230, pp. 31–45. doi. 10.1016/j.fcr.2018.10.006.

- Marchesi, Claudia, James F. Thompson, and Richard E Plant (2010). “Factors Underlying Spatial Variability in Rice (*Oryza sativa* L.) Grain Quality at Field and Regional Level”. In: *Agrociencia Uruguay* 17.1, pp. 55–64.
- Mazoyer, Marcel and Laurence. Roudart (2006). “A history of world agriculture : from the neolithic age to the current crisis”. In: p. 528.
- Mbow, Cheikh et al. (2019). “Food security”. In: *Climate Change and Land: an IPCC special report on climate change, desertification, land degradation, sustainable land management, food security, and greenhouse gas fluxes in terrestrial ecosystems*. IPCC. Chap. 5, pp. 437–550.
- McCann, Cooper, Kevin S. Repasky, Rick Lawrence, and Scott Powell (2017). “Multi-temporal mesoscale hyperspectral data of mixed agricultural and grassland regions for anomaly detection”. In: *ISPRS Journal of Photogrammetry and Remote Sensing* 131, pp. 121–133. doi. 10.1016/j.isprsjprs.2017.07.015.
- McCuen, Richard H. (2017). *Hydrologic Analysis And Design*. 4th ed. Maryland: Pearson.
- McDonald, John (2014). *Handbook of Biological Statistics*. 3rd. Baltimore, Maryland: Sparky House Publishing.
- McKee, Thomas B., Nolan J. Doesken, and John Kleist (1993). “The relationship of drought frequency and duration to time scales”. In: *Proceedings of the Eighth Conference on Applied Climatology*. Anaheim, USA,
- McNairn, Heather and Jiali Shang (2016). *A Review of Multitemporal Synthetic Aperture Radar (SAR) for Crop Monitoring*. Springer, Cham, p. 445. doi. 10.1007/978-3-319-47037-5.
- McNairn, Heather, Catherine Champagne, Jiali Shang, Delmar Holmstrom, and Gordon Reichert (2009a). “Integration of optical and Synthetic Aperture Radar (SAR) imagery for delivering operational annual crop inventories”. In: *ISPRS Journal of Photogrammetry and Remote Sensing* 64.5, pp. 434–449. doi. 10.1016/j.isprsjprs.2008.07.006.
- McNairn, Heather, Jiali Shang, Xianfeng Jiao, and Catherine Champagne (2009b). “The contribution of ALOS PALSAR multipolarization and polarimetric data to crop classification”. In: *IEEE Transactions on Geoscience and Remote Sensing* 47.12, pp. 3981–3992. doi. 10.1109/tgrs.2009.2026052.
- McNairn, Heather, Xianfeng Jiao, Anna Pacheco, Abhijit Sinha, Weikai Tan, and Yifeng Li (2018). “Estimating canola phenology using synthetic aperture radar”. In: *Remote Sensing of Environment* 219. July, pp. 196–205. doi. 10.1016/j.rse.2018.10.012.
- McPhee, John E., Diogenes L. Antille, Jeff N. Tullberg, Richard B. Doyle, and Mark Boersma (2020). “Managing soil compaction - A choice of low-mass autonomous

- vehicles or controlled traffic?” In: *Biosystems Engineering* 195, pp. 227–241. doi. 10.1016/j.biosystemseng.2020.05.006.
- Meier, U. et al. (2009). “The BBCH system to coding the phenological growth stages of plants-history and publications”. In: *Journal für Kulturpflanzen* 61.2, pp. 41–52. doi. 10.5073/jfk.2009.02.01.
- Meier, Uwe, ed. (2001). *Growth stages of mono-and dicotyledonous plants. BBCH monograph*. 2nd ed. Vol. 49(2), pp. 66–70.
- Méndez-Vázquez, L. Josué, Andrés Lira-Noriega, Rodrigo Lasa-Covarrubias, and Sergio Cerdeira-Estrada (2019). “Delineation of site-specific management zones for pest control purposes: Exploring precision agriculture and species distribution modeling approaches”. In: *Computers and Electronics in Agriculture* 167, p. 105101.
- Meroni, Michele, Michel M. Verstraete, Felix Rembold, Ferdinando Urbano, and François Kayitakire (2014). “A phenology-based method to derive biomass production anomalies for food security monitoring in the Horn of Africa”. In: *International Journal of Remote Sensing* 35.7, pp. 2472–2492. doi. 10.1080/01431161.2014.883090.
- Meroni, Michele, Dominique Fasbender, Felix Rembold, Clement Atzberger, and Anja Klisch (2019). “Near real-time vegetation anomaly detection with MODIS NDVI: Timeliness vs. accuracy and effect of anomaly computation options”. In: *Remote Sensing of Environment* 221, pp. 508–521. doi. 10.1016/j.rse.2018.11.041.
- Midi, Habshah, S.K. Sarkar, and Sohel Rana (2013). “Collinearity diagnostics of binary logistic regression model”. In: *Journal of Interdisciplinary Mathematics* 13.3, pp. 253–267. doi. 10.1080/09720502.2010.10700699.
- Minasny, Budiman, Dian Fiantis, Kurniatun Hairiah, and Meine Van Noordwijk (2021). “Applying volcanic ash to croplands – The untapped natural solution”. In: *Soil Security* 3, p. 100006. doi. 10.1016/j.soisec.2021.100006.
- Ministerio de Agricultura y Desarrollo Rural (2019). *Evaluaciones Agropecuarias Municipales*. Bogota.
- Mishra, Subhadra, Debahuti Mishra Santra, and Gour Hari (2016). “Applications of Machine Learning Techniques in Agricultural Crop Production: A Review Paper”. In: *Indian Journal of Science and Technology* 9.38, pp. 1–14. doi. 10.17485/ijst/2016/v9i38/95032.
- Mkhabela, M. S., P. Bullock, S. Raj, S. Wang, and Y. Yang (2011). “Crop yield forecasting on the Canadian Prairies using MODIS NDVI data”. In: *Agricultural and Forest Meteorology* 151.3, pp. 385–393. doi. 10.1016/j.agrformet.2010.11.012.

- Mokhtari, Ali, Hamideh Noory, and Majid Vazifedoust (2018). “Improving crop yield estimation by assimilating LAI and inputting satellite-based surface incoming solar radiation into SWAP model”. In: *Agricultural and Forest Meteorology* 250-251. December 2017, pp. 159–170. doi. 10.1016/j.agrformet.2017.12.250.
- Moldenhauer, Karen, Paul Counce, and Jarrod Hardke (2013). “Rice Growth and Development”. In: *Arkansas Rice Production Handbook - MP192*. Ed. by Jarrod T. Hardke. Little Rock, United States of America: University of Arkansas Division of Agriculture. Chap. 2.
- Molina-Maturano, Janet, Stijn Speelman, and Hans De Steur (2020). “Constraint-based innovations in agriculture and sustainable development: A scoping review”. In: *Journal of Cleaner Production* 246, p. 119001. doi. 10.1016/j.jclepro.2019.119001.
- Mondal, Pinaki and Manisha Basu (2009). *Adoption of precision agriculture technologies in India and in some developing countries: Scope, present status and strategies*. doi. 10.1016/j.pnsc.2008.07.020.
- Montgomery, Douglas C, Elizabeth A Peck, G Geoffrey Vining, and G Geoffrey Vining (2012). *Introduction to Linear Regression Analysis*. Hoboken, United States: John Wiley and Sons, Incorporated.
- Moon, Minkyu, Andrew D. Richardson, and Mark A. Friedl (2021). “Multiscale assessment of land surface phenology from harmonized Landsat 8 and Sentinel-2, PlanetScope, and PhenoCam imagery”. In: *Remote Sensing of Environment* 266, p. 112716. doi. 10.1016/j.rse.2021.112716.
- Moral, F. J., J. M. Terrón, and J. R. Marques da Silva (2010). “Delineation of management zones using mobile measurements of soil apparent electrical conductivity and multivariate geostatistical techniques”. In: *Soil and Tillage Research* 106.2, pp. 335–343. doi. 10.1016/j.still.2009.12.002.
- Moreira, Alberto, Pau Prats-Iraola, Marwan Younis, Gerhard Krieger, Irena Hajnsek, and Konstantinos P. Papathanassiou (2013). “A tutorial on synthetic aperture radar”. In: *IEEE Geoscience and Remote Sensing Magazine* 1.1, pp. 6–43. doi. 10.1109/mgrs.2013.2248301.
- Moulin, Sophie, Alberte Fischer, Gérard Dedieu, and Richard Delécolle (1995). “Temporal variations in satellite reflectances at field and regional scales compared with values simulated by linking crop growth and SAIL models”. In: *Remote Sensing of Environment* 54.3, pp. 261–272. doi. 10.1016/0034-4257(95)00141-7.
- Mouret, Florian, Mohanad Albughdadi, Sylvie Duthoit, Denis Kouamé, Guillaume Rieu, and Jean-Yves Tournet (2021). “Outlier Detection at the Parcel-Level in Wheat and Rapeseed Crops Using Multispectral and SAR Time Series”. In: *Remote Sensing* 13.5, p. 956. doi. 10.3390/rs13050956.

- Mudereri, B T et al. (2019). “A comparative analysis of PlanetScope and Sentinel-2 space-borne sensors in mapping Striga weed using Guided Regularised Random Forest classification ensemble”. In: *ISPRS Geospatial Week*. Enschede, The Netherlands. doi. 10.5194/isprs-archives-xlii-2-w13-701-2019.
- Mulla, D and R Khosla (2015). “Historical Evolution and Recent Advances in Precision Farming”. In:
- Mulla, David J (2013). “Twenty five years of remote sensing in precision agriculture: Key advances and remaining knowledge gaps”. In: *Biosystems Engineering* 114.4, pp. 358–371. doi. 10.1016/j.biosystemseng.2012.08.009.
- Murphy, Kevin P (2012). *Machine Learning : A Probabilistic Perspective*. Cambridge, United States: MIT Press.
- Mzuku, M, R Khosla, R Reich, D Inman, F Smith, and L MacDonald (2005). “Spatial Variability of Measured Soil Properties across Site-Specific Management Zones”. In: *Soil Science Society of America Journal* 69.5, pp. 1572–1579. doi. <https://doi.org/10.2136/sssaj2005.0062>.
- Naes, Tormod and Bjørn-Helge Mevik (2001). “Understanding the collinearity problem in regression and discriminant analysis”. In: *Journal of Chemometrics* 15.4, 413–426. doi. 10.1002/cem.676.
- Nawar, Said, Ronald Corstanje, Graham Halcro, David Mulla, and Abdul M Mouazen (2017). “Chapter Four - Delineation of Soil Management Zones for Variable-Rate Fertilization: A Review”. In: ed. by Donald L B T *Advances in Agronomy Sparks*. Vol. 143. Academic Press, pp. 175–245. doi. 10.1016/bs.agron.2017.01.003.
- Nguyen, Duy Ba, Alexander Gruber, and Wolfgang Wagner (2016). “Mapping rice extent and cropping scheme in the Mekong Delta using Sentinel-1A data”. In: <http://dx.doi.org/10.1080/2150704X.2016.1225172> 7.12, pp. 1209–1218. doi. 10.1080/2150704x.2016.1225172.
- Nguyen, Thi Thu Ha, C. A.J.M. J M de Bie, Amjad Ali, E. M.A. A Smaling, and Thai Hoanh Chu (2012). “Mapping the irrigated rice cropping patterns of the Mekong delta, Vietnam, through hyper-temporal spot NDVI image analysis”. In: *International Journal of Remote Sensing* 33.2, pp. 415–434. doi. 10.1080/01431161.2010.532826.
- Ntoumanis, N (2002). “Motivational clusters in a sample of British physical education classes”. In: *Psychology of Sport and Exercise* 3.3, pp. 177–194. doi. 10.1016/s1469-0292(01)00020-6.
- Núñez Tello, Alberto and Hernando Lozano Quiroga (2017). *Origen y características geológicas de la Meseta de Ibagué*.

- Oberthür, Thomas, James Cock, Meike S. Andersson, Rosa N. Naranjo, Dario Castañeda, and Matthew Blair (2007). “Acquisition of low altitude digital imagery for local monitoring and management of genetic resources”. In: *Computers and Electronics in Agriculture* 58.1, pp. 60–77. doi. 10.1016/j.compag.2006.08.005.
- Ohana-Levi, Noa et al. (2019). “A weighted multivariate spatial clustering model to determine irrigation management zones”. In: *Computers and Electronics in Agriculture* 162, pp. 719–731. doi. 10.1016/j.compag.2019.05.012.
- Okada, Kensuke and Lorena Lopez-Galvis (2018). “Improving Resource Utilization Efficiency in Rice Production Systems with Contour-Levee Irrigation in Colombia: Application of Cutting-edge Science and Technology in Developing Countries”. In: *Crop Production under Stressful Conditions: Application of Cutting-edge Science and Technology in Developing Countries*. Chap. 5, pp. 71–86. doi. 10.1007/978-981-10-7308-3{\\\_}5.
- Oliver, C and S Quegan (2004). “Understanding Synthetic Aperture Radar Images”. In: Olson, Randal S. and Jason H. Moore (2019). “TPOT: A Tree-Based Pipeline Optimization Tool for Automating Machine Learning”. In: *Automated Machine Learning - Methods, Systems, Challenges*. Springer. Chap. 8, pp. 151–160.
- Olsson, Lennart et al. (2019). “Land degradation”. In: *Climate Change and Land: an IPCC special report on climate change, desertification, land degradation, sustainable land management, food security, and greenhouse gas fluxes in terrestrial ecosystems*. IPCC. Chap. 4, pp. 345–436.
- Organisation for Economic Co-operation and Development (OECD) and Food and Agriculture Organization (FAO) (2019). *OECD-FAO Agricultural Outlook 2019-2028*. Ed. by OECD-FAO. OECD-FAO Agricultural Outlook. OECD. doi. 10.1787/agr{\\\_}outlook-2019-en.
- (2021). *OECD-FAO Agricultural Outlook 2021-2030*. Paris: OECD. doi. 10.1787/19428846-en.
- Oza, S. R., S. Panigrahy, and J. S. Parihar (2008). “Concurrent use of active and passive microwave remote sensing data for monitoring of rice crop”. In: *International Journal of Applied Earth Observation and Geoinformation* 10.3, pp. 296–304. doi. 10.1016/j.jag.2007.12.002.
- Palacios-Orueta, Alicia et al. (2012). “Derivation of phenological metrics by function fitting to time-series of Spectral Shape Indexes AS1 and AS2: Mapping cotton phenological stages using MODIS time series”. In: *Remote Sensing of Environment* 128.2, pp. 148–159. doi. 10.1016/j.apgeog.2007.07.013.
- Palmer, Wayne C. (1965). “Meteorological Drought”. Washington DC.
- Pan, Yaozhong, Le Li, Jinshui Zhang, Shunlin Liang, Xiufang Zhu, and Damien Sulla-Menashe (2012). “Winter wheat area estimation from MODIS-EVI time series data

- using the Crop Proportion Phenology Index”. In: *Remote Sensing of Environment* 119, pp. 232–242. doi. 10.1016/j.rse.2011.10.011.
- Pan, Zhuokun et al. (2015). “Mapping crop phenology using NDVI time-series derived from HJ-1 A/B data”. In: *International Journal of Applied Earth Observation and Geoinformation* 34.1, pp. 188–197. doi. 10.1016/j.jag.2014.08.011.
- Panda, Sudhanshu Sekhar, Daniel P. Ames, and Suranjan Panigrahi (2010). “Application of Vegetation Indices for Agricultural Crop Yield Prediction Using Neural Network Techniques”. In: *Remote Sensing 2010, Vol. 2, Pages 673-696* 2.3, pp. 673–696. doi. 10.3390/rs2030673.
- Pang, Jiatai et al. (2021). “Pixel-level rice planting information monitoring in Fujin City based on time-series SAR imagery”. In: *International Journal of Applied Earth Observation and Geoinformation* 104, p. 102551. doi. 10.1016/j.jag.2021.102551.
- Pantazi, X E, D Moshou, T Alexandridis, R L Whetton, and A M Mouazen (2016). “Wheat yield prediction using machine learning and advanced sensing techniques”. In: *Computers and Electronics in Agriculture* 121, pp. 57–65. doi. 10.1016/j.compag.2015.11.018.
- Paulhus, J L H and M A Kohler (1952). “Interpolation of missing precipitation records”. English. In: *Monthly Weather Review* 80.8, pp. 129–133. doi. 10.1175/1520-0493(1952)080<0129:iompr>2.0.co;2.
- Peace Corps (1982). *Rice Production. A Training Manual and Field Guide to Small-Farm Irrigated Rice Production. Appropriate Technologies for Development*. Ed. by Michael Morris, p. 106.
- Pedelty, Jeffrey et al. (2007). “Generating a long-term land data record from the AVHRR and MODIS instruments”. In: *2007 IEEE international Geoscience and remote sensing Symposium*. IEEE, pp. 1021–1025.
- Pedregosa, Fabian et al. (2011). *Scikit-learn: Machine Learning in Python*. Tech. rep., pp. 2825–2830.
- Pérez, A. J., F. López, J. V. Benlloch, and S. Christensen (2000). “Colour and shape analysis techniques for weed detection in cereal fields”. In: *Computers and Electronics in Agriculture* 25.3, pp. 197–212. doi. 10.1016/s0168-1699(99)00068-x.
- Perfetti, Juan José, Álvaro Balcazar, Antonio Hernández, and José Leibovich (2013). *Políticas para el desarrollo de la agricultura en Colombia*. Bogota, pp. 187–247.
- Pete Bunting and Daniel Clewley (2020). *RSGISLib Image Registration Module*.
- Peterson, Thomas C et al. (1998). “Homogeneity adjustments of in situ Atmospheric Climate Data: A review”. In: *International Journal of Climatology* 18, pp. 1493–1517.

- Phan, Hoa, Thuy Le Toan, and Alexandre Bouvet (2021). “Understanding Dense Time Series of Sentinel-1 Backscatter from Rice Fields: Case Study in a Province of the Mekong Delta, Vietnam”. In: *Remote Sensing 2021, Vol. 13, Page 921* 13.5, p. 921. doi. 10.3390/rs13050921.
- Ping, J. L. and A. Dobermann (2005). “Processing of Yield Map Data”. In: *Precision Agriculture 2005* 6:2 6.2, pp. 193–212. doi. 10.1007/s11119-005-1035-2.
- Planet Labs (2019). *Planet Imagery Product Specifications*.
- Planet Labs Inc. (2021). *Planet Explorer*.
- Planet Labs Inc (2021). *Understanding PlanetScope Instruments*.
- Poghosyan, Armen and Alessandro Golkar (2017). “CubeSat evolution: Analyzing CubeSat capabilities for conducting science missions”. In: *Progress in Aerospace Sciences* 88, pp. 59–83. doi. 10.1016/j.paerosci.2016.11.002.
- Prudente, Victor Hugo Rohden, Vitor Souza Martins, Denis Corte Vieira, Nildson Rodrigues de França e. Silva, Marcos Adami, and Ieda Del Arco Sanches (2020). “Limitations of cloud cover for optical remote sensing of agricultural areas across South America”. In: *Remote Sensing Applications: Society and Environment* 20, p. 100414. doi. 10.1016/j.rsase.2020.100414.
- Puth, Marie Therese, Markus Neuhäuser, and Graeme D. Ruxton (2015). “Effective use of Spearman’s and Kendall’s correlation coefficients for association between two measured traits”. In: *Animal Behaviour* 102, pp. 77–84. doi. 10.1016/j.anbehav.2015.01.010.
- QGIS.org (2021). *QGIS Geographic Information System*.
- Qiu, Bingwen, Weijiao Li, Zhenghong Tang, Chongcheng Chen, and Wen Qi (2015). “Mapping paddy rice areas based on vegetation phenology and surface moisture conditions”. In: *Ecological Indicators* 56, pp. 79–86. doi. 10.1016/j.ecolind.2015.03.039.
- Quinlan, J. R. (1987). “Simplifying decision trees”. In: *International Journal of Man-Machine Studies* 27.3, pp. 221–234. doi. 10.1016/s0020-7373(87)80053-6.
- R Core Team (2018). *R: A Language and Environment for Statistical Computing*. Vienna, Austria.
- Rafiei Sardooi, Elham, Ali Azareh, Bahram Choubin, Saeed Barkhori, Vijay P. Singh, and Shahaboddin Shamshirband (2019). “Applying the remotely sensed data to identify homogeneous regions of watersheds using a pixel-based classification approach”. In: *Applied Geography* 111, p. 102071. doi. 10.1016/j.apgeog.2019.102071.
- Raney, R Keith (1998). “Radar Fundamentals: Technical Perspective”. In:
- Rashmi, K. V. and Ran Gilad-Bachrach (2015). “DART: Dropouts meet Multiple Additive Regression Trees”. In:



- Read, C B (1994). “Conditioning Diagnostics: Collinearity and Weak Data in Regression”. In: *Biometrics* 50.1, pp. 314–315.
- Reback, Jeff et al. (2021). *pandas-dev/pandas: Pandas 1.3.4*. doi. 10.5281/zenodo.5574486.
- Rembold, Felix, Clement Atzberger, Igor Savin, and Oscar Rojas (2013). “Using low resolution satellite imagery for yield prediction and yield anomaly detection”. In: *Remote Sensing* 5.4, pp. 1704–1733. doi. 10.3390/rs5041704.
- Rembold, Felix et al. (2015). “Remote sensing time series analysis for crop monitoring with the SPIRITS software: New functionalities and use examples”. In: *Frontiers in Environmental Science* 3.JUL. doi. 10.3389/fenvs.2015.00046.
- Rembold, Felix et al. (2019). “ASAP: A new global early warning system to detect anomaly hot spots of agricultural production for food security analysis”. In: *Agricultural Systems* 168, pp. 247–257. doi. 10.1016/j.agry.2018.07.002.
- Risal, Sandesh, Weihang Zhu, Pablo Guillen, and Li Sun (2021). “Improving phase prediction accuracy for high entropy alloys with Machine learning”. In: *Computational Materials Science* 192, p. 110389. doi. 10.1016/j.commatsci.2021.110389.
- Rodrigues, Arlete, André R S Marcal, and Mário Cunha (2016). “PhenoSat – A Tool for Remote Sensing Based Analysis of Vegetation Dynamics”. In: *Multitemporal Remote Sensing: Methods and Applications*. Ed. by Yifang Ban. Cham: Springer International Publishing, pp. 195–215. doi. 10.1007/978-3-319-47037-5\_{\\_}10.
- Rokach, Lior. and Oded Z Maimon (2008). *Data mining with decision trees theory and applications*. Series in machine perception and artificial intelligence ; v. 69. Singapore: World Scientific.
- Rosipal, Roman, Mark Girolami, Leonard J. Trejo, and Andrzej Cichocki (2001). “Kernel PCA for Feature Extraction and De-Noising in Nonlinear Regression”. In: *Neural Computing and Applications* 2001 10:3 10.3, pp. 231–243. doi. 10.1007/s521-001-8051-z.
- Rouse, J W, R H Haas, J A Schell, and D W Deering (1973). “Monitoring vegetation systems in the Great Plains with ERTS”. In: *Proceedings of the Third ERTS Symposium*. Vol. 1. Washington DC, pp. 309–317. doi. citeulike-article-id: 9507328.
- Saberioon, M M, M S M Amin, W Aimrun, A R Anuar, A Gholizadeh, and others (2013). “Multi-spectral images tetracam agriculture digital camera to estimate nitrogen and grain yield of rice at different growth stages”. In: *The Philippine Agricultural Scientist* 96.1, pp. 108–112.

- Sacks, William J., Delphine Deryng, Jonathan A. Foley, and Navin Ramankutty (2010). “Crop planting dates: An analysis of global patterns”. In: *Global Ecology and Biogeography* 19.5, pp. 607–620. doi. 10.1111/j.1466-8238.2010.00551.x.
- Sadeh, Yuval, Xuan Zhu, Karine Chenu, and David Dunkerley (2019). “Sowing date detection at the field scale using CubeSats remote sensing”. In: *Computers and Electronics in Agriculture* 157, pp. 568–580. doi. 10.1016/j.compag.2019.01.042.
- Sadeh, Yuval et al. (2021). “Fusion of Sentinel-2 and PlanetScope time-series data into daily 3 m surface reflectance and wheat LAI monitoring”. In: *International Journal of Applied Earth Observation and Geoinformation* 96, p. 102260. doi. 10.1016/j.jag.2020.102260.
- Sagan, Vasit et al. (2021). “Field-scale crop yield prediction using multi-temporal WorldView-3 and PlanetScope satellite data and deep learning”. In: *ISPRS Journal of Photogrammetry and Remote Sensing* 174, pp. 265–281. doi. 10.1016/j.isprsjprs.2021.02.008.
- Sakamoto, Toshihiro, Masayuki Yokozawa, Hitoshi Toritani, Michio Shibayama, Naoki Ishitsuka, and Hiroyuki Ohno (2005). “A crop phenology detection method using time-series MODIS data”. In: *Remote Sensing of Environment* 96.3-4, pp. 366–374. doi. 10.1016/j.rse.2005.03.008.
- Salcedo, Iván Alberto Lizarazo and Oscar Alberto Alfonso Carvajal (2021). “Aplicaciones de la agricultura de precisión en palma de aceite “*Elaeis Guineensis*” e híbrido O x G”. In: *Revista de Ingeniería* 33, pp. 124–130. doi. 10.16924/revinge.33.12.
- Schläpfer, D. and R. Richter (2010). “Geo-atmospheric processing of airborne imaging spectrometry data. Part 1: Parametric orthorectification”. In: *International Journal of Remote Sensing* 23.13, pp. 2609–2630. doi. 10.1080/01431160110115825.
- Schlemmer, M. et al. (2013). “Remote estimation of nitrogen and chlorophyll contents in maize at leaf and canopy levels”. In: *International Journal of Applied Earth Observation and Geoinformation* 25.1, pp. 47–54. doi. 10.1016/j.jag.2013.04.003.
- Schwalbert, Raí A., Telmo Amado, Geomar Corassa, Luan Pierre Pott, P. V. Vara Prasad, and Ignacio A. Ciampitti (2020). “Satellite-based soybean yield forecast: Integrating machine learning and weather data for improving crop yield prediction in southern Brazil”. In: *Agricultural and Forest Meteorology* 284, p. 107886. doi. 10.1016/j.agrformet.2019.107886.
- Segarra, Joel, Maria Luisa Buchailot, Jose Luis Araus, and Shawn C. Kefauver (2020). “Remote Sensing for Precision Agriculture: Sentinel-2 Improved Features and Ap-

- plications”. In: *Agronomy* 2020, Vol. 10, Page 641 10.5, p. 641. doi. 10.3390/agronomy10050641.
- Segurado, Pedro and Miguel B. Araújo (2004). “An evaluation of methods for modelling species distributions”. In: *Journal of Biogeography* 31.10, pp. 1555–1568. doi. 10.1111/j.1365-2699.2004.01076.x.
- Semeraro, Teodoro, Giovanni Mastroleo, Alessandro Pomes, Andrea Luvisi, Elena Gissi, and Roberta Aretano (2019). “Modelling fuzzy combination of remote sensing vegetation index for durum wheat crop analysis”. In: *Computers and Electronics in Agriculture* 156, pp. 684–692. doi. 10.1016/j.compag.2018.12.027.
- Serrano, Lydia, Iolanda Filella, Josep Peñuelas, and Josep Peñ (2000). *No Title*. doi. 10.2135/cropsci2000.403723x.
- Shafi, Uferah, Rafia Mumtaz, José García-Nieto, Syed Ali Hassan, Syed Ali Raza Zaidi, and Naveed Iqbal (2019). “Precision Agriculture Techniques and Practices: From Considerations to Applications”. In: *Sensors* 2019, Vol. 19, Page 3796 19.17, p. 3796. doi. 10.3390/s19173796.
- Shahhosseini, Mohsen, Rafael A Martinez-Feria, Guiping Hu, and Sotirios V Archontoulis (2019). “Maize yield and nitrate loss prediction with machine learning algorithms”. In: *Environmental Research Letters* 14.12, p. 124026. doi. 10.1088/1748-9326/ab5268.
- Shanahan, John F. et al. (2001). “Use of Remote-Sensing Imagery to Estimate Corn Grain Yield”. In: *Agronomy Journal* 93.3, pp. 583–589. doi. 10.2134/agronj2001.933583x.
- Shang, Jiali et al. (2015). “Mapping spatial variability of crop growth conditions using RapidEye data in Northern Ontario, Canada”. In: *Remote Sensing of Environment* 168, pp. 113–125. doi. 10.1016/j.rse.2015.06.024.
- Shapiro, S S and M B Wilk (1965). “An Analysis of Variance Test for Normality (Complete Samples)”. In: *Biometrika* 52.3/4, pp. 591–611. doi. 10.2307/2333709.
- Shaw, D. R. and F. S. Kelley (2005). “Evaluating Remote Sensing for Determining and Classifying Soybean Anomalies”. In: *Precision Agriculture* 6.5, pp. 421–429. doi. 10.1007/s11119-005-3681-9.
- Shendryk, Yuri, Yannik Rist, Catherine Ticehurst, and Peter Thorburn (2019). “Deep learning for multi-modal classification of cloud, shadow and land cover scenes in PlanetScope and Sentinel-2 imagery”. In: *ISPRS Journal of Photogrammetry and Remote Sensing* 157, pp. 124–136. doi. 10.1016/j.isprsjprs.2019.08.018.
- Shepherd, J D and J R Dymond (2003). “Correcting satellite imagery for the variance of reflectance and illumination with topography”. In: *International Journal of Remote Sensing* 24.17, pp. 3503–3514. doi. 10.1080/01431160210154029.

- Shoji, Sadao and Tadashi Takahashi (2002). “Environmental and agricultural significance of volcanic ash soils”. In: *Global Environmental Research-English Edition* 6.2, pp. 113–135.
- Sidak, Zbynek (1967). “Rectangular Confidence Regions for the Means of Multivariate Normal Distributions”. In: *Journal of the American Statistical Association* 62.318, pp. 626–633. doi. 10.2307/2283989.
- Silva-perez, Cristian, Armando Marino, and Iain Cameron (2020). “Monitoring Agricultural Fields Using Sentinel-1 and Temperature Data in Peru : Case Study of Asparagus ( *Asparagus officinalis* L .)” In: pp. 1–24. doi. 10.3390/rs12121993.
- Silvero, Nélica E.Q. et al. (2021). “Soil property maps with satellite images at multiple scales and its impact on management and classification”. In: *Geoderma* 397, p. 115089. doi. 10.1016/j.geoderma.2021.115089.
- Sishodia, Rajendra P., Ram L. Ray, and Sudhir K. Singh (2020). “Applications of remote sensing in precision agriculture: A review”. In: *Remote Sensing* 12.19, pp. 1–31. doi. 10.3390/rs12193136.
- Skakun, Sergii, Christopher O. Justice, Eric Vermote, and Jean-Claude Roger (2017). “Transitioning from MODIS to VIIRS: an analysis of inter-consistency of NDVI data sets for agricultural monitoring”. In: *International Journal of Remote Sensing* 39.4, pp. 971–992. doi. 10.1080/01431161.2017.1395970.
- Small, David (2011). “Flattening gamma: Radiometric terrain correction for SAR imagery”. In: *IEEE Transactions on Geoscience and Remote Sensing* 49.8, pp. 3081–3093. doi. 10.1109/tgrs.2011.2120616.
- Sokolova, Ekaterina, Oscar Ivarsson, Ann Lillieström, Nora K. Speicher, Henrik Rydberg, and Mia Bondelind (2022). “Data-driven models for predicting microbial water quality in the drinking water source using E. coli monitoring and hydrometeorological data”. In: *Science of The Total Environment* 802, p. 149798. doi. 10.1016/j.scitotenv.2021.149798.
- Sokolova, Marina, Nathalie Japkowicz, and Stan Szpakowicz (2006). “Beyond Accuracy, F-Score and ROC: A Family of Discriminant Measures for Performance Evaluation”. In: *AI 2006: Advances in Artificial Intelligence*. Ed. by Abdul Sattar and Byeong-ho Kang. Berlin, Heidelberg: Springer Berlin Heidelberg, pp. 1015–1021.
- Song, Conghe, Curtis E. Woodcock, Karen C. Seto, Mary Pax Lenney, and Scott A. Macomber (2001). “Classification and Change Detection Using Landsat TM Data: When and How to Correct Atmospheric Effects?” In: *Remote Sensing of Environment* 75.2, pp. 230–244. doi. 10.1016/s0034-4257(00)00169-3.
- STARS project (2017). *Image co-registration*.
- Student (1908). “The probable error of a mean”. In: *Biometrika*, pp. 1–25.

- Subdirección de Agrología (2004). *Estudio general de suelos y zonificación de tierras. Departamento del Tolima. Escala 1: 100000*. Tech. rep. Instituto Geográfico Agustín Codazzi (IGAC).
- Sudduth, Kenneth A. and Scott T. Drummond (2007). “Yield editor: Software for removing errors from crop yield maps”. In: *Agronomy Journal* 99.6, pp. 1471–1482. doi. 10.2134/agronj2006.0326.
- Sun, Wei, Brett Whelan, Alex B. McBratney, and Budiman Minasny (2013). “An integrated framework for software to provide yield data cleaning and estimation of an opportunity index for site-specific crop management”. In: *Precision Agriculture* 14.4, pp. 376–391. doi. 10.1007/s11119-012-9300-7.
- Taddeo, Sophie, Iryna Dronova, and Nicholas Depsky (2019). “Spectral vegetation indices of wetland greenness: Responses to vegetation structure, composition, and spatial distribution”. In: *Remote Sensing of Environment* 234, p. 111467. doi. 10.1016/j.rse.2019.111467.
- Takeda, Naoya et al. (2019). “Evaluation of water dynamics of contour-levee irrigation system in sloped rice fields in Colombia”. In: *Agricultural Water Management* 217. February, pp. 107–118. doi. 10.1016/j.agwat.2019.02.032.
- Tatsumi, Kenichi, Yosuke Yamashiki, Miguel Angel Canales Torres, and Cayo Leonidas Ramos Taipe (2015). “Crop classification of upland fields using Random forest of time-series Landsat 7 ETM+ data”. In: *Computers and Electronics in Agriculture* 115, pp. 171–179. doi. 10.1016/j.compag.2015.05.001.
- Teillet, P M, B Guindon, and D G Goodenough (1982). “On the Slope-Aspect Correction of Multispectral Scanner Data”. In: *Canadian Journal of Remote Sensing* 8.2, pp. 84–106. doi. 10.1080/07038992.1982.10855028.
- Tewkesbury, Andrew P., Alexis J. Comber, Nicholas J. Tate, Alistair Lamb, and Peter F. Fisher (2015). “A critical synthesis of remotely sensed optical image change detection techniques”. In: *Remote Sensing of Environment* 160, pp. 1–14. doi. 10.1016/j.rse.2015.01.006.
- Tharwat, Alaa (2021). “Classification assessment methods”. In: *Applied Computing and Informatics* 17.1, pp. 168–192. doi. 10.1016/j.aci.2018.08.003.
- Thomas, Nathan, Peter Bunting, Richard Lucas, Andy Hardy, Ake Rosenqvist, and Temilola Fatoyinbo (2018). “Mapping Mangrove Extent and Change: A Globally Applicable Approach”. In: *Remote Sensing* 10.9, p. 1466. doi. 10.3390/rs10091466.
- Thylen, Lars, P A Algerbo, Antje Giebel, Pierre C Robert, Richard H Rust, and William Earl Larson (2000). “An expert filter removing erroneous yield data.” In: *5th International Conference on Precision Agriculture*, Madison.

- Tibshirani, Robert (1996). “Regression Shrinkage and Selection Via the Lasso”. In: *Journal of the Royal Statistical Society: Series B (Methodological)* 58.1, pp. 267–288. doi. 10.1111/j.2517-6161.1996.tb02080.x.
- Toms, Silas (2015). *ArcPy and ArcGIS - Geospatial Analysis with Python*. Olton Birmingham, United Kingdom: Packt Publishing, Limited.
- Touzi, Ridha (2007). “Target scattering decomposition in terms of roll-invariant target parameters”. In: *IEEE Transactions on Geoscience and Remote Sensing* 45.1, pp. 73–84. doi. 10.1109/tgrs.2006.886176.
- Tricht, Kristof Van and Jeroen Dries (2019). “Terrascope Sentinel -1. Algorithm Theoretical Base Document”. In: pp. 1–21.
- Tripathi, Rahul et al. (2015). “Delineation of soil management zones for a rice cultivated area in eastern India using fuzzy clustering”. In: *CATENA* 133, pp. 128–136. doi. 10.1016/j.catena.2015.05.009.
- Tucker, C J and P J Sellers (1986). “Satellite remote sensing of primary production”. In: *International Journal of Remote Sensing* 7.11, pp. 1395–1416. doi. 10.1080/01431168608948944.
- Tufféry, Stéphane and Stéphane Tufféry (2011). *Data Mining and Statistics for Decision Making*. John Wiley and Sons, Incorporated.
- United Nations (2019). *World population prospects 2019*. 141. New York: United Nations.
- USDA Forest Service (2015). *Pest risk modelling and mapping for invasive alien species*. Ed. by Robert Venette. CABI. doi. 10.1079/9781780643946.0000.
- Van Zyl, Jakob and Yunjin Kim (2010). *Synthetic Aperture Radar Polarimetry*. Ed. by Joseph H. Yuen. Pasadena: NASA Jet Propulsion Laboratory, California Institute of Technology, p. 313.
- Vanino, Silvia et al. (2018). “Capability of Sentinel-2 data for estimating maximum evapotranspiration and irrigation requirements for tomato crop in Central Italy”. In: *Remote Sensing of Environment* 215, pp. 452–470. doi. 10.1016/j.rse.2018.06.035.
- Veloso, Amanda et al. (2017). “Understanding the temporal behavior of crops using Sentinel-1 and Sentinel-2-like data for agricultural applications”. In: *Remote Sensing of Environment* 199, pp. 415–426. doi. 10.1016/j.rse.2017.07.015.
- Vera, C et al. (2006). *The South American Low-Level Jet Experiment*. Tech. rep. January, pp. 63–78.
- Verbeiren, Sara, Herman Eerens, Isabelle Piccard, Ides Bauwens, and Jos Van Orshoven (2008). “Sub-pixel classification of SPOT-VEGETATION time series for the assessment of regional crop areas in Belgium”. In: *International Journal of Applied*

- Earth Observation and Geoinformation* 10.4, pp. 486–497. doi. 10.1016/j.jag.2006.12.003.
- Verbesselt, Jan, Achim Zeileis, and Martin Herold (2012). “Near real-time disturbance detection using satellite image time series”. In: *Remote Sensing of Environment* 123, pp. 98–108. doi. 10.1016/j.rse.2012.02.022.
- Verma, J P and Abdel-Salam G Abdel-Salam (2019). *Testing Statistical Assumptions in Research*. Newark, United States: John Wiley and Sons, Incorporated.
- Vermote, Eric F., Didier Tanré, Jean Luc Deuzé, Maurice Herman, and Jean Jacques Morcrette (1997). “Second simulation of the satellite signal in the solar spectrum, 6s: an overview”. In: *IEEE Transactions on Geoscience and Remote Sensing* 35.3, pp. 675–686. doi. 10.1109/36.581987.
- Vieira, Matheus Alves, Antonio Roberto Formaggio, Camilo Daleles Rennó, Clement Atzberger, Daniel Alves Aguiar, and Marcio Pupin Mello (2012). “Object Based Image Analysis and Data Mining applied to a remotely sensed Landsat time-series to map sugarcane over large areas”. In: *Remote Sensing of Environment* 123, pp. 553–562. doi. 10.1016/j.rse.2012.04.011.
- Vigneau, E., E. M. Qannari, and D. Bertrand (2002). “A new method of regression on latent variables. Application to spectral data”. In: *Chemometrics and Intelligent Laboratory Systems* 63.1, pp. 7–14. doi. 10.1016/S0169-7439(02)00032-1.
- Viña, Andres, Anatoly A. Gitelson, Anthony L. Nguy-Robertson, and Yi Peng (2011). “Comparison of different vegetation indices for the remote assessment of green leaf area index of crops”. In: *Remote Sensing of Environment* 115.12, pp. 3468–3478. doi. 10.1016/j.rse.2011.08.010.
- Vories, Earl, William Gene Stevens, Matthew Rhine, and Zachary Straatmann (2017). “Investigating irrigation scheduling for rice using variable rate irrigation”. In: *Agricultural Water Management* 179, pp. 314–323. doi. 10.1016/j.agwat.2016.05.032.
- Vreugdenhil, Mariette et al. (2020). “Sentinel-1 cross ratio and vegetation optical depth: A comparison over Europe”. In: *Remote Sensing* 12.20, pp. 1–19. doi. 10.3390/rs12203404.
- Vrieling, Anton, Kirsten M de Beurs, and Molly E Brown (2008). “Recent trends in agricultural production of Africa based on AVHRR NDVI time series”. In: *SPIE Remote Sensing*. Vol. 7104. October 2008. Cardiff, Wales, United Kingdom, pp. 1–10. doi. 10.1117/12.799824.
- Vu, D. H., K. M. Muttaqi, and A. P. Agalgaonkar (2015). “A variance inflation factor and backward elimination based robust regression model for forecasting monthly

- electricity demand using climatic variables”. In: *Applied Energy* 140, pp. 385–394. doi. 10.1016/j.apenergy.2014.12.011.
- Vuolo, Francesco, Martin Neuwirth, Markus Immitzer, Clement Atzberger, and Wai Tim Ng (2018). “How much does multi-temporal Sentinel-2 data improve crop type classification?” In: *International Journal of Applied Earth Observation and Geoinformation* 72, pp. 122–130. doi. 10.1016/j.jag.2018.06.007.
- Wang, Fu-min, Jing-feng Huang, Yan-lin Tang, and Xiu-zhen Wang (2007). “New Vegetation Index and Its Application in Estimating Leaf Area Index of Rice”. In: *Rice Science* 14.3, pp. 195–203. doi. 10.1016/s1672-6308(07)60027-4.
- Wang, Lin, Fu Cun Zhang, Yuan Shu Jing, Xiao Dong Jiang, Shen Bin Yang, and Xiao Mei Han (2014). “Multi-temporal detection of rice phenological stages using canopy stagespectrum”. In: *Rice Science* 21.2, pp. 108–115. doi. 10.1016/s1672-6308(13)60170-5.
- Wang, Lingli, John J. Qu, Xianjun Hao, and Qingping Zhu (2008). “Sensitivity studies of the moisture effects on MODIS SWIR reflectance and vegetation water indices”. In: *International Journal of Remote Sensing* 29.24, pp. 7065–7075. doi. 10.1080/01431160802226034.
- Wang, Tianxin et al. (2021). “Evaluation of crop coefficient and evapotranspiration data for sugar beets from landsat surface reflectances using micrometeorological measurements and weighing lysimetry”. In: *Agricultural Water Management* 244, p. 106533. doi. 10.1016/j.agwat.2020.106533.
- Wang, Wei et al. (2012). “Common Spectral Bands and Optimum Vegetation Indices for Monitoring Leaf Nitrogen Accumulation in Rice and Wheat”. In: *Journal of Integrative Agriculture* 11.12, pp. 2001–2012. doi. 10.1016/s2095-3119(12)60457-2.
- Weiss, M., F. Jacob, and G. Duveiller (2020). “Remote sensing for agricultural applications: A meta-review”. In: *Remote Sensing of Environment* 236. August 2019, p. 111402. doi. 10.1016/j.rse.2019.111402.
- Welch, Bernard Lewis (1947). “The generalisation of student’s problems when several different population variances are involved.” eng. In: *Biometrika* 34.1-2, pp. 28–35. doi. 10.1093/biomet/34.1-2.28.
- Whelan, Brett and James Taylor (2013). *Precision Agriculture for Grain Production Systems*. CSIRO Publishing, p. 208. doi. 10.1071/9780643107489.
- Whitcraft, Alyssa K., Eric F. Vermote, Inbal Becker-Reshef, and Christopher O. Justice (2015). “Cloud cover throughout the agricultural growing season: Impacts on passive optical earth observations”. In: *Remote Sensing of Environment* 156, pp. 438–447. doi. 10.1016/j.rse.2014.10.009.



- Wicaksono, Pramaditya and Wahyu Lazuardi (2018). “Assessment of PlanetScope images for benthic habitat and seagrass species mapping in a complex optically shallow water environment”. In: *International Journal of Remote Sensing* 39.17, pp. 5739–5765. doi. 10.1080/01431161.2018.1506951.
- Wiegand, C. L., A. J. Richardson, D. E. Escobar, and A. H. Gerbermann (1991). “Vegetation indices in crop assessments”. In: *Remote Sensing of Environment* 35.2-3, pp. 105–119. doi. 10.1016/0034-4257(91)90004-p.
- Wiegand, Craig, Gerry Anderson, Sarah Lingle, and David Escobar (1996). “Soil Salinity Effects on Crop Growth and Yield - Illustration of an Analysis and Mapping Methodology for Sugarcane”. In: *Journal of Plant Physiology* 148.3-4, pp. 418–424. doi. 10.1016/s0176-1617(96)80274-4.
- Wirth, Michael A (2004). *Morphological Image Analysis*.
- Wiseman, Grant, Heather McNairn, Saeid Homayouni, and Jiali Shang (2014). “RADARSAT-2 Polarimetric SAR response to crop biomass for agricultural production monitoring”. In: *IEEE Journal of Selected Topics in Applied Earth Observations and Remote Sensing* 7.11, pp. 4461–4471. doi. 10.1109/jstars.2014.2322311.
- Witten, Ian H., Frank Eibe, and Mark Hall (2011). *Data mining practical machine learning tools and techniques*. 3rd ed. The Morgan Kaufmann Series in Data Management Systems. Amsterdam: Elsevier/Morgan Kaufmann.
- Wohlmeyer, Heinrich and Theodor Quendler (2002). *The WTO, Agriculture and Sustainable Development*. Sheffield, UNITED KINGDOM: Taylor and Francis Group.
- Wójtowicz, M, A Wójtowicz, and J Piekarczyk (2016). *Application of remote sensing methods in agriculture*. Tech. rep., pp. 31–50.
- Wolfert, Sjaak, Lan Ge, Cor Verdouw, and Marc Jeroen Bogaardt (2017). “Big Data in Smart Farming – A review”. In: *Agricultural Systems* 153, pp. 69–80. doi. 10.1016/j.agsy.2017.01.023.
- Woodhouse, I. H., A. Marino, and I. Cameron (2011). “A standard index of spatial resolution for distributed targets in synthetic aperture radar imagery”. In: *International Journal of Remote Sensing* 32.23, pp. 7929–7938. doi. 10.1080/01431161.2010.502546.
- Woodhouse, Iain (2021). *What is Radar Backscatter? – EO College*.
- Woodhouse, Iain H (2006). *Introduction to microwave remote sensing*. Boca Raton: TaylorandFrancis.
- World Meteorological Organization (2012). *Standardized Precipitation Index User Guide*. Geneva, Switzerland.
- Xiang, Jing et al. (2013). “Australian Journal of Crop Science - Effect of deep placement of nitrogen fertilizer on growth, yield, and nitrogen uptake of aerobic rice”. In: *Australian Journal of Crop Science* 7.6, pp. 870–877.

- Xie, Qiaoyun et al. (2018). “Vegetation Indices Combining the Red and Red-Edge Spectral Information for Leaf Area Index Retrieval”. In: *IEEE Journal of Selected Topics in Applied Earth Observations and Remote Sensing* 11.5, pp. 1482–1492. doi. 10.1109/jstars.2018.2813281.
- Xiong, Jun et al. (2017). “Automated cropland mapping of continental Africa using Google Earth Engine cloud computing”. In: *ISPRS Journal of Photogrammetry and Remote Sensing* 126, pp. 225–244. doi. 10.1016/j.isprsjprs.2017.01.019.
- Xu, Chenyang, John J. Qu, Xianjun Hao, Michael H. Cosh, Zhiliang Zhu, and Laurel Gutenberg (2020). “Monitoring crop water content for corn and soybean fields through data fusion of MODIS and Landsat measurements in Iowa”. In: *Agricultural Water Management* 227, p. 105844.
- Xu, Xiangying et al. (2019). “Design of an integrated climatic assessment indicator (ICAI) for wheat production: A case study in Jiangsu Province, China”. In: *Ecological Indicators* 101, pp. 943–953. doi. 10.1016/j.ecolind.2019.01.059.
- Xue, Jinru and Baofeng Su (2017). “Significant Remote Sensing Vegetation Indices: A Review of Developments and Applications”. In: *Journal of Sensors* 2017. Ed. by Chenzong Li, p. 1353691. doi. 10.1155/2017/1353691.
- Yang, Huijin, Bin Pan, Ning Li, Wei Wang, Jian Zhang, and Xianlong Zhang (2021). “A systematic method for spatio-temporal phenology estimation of paddy rice using time series Sentinel-1 images”. In: *Remote Sensing of Environment* 259, p. 112394. doi. 10.1016/j.rse.2021.112394.
- Yang, Zheng Rong (2010). *Machine Learning Approaches To Bioinformatics*. Singapore, SINGAPORE: World Scientific Publishing Company.
- Yao, Rong Jiang et al. (2014). “Determination of site-specific management zones using soil physico-chemical properties and crop yields in coastal reclaimed farmland”. In: *Geoderma* 232-234, pp. 381–393. doi. 10.1016/j.geoderma.2014.06.006.
- Yin, He, Thomas Udelhoven, Rasmus Fensholt, Dirk Pflugmacher, and Patrick Hostert (2012). “How Normalized Difference Vegetation Index (NDVI) Trends from Advanced Very High Resolution Radiometer (AVHRR) and Système Probatoire d’Observation de la Terre VEGETATION (SPOT VGT) Time Series Differ in Agricultural Areas: An Inner Mongolian Case Study”. In: *Remote Sensing 2012, Vol. 4, Pages 3364-3389* 4.11, pp. 3364–3389. doi. 10.3390/rs4113364.
- Yoosefzadeh-Najafabadi, Mohsen, Hugh J. Earl, Dan Tulpan, John Sulik, and Milad Eskandari (2021). “Application of Machine Learning Algorithms in Plant Breeding: Predicting Yield From Hyperspectral Reflectance in Soybean”. In: *Frontiers in Plant Science* 0, p. 2169. doi. 10.3389/fpls.2020.624273.

- You, Xingzhi, Jihua Meng, Miao Zhang, and Taifeng Dong (2013). “Remote sensing based detection of crop phenology for agricultural zones in China using a new threshold method”. In: *Remote Sensing* 5.7, pp. 3190–3211. doi. 10.3390/rs5073190.
- Yousif, Osama and Yifang Ban (2016). “Object-Based Change Detection in Urban Areas Using Multitemporal High Resolution SAR Images with Unsupervised Thresholding Algorithms”. In: *Multitemporal Remote Sensing: Methods and Applications*. Ed. by Yifang Ban. Cham: Springer International Publishing, pp. 89–105. doi. 10.1007/978-3-319-47037-5{\\\_}5.
- Yuan, Lin, Jingcheng Zhang, Yeyin Shi, Chenwei Nie, Liguang Wei, and Jihua Wang (2014). “Damage Mapping of Powdery Mildew in Winter Wheat with High-Resolution Satellite Image”. In: *Remote Sensing 2014, Vol. 6, Pages 3611-3623* 6.5, pp. 3611–3623. doi. 10.3390/rs6053611.
- Yzarra Tito, Wilfredo Juliaa and Francisco Martiin Lopez Rios (2011). *Manual de Observaciones Fenológicas*. Lima, Peru: Servicio Nacional de Meteorología e hidrología.
- Zabel, Florian, Ruth Delzeit, Julia M. Schneider, Ralf Seppelt, Wolfram Mauser, and Tomáš Václavík (2019). “Global impacts of future cropland expansion and intensification on agricultural markets and biodiversity”. In: *Nature Communications 2019 10:1* 10.1, pp. 1–10. doi. 10.1038/s41467-019-10775-z.
- Zaghloul, Mohamed Sherif, Oliver Terna Iorhemen, Rania Ahmed Hamza, Joo Hwa Tay, and Gopal Achari (2021). “Development of an ensemble of machine learning algorithms to model aerobic granular sludge reactors”. In: *Water Research* 189, p. 116657. doi. 10.1016/j.watres.2020.116657.
- Zhang, Ke et al. (2019a). “Predicting rice grain yield based on dynamic changes in vegetation indexes during early to mid-growth stages”. In: *Remote Sensing* 11.4. doi. 10.3390/rs11040387.
- Zhang, Lei et al. (2015a). “Consensus Forecasting of Species Distributions: The Effects of Niche Model Performance and Niche Properties”. In: *PLOS ONE* 10.3. Ed. by Stefan Lötters, e0120056. doi. 10.1371/journal.pone.0120056.
- Zhang, Lei et al. (2019b). “Using boosted tree regression and artificial neural networks to forecast upland rice yield under climate change in Sahel”. In: *Computers and Electronics in Agriculture* 166, p. 105031. doi. 10.1016/j.compag.2019.105031.
- Zhang, Qin (2016). *Precision agriculture technology for crop farming*. eng. Ed. by Qin Zhang.
- Zhang, Ting Ting, Jia Guo Qi, Yu Gao, Zu Tao Ouyang, Sheng Lan Zeng, and Bin Zhao (2015b). “Detecting soil salinity with MODIS time series VI data”. In: *Ecological Indicators* 52, pp. 480–489. doi. 10.1016/j.ecolind.2015.01.004.

- Zhang, Xiaodong, Lijian Shi, Xinhua Jia, George Seielstad, and Craig Helgason (2010). “Zone mapping application for precision-farming: A decision support tool for variable rate application”. In: *Precision Agriculture* 11.2, pp. 103–114. doi. 10.1007/s11119-009-9130-4/tables/2.
- Zhang, Xiaoyang et al. (2003). “Monitoring vegetation phenology using MODIS”. In: *Remote Sensing of Environment* 84.3, pp. 471–475. doi. [https://doi.org/10.1016/S0034-4257\(02\)00135-9](https://doi.org/10.1016/S0034-4257(02)00135-9).
- Zhang, Zhongxing et al. (2018). “Exploring the clinical features of narcolepsy type 1 versus narcolepsy type 2 from European Narcolepsy Network database with machine learning”. In: *Scientific Reports* 8.1, p. 10628. doi. 10.1038/s41598-018-28840-w.
- Zhao, Wenjing, Masayuki Tamura, and Hidenori Takahashi (2001). “Atmospheric and spectral corrections for estimating surface albedo from satellite data using 6S code”. In: *Remote Sensing of Environment* 76.2, pp. 202–212. doi. 10.1016/S0034-4257(00)00204-2.
- Zheng, Hengbiao et al. (2016). “Detection of rice phenology through time series analysis of ground-based spectral index data”. In: *Field Crops Research* 198, pp. 131–139. doi. 10.1016/j.fcr.2016.08.027.
- Zhou, X. et al. (2017). “Predicting grain yield in rice using multi-temporal vegetation indices from UAV-based multispectral and digital imagery”. In: *ISPRS Journal of Photogrammetry and Remote Sensing* 130, pp. 246–255. doi. 10.1016/j.isprsjprs.2017.05.003.
- Zhu, LiuJun, Jeffrey P. Walker, Nan Ye, and Christoph Rüdiger (2019). “Roughness and vegetation change detection: A pre-processing for soil moisture retrieval from multi-temporal SAR imagery”. In: *Remote Sensing of Environment* 225, pp. 93–106. doi. 10.1016/j.rse.2019.02.027.
- Zhu, Xiufang, Rui Guo, Tingting Liu, and Kun Xu (2021). “Crop Yield Prediction Based on Agrometeorological Indexes and Remote Sensing Data”. In: *Remote Sensing 2021, Vol. 13, Page 2016* 13.10, p. 2016. doi. 10.3390/rs13102016.
- Zorrilla, Gonzalo, Cesar Martinez, Luis Berrio, Edgar Corredor, Luciano Carmona, and Edward Pulver (2012). “Improving Rice Production Systems in Latin America and the Caribbean”. In: *Eco-Efficiency: from vision to reality*. Cali, Colombia: International Center for Tropical Agriculture (CIAT). Chap. 10.
- Zyl, Jakob J van (2011). *Synthetic Aperture Radar Polarimetry*. Hoboken, United States: John Wiley and Sons, Incorporated.

## LIST OF PUBLICATIONS

One publication, shown below, has been created directly from the thesis, from which large portions of this published work is used within Chapter 5:

Liliana Castillo-Villamor et al. (2021b). “The Earth Observation-based Anomaly Detection (EOAD) system: A simple, scalable approach to mapping in-field and farm-scale anomalies using widely available satellite imagery”. In: *International Journal of Applied Earth Observation and Geoinformation* 104, p. 102535. doi. <https://doi.org/10.1016/j.jag.2021.102535>

# **Appendices**

## **Appendix A**

### **One-way Data Transfer Agreement**

### One-Way Data Transfer Agreement

THIS AGREEMENT dated 13<sup>th</sup> OF MARCH, 2019, is made BETWEEN:

BETWEEN

- (1) **ABERYSTWYTH UNIVERSITY** (registered charity number 1145141), whose administrative offices are at Research, Business & Innovation, Aberystwyth University, Visualisation Centre, Penglais Campus, Aberystwyth, Ceredigion, SY23 3BF (the "University"); and
- (2) **INVERSIONES AGROPECUARIAS DOIMA S.A.**, a company registered in Colombia under number NIT 890 700 056-5, whose registered address is KILOMETRO 11 VIA A GIRARDOT, PICALÉÑA, IBAGUE, DEPARTAMENTO DEL TOLIMA (the "Company")

Which are also referred to individually herein as "a Party" or collectively as the "the Parties".

### BACKGROUND

- (A) The University has entered into a Grant Agreement with Environment Systems Ltd dated 7<sup>th</sup> March 2017 for the Project entitled: "EO4cultivar – delivering analysis-ready and value-added data to the South American agricultural supply chain and farmer advisory services" funded by the UK Space Agency;
- (B) As part of the Project, three PhD studentships will be undertaken and the Company wishes to provide additional data to the University relating to the Project to enable the Student to carry out a research Project and submit a related thesis for examination in accordance with the University's regulations governing post-graduate study in fulfilment of the requirements of a higher degree of the University. The Parties further acknowledge that the research Project and associated work is intended to lead to academic publications and furtherance of the Student's career ("Permitted Purposes").
- (C) The Parties further acknowledge that in the course of the studentship the Parties may be exposed to proprietary and commercially valuable information or materials of the Company and/or the University. All Parties recognise the importance of holding in confidence such information or materials.

### TERMS AND CONDITIONS

#### 1. Defined Terms

For the purpose of this Agreement, the following terms shall be understood to mean:

"Confidential Information"	Information provided in documentary or by way of model or in other tangible form, information which at the time of provisions is marked or otherwise designated to show expressly or by necessary implication that it is imparted in confidence; and in respect of information that is imparted orally, any information that the Disclosing Party or its representatives informed the Receiving Party or its representatives at the time of disclosure was imparted in
----------------------------	--



	confidence; and in respect of Confidential Information imparted orally, any note or record of the disclosure; any copy of the foregoing; and the fact that discussions are taking place between the Parties.
"Disclosing Party"	Means the Party that discloses Confidential Information to the Receiving Party.
"Company Data"	Means field records per crop plot in "Hacienda el Escobal" including the following items: <ul style="list-style-type: none"> <li>• Sowing and harvesting dates of rice and sugar cane</li> <li>• Rice yield maps</li> <li>• Sugar cane and panela yields</li> <li>• Rice yield</li> <li>• Crop management activities performed per date</li> <li>• Location and values of crop progress monitoring measurements</li> <li>• Presence of pest and diseases (when available)</li> <li>• Sampling measurements taken as part of the student fieldwork.</li> <li>• Plants phenological stage over time (when available)</li> <li>• Crop plots boundaries</li> <li>• Crop varieties</li> <li>• Irrigation dates</li> </ul>
"Effective Date"	the date 1st written above.
"Information"	shall include information and data in the Field provided directly or indirectly by the Disclosing Party to the Receiving Party in oral or documentary form or by way of models, biological or chemical materials or other tangible form or by demonstrations and whether before, on or after the Effective Date. 'Information' includes without limitation both scientific and commercial information, including business plans and ideas.
"Project"	Means the research project carried out by University under the Grant Agreement dated 7 <sup>th</sup> March 2017 and includes the Student's PhD.
"Receiving Party"	Means the Party who receives Confidential Information from the Disclosing Party.
"Student"	Means Lliana Castillo Villamor of the University.
"Term"	Means from the last date of signature hereof until the submission of the thesis.

## 2. Ownership of the Company Data

2.1 The Company shall retain ownership of the Company Data at all times, and no rights, title or interest in or to the Company Data is hereby granted to the University, except as expressly provided in this Agreement.

## 3. Use of Company Data

3.1 The Company Data and other Confidential Information disclosed by the Company is provided for the Permitted Purposes, and shall only be used for the Permitted Purposes and not for commercial purposes.

3.2 The University undertakes to make no attempt to link the Company Data to other datasets held by the University and/or third parties, without prior written consent from the Company, provided that this shall not prevent the University from using the Company Data to complete the Permitted Purposes.

3.3 The University shall be responsible for the proper and safe handling, storage and use of the Company Data in accordance with instructions or advice which may be given by the Company, and in accordance with all applicable laws and regulations.

3.4 The Company Data and/or the Confidential Information disclosed by the Company or Disclosing Party shall not be provided to any third party without the prior written consent of the Company in relation to the Company Data or Disclosing Party in relation to the Confidential Information.

#### 4. Term and early termination

4.1 This Agreement shall have effect from the Effective Date, and shall then terminate automatically at the end of the Term, subject always to each Party's right to request the return of the Confidential Information (including Company Data) disclosed by them on two month's written notice.

4.2 On completion of the Permitted Purposes or earlier termination or expiry of this Agreement, whichever is earlier, the Receiving Party shall, at the request of the Disclosing Party return all Confidential Information disclosed by the Disclosing Party (including the Company Data) in its possession and (to the extent possible to do so) delete all copies of all Confidential Information disclosed by the Disclosing Party (including the Company Data) from its computer systems and or make such other disposal thereof as may be stipulated by the Disclosing Party.

4.3 Termination of this Agreement shall not affect any obligations that came into or continue in effect on or following termination of this Agreement.

4.4 Clauses 5 to 8 inclusive shall survive termination, for whatever reason, of this Agreement.

#### 5. Results and Intellectual Property

5.1 The present Agreement conveys no rights to either Party's intellectual property except that:

5.1.1 The Company grants the University the right to use the Company Data for the Permitted Purposes.

5.2 Subject to third party rights, the University agrees to notify the Company of any inventions made by University that include the Company Data.

5.3 Nothing in this Agreement shall be construed as conferring right to use the name of either Party or any of its proprietary name and/or trademarks in an advertising, publicity or commercial disclosure without obtaining the agreement of such Party.

## 6. Confidentiality

6.1 For the term of five (5) years from the Effective Date, the the Receiving Party undertakes to:

6.1.1 keep the Confidential Information as secret and confidential;

6.1.2 only disclose the Confidential Information under binding obligations of confidentiality (which it undertakes to enforce and for which it is legally responsible) only to those of its employees, students, sub-contractors, officers, consultants, subsidiaries, collaborators or agents who need to have access to it wholly necessarily and exclusively for the Permitted Purpose whose identity the Company shall provide to AU at AU's request;

6.1.3 use the Confidential Information only for the Permitted Purpose;

6.1.4 not to disclose or cause the Confidential Information to be disclosed to any third party without the prior written consent of AU;

6.1.5 to return all copies of AU's Confidential Information promptly at the request of AU.

6.2 The obligation in Clause 6.1 shall not apply where the Receiving Party can prove by written evidence that the Confidential Information:

6.2.1 was known to it prior to its receipt ; or

6.2.2 was in the public domain prior to its receipt ; or

6.2.3 becomes part of the public domain through no fault of the Company; or

6.2.4 becomes known to the Company through the action of a third party not in breach of any relevant legal obligation of confidentiality to AU disclosing such Confidential Information;

6.2.5 was already known to the Receiving Party, prior to disclosure by the Disclosing Party; or

6.2.6 it is required to disclose by an order of any court of competent jurisdiction provided that reasonable efforts shall be used by the Company to secure a protective order or equivalent over such information and provided further that the University shall be informed as soon as possible and be given an opportunity, if time permits, to make appropriate representations to such court, authority or stock exchange to attempt to secure that the information is kept confidential.

## 7. Publications

7.1 The University will form part of the actual carrying out of primary charitable purpose; that is, the advancement of education through teaching and research. There must therefore be some element of public benefit arising from the Project, and this is secured through the following sub-clauses.

7.1.1 This Agreement shall not prevent or hinder registered students including the Student of the University from submitting for degrees of that Party theses based on results obtained during the course of work undertaken as part of the Project including the work

undertaken under this Agreement; or from following the University's procedures for examination and for admission to postgraduate degree status.

7.1.2 In accordance with normal academic practice, all employees, students, agents or appointees of the Parties (including those who work on the Project) shall be permitted:-

7.1.2.1 following the procedures laid down in Clause 7.2, to publish results, jointly where applicable, obtained during the course of work undertaken as part of the Project; and

7.1.2.2 in pursuance of the University's academic functions, to discuss work undertaken as part of the Project in internal seminars and to give instruction within their organisation on questions related to such work.

7.2 At least thirty (30) days prior to any public presentation or publication related to the Project and the Company Data, the University<sup>[17(1)]</sup> shall supply the Company with a copy of any such proposed disclosure for review. The Company shall have thirty (30) days from receipt of such proposed disclosure to notify the University if a delay in publication is necessary in order for the Company to modify the proposed publication in order to protect any of its Confidential Information. A delay imposed on submission for proposed publication as a requirement made by the Company shall not last longer than is absolutely necessary; and shall not exceed three (3) months from the date of receipt of such proposed disclosure. Notification of the requirement for delay in submission for such proposed disclosure must be received by the University within thirty (30) days after the receipt of the proposed disclosure by the Company, failing which the University shall be free to assume that the Company has no objection to the proposed disclosure.

7.3 The University shall acknowledge the Company as the source of the Company Data in any and all publications reporting their use of the Company Data.

## 8. Liability and guarantees

8.1 The Company Data is experimental in nature, and accordingly:

8.1.1 The Company makes no representations of any kind, either express or implied, of merchantability or fitness for a particular purpose, or that the use of the Company Data will not infringe any patent, copyright, trademark or other proprietary rights and fitness for a particular purpose, or that the use of the Company Data will not infringe any patent, copyright, trademark or other proprietary rights; and

8.3 The Company shall not be liable to University in relation to the supply of the Company Data to University or its use by University. Except to the extent prohibited by law, the University shall indemnify and keep indemnified the Company from any and all claims, suits and liabilities arising from any use, storage or disposal of the Company Data by the University.

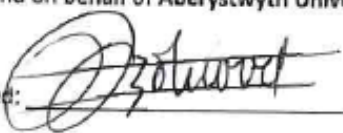
## 9. Applicable law and jurisdiction

English and Welsh law shall govern this Agreement and the English and Welsh courts shall have exclusive jurisdiction over any matter relating to it.

## 10. General

- 10.1 Clause headings are inserted in this Agreement for convenience only, and they shall not be taken into account in the interpretation of this Agreement.
- 10.2 Nothing in this Agreement shall create, imply or evidence any partnership or joint venture between the Parties or the relationship between them of principal and agent.
- 10.3 Each Party shall ensure that it has well defined arrangements for investigating and resolving allegations of research misconduct. Where an allegation of research misconduct arises in respect of an Individual Party's participation in the Project and leads to a subsequent formal investigation, the relevant Party shall inform the other of the investigation and its outcome.
- 12.5 No Party shall use the name or any trademark or logo of another Party or the name of any of its staff or students in any press release or product advertising, or for any other commercial purpose, without the prior written consent of the other Party.
- 12.6 Except as otherwise expressly provided for herein, the Parties confirm that nothing in this Agreement shall confer or purport to confer on any third party any benefit or any right to enforce any term of this Agreement for the purposes of the Contracts (Rights of Third Parties) Act 1999.
- 12.7 Any variation to this Agreement shall be in writing and signed by authorised signatories for each Party.
- 12.8 If any dispute arises out of this Agreement the Parties will first attempt to resolve the matter informally through designated senior representatives of each Party to the dispute, who are not otherwise involved with the Project. If the Parties are not able to resolve the dispute informally within a reasonable time not exceeding two (2) months from the date the informal process is requested by notice in writing they will attempt to settle it by mediation in accordance with the Centre for Effective Dispute Resolution (CEDR) Model Mediation Procedure.
- 12.10 If any one or more clauses or sub-clauses of this Agreement would result in this Agreement being prohibited pursuant to any applicable competition law then it or they shall be deemed to be omitted. The Parties shall uphold the remainder of this Agreement, and shall negotiate an amendment which, as far as legally feasible, maintains the economic balance between the Parties.
- 12.11 This Agreement may be executed in any number of counterparts, each of which when executed (and delivered) will constitute an original of this Agreement, but all counterparts will together constitute the same agreement. No counterpart will be effective until each Party has executed at least one counterpart.

For and on behalf of Aberystwyth University

Signed:   
 Name: Peter Botwood

Date: 21/03/19  
 Title: Head of Research Grants

For and on behalf of COMPANY

Signed: [Signature]  
Name: JOSE MARIA MADRIDDate: 13 DE MARZO, 2019  
Title: REPRESENTANTE LEGAL

I, the Academic Supervisor, acknowledge that I have read and understood the terms and conditions of this Agreement and accept to be bound personally by clauses 5, 6 and 7. I also agree to use all reasonable endeavours to enable the University to comply with its obligations under this Agreement.

Signature [Signature]Name: DR ANDY HARDY

I, the Student, acknowledge that I have read and understood the terms and conditions of this Agreement and accept to be bound personally by clauses 5, 6 and 7. I also agree to use all reasonable endeavours to enable the University to comply with its obligations under this Agreement.

Signature [Signature]Name: Liliana Castillo Villamor

## **Appendix B**

### **Pictures Taken During the Field Visit**





Farm staff performing *in-situ* yield and moisture measurements during the harvest.



Farm staff during a training session on data collection and management in the software QGIS.



Trenches built to control water flow in the plot head (highest part of the plot).



Levees construction using a ridge plough



Rice field at the seedling stage



Rice field at the tillering stage.



## **Appendix C**

### **Validation Points Records**



<b>ID:</b> P-01	<b>Date:</b> 13/01/2020
<b>Age:</b> 37 DAE	<b>Anomaly:</b> Yes
<b>Description:</b> Lower plant density	



<b>ID:</b> P-02	<b>Date:</b> 13/01/2020
<b>Age:</b> 37 DAE	<b>Anomaly:</b> Yes
<b>Description:</b> Lower plant density	



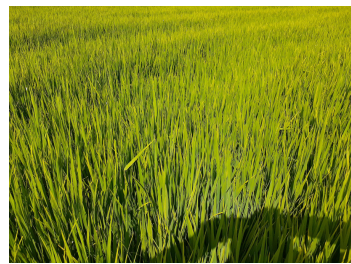
<b>ID:</b> P-03	<b>Date:</b> 13/01/2020
<b>Age:</b> 37 DAE	<b>Anomaly:</b> No
<b>Description:</b>	



<b>ID:</b> P-04	<b>Date:</b> 13/01/2020
<b>Age:</b> 37 DAE	<b>Anomaly:</b> Yes
<b>Description:</b> Water shortage, Lower canopy development	



<b>ID:</b> P-05	<b>Date:</b> 13/01/2020
<b>Age:</b> 37 DAE	<b>Anomaly:</b> Yes
<b>Description:</b> Lower plant density	



<b>ID:</b> P-06	<b>Date:</b> 16/01/2020
<b>Age:</b> 70 DAE	<b>Anomaly:</b> No
<b>Description:</b>	



<b>ID:</b> P-07	<b>Date:</b> 16/01/2020
<b>Age:</b> 70 DAE	<b>Anomaly:</b> No
<b>Description:</b>	



<b>ID:</b> P-08	<b>Date:</b> 16/01/2020
<b>Age:</b> 70 DAE	<b>Anomaly:</b> No
<b>Description:</b>	



<b>ID:</b> P-09	<b>Date:</b> 16/01/2020
<b>Age:</b> 70 DAE	<b>Anomaly:</b> No
<b>Description:</b>	



<b>ID:</b> P-10	<b>Date:</b> 16/01/2020
<b>Age:</b> 70 DAE	<b>Anomaly:</b> No
<b>Description:</b>	



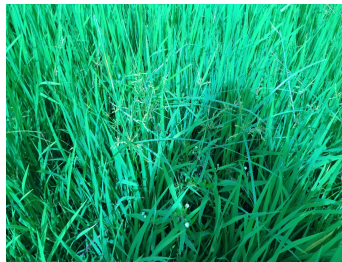
<b>ID:</b> P-11	<b>Date:</b> 16/01/2020
<b>Age:</b> 70 DAE	<b>Anomaly:</b> No
<b>Description:</b>	



<b>ID:</b> P-12	<b>Date:</b> 16/01/2020
<b>Age:</b> 70 DAE	<b>Anomaly:</b> No
<b>Description:</b>	



<b>ID:</b> P-13	<b>Date:</b> 16/01/2020
<b>Age:</b> 70 DAE	<b>Anomaly:</b> Yes
<b>Description:</b> Weeds presence	



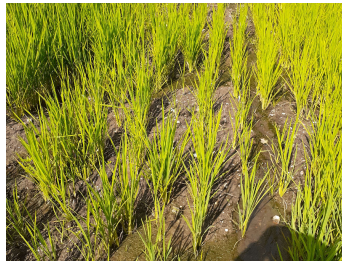
<b>ID:</b> P-14	<b>Date:</b> 16/01/2020
<b>Age:</b> 70 DAE	<b>Anomaly:</b> Yes
<b>Description:</b> Weeds presence	



<b>ID:</b> P-15	<b>Date:</b> 16/01/2020
<b>Age:</b> 70 DAE	<b>Anomaly:</b> No
<b>Description:</b>	



<b>ID:</b> P-16	<b>Date:</b> 16/01/2020
<b>Age:</b> 70 DAE	<b>Anomaly:</b> No
<b>Description:</b>	



<b>ID:</b> P-17	<b>Date:</b> 16/01/2020
<b>Age:</b> 70 DAE	<b>Anomaly:</b> Yes
<b>Description:</b> Lower plant density	



<b>ID:</b> P-18	<b>Date:</b> 16/01/2020
<b>Age:</b> 22 DAE	<b>Anomaly:</b> No
<b>Description:</b>	





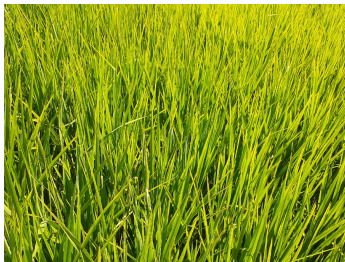
<b>ID:</b> P-19	<b>Date:</b> 16/01/2020
<b>Age:</b> 70 DAE	<b>Anomaly:</b> No
<b>Description:</b>	



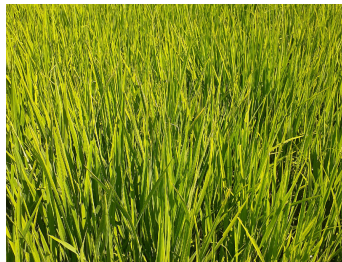
<b>ID:</b> P-20	<b>Date:</b> 16/01/2020
<b>Age:</b> 70 DAE	<b>Anomaly:</b> Yes
<b>Description:</b> Lower plant density	



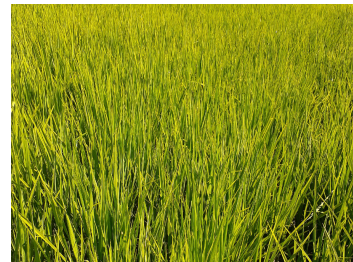
<b>ID:</b> P-21	<b>Date:</b> 16/01/2020
<b>Age:</b> 70 DAE	<b>Anomaly:</b> No
<b>Description:</b>	



<b>ID:</b> P-22	<b>Date:</b> 16/01/2020
<b>Age:</b> 70 DAE	<b>Anomaly:</b> No
<b>Description:</b>	



<b>ID:</b> P-23	<b>Date:</b> 16/01/2020
<b>Age:</b> 70 DAE	<b>Anomaly:</b> No
<b>Description:</b>	



<b>ID:</b> P-24	<b>Date:</b> 16/01/2020
<b>Age:</b> 70 DAE	<b>Anomaly:</b> No
<b>Description:</b>	



<b>ID:</b> P-25	<b>Date:</b> 16/01/2020
<b>Age:</b> 36 DAE	<b>Anomaly:</b> Yes
<b>Description:</b> Water shortage, Lower plant density, Lower canopy development	



<b>ID:</b> P-26	<b>Date:</b> 16/01/2020
<b>Age:</b> 36 DAE	<b>Anomaly:</b> Yes
<b>Description:</b> Water shortage, Lower canopy development	



<b>ID:</b> P-27	<b>Date:</b> 16/01/2020
<b>Age:</b> 36 DAE	<b>Anomaly:</b> Yes
<b>Description:</b> Water shortage, Lower canopy development	



<b>ID:</b> P-28	<b>Date:</b> 16/01/2020
<b>Age:</b> 36 DAE	<b>Anomaly:</b> Yes
<b>Description:</b> Water shortage, Lower canopy development	



<b>ID:</b> P-29	<b>Date:</b> 16/01/2020
<b>Age:</b> 33 DAE	<b>Anomaly:</b> No
<b>Description:</b>	



<b>ID:</b> P-30	<b>Date:</b> 17/01/2020
<b>Age:</b> 33 DAE	<b>Anomaly:</b> Yes
<b>Description:</b> Lower plant density	



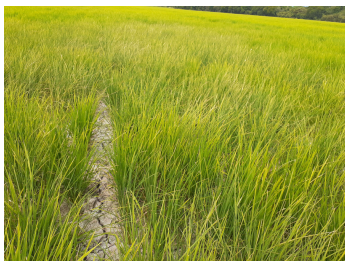
<b>ID:</b> P-31	<b>Date:</b> 17/01/2020
<b>Age:</b> 33 DAE	<b>Anomaly:</b> Yes
<b>Description:</b> Lower plant density	



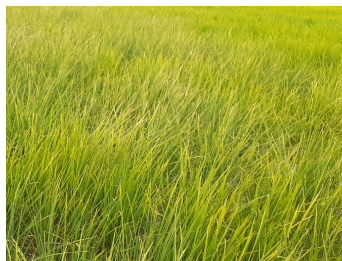
<b>ID:</b> P-32	<b>Date:</b> 17/01/2020
<b>Age:</b> 33 DAE	<b>Anomaly:</b> No
<b>Description:</b>	



<b>ID:</b> P-33	<b>Date:</b> 17/01/2020
<b>Age:</b> 33 DAE	<b>Anomaly:</b> No
<b>Description:</b>	



<b>ID:</b> P-34	<b>Date:</b> 20/01/2020
<b>Age:</b> 44 DAE	<b>Anomaly:</b> Yes
<b>Description:</b> Water shortage, Lower plant density, Lower canopy development	



<b>ID:</b> P-35	<b>Date:</b> 20/01/2020
<b>Age:</b> 44 DAE	<b>Anomaly:</b> No
<b>Description:</b>	



<b>ID:</b> P-36	<b>Date:</b> 13/01/2020
<b>Age:</b> 37 DAE	<b>Anomaly:</b> Yes
<b>Description:</b> Lower plant density	